Design and Development of Planar Antennas and Dielectric Devices for use at W Band Frequencies

Presented by,

Mark Deegan, B.Sc.

A thesis submitted for the degree of

Master of Science

Department of Experimental Physics

Maynooth University

Maynooth

Co. Kildare, Ireland

September 2018

Head of Department

Prof. J. Anthony Murphy

Research Supervisor

Dr. Neil Trappe

Contents

Contents
Abstract
Acknowledgements
Chapter 1 Background 1
  1.1 Overview 1
  1.2 The Universe at terahertz wavelengths 2
    1.2.1 Atmospheric transmission 3
    1.2.2 Standard cosmological model 4
    1.2.3 CMB 5
  1.3 Current scientific missions 7
    1.3.1 Ground based missions 8
    1.3.2 Space based missions 9
  1.4 Applications of terahertz research 11
    1.4.1 Medical imaging 11
    1.4.2 Spectroscopy 12
    1.4.3 Security Imaging 12
  1.5 Thesis outline 13
Chapter 2 Related theory 16
  2.1 Overview 16
  2.2 CST Studio Suite 17
    2.2.1 Finite Element Method 18
    2.2.2 Frequency solver 19
    2.2.3 Tetrahedral meshing 19
    2.2.4 Ports 20
    2.2.5 Farfield pattern 21
  2.3 Antenna theory 22
    2.3.1 S-parameters 22
    2.3.2 Farfield 24
  2.4 Printed Circuit Boards 25

2.5 Planar antennas 26
2.6 Horn antennas 28
2.7 Waveguides 29
  2.7.1 Rectangular waveguides 30
  2.7.2 Microstrip 31
  2.7.3 Coaxial cable 31
2.8 Vector Network Analyser 32
Chapter 3 W band patch antenna 35
3.1 Overview 35
3.2 Circular patch antenna 36
3.3 Rectangular patch antenna 46
3.4 Crosstalk between patch antenna 54
3.5 Coupling a wire feed to WR10 waveguide 65
3.6 Design parameters 70
3.7 Manufacture of prototype patch antennas 71
  3.7.1 Manufacturing process 71
  3.7.2 Testing process 74
  3.7.3 Results 75
3.8 Conclusion 77
Chapter 4 Side-fed patch antenna 79
4.1 Overview 79
4.2 Equipment 79
4.3 Coaxial short test 83
4.4 Rectangular fed patch antenna 85
4.5 Inset patch antenna 87
  4.5.1 Simulations of inset patch antenna 89
  4.5.2 Manufacture of inset patch antenna and design of connecting system 97
  4.5.3 Measurement of inset patch antenna 99
4.6 Thin dielectric inset patch antenna 102
  4.6.1 Simulations of thin dielectric side-fed patch antenna 103
  4.6.2 Measurement of thin dielectric patch antenna 107
4.7 Conclusion 113
Chapter 5 Alternative planar antenna designs 115
5.1 Overview 115

5.2 Design of endfire antennas 115

5.3 Slot antenna with coaxial feed 120

5.3.1 Simulation 120

5.3.2 Test of slot antenna with supporting structure 128

5.3.3 Test of slot antenna without supporting structure 131

5.4 Windowed metallic superstrate slot 135

5.5 U and E slot antennas 137

5.6 Conclusion 140

Chapter 6 Lenslet design 142

6.1 Overview 142

6.2 Lenslet design for planar antennas 142

6.2.1 Hemisphere lens 143

6.2.2 Cylindrical and elliptical cylindrical lenses 145

6.2.3 Plano-convex lens 150

6.2.4 Truncated plano-convex lens 153

6.3 Crosstalk analysis with plano-convex lens 157

6.3.1 Crosstalk in a $\mathbf{2} \times \mathbf{1}$-lenslet array 159

6.3.2 Crosstalk in a $\mathbf{3} \times \mathbf{1}$-lenslet array 164

6.4 Probe array lenslet design 168

6.4.1 Simulations of waveguide probes 170

6.4.2 Simulations of probe with plano-convex lens 172

6.4.3 Simulations of probe with truncated plano-convex lens 174

6.5 Lenses measurement 176

6.6 Waveguide probe array crosstalk 181

6.6.1 Simulation of crosstalk 181

6.6.2 Measurement of crosstalk 183

6.7 Conclusion 188

Chapter 7 Gaussian beam mode analysis 190

7.1 Overview 190

7.2 GBMA Theory 191

7.2.1 Describing the beam propagation 191

7.2.2 Gaussian beam decomposition 192

7.2.3 Edge taper and truncated plane 193

7.3 Truncation code implementation ... 195
  7.3.1 1-D model of diffraction from a slit ... 195
  7.3.2 2-D model ... 198
  7.3.3 Horn antenna with truncation ... 200
7.4 Pyramidal horn antenna analysis ... 203
  7.4.1 Experimental configuration ... 203
  7.4.2 Simulation of pyramidal horn antenna ... 204
  7.4.3 Comparison to expected ... 205
  7.4.4 Rectangular and circular truncation of pyramidal horn fields ... 207
7.5 Conclusion ... 212
Chapter 8 Conclusion and future work ... 213
8.1 Summary ... 213
8.2 Future Work ... 217
Chapter 9 Appendix ... 218
9.1 Glossary of terms ... 218
Bibliography ... 220

Abstract

The main topic examined in this thesis is the development of planar antennas for observations at W band frequencies. A large portion of this analysis is based on the specific development of devices as part of an ESA research package entitled “New Technology High Efficiency Horn Antennas for CMB Experiments and Far-Infrared Astronomy”. The development of W band focal plane pixels (planar antenna with small lenses) was part of the research in this work package. Several planar antenna designs are modelled and optimised in CST Studio Microwave Suite, a commercially available computer modelling software used extensively in order to predict the device performance around 100 GHz. The final designs were manufactured and their beam patterns were measured in the Vector Network Analyser (VNA) setup.

The main body of this research consisted of the development and analysis of patch antennas. The design of back-fed and side-fed patch antennas are modelled in the CST work environment, manufactured in-house and measured with the VNA.

A number of lenslet (small lenses for each planar antenna in the array) designs constructed from High Density Polyethylene (HDPE) are developed as part of this ESA contract in order to develop a lens array for a planar antenna array. A particular focus was put on reducing the potential crosstalk between neighbouring pixels and optimising the lens shape. The lenslets examined included a hemisphere, a cylindrical and a plano-convex lens. A novel truncated plano-convex lens was also analysed for the task of reducing crosstalk between neighbouring pixels. Plano-convex lenses with cleaved sides (referred to as a truncated lens) were manufactured and tested with the VNA. The crosstalk signal level caused by these lenslets between neighbouring pixels were considered and measured.

Additional topics developed include the analysis of a multi-moded terahertz horn antenna measured in an experimental setup in Cardiff University using GBMA (Gaussian Beam Mode Analysis). This 2.7 – 5 THz pyramidal horn antenna couples to Transition Edge Sensor detectors (TESs) and was placed in a cryogenic chamber to measure the farfield pattern. The antenna was illuminated by a terahertz source through a window in the cryostat. A GBMA model was extended to include truncation of the beam at this window in order verify no loss of signal and to ensure all power propagated though this window.

Acknowledgements

I would like to give special thanks to my supervisor Dr. Neil Trappe for all his help and insight over the course of this thesis and his enthusiasm as a lecturer. I’d like to thank the all the staff members of the Experimental Physics Department at Maynooth University for the help and feedback over the course of my time here in Maynooth. I would like to thank Pat Seery and David Watson and the Maynooth Engineering Department for all of their assistance and expertise with manufacturing equipment throughout this project. I’d like to thank Prof. Anthony Murphy for his help with Gaussian beam modes. I am also particularly grateful to Dr. Marcin Gradziel for his time and assistance in the VNA lab.

I would like to thank my fellow postgrads of the Experimental Physics department for all of the support, laughs and memories. Thanks to Sharon, Joe, Eoin, Aishling, Julianne and James for proof-reading my thesis. Thanks to Eimante for her help with plotting in Mathematica. Special thanks to Adam and Benraad for all the company in the office. Lastly, I also want to thank my family, Mum, Dad, Robert, Ross, Nana and Cecil, for their support over the course of my education.

Chapter 1 Background

1.1 Overview

The work presented in this thesis was completed as part of a MSc through research and undertaken from October 2016 to September 2018. This includes research in a number of topics including antenna design and testing, planar antenna development, dielectric lenses at W band frequencies (75 to 110 GHz) and terahertz multi-moded horn analysis. In this thesis, to avoid confusion, the phrase terahertz band is used to refer to the general frequency range between roughly 30 GHz to 3 THz. This frequency regime is often divided between the millimetre (30 GHz → 300 GHz) and submillimetre band, (300 GHz → 3THz).

As part of a European Space Agency (ESA) research contract (**ITT AO/1-7393/12/NL/MH**) entitled "New Technology High Efficiency Horn antennas for Cosmic Microwave Background (CMB) Experiments and Far-Infrared Astronomy", planar antennas operating with small dielectric lenses (lenslets) were designed, manufactured and tested. Specifically Work Package 2.1 (defined later in this chapter) outlines the development of a W band detector pixel using a planar antenna with a small dielectric lens as an alternative geometry to the traditional horn antenna.

Planar antennas are the classification given to small antennas (less than a wavelength in length) created on top of dielectric material, such as Printed Circuit Boards (PCB), which include (for example) patch and slot antennas, as well as more complex designs. Planar antennas are widely used in mobile phone and wireless applications (between 1 → 10 GHz), but the dimensions and wiring become difficult towards W band frequencies with the shorter wavelengths. A number of different planar antenna designs and experimental results are presented. The Vector Network Analyzer (VNA) facility in the Experimental Physics Department at Maynooth University operating at W band around 100 GHz was used to test these devices. This work was the first attempt of planar antenna design, manufacture and testing at exceptionally high frequencies within the Experimental Physics Department.

A core component of this thesis was to create dielectric lenses for planar antenna arrays operating at W band. As part of this development, methods to reduce crosstalk (coupled signal between antennas) caused by the introduction of these lenses were investigated. The scientific motivation for creating these arrays was to observe of B-mode polarization of the CMB. As this is a weak signal, any source of additional background noise present in an array system, such as crosstalk, needs to be accounted for precisely.

The terahertz region is a transition state between the upper ends of the radio bands and the infrared regions (see **Figure 1-1**). As a result, technology used at these frequencies is a combination of radio technology, such as horn antennas and waveguides, and more traditional optical devices such as lenses, mirrors and detector arrays. This chapter will outline the background information relating terahertz wave astronomy to the CMB radiation which has its peak signal strength in this frequency regime at roughly 160 GHz [1]. A brief history of research into CMB measurement will be provided, including more recent developments in the field of cosmology, followed by a general outline of terahertz terrestrial applications.

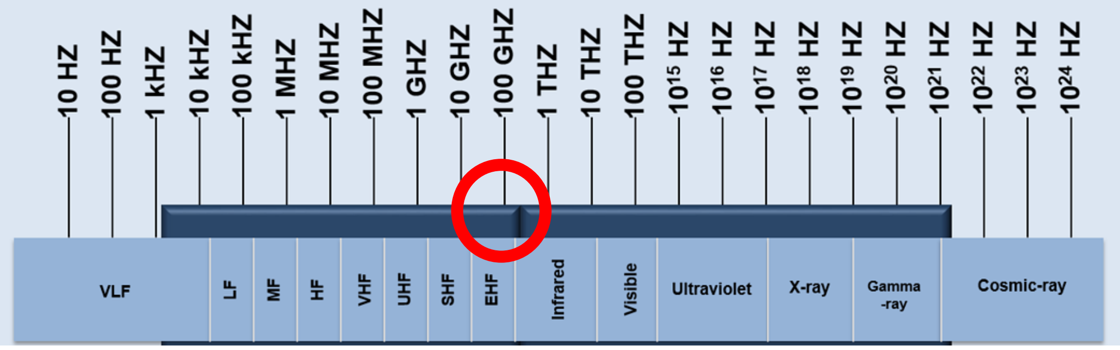

Figure 1-1: The EM spectrum from radio to cosmic-rays, arranged by increasing frequency. The terahertz band was the primary frequency range of interest for this thesis and this band was highlighted within the red circle. Image credit: NASA [2].

There have been a number of terahertz astronomical science missions examining sources where atmospheric transmission allows these telescopes to operate on ground-based receivers in very dry conditions. In order to achieve high sensitivity and wide bandwidth, space-based satellites are required at these frequencies. The Herschel Space Observatory and the Planck mission are examples of dedicated observatories in this portion of the EM spectrum. The current missions and research in terahertz astronomy is also briefly discussed below.

1.2 The Universe at terahertz wavelengths

A number of astronomical phenomenon are visible in the terahertz band, such as interstellar medium (ISM) chemistry, molecular clouds, the CMB and young stars. Clouds of space dust and gas present in our galaxy can be directly observed in the terahertz band.

There are a number of different challenges faced by astronomers wanting to examine astronomical sources at these frequencies. Terahertz radiation is absorbed by Earth's atmosphere apart from a few narrow windows. This can lower visibility or render the atmosphere completely opaque within some frequency ranges.

The interstellar medium (ISM) is the collection of dust and gas found in the region between stars. This medium is of interest to astronomers as it plays a pivotal role in the life-cycle of stars [3]. We can probe the ISM using a number of common molecules, such as O_2, CO and water, which radiate prominently in the terahertz band.

Larger concentrations of dust can group together to form Giant Molecular Clouds (GMC). These larger molecular clouds are the primary location of star formation and are referred to as "stellar nurseries" [3]. Due to the large amount of dust present observing these faint young stars in these clouds is impossible at visible wavelengths. These clouds can however be examined by terahertz and high frequency radio telescopes, providing detail on early star formation [3].

1.2.1 Atmospheric transmission

In the terahertz range, there are several gases in the atmosphere that absorb and scatter radiation (see **Figure 1-2**). A significant amount of light is absorbed by water vapour at these frequencies. Small diatomic molecules, such as carbon monoxide, are likely to rotate when exposed to terahertz radiation and absorb strongly. Additionally, several atmospheric absorption lines are present in the terahertz region [3].

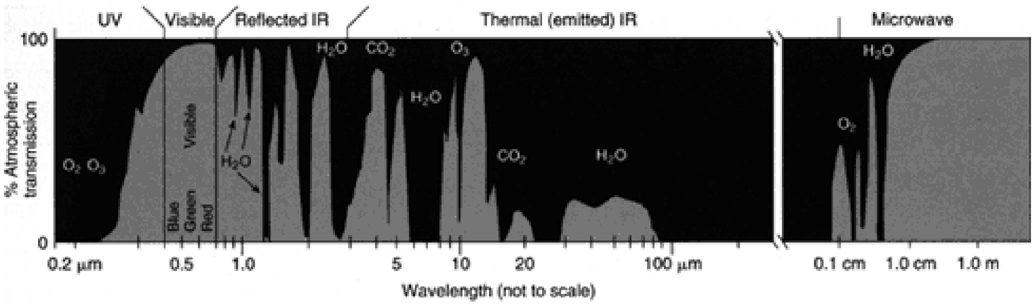

Figure 1-2: Atmospheric transmission across the electromagnetic spectrum. Gases which absorb light are also indicated on the graph. Terahertz band signals (0.3 mm → 30 mm, on the right-hand side) have high atmospheric opacity, which explains the development of terahertz satellites. Image Credit: NASA [4].

Due to atmospheric absorption, telescopes require their observation site to occupy a region with a dry/low humidity climate to reduce H_2O absorption. As such, experiments in this frequency range are performed in deserts climates (such as the Atacama Large Millimetre array (ALMA) [5]) or in Antarctic (such as BICEP (Background Imaging of Cosmic Extragalactic Polarization) [6]). A number of experiments are performed at high altitudes by balloon (Spider [7]) to avoid the loss of signal caused by the atmosphere. Space missions have also played a key role in exploring the Universe at these frequencies (Cosmic Background Explorer (COBE) [3], Wilkinson Microwave Anisotropy Probe (WMAP) [3], Hershel and Planck [8]) and have helped develop and establish receiver and detector technology to expand observational capabilities.

Letter designation	Frequency band	Letter designation	Frequency band
L	1 - 2 GHz	K	18 - 27 GHz
S	2- 4 GHz	Ka	27 - 40 GHz
C	4 - 8 GHz	V	40 - 75 GHz
X	8 - 12 GHz	W	75 - 110 GHz
Ku	12 - 18 GHz	mm	110 – 300 GHz

Table 1-1: Letter designation of each frequency band as per the IEEE standard [9]. This thesis will use these letters to define the frequency band of each device

The terahertz region is further divided up into distinct frequency bands according to an IEEE standard (see **Table 1-1** for outline of different frequency bands) [9]. For example, the hydrogen

21 cm line used in spectroscopy is located within the L Band (1-2 GHz). The work performed by the author in this thesis is carried out almost entirely within the W band region (75-110 GHz).

1.2.2 Standard cosmological model

The most commonly cited model used to explain the formation of the Universe is the Lambda Cold Dark Matter (ΛCDM) model ([6], [10], [11]). This model includes several components, such as the Big Bang Theory, Inflation and the accelerated expansion of the Universe. Additionally, it is assumed that the Universe is both homogenous and isotropic at large scales. Under this standard model, the primordial Universe begins as a hot dense structure. The Big Bang causes this dense structure to expand. The Universe then goes through a fast period of expansion known as Inflation. The Universe today is roughly 13.7 billion light years across and it is expected to continue to expand into future [3].

In this model, the Universe is homogenous, with some small quantum fluctuations causing some small regions of inhomogeneity. Inflation is the theoretical rapid expansion of the Universe, by about 21 orders of magnitude, soon after the Big Bang [1]. The rapid growth caused these small quantum fluctuations to grow into the larger in-homogeneities. Additionally, this expansion should also cause the creation of so-called primordial B modes. These are patterns in the CMB which are caused by a tensor effect, such as the rapid expansion of the Universe (more detail on the CMB is provided in **Section 1.2.3**). Detecting these B modes will allow us to prove or to constrain inflationary models.

As the Universe is expanding in size, the distances of far-away galaxies and structures are observed with higher redshifts. The emission lines of far-way galaxies appear to have a longer wavelength due to cosmological expansion. The light from these distance galaxies is stretched or red shifted, z, as space expands. Further away galaxies have a larger redshift. The furthest away observed galaxy MACS0647-JD has a redshift of between $10.3 \rightarrow 11.3$ [12]. The CMB has a redshift of approximately $z \approx 1000$ [1].

In the standard ΛCDM model, the primordial Universe begins as a hot and dense structure, which begins to expand and cool. Following sufficient cooling and expansion, the free-moving particles (mostly electrons and protons) condense to create the first atoms. This event is known as recombination and this would have resulted in visible or UV light being emitted from the newly created atoms. This event is thought to have occurred 380,000 years after the Big Bang [3]. As the Universe expands, the light left over from recombination would have redshifted to terahertz wavelengths [1].

After this recombination event, the Universe starts to appear similar to the form we see it today and the Universe continued to expand to its current size. Stars and galaxies started to form from the matter generated by recombination. Supernovae explosions of massive stars spreads heavier elements throughout the Universe, which are used to form other familiar astrophysical structures, such as planets and asteroids. Finally, we reach the Universe as we observe it today (z = 0) [3].

In the ΛCDM model [1], ordinary baryonic matter, such as stars, dust and planets, comprise only a small minority (4.6 % as seen in **Figure 1-3**) of mass energy in the Universe. Dark matter comprises a larger component of mass-energy in the Universe and accounts for the orbits of the outer most stars around planets, among other properties. Dark energy comprises the majority of mass-energy in the Universe and accounts for the acceleration of the expansion of the Universe. However, less is understood about dark energy than the other two types of mass-energy [3].

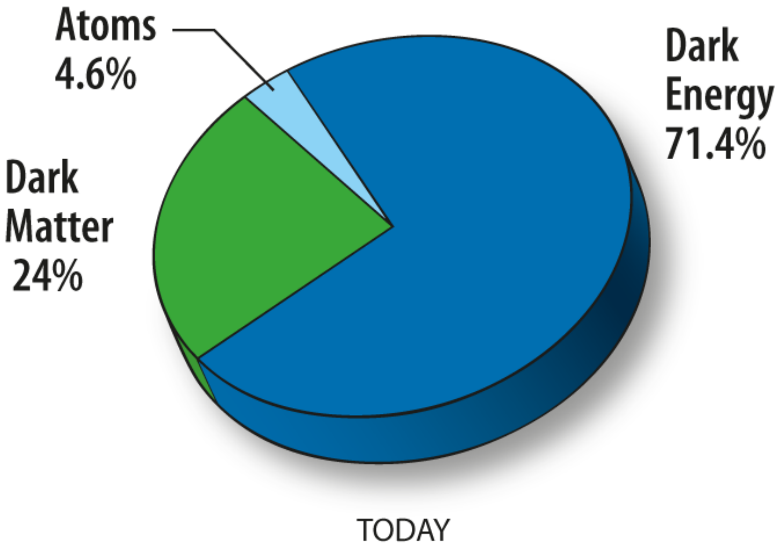

Figure 1-3: Under the ΛCDM model, the Universe is broken down into three distinct groups of mass-energy: normal baryonic matter, dark matter and dark energy. Their relative quantities, in the Universe today, are shown in this figure. Image credit: NASA/WMAP Science Team [13].

1.2.3 CMB

The CMB radiation is a (mostly) isotropic source of energy detected from deep space. The CMB is the oldest known phenomenon that can be observed from Earth, thus it can reveal information on the early universe. The intensity of light from the CMB is a near exact fit for the Planck blackbody radiation curve and so is a near perfect blackbody source. The data from FIRAS (the Far Infra-Red Absolute Spectrophotometer) and the WMAP satellite gives a weighted average temperature of the CMB of 2.72548 ± 0.00057 K [14]. As the CMB is an old source of light and is from a time where the Universe was smaller, the small anisotropies we observed grow into the larger structures we see in the Universe today, such as galaxies and clusters of galaxies [1].

There are three main anisotropies present in the CMB caused by different sources. The dipole anisotropy is the easiest to detect, and this is caused by the motion of our solar system relative to the CMB. The temperature anisotropy is caused by small scale temperature variations at specific positions in our Universe. The third anisotropy is the polarization of the CMB. Several experiments have performed observations of the CMB, either by ground-based mission, such as South Pole Telescope (SPT), or by satellite missions such as WMAP and Planck (**Figure 1-4**).

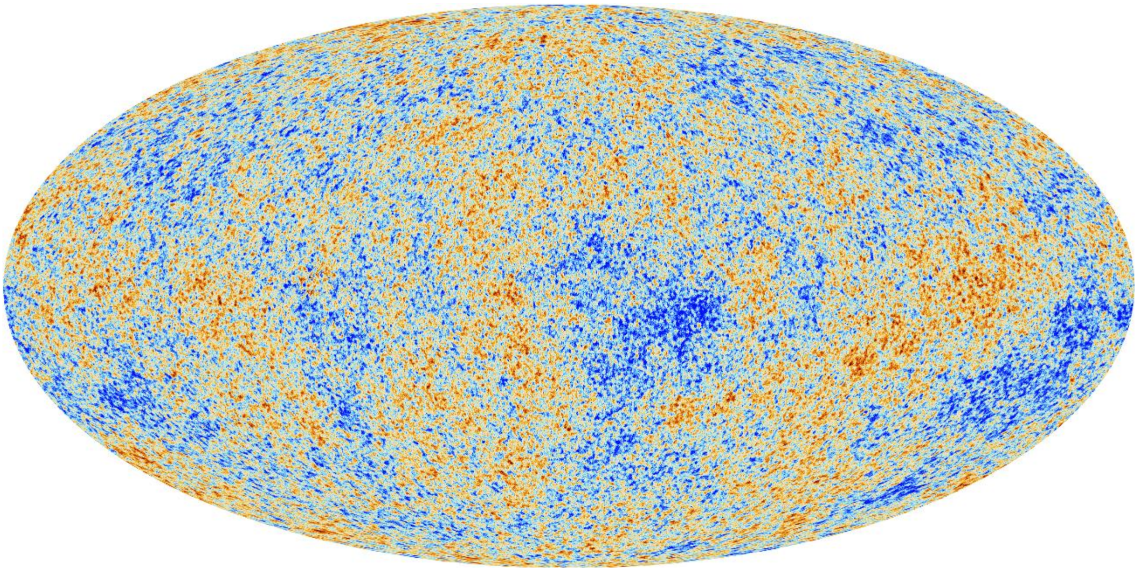

Figure 1-4: Temperature anisotropies in the CMB detected by Planck [15]. The data received from Planck represents the most up-to-date picture of the CMB currently available. Image credit: Planck [15].

The anisotropy currently examined, or planned to be examined by a number of CMB missions, is the polarization anisotropy. Any light wave can be broken down into distinct polarizations (**Figure 1-5**). The Stoke parameters are used to characterize the polarization of this light wave. The Q parameter (or S_{LHP}) is the up-down (N-S) motion of the vector and the U parameter (or S_{L+45P}) parameter is the diagonal (NE-SW) motion of the vector [16]. It is these different parameters that are measured when observing the CMB polarization.

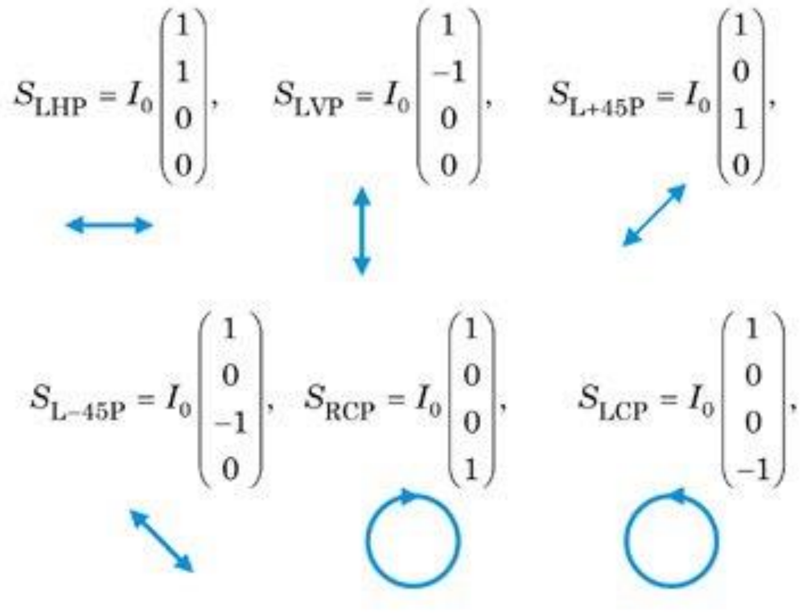

Figure 1-5: Stoke polarization parameters of light. Image Credit: [16]

The polarization of the CMB can be broken down into two specific components: E-mode (divergent) polarization and B-mode (curl) polarization. E-modes modes are caused by Thomson scattering, B modes are caused by gravitational waves and both are caused by gravitational lensing. By examining the B-mode polarization of the CMB, primordial gravitational waves (gravitational waves created before recombination), that are thought to exist with current inflationary theories could be detected. The signal from the temperature of the CMB and from the E-mode polarization are more powerful than the signal from the B-mode polarization [17]. As a result, much higher levels of sensitivity are required to measure this signal. An outline of missions examining this polarization are provided in **Section 1.3**.

The CMB is the furthest away source we can currently detect. If we assume that CMB is equidistance in every direction, we can imagine a celestial sphere with the Earth in the centre of this sphere. However, when we are observing the CMB from Earth, we observe a 2-D image of the sky, which can be mathematically described in terms of spherical harmonics function Y_l^m.The multipole, l, describes the angular size of the observation.

Observing large multipoles requires examining small angular scale and good optical resolution. For example, Q/U Imaging ExperimenT (QUIET) examines multipoles between 25 → 475 in the Q band (33 → 50 GHz) and between 25 → 975 in the W band [18]. The polarizations can be distorted (or lensed) as they propagate though the Universe. This can lead to difficulty in determining the true source of polarization.

The B-mode polarization of the CMB is notoriously difficult to detect. In 2014, BICEP2 had announced the detection of B-mode polarization in the CMB at a scalar to tensor ratio of 0.2 [11]. However, new data from Planck placed further restraints on the experiment. These restrictions suggest that distortion caused by polarized dust is larger than initially expected.

1.3 Current scientific missions

There several scientific missions currently probing the Universe at terahertz frequencies. The sensitive detectors operating at terahertz wavelengths for these missions are typically constructed using cryogenic superconducting technology. Different semiconductor technologies are typically used as detectors where high sensitivity is required and an outline of these various technologies used are described in the following paragraphs.

Transition Edge Sensor (TES) bolometers are detectors used on telescopes such as the Keck Array [19] and CLASS [20]. These devices operate by absorbing an EM signal and recording the temperature change caused by absorbing that signal. These devices are constructed from semiconductor technology, typically built on silicon wafers [21]. There is ongoing research into these devices in order to create a TES with a low Noise Equivalent Power (NEP), which is effectively the sensitivity of the detector. For example, BICEP2 has a minimum measured NEP of 75×10^{-18} W / $\sqrt{\text{Hz}}$ [22]. A new TES design being developed for the potential SPICA (SPace Infrared telescope for Cosmology and Astrophysics) telescope reports a measured NEP of 0.76×10^{-18} W / $\sqrt{\text{Hz}}$ [21].

Another type of technology used as detectors are Kinetic Inductance Detectors (KIDs) [23]. These devices are also constructed from superconductors and operate at low temperature. As such, a majority of the charge carriers are Cooper pairs (paired electrons). A photon with significant energy incident on the device will break up the Cooper pair, which increases the impedance of the device, which in turn allows a measurement to be digitally recorded.

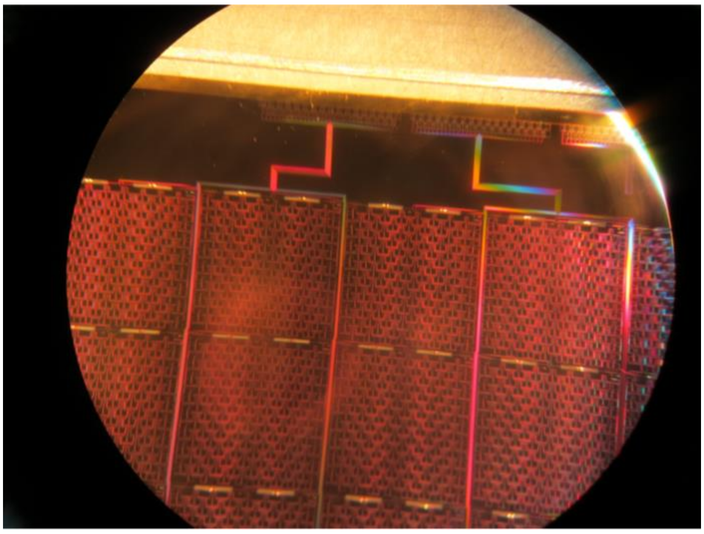

Figure 1-6: Array of antennas for BICEP3 pixels. Image taken under microscope. Image Credit: [6].

The detectors generate some waste heat from their electronic components and these heat sources will generate a detectable signal at terahertz frequencies. These instruments, both KIDs and TESs, require low temperatures in order to function optimally [22]. For example, the Keck array, located at the South Pole, required a cryostat that can reach temperatures as low as 250 mK [19].

1.3.1 Ground based missions

Despite the difficulties presented by the opaqueness of the atmosphere, there are several locations on the Earth's surface which are suitable for making observations at terahertz frequencies within defined bandwidths. The Atacama Desert is the location of several telescopes (such as the Atacama Cosmology Telescope (ACT) [24]) due to the high attitude and dry air. Antarctica is also a particularly good region for an observation site due to the long nights and cold dry climate. Several CMB missions, such as the South Pole Telescope (SPT) [25] and BICEP [26] operate (or have operated) at the South Pole.

ALMA is an astronomical facility which operates two large arrays at millimetre/submillimetre frequencies [5]. The 12 m diameter telescopes operating here (see **Figure 1-7**) perform between 31 GHz → 950 GHz. The first array consists of 64 antennas and the other consisting of 16 telescopes, packed into a smaller configuration. The first array comprises of identical 12 m diameter antennas which can be reorganised to create an array with baselines ranging from 15 m to 15 km. The second array is comprised of a mixture of 12 m and 7 m diameter telescopes. These arrays have been designed to detect spectral lines of molecules in our galaxy, study young stellar objects and to image objects at a resolution of 0.1 arc-seconds [27].

Figure 1-7: Aerial view of ALMA antennas in the Chajnator Plateau in the Atacama Desert. Image Credit: Carlos Padilla – AUI/NRAO [28].

The Q/U Imaging ExperimenT (QUIET) is an experiment set in the Chilean Andes which aimed to measure the polarization of the CMB [18]. The telescope created for QUIET has a Dragonian optical design in order to provide a wide field of view. The instrument sensitivity for the Q and W bands were 69 $\mu\text{K s}^{1/2}$ and 87 $\mu\text{K s}^{1/2}$ respectively. The optics direct the signal to a cryostat, which contains the feed horns and detectors. The feed horns consist of corrugated feed horns and HEMT (High-electron-mobility transistor) detectors. Individual HEMT detector elements are compiled into an array constructed on a PCB. These detector arrays operated at W band (centered at 95 GHz) and at Q band (centered at 43 GHz) frequencies and the Q and U Stoke parameters are measured simultaneously by each detector.

BICEP3 [6] is a telescope currently operating at the Amundsen-Scott South Pole Station. This telescope is an upgrade of the previous BICEP missions and as such it contains a number of technical improvements to previous designs. Each pixel is comprised of antennas, absorbers and TES devices. BICEP3 is a refracting telescope and uses alumina lenses with an anti-reflecting layer. BICEP3 is of particular interest as it has a number of similarities to the devices that will be discussed later in this thesis, as it uses semiconductor technology, dielectric lenses and also operates at W band frequencies, specifically at 90.4 GHz with a bandwidth of 24.7 GHz [26].

1.3.2 Space based missions

Two recent space missions are the Herschel Space Observatory (**Figure 1-8**) and the Planck telescope (**Figure 1-9**). Both missions were commissioned by ESA, with assistance from NASA and were launched together by ESA in 2009. Herschel was the larger telescope, with a 3.5 m primary mirror. Herschel was designed to examine star formation, examine distant galaxies and study the chemistry of space molecules [29].

Figure 1-8: Artist depiction of Herschel Space Observatory. Image Credit: [30].

Several space-based missions have observed the anisotropies in the CMB. NASA launched and operated two satellites [31]: COBE (1989-1994) and WMAP, launched in 2001 and operated by NASA until 2010 [32]. The latest of these missions was Planck (2009-2013) which was operated by ESA.

COBE performed a full sky measurement of the CMB at far-infrared frequencies [31]. The main aims were to measure temperature anisotropies and the spectrum of the CMB. WMAP attempted to improve on the precession of the full sky observations of the CMB originally made by COBE [32]. The satellite operated over 5 different frequency bands (K, Ka, Q, V and W bands). From this satellite, the age of the Universe has been determined to be approximately 13.77 billion years old and the Hubble constant has been determined to be approximately 69.3 km s^{-1} Mpc^{-1}.

Planck, with a 1.5 m primary mirror was designed to specifically measure temperature anisotropies in the CMB. The Planck satellite had two sets of instruments, one for lower bands , which measures between 30 → 70 GHz [33] and one for higher bands between 100 → 850 GHz [34]. Both of these instruments were made up of HEMT receivers. One major result from Planck was the full sky map of temperature variations in the CMB (see **Figure 1-4**).

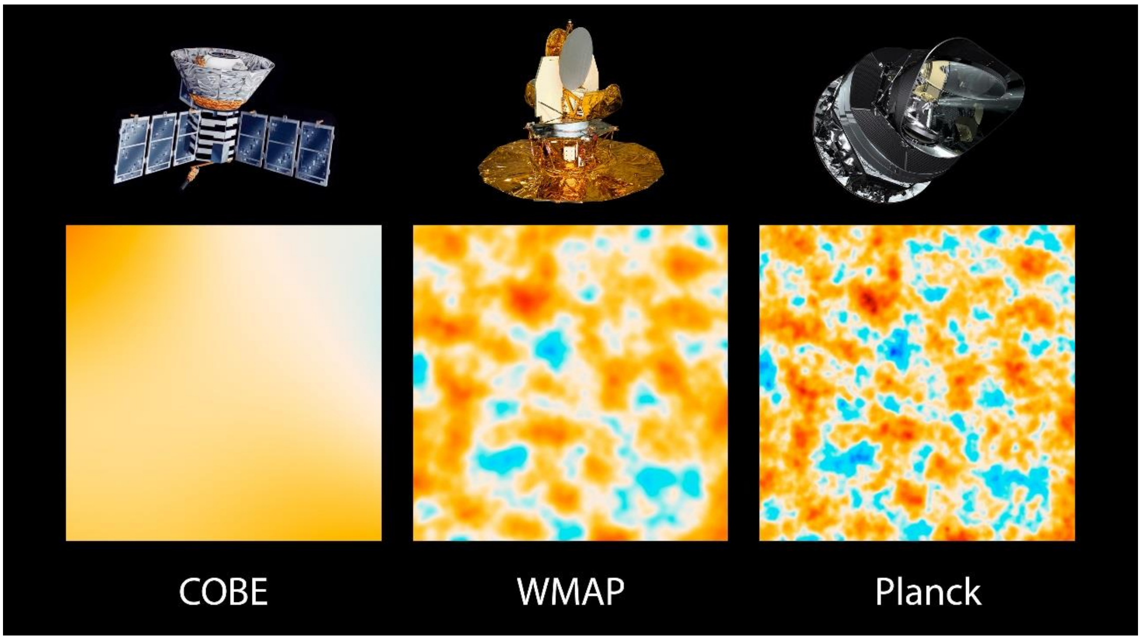

Figure 1-9: Comparison between the CMB satellites missions COBE, WMAP and Planck. The small temperature differences are not visible in COBE's data. The later telescopes of WMAP and Planck have higher levels of antenna sensitivity and can pick up smaller temperature differences. Image Credit: [35].

1.4 Applications of terahertz research

Outside the field of astronomy, terahertz radiation has potential applications in terrestrial commercial applications in the near future. Applications include detecting defects in materials, security scanners and medical imaging equipment [36] [37] [38].

1.4.1 Medical imaging

Terahertz radiation has the ability to differentiate between different tissue types when used to image biological matter [29] [37] [39]. Additionally, terahertz radiation, which is non-ionising, can examine tissue without causing potential damage due to higher energy x-ray radiation.

The absorption of light is dependent on the refractive index and the thickness of the tissue sample. Different tissues have different levels of water content and relative dielectric permittivity. By using terahertz imaging, it is theoretically possible to distinguish between healthy and diseased (cancerous) tissue [37]. Specifically, in the field of osteology, terahertz radiation can distinguish between spongey and compact types of bone tissue [36].

The difficulty with using terahertz radiation to create an image is the low penetration depth of the radiation through living tissue, especially when compared to other imaging techniques, such as MRI and X-ray scans. The low penetration depth of terahertz radiation is due to the strong absorption of this radiation by water. However, this imaging technique is viable for examining living skin. The low penetration depth is enough to allow imaging in blood vessels beneath the skin [39]. Ultimately, this technology is still in the process of being developed and applications still face some practical issues [37].

1.4.2 Spectroscopy

Some molecules have vibrational or rotational energy levels which radiate light at terahertz frequencies when there is a transition between energy levels. Spectroscopy is the technique used to study the chemical composition of a material by examining the light emitted by these energy level transitions (emission and absorption). These spectrometers operate by probing the sample or material with terahertz radiation and then measuring the output signal. Electrons in an atom emit light when moving from a high energy level to a lower energy level or in vibrational or rotational changes of state. The frequency of the light emitted depends on the energy difference between these states.

Spectroscopy in terahertz regions have been used to study biomolecules as some of these molecules have vibrational or rotational energy levels, which radiate light at terahertz frequencies when there is a transition between energy levels [37]. A number of biomolecules have energy level transition states at terahertz frequencies and this allows spectroscopy to be performed on biological tissue. Biomolecules can be distinguished from each other as each have their own specific frequency of light observed when a transition occurs. For example, the four different nucleic acids, which together are used to create DNA, are similar in their makeup, but they can be distinguished using terahertz spectroscopy. This can be used to determine the relative amounts of different molecules in each sample. However, some practical problems still remain. Water, which strongly absorbs terahertz radiation, limits the resolution of spectroscopy for molecules in an aqueous solution [37].

In the field of semiconductor research, technology is used to study charge carrier dynamics or electron mobility in these devices. In semiconductors, the emitted radiation is proportional to the photoconductivity of the material [40]. Several semiconductor materials, such as solar cell materials [41] and semiconductor nanocrystals [40] have been examined using terahertz spectroscopy.

1.4.3 Security Imaging

Dielectric materials tend to behave differently at terahertz frequencies than at optical frequencies. Some material that is transparent at optical frequencies, such as glass, is opaque at terahertz frequencies. Other dielectric materials such as High Density Polyethylene (HDPE), paper and plastic, which are opaque at visible frequencies, are transparent at terahertz frequencies [42]. Metals remain reflective at both optical and terahertz frequencies.

The figure below (**Figure 1-10**) shows applications of this technology for detecting dangerous objects inside containers by showing images of briefcases taken at 200 GHz [38]. The (dielectric) leather cover of the briefcase is transparent at 200 GHz, however, the (metal) knife is highly reflective and appears as black in the image.

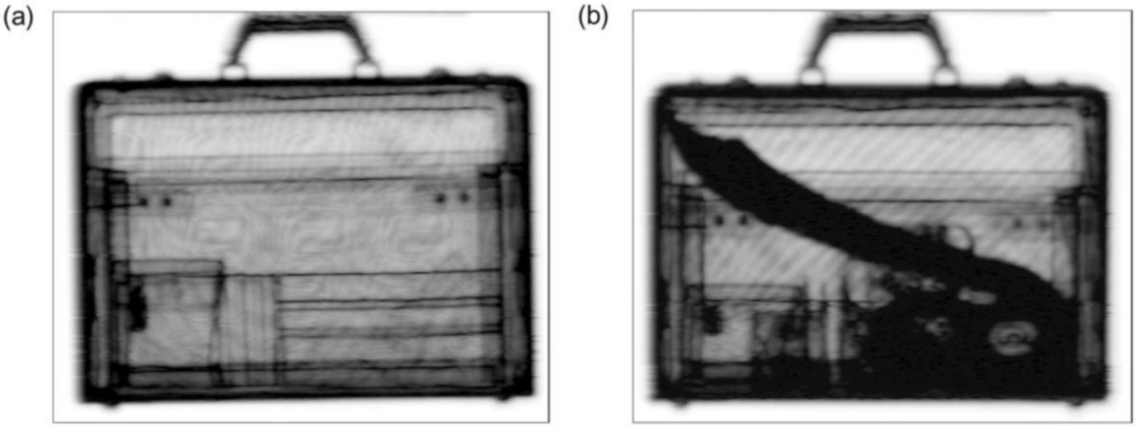

Figure 1-10: Images taken of briefcases using a 200 GHz scan. a) showed an empty briefcase and b) showed a briefcase containing a large knife and several harmless items. Image Credit: [38].

1.5 Thesis outline

The core component of this thesis was the simulation and experimental measurement of planar antennas and dielectric lenses for W band frequencies. This work was carried out as part of an ESA research contract entitled, “New Technology High Efficiency Horn antennas for CMB Experiments and Far-Infrared Astronomy”. The author’s contribution to the contract was to develop W band lenslet arrays fed by planar structures.

The results from the tests performed on these devices with the VNA (Vector Network Analyser) are also presented for different designed and manufactured planar antenna and dielectric lens designs, with comparisons between the results from simulations. Additionally, in parallel Gaussian Beam Mode Analysis (GBMA) was applied to investigate the influence of truncation due to a cryostat window on a multi-moded horn field as it propagates to the farfield. The following subsections describe the content of each chapter.

Chapter 2

This chapter provides an outline of the background theory and simulation techniques used to design and develop the planar antenna devices described later in the thesis. This includes a description of the different antenna systems and the different waveguide systems used throughout the thesis. Specifically, general antenna theory and planar patch antenna theory are outlined. The analytical and manufacturing techniques used to design and build these systems is also described in detail. This includes a description of the Electro-Magnetic (EM) simulation software used to analyse these systems. In particular, CST Microwave Studio Suite is introduced and the underlying algorithms used in this package are described

Chapter 3

This chapter presents the design, analysis and experimental measurements completed by the author for various W band patch antenna designs. The author presents the electromagnetic analysis of these devices using CST. Also presented are the results of experiments and measurements, performed by the author, on the antennas manufactured in the Experimental Physics department. Potential issues these devices encounter at W band frequencies, such as the effect of dielectric thickness and efficient coupling to the test source, are also examined. An analysis of an array of these devices is presented in order to establish the degree of crosstalk present in such an array system. Finally, the results from the measurements performed on these devices by our in-house VNA are presented.

Chapter 4

In this chapter, the analysis and development of an alternative planar antenna (referred to as a side-fed patch antennas) is described. These devices are similar in theory to the back-fed patch antennas in **Chapter 3**, however, they are fed via a different technique. An inset structure on the patch surface is described, which was introduced to try to reduce return losses. As part of this development cycle, two new thinner PCBs were acquired in order to manufacture patch antennas. Analysis based on these PCBs is also described. The author's work in this chapter comprises the initial design choices of the structure and the resulting measurements with the VNA.

Chapter 5

Alternative design options for W band antennas are examined in **Chapter 5**. This chapter introduces and examines so called "endfire" devices, which radiate in the orthogonal direction to patch structures. The author examined several novel antenna designs that could provide an alternative to patch antenna structures examined in **Chapter 3** and **Chapter 4**. These designs are analysed using the CST software. A number of these devices were then manufactured. The experimental testing on these devices is also described in this chapter. A brief overview of "E" and "U" antennas designs were also examined. These devices are beyond the manufacturing capabilities of the workshop; however, they are presented in this chapter as they have potential for future research.

Chapter 6

This chapter reports on the design and analysis of W band lenses to increase the inherent gain of the planar antennas. These small lenses are often referred to as lenslets. As well as presenting the results of experimental W band measurements performed on these lenses, several potential designs were created in CST and their farfield patterns and S-parameters were examined to potentially reduce crosstalk or leaked power to neighbouring pixels. Two promising lens design options were selected and manufactured. The tests performed on these lenses when coupled to W band waveguide probes are outlined and the results (including a measurement of crosstalk performed by the author) are presented.

Chapter 7

This chapter details work done designing a planar horn antenna using Gaussian Beam Mode (GBM) analysis. This chapter presents the author’s application of this theory to a specific case investigating the influence of truncation due to a cryostat window on a multi-moded horn field as it propagates at a frequency of 2.7 THz. The implementation of this code in *Wolfram Mathematica* is also discussed.

Chapter 8

This chapter contains an overall conclusion on the work completed in this thesis. This section also delivers a look into future work which leads from the research presented.

Chapter 2 Related theory

2.1 Overview

This chapter details the theoretical and experimental techniques used during this project. The background definitions and terminology used throughout the thesis for antennas are also formally defined.

In the process of investigating planar antennas operating at W band frequencies, several different configurations were analysed, which could also be manufactured and tested using facilities available in the Department of Experimental Physics. Many planar solutions are well known and widely used at lower GHz frequency bands, but start to pose many manufacturing challenges at higher W band wavelengths (2.7 - 4.0 mm) as many aspects of the planar designs are of sub wavelength dimension and start to become challenging for manufacturing processes. Additionally, the thickness of the dielectric substrate over a ground plane becomes a limitation as will be discussed later. Patch, slot, ring, and spiral are all commonly used planar antenna geometries at lower wavelengths, however, for a number of practical manufacturing reasons; emphasis was placed on patch antenna designs.

Electromagnetic analysis of these potential antenna designs was carried out using CST Studio Suite [43], a powerful commercial software package designed for electromagnetic modelling and analysis in many different situations and used extensively in this thesis. The software operates by dividing the device under test (DUT) into distinct mesh cells and solving Maxwell’s equations in each of these cells numerically. The frequency domain solver is used extensively here to calculate the S-parameters for all of the ports in the system over a bandwidth. Time domain analysis is sometimes also desirable to use where wide bandwidths are under investigation. CST inbuilt monitors are used to obtain additional information of the structure’s EM behaviour, such as the farfield beam patterns, the power flow or electric field calculations at any point. The S-parameters are used to describe the ability of the antenna to receive power from the source and then match the radiation to the antenna and radiation to free space. This value will be reported for each simulation as it can be directly measured with our Vector Network Analyser (VNA) at different frequencies instantaneously.

Electrically large antennas, such as dish or horn antennas, have an aperture larger than one wavelength. However, planar antennas built on PCBs are electrically small devices, as the device is smaller than one wavelength. Different planar antenna geometries were examined here as well as the influence of the dielectric circuit board size used, as this plays a key role at higher frequencies as it is a significant fraction of the wavelength of the radiation. The geometry with the largest directivity and lowest return loss over the bandwidth of interest (S_{11} parameter) will be chosen as the best design to test and investigate for a W band lenslet array, as described later in this thesis. The processes behind the manufacturing process and experimental testing is also discussed.

Various computer simulation software packages can be used to develop technology at these frequencies. There are commercial programs and in-house software that will be used in this thesis for this process. The commercial tools include CST, which solves Maxwell's equations for a structure. In-house software developed in the Experimental Physics Department includes, GMB analysis and Scatter (waveguide EM software). The code developed in-house is not suitable for planar antennas, so CST was mostly used for this project.

The power transferred in a two-port system are described using the generalized two-port network S-parameter model. The S-parameters in this context are used to describe the flow of power though the structure and are described in detail in **Section 2.3**.

2.2 CST Studio Suite

CST Studio Suite is a commercial software program used to solve Maxwell's equations in a given 3-D structure [44]. The solvers for CST are separated into distinct "studios", each suitable for a different area of physics. The "CST MICROWAVE STUDIO" is used for high frequency simulations and is used extensively in this project. Features utilised for this research in this studio include:

- Calculation of power patterns for antennas
- Design of waveguides at microwave frequencies
- Calculation of the S-parameters for multi-port systems.

CST was the main simulation tool used for design and analysis of planar antennas, as the software can handle both resonant structures and waveguides. The structures are created from editing a collection of basic shapes. Ports are used to simulate a connection to some power source (see **Figure 2-1**), while monitors are used to collect output data from the structure.

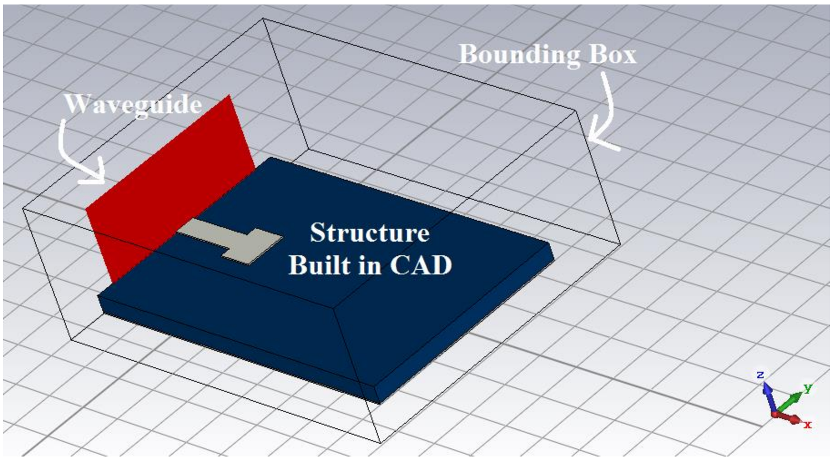

Figure 2-1: Image of a planar antenna structures created inside CST's CAD environment. The port at the back of the structure (in this case representing a microstrip waveguide connection) feeds power into the simulated structure.

The main metric used in comparing different designs was the directivity (associated with the radiation pattern) and the S-parameters of the antenna (associated with the resonant behaviour at the input side). These results were calculated by CST using several different algorithms as described in this subsection.

The simulation is defined inside the CST work environment (**Figure 2-2**). The navigation tree is used to isolate a component or to show results. The parameter list is used to alter the shape of the structure in the CAD environment.

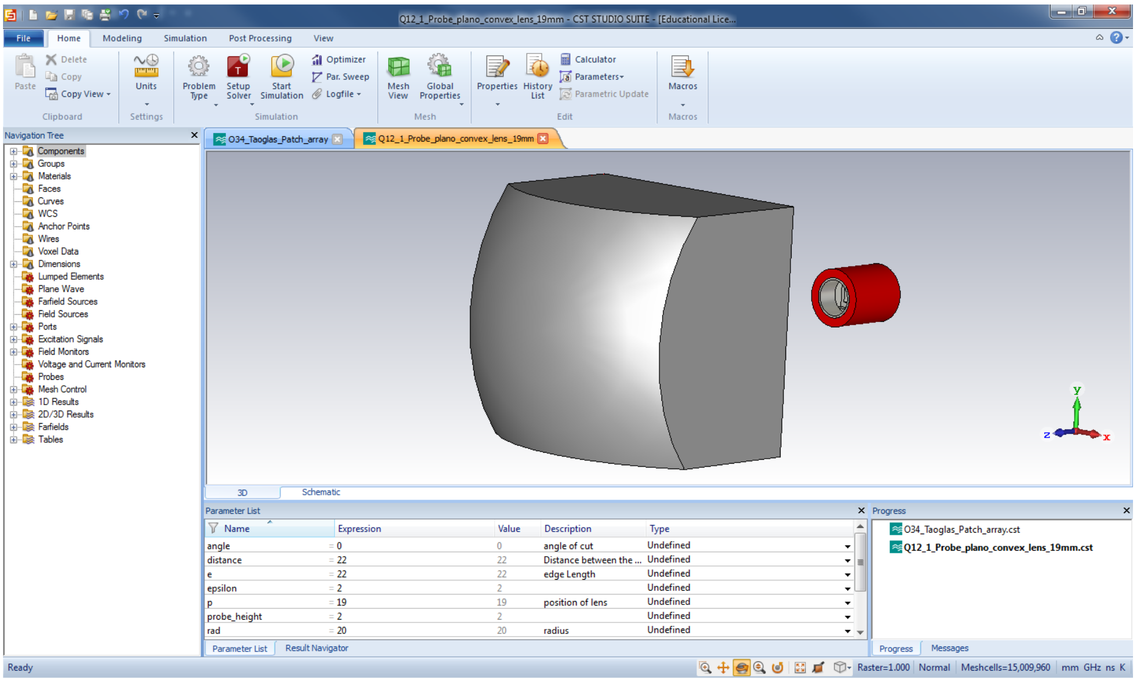

Parameter List

Name	Expression	Value	Description	Type
angle	= 0	0	angle of cut	Undefined
distance	= 22	22	Distance between the ...	Undefined
e	= 22	22	edge Length	Undefined
epsilon	= 2	2		Undefined
p	= 19	19	position of lens	Undefined
probe_height	= 2	2		Undefined
rad	= 20	20	radius	Undefined

Figure 2-2: Image of CST Studio Suite 2016 work environment illustrating the menu (top), the navigation tree (left), the CAD environment (centre) and the parameter list (bottom).

2.2.1 Finite Element Method

Finite Element Method (FEM) is an analytical technique used to solve partial differential equations using boundary conditions. The problem is divided into smaller parts (volumes) called finite elements. The size of the finite elements is determined by meshing. Meshing is used to divide the structure into regions of cells. Geometrically complex regions contain small finite elements, while ordered regions contain a few large elements. The equation for all these finite elements are combined into a large system of equations for modelling the entire system.

The CST project wizard was used to recommend a default solver for the structure. There are six different solvers in the MICROWAVE STUDIO, time domain solver, frequency solver, Eigen-mode solver, integral solver, asymptotic solver and multilayer solver. The time domain solver is recommended for a broadband antenna (such as a horn antenna), while the frequency domain solver is recommended for resonant antennas (such as patch antennas). These two solvers are used for the simulations presented in this thesis. In general, the two solvers will give the same outputs, but time of calculation could be longer for frequency domain calculations depending on the problem.

2.2.2 Frequency solver

The frequency domain solver transforms the Maxwell equations into the frequency domain and solves them at specific frequencies. A frequency sweep is used to obtain results over a user defined frequency range. The “General Purpose sweep” obtains a solution without solving the equations at each frequency. This frequency sweep is used as the default.

The frequency domain solver was used to solve the S-parameters for all of the ports in the system. A monitor is used to obtain additional information of the structure, such as the farfield pattern and the power flow. The frequency solver finds the value of these attributes only at the frequency for which the monitor is defined.

2.2.3 Tetrahedral meshing

Structures in CST are created from a collection of basic shapes and then CST divides the system into a grid of mesh cells. Maxwell’s equations are numerically solved in each of these mesh cells. Two mesh generation algorithms are available: hexagonal meshing and tetrahedral meshing. The tetrahedral mesh is recommended as the default for the frequency domain solver.

The tetrahedral meshing algorithm uses the manifold model to mesh the structure (**Figure 2-3**). The resulting mesh cells are tetrahedrons in shape. Points along the surface of each component are chosen. These points are then joined up to mesh the structure’s interior. The sampling rate for this algorithm is the amount of mesh lines per wavelength. For the tetrahedral mesh, a minimum of 4 per wavelength is recommended. Therefore, the amount of meshes used in each simulation can vary significantly, depending on the accuracy required.

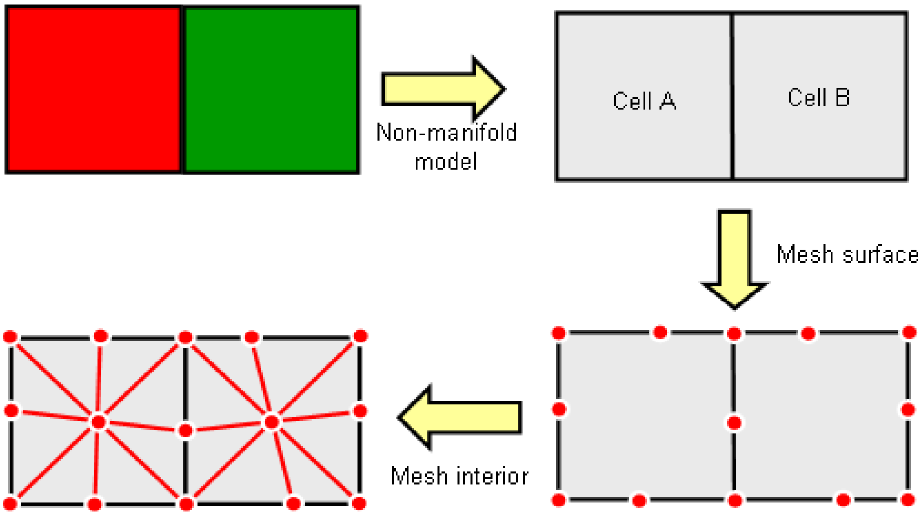

Figure 2-3: Visual diagram of each stage in the Tetrahedral meshing algorithm [44] used by CST for some example structure comprised of red and green material components.

For planar antennas, the small finite thickness of the conductor can lower the quality of the mesh. The mesh quality can be improved at specific hard to mesh regions using Adaptive Mesh Refinement (AMR), which reruns the tetrahedral meshing algorithm. CST was set to automatically run AMR at these low mesh quality regions. This can be seen in **Figure 2-4**, as the edge regions have a higher mesh density that the centre of each material.

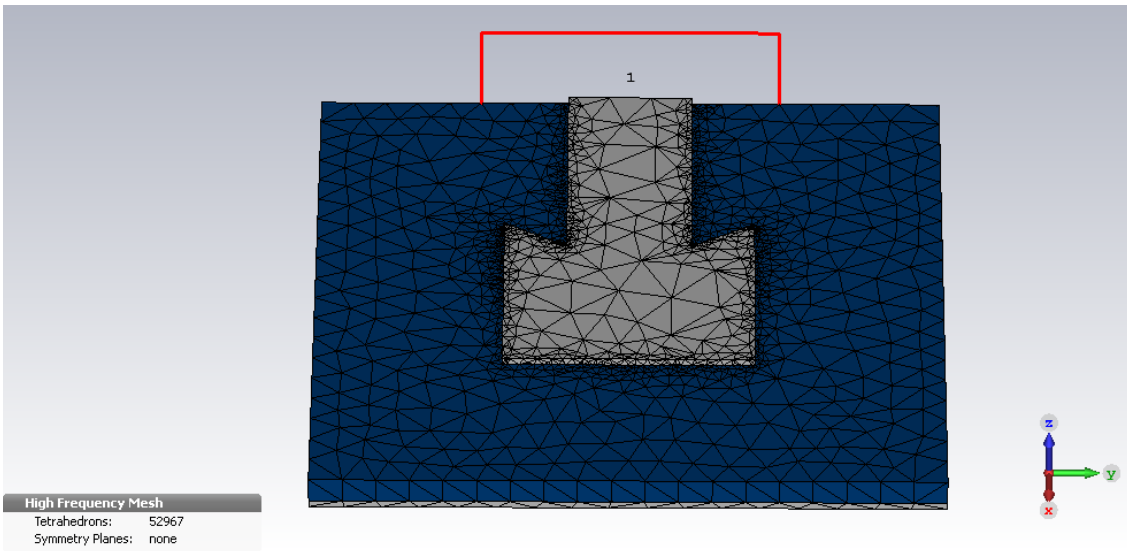

High Frequency Mesh

Tetrahedrons: 52967

Symmetry Planes: none

Figure 2-4: Mesh of patch antenna created using tetrahedral meshing algorithm. The algorithm puts more mesh cells in difficult to calculate regions, such as at the boundary between two materials. This increases computation time and to compensate, less mesh cells are put in uniform regions of the structure.

Boundary conditions were set in CST to describe the properties of the field at the boundaries of the system. The "open" and "open (add)" boundary condition represents free space. Waves experience minimal reflections when they pass through this boundary. A symmetry boundary condition was used to reduce the computation time of the simulation (where possible). If along an axis, one side of the system is a mirror image of the other side, then a boundary condition could be applied, which halves the computation time required. However not all systems that look identical are electromagnetically identical, due to boundary conditions.

2.2.4 Ports

A port is used in CST to simulate a connection to a power source or as the initial stimulus for some given device. Using this tool, the waveguide structures described in **Section 2.2** can be created. The coaxial cable and rectangular waveguide are simple to create, as the port only needed to enclose one side of the structure. However, the port for the microstrip waveguide (see **Section 2.7.2**) needed to include both the dielectric and the surrounding air (as shown in **Figure 2-5**).

A port size that is too small will not correctly simulate the quasi-TEM mode of the microstrip, but a port size that is too large will also allow higher order modes to propagate. A "macro" (embedded coding option for the user) in CST calculates the expansion coefficient for a given microstrip contact to an antenna to ensure the correct dimensions are used. This coefficient, written as “*k*” in the above figure, expands the size of the port to a size that is optimum for this test case.

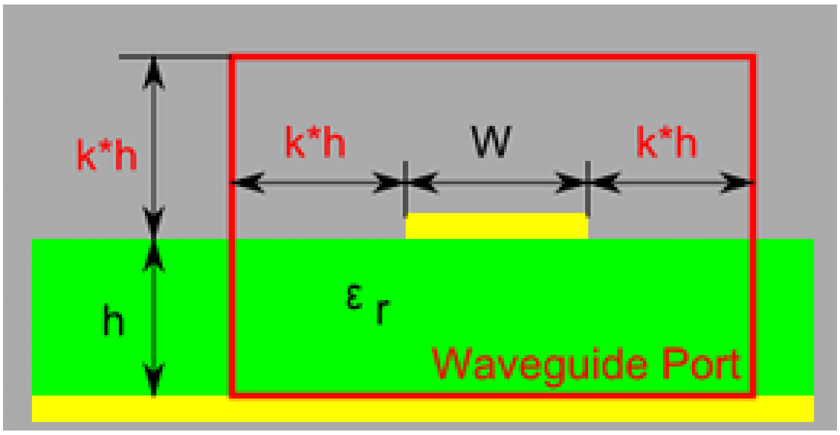

Figure 2-5: Port dimensions for microstrip waveguide, which is used for several designs in **Chapter 4**. The port expansion coefficient [43] is used to create ports which correctly model microstrips. Yellow represents metal and green is the dielectric material.

The total power is the amount of power entering the structure, which is also referred to as accepted power. Power can leave a structure in three ways, through losses, by leaving through another port or by radiating away. The power radiated is the amount of power leaving into free space. For an antenna, this radiated value is desired and should be maximized.

2.2.5 Farfield pattern

The farfield monitor in CST calculates the farfield pattern of an antenna and also records the gain and directivity of the antenna [43]. This calculation will be described in detail as it will be a main result from these simulations. The directivity of the farfield is measured by CST as described in **Equation (2.2)**. CST outputs the directivity and its associated farfield pattern in a linear or non-linear (decibel) form.

The farfield monitor in CST calculates the farfield pattern and this monitor needs to be defined for a specific frequency. Several farfield monitors can be defined in CST, however each additional monitor will increase the simulation time. The farfield pattern can be plotted in CST in several different forms. The two mostly used in this thesis are the 3-D (**Figure 2-6a**) and Cartesian (**Figure 2-6b**) plots.

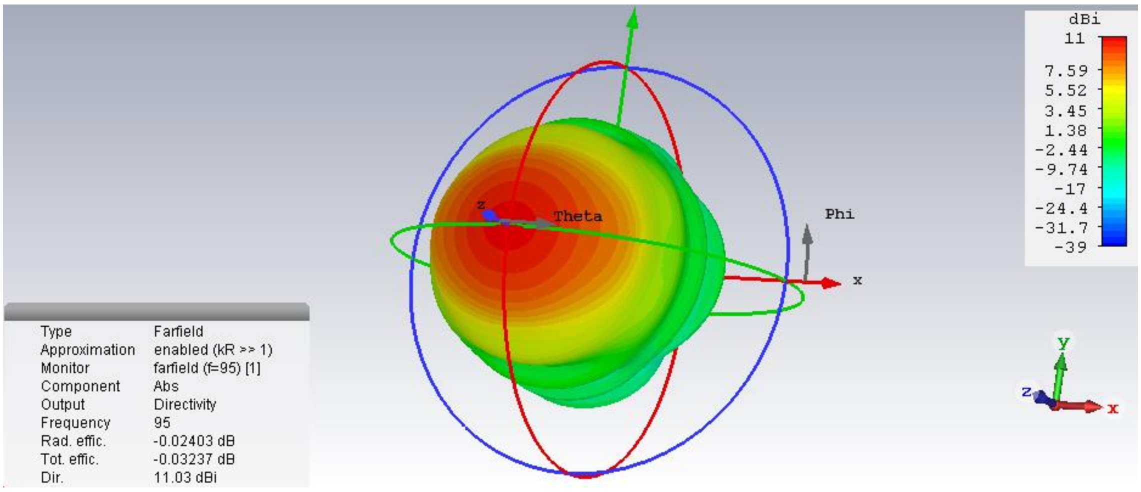

Type	Farfield
Approximation	enabled (kR >> 1)
Monitor	farfield (f=95) [1]
Component	Abs
Output	Directivity
Frequency	95
Rad. effic.	-0.02403 dB
Tot. effic.	-0.03237 dB
Dir.	11.03 dBi

Figure 2-6a: 3-D view of antenna's farfield intensity pattern as calculated by CST. For these calcualtions CST uses a dBi intensity scale (top right). The pattern can be rotated inside of CST's CAD enviroment. The calculated farfield pattern was overlade upon the antenna.

The 3-D plot is useful in showing the direction of the antenna's beam (**Figure 2-6a**). The small table in the left-hand corner records the different results from the simulation, such as the directivity (listed as Dir in the table). The calculation that CST performs describes the beam in polar coordinates, where theta, θ, is the angular offset relative to the z-axis (axis of propagation) and phi, φ, is the counter-clockwise angular offset from the positive x-axis.

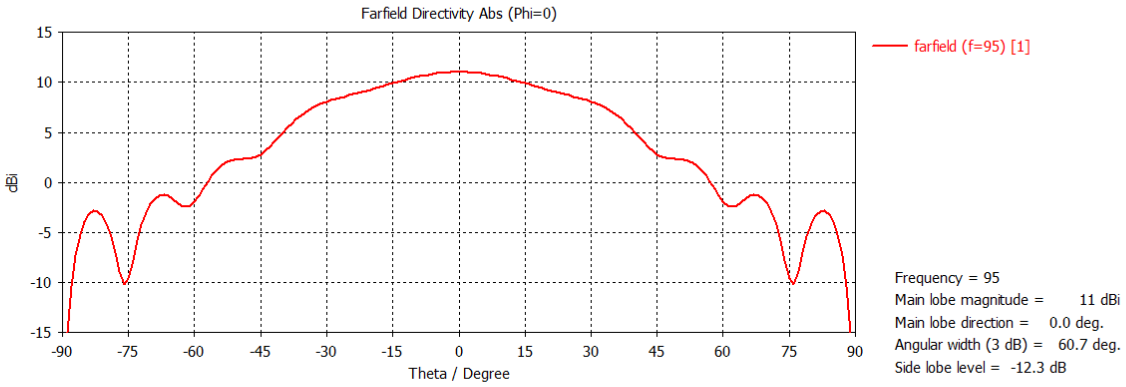

Frequency = 95
Main lobe magnitude = 11 dBi
Main lobe direction = 0.0 deg.
Angular width (3 dB) = 60.7 deg.
Side lobe level = -12.3 dB

Figure 2-6b: Cartesian farfield view of probe antenna in CST along the φ = 0° axis. Useful data on the performance of the device can be extracted from reading the graphs. A summary of this data is provided in the bottom right hand corner.

The two forms of representing the same data are shown in **Figure 2-6**. The Cartesian plot is useful in examining a specific cut section of the antenna's beam pattern. The table on the right-hand side provides information on the beam's properties. Polar plots are also available in CST, but are not used in this thesis.

2.3 Antenna theory

2.3.1 S-parameters

At lower frequencies an electrical device is described in terms of resistance, capacitance and inductance, however this lumped (or combined) circuit theory tends to break down at microwave frequencies [45]. Instead, the circuit can be described using S-parameters (see **Figure 2-7**), which describe the transfer of power between ports [45].

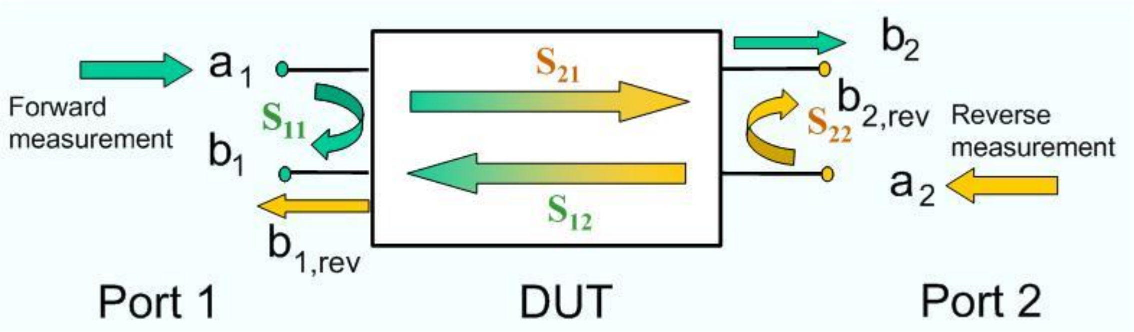

Figure 2-7: The two port S-parameters describe the flow of power between two ports. Image Credit: Rohde & Schwarz GmbH & Co. (http://labrf.av.it.pt/Data/Manuais%20&%20Tutoriais/40b%20-%20VNA%20-%20ZVB20/CD/documents/Help_Files/WebHelp_ZVT/Start.htm#System_Overview/Measurement_Parameters/S-Parameters.htm)

The “S” in S-parameters refers to the scattering matrix, which refers to the effect on the wave as the coupling of the transmission line changes. The matrices ‘a’ and ‘b’ are the incident and reflected scattering wave variables. This relates the S-parameters to the transmission and reflection coefficients. The relationship between these variables is given by:

$$[\mathrm{b}] = [\mathrm{S}] \times [\mathrm{a}] \ = \begin{pmatrix} S_{11} & S_{12} \\ S_{21} & S_{22} \end{pmatrix} \times \begin{pmatrix} a_1 \\ a_2 \end{pmatrix} \tag{2.1}$$

For some system with N ports, there are N^2 S-parameters. The power transferred in a two-port system such as the VNA is described using a Scattering Matrix with 4 S-parameters, as shown in **Figure 2-7**. Of primary interest to us is the S_{11} parameter and the S_{21} parameter. The S_{11} parameter is the power launched to the device under test by the VNA that is reflected back into the VNA. The S_{21} parameter is the power sent from the antenna to the detector (see **Figure 2-8**).

A S_{11} parameter of below -10 dB is a good performance, as this is equivalent to a return loss of less than 10%. There is no exact requirement for the S_{21} parameter, but these should be some easily identifiable region where this parameter reaches a maximum. This region is referred to as the “main lobe” of the antenna. CST obtains the S-parameters from its simulations, this can be used to compare to the measured value.

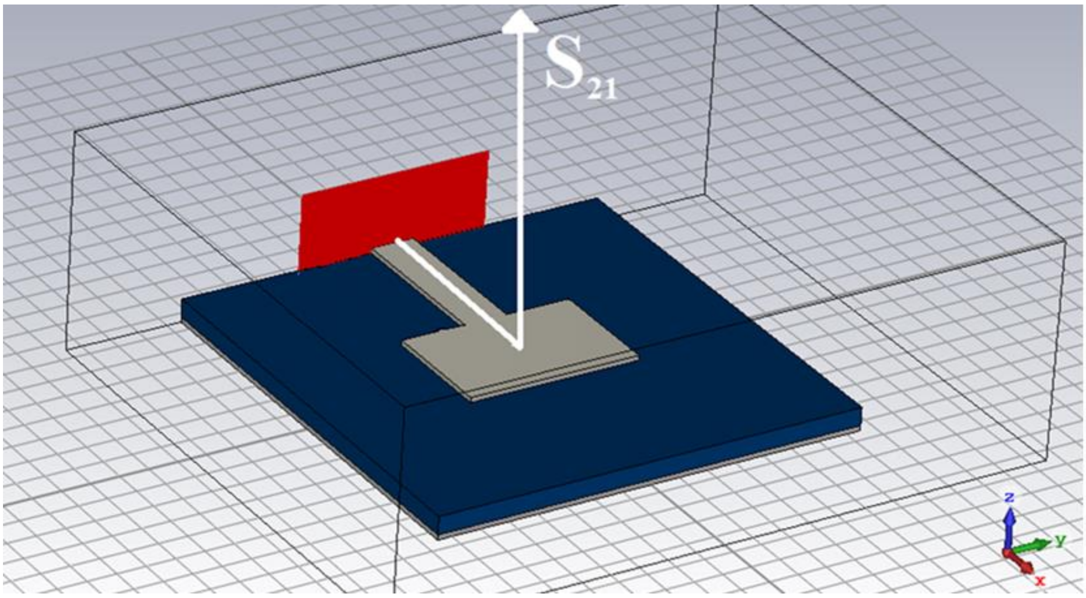

Figure 2-8: S_{21} parameter in the context of an antenna system describes the power leaving the antenna structure and detected by the receiving system.

Crosstalk is a measure of coupling between two circuits [46]. In the context of an antenna array, the crosstalk in the power transferred between one antenna to another and is an unwanted source of noise. It should be reduced to as low a value as possible in an array structure.

2.3.2 Farfield

The farfield (or Fraunhofer zone) of an antenna is the region where the beam produced by the antenna retains its angular power distribution with distance. The farfield is obtained when the detector of the device under test is sufficiently far away, that the beam can be considered a plane wave. This condition removes the need to analyse near field effects.

The directivity describes the sensitivity of the antenna in a particular direction [47]. Typically, this direction is given in polar coordinates, which consist of azimuth, φ and altitude, θ. the directivity of the antenna can be described at some position (φ, θ), however the maximum directivity is normally stated, when comparing different antennas [47].

$$D(\theta,\varphi) = \frac{\text{Radiated flux desity of antenna in direction } (\theta,\varphi)}{\text{Radiated power density of isotrope in direction } (\theta,\varphi)} \tag{2.2}$$

The radiated power of the antenna is compared to the radiated power of an isotopic antenna. For example, an isotropic antenna, or an antenna that radiates perfectly in every direction has a durativity of 0 dBi, while a high-performance horn antenna can have a directivity of approximately 25 dBi. Commercial patch antennas at lower frequencies have typical directivities of 6-8 dBi.

The gain of an antenna is a measure of how well the antenna propagates power (for a transmission antenna) or receives power (for a receiving antenna) in a given direction [47]. Similarly, to directivity, the gain can be described in polar coordinates as $G(\theta,\varphi)$. A plot of $G(\theta,\varphi)$ traced from the origin creates a surface known as the radiation pattern of the antenna [47].

The power absorbed, P_r, by this antenna, pointed at a source radiating a total power of P depends of the gain function of the receiver, $G_{antenna}$ and the source, G_{source}. The gain function and the directivity function of an antenna differ from each other by a scaler value. The Friis equation describes the amount of power absorbed, $P_{antenna}$, by this antenna at a distance, d, from the source [47]:

$$P_{antenna} = \frac{P\ G_{source}\ G_{antenna}\ \lambda^2}{16\ \pi\ d^2} \tag{2.3}$$

Therefore, in order to maximize the power received by the antenna, it is necessary to maximise the gain of the receiver. The difference between the two points at which the beam reaches half of its maximum directivity is known as the Full Width Half Maximum (FWHM). This can be used to quantify the spread of the beam.

The polarization of the wave describes the motion of the electric field vector as the wave propagates [47]. The wave is broken down into two electric field components E_x and E_y, each with their own respective phase shift. The relative difference between these two-phase shifts, $\Delta\theta$, determines the type of polarization.

In general, the beam will be elliptically polarized, this is where the trace of the combination of the two electric fields create an ellipse when plotted [47]. Linear polarization is a specific type of polarization when the relative phase shift difference, $\Delta\theta$ is equal to zero or $\pm \pi$. Similarly, circular polarization occurs when the phase shift difference, $\Delta\theta$ is $\pm \pi/2$.

A partially polarized beam can be broken down into two distinct polarizations, a co-polar component and a cross-polar-component. The co-polar component is the part of the linear polarization that contains the majority of the power. The cross-polar component (in the orthogonal linear polarization) contains the remainder of the power and can be considered to be an added noise to the system if only sensitive to one polarization.

2.4 Printed Circuit Boards

In this thesis, planar antennas are constructed on printed circuit boards (PCB). These boards consist of a dielectric material, with a metallic plate, typically copper, on one or two sides of the dielectric. A wide variety of dielectric materials are used in circuit boards, but the dielectric constant for the PCB used in this thesis are between 2.5 → 4.

Photolithography and milling are the manufacturing techniques used in this thesis to form or to etch structures onto PCB metal surface. Photolithography techniques uses a photoresist layer in conjunction with an optical mask and a chemical bath to remove copper on the PCB.

The devices created using photolithography were manufactured in the Experimental Physics department in Maynooth University. This technique can only be used on commercial PCB that have a uniform photoresist layer on the copper when purchased.

This technique requires: a mask, an ultra-violet (UV) light chamber and several chemicals, all of which were available in-house. The mask is an image of the desired pattern for the antenna printed on a sheet of transparent paper. The image is created from black ink, which can absorb UV light. The resolution of the mask is determined by the printing resolution or the dots per inch (DPI). Printers with a higher DPI will be able to create a higher resolution mask. The printer in the Experimental Physics department, a Xerox WorkCentre 7835, has a maximum resolution of DPI of 1200 x 2400.

A typical procedure to etch a planar antenna involves the following steps. Firstly, a mask was placed on a strip (small section) of the PCB and the strip was placed in a UV chamber. The strip was illuminated with UV light which polymerized the exposed photoresist on the strip. The mask was then removed from the strip. A chemical solution was used to remove the polymerized photoresist. This left part of the copper exposed. A beaker of FeCl was heated to about 30° C and this was used to etch away the exposed copper. The strip was placed back in the UV chamber without the mask and the remaining photoresist was removed. After this process the board had a copper structure on top of the dielectric layer in the desired shape for the antenna.

2.5 Planar antennas

Planar antennas are relatively small and simple antennas, commonly used at lower frequencies (MHz/GHz), consisting of a dielectric substrate sandwiched between two metal layers [47]. Circuit board etching techniques can be used to manufacture these antennas readily and so are the preferred option to analyse at higher W band frequencies. Good resolution means that sub 1 mm accuracy was possible on bi-layer PCB that can be easily sourced commercially. The printer has a much lower level of accuracy available, but the etching process puts other constraints on the resolution of devices.

These antennas were fed by either a wire connector from below the antenna or by a surface microstrip metal line (sometimes referred to as a planar waveguide). The wire or the microstrip can then in turn be connected to a waveguide or a high frequency coaxial cable (referred to as a 1 mm coax).

One of the most common planar antenna is the patch antenna (see **Figure 2-9**). One copper layer (referred to as the top layer) was etched to make the patch antenna shape structure and the second copper layer (on the other side of the dielectric substrate) becomes the ground plane. The patch can be a different shape, depending on the application and it is fed a signal by either a wire, like the back-fed patch antenna where the wire comes perpendicular to the patch through the ground plane to the patch surface, or by a surface microstrip (parallel to patch surface).

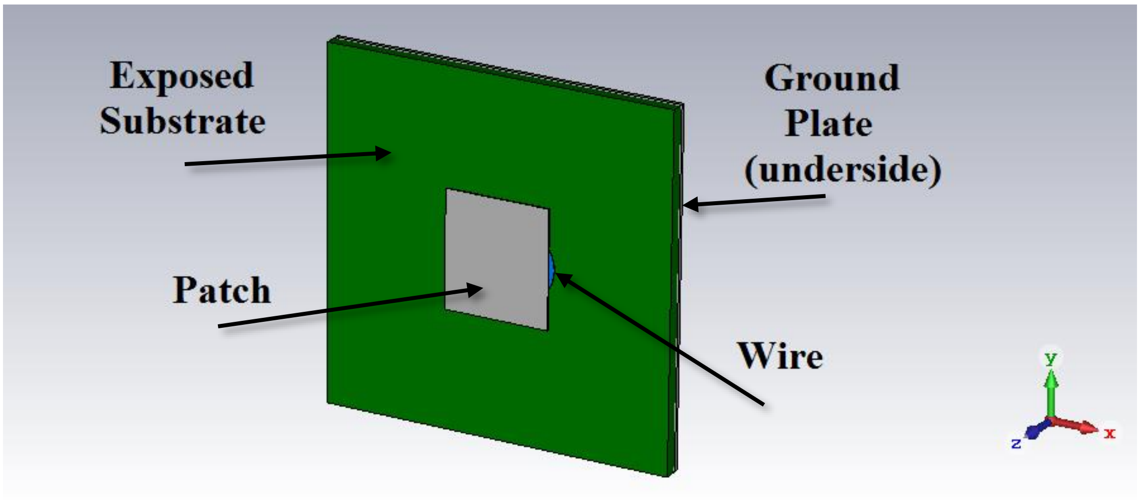

Figure 2-9: Diagram of patch antenna viewed in CST CAD environment. The device will radiate a signal along the positive *z*-axis.

Patch antennas are “resonant devices” and only operate efficiently at over a narrow frequency bandwidth. The frequency at which the patch operates most efficiently is dependent on the size of the patch. Generally, a smaller antenna will operate efficiently at a higher frequency, though the shape of the patch also effects the resonant frequency, the radiation efficiency and S-parameter matching. The substrate thickness needed to be small relative to the wavelength in order for the antenna to operate well and this becomes an issue at these higher W band frequencies as wavelength reduces. These antennas are also quite light due to their small sizes and so have applications where weight is an issue [47].

Different coupling techniques were investigated for this antenna. Some techniques were preferred in order to keep the project within our budget and local workshop capabilities. For example, there was a limited amount of connectors available for this project, as a simple 1 mm coaxial connector costs approximately €1000. Both rectangular and circular patch antennas were examined initially as radiating structures. Waveguide coupled and coaxial cable fed antenna structures were both investigated. In the case of the waveguide feed, a metal wire sitting in a WR10 waveguide was used to feed power through to the back of the antenna (through ground plane and substrate) to connect the patch to the power source. For the coaxial connection, a 1 mm coaxial-to-WR10 adaptor was used to feed the antenna and the signal was fed from a coaxial connector to antenna via a microstrip line of copper.

In the cavity method [47] of analysing patch antennas, it is assumed that the thickness of the substrate is small compared to the wavelength. This reduces the complexity of the problem from a 3-D to a 2-D situation. The dielectric substrate between the patch and the ground plate can be thought of as a resonant electromagnetic cavity. The electric field is contained within this cavity, and any radiation is due to the electric field leaking from the sides of the cavity.

The antenna will not work effectively if the operating frequency is not the same as the antenna's resonant frequency. There will be some radiation from the antenna, but these antennas radiate most efficiency at their resonant frequency over about a 10% bandwidth [47]. If the gap is small relative to the wavelength of the wave, the problem can be solved with the Helmholtz equation [47]:

$$\nabla^2 E + \omega\epsilon\mu E = 0 \qquad (2.4)$$

Once the correct boundary conditions were imposed on this equation for a rectangular patch (for example), this yields the resonant frequency to be [47]:

$$f_{res} = \frac{c}{2 \times L \times \sqrt{\epsilon_r}} \qquad (2.5)$$

where L is the length of the shorter end of the patch, c is the speed of light and ϵ_r is the dielectric constant of the substrate. Similarly, for a circular patch [47]:

$$f_{res} = \frac{1.841 \times c}{2\pi \times r \times \sqrt{\epsilon_r}} \qquad (2.6)$$

where r is the radius of the patch [47]. The resonant frequency for a patch antenna is inversely proportional to the size of the patch. So, for a typical patch operating at W band frequencies, the size of the patch is of the order of 1 mm.

2.6 Horn antennas

This section will outline the properties of horn antennas. These devices are used in this thesis either as detectors or as radiators and some background on these devices is required.

Horn antennas are the transition volume from a bounded waveguide to free-space and act as an impedance matching volume. They are typically conical or rectangular in geometry depending on the feed waveguide. In modelling horn antennas, they are electrically large devices and are simulated using full electromagnetic techniques. These devices radiate over a relatively large bandwidth (30%), especially when compared to patch antennas. They also have relatively large directivity in the region of between 25-30 dBi.

In this thesis, a W-Band probe antenna was typically used as the detector antenna (detailed description of device shown in **Figure 2-10**). These probe antennas are simply smaller horn antennas used to couple received signal without effecting the farfield of the radiating antenna radically, as the probe field pattern is quite isotropic. The probe antennas used in this thesis were manufactured by SWISSto12 and are available in two varieties, a circular waveguide probe and a rectangular waveguide probe. Both of these devices feed WR10 waveguides to and from the VNA high frequency multiplier heads.

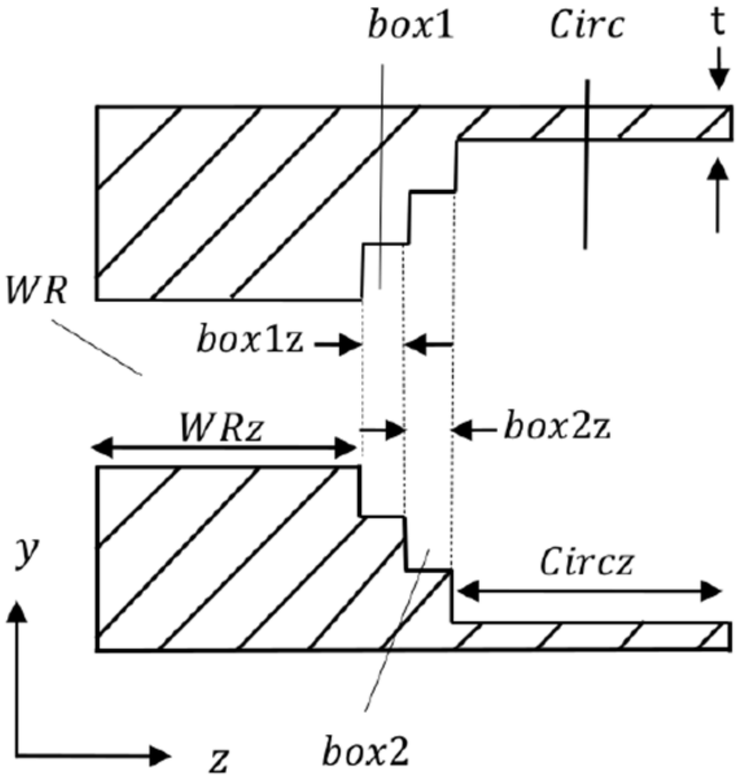

Figure 2-10a: Cross section through diagram of the circular waveguide probe antenna.

Figure 2-10b: WR10 Circular waveguide probe antennas (left) and the same antenna on a VNA port (right). The VNA is described later in **Section 2.8**.

Parameter	Value	Parameter	Value	Parameter	Value
box1a	2.396 mm	box2a	3.092 mm	radius	1.6 mm
box1b	1.535 mm	box2b	2.422 mm		
box1z	0.879 mm	box2z	0.846 mm		

Table 2-1: Values for each parameter for the circular waveguide antenna.

2.7 Waveguides

A waveguide is a device used to transfer power and are used extensively in this thesis to feed power into the antenna structure. There are a number of different techniques and devices that can be used to feed an input signal. The three different waveguides are detailed in this section: rectangular waveguides, microstrip waveguides and coaxial cables [48]. Commercial rectangular waveguides and coaxial cables are used in this thesis, while a few microstrip waveguides will be designed and manufactured by the author.

Each of these different devices can be modelled as transmission lines and as such have a corresponding characteristic impedance, Z_0, which is dependent on the design of the waveguide. This impedance is an analogue to low frequency theory as the characteristic impedance is a ratio of the voltage waves to current waves in the transmission line. As power in a transmission line passes from medium one to medium two, part of the wave is reflected back into medium one. The ratio of the incident wave to reflected wave is measured in the VNA as the S_{11} parameter. Ideally the S_{11} parameter should be minimised [49].

In each of these waveguides, the power can propagate through the waveguide in several different forms and are referred to as modes. There are four distinct modes: Transverse Electro-Magnetic (TEM), Transverse Electric (TE), Transverse Magnetic (TM) and Hybrid modes [48]. A wave operating in TEM mode has both the electric and magnetic component moving transverse to the direction of propagation. A TE or TM mode has the electric or magnetic field respectively moving transverse to the direction of propagation. Hybrid modes contain a combination of TE and TM modes.

$$\text{TE}: \vec{E} = \{E_x, 0, E_z\}, \vec{H} = \{0, H_y, 0\} \tag{2.7}$$

$$\text{TM}: \vec{E} = \left\{0, E_y, 0\right\}, \vec{H} = \{H_x, 0, H_z\} \tag{2.8}$$

2.7.1 Rectangular waveguides

Inside a rectangular waveguide, the electromagnetic wave can only travel as either TE or TM modes. The dimension of the waveguide effects the cut-off frequency. As a simple rule of thumb, the largest wavelength that will propagate though a waveguide is twice the larger size of the waveguide [48].

The WR waveguide are standardized rectangular waveguides (**Figure 2-11**). The larger size of the waveguide is roughly half the wavelength, and the smaller side is half of the larger side. WR10 waveguides are the type of rectangular waveguide used at W band frequencies. A WR10 waveguide is consists of a block of metal with a 2.54 × 1.27 mm rectangular cross section. There are additional shaped waveguides to allow for redirecting the signal: E-plane bend, H-plane bend and twist waveguides.

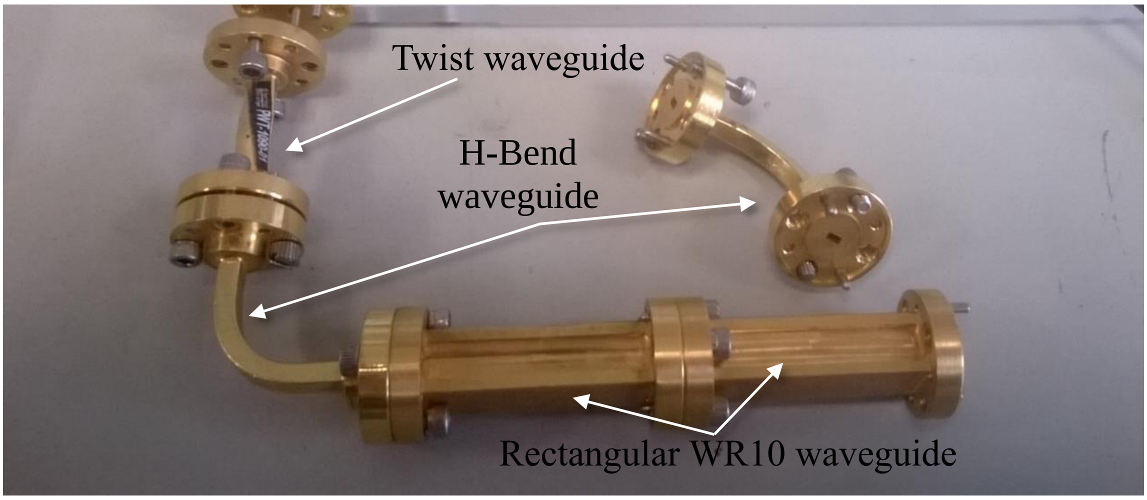

Figure 2-11: Collection of WR10 waveguides. Shown in this figure are rectangular waveguide, H-bend waveguides and twist waveguides.

2.7.2 Microstrip

A microstrip (**Figure 2-12**) is a waveguide consisting of a dielectric sandwiched between two metallic plates and is typically manufactured on PCB [45]. Energy is transferred in both the dielectric and the air above. Due to different dielectrics present, the modes of the microstrip are mixed to some degree. Most of the energy is transmitted in a quasi-TEM mode. The microstrip should be designed to prevent the higher order modes propagating, as these higher modes should be avoided to obtain good directivity.

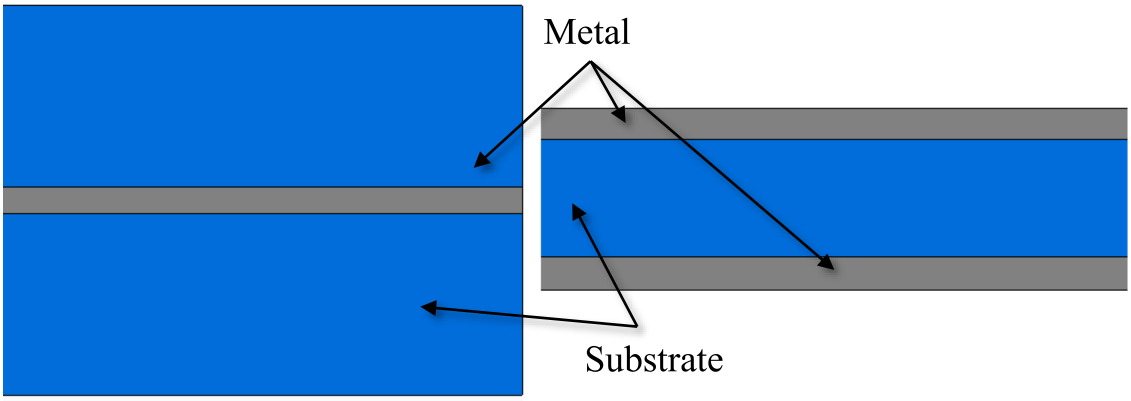

Figure 2-12: Microstrip waveguide constructed from PCB, as viewed from top (left) and from side (right). Most of the energy is transferred in-between the two metal plates but, as the plates are not fully enclosed, part of the energy is transferred in the air.

The microstrip can be approximated to be a dual filled capacitor, partly filled with air and partly filled with dielectric [45]. The primary use of these waveguides in this thesis is to provide connection between structures constructed on PCB.

2.7.3 Coaxial cable

A coaxial cable is a cylindrical waveguide, with an inner conductor, of radius b, a dielectric surrounding the wire, with an outer radius of a, surrounded by an outer conductor [45]. In a coaxial cable, for frequencies below a specific cut-off frequency, f_c, the wave travels only in a TEM mode. This single mode of propagation is desirable. The cut off frequency of the higher order modes are larger than the cut off frequency of the first mode and can be ignored. The cut off frequency for the TM modes and TE modes are given by the following [45]:

$$\text{For TM mode: } f_c = \frac{c}{2(a-b)} \tag{2.9}$$

$$\text{For TE mode: } f_c = \frac{c}{\pi(a+b)} \tag{2.10}$$

As the equations show, the cut off frequency of the TM mode will be larger than that for the TE mode. The cut off frequencies are only dependant on the size of the coaxial cable. Therefore, as long as the coaxial cable is too small to allow the propagation of the TE mode, only the TEM mode will propagate. In practical terms, this means that the inner wire and surrounding dielectric need to be on the order of 1 mm in size in order to operate at W band frequencies.

2.8 Vector Network Analyser

The VNA is a two-port system used to measure the internal reflection, gain and loss of a device by directly measuring the S-parameters. The VNA used in the Experimental Physics Department is a two port Rohde and Schwarz ZVA-24, with an accompanying ZVA-Z110 converter head system (**Figure 2-13**) to allow for operation at W band frequencies (75 GHz → 110 GHz) with full capability to measure all four S-parameters.

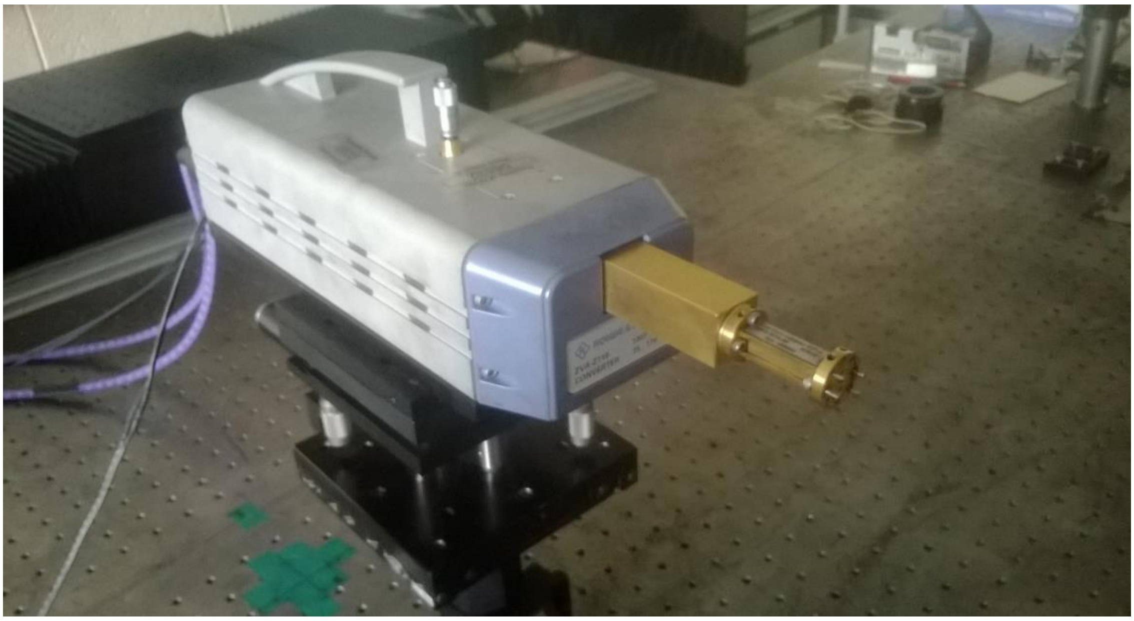

Figure 2-13: ZVA-Z110 VNA port head in the Experimental Physics department.

The maximum power is sent from one component to another when the impedance of the two structures match [49]. When the two components differ in impedance, some power is reflected during the transition. The reflection coefficient describes how much power is reflected back into the source and the transmission coefficient describes the amount of power transferred from one reference plane to the next. In the departmental VNA, the S-parameters are measured and a monitor was used to display the magnitude and/or the phase of the S-parameters. The transmission coefficient is not directly measured, rather the S_{21} and S_{12} parameters are measured, which are related to the transmission coefficient. Similarly, the S_{11} and S_{22} parameters are measured, which are related to the reflection coefficient for port 1 and port 2 respectively.

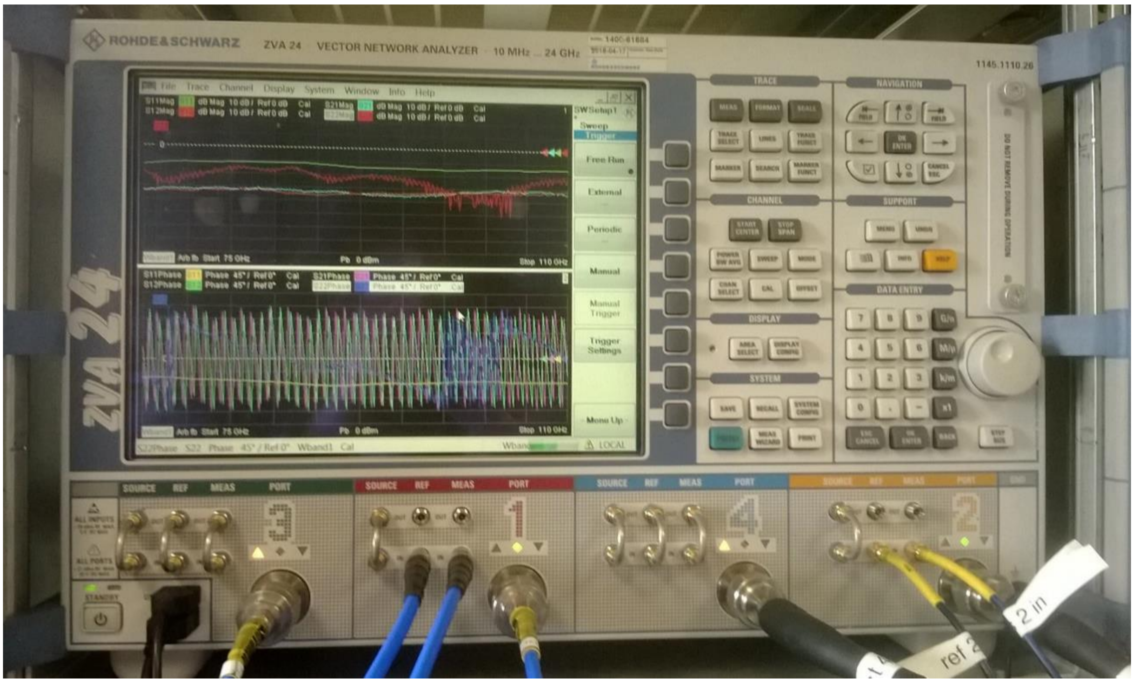

Figure 2-14: VNA with S-parameters presented on the screen. The wires are connected at the back of a ZVA-Z110 W band port head (**Figure 2-13**).

The VNA needs to be calibrated before taking a measurement. The VNA, port 1 and port 2 are switched on roughly 3 hours before beginning of a test. This is done to ensure that the VNA is in thermal equilibrium before a calibration is made. Additionally, the wires connecting the VNA to the extension heads need to be as straight as possible as wire bending can increase losses in the system. For the calibration procedure applied, the number of points is set to 3501 and the frequency range is set to the entire W band range, i.e. 75 GHz → 110 GHz. This gives a measurement every 10 MHz, which is sufficient for accurate measurement in our experimental arrangement, but different frequency resolutions are possible.

The WR10 calibration kit consists of a short, a match and an offset, all which can be connected to WR10 waveguides. There are two calibration methods: the TOSM (Through, Offset, Short, Match) method and the UOSM (Unknown, Offset, Short, Match) method. In both of these methods, the S-parameters for four specified scenarios are measured on both ports. For both methods the “Offset”, “Short” and “Match” are measured and, depending on what method is used, either the “Through” or the “Unknown” is measured.

A short is a device consisting of a waveguide connected to a large piece of metal, which ensures a signal sent to the short will be reflected back. An offset is a thin waveguide (dimensions), used to extend the distance between two adjoining waveguides. A match is a waveguide that terminates in some absorber material.

The two different methods initially follow the same procedure. The S-parameters are recorded when either the short (for “Short”), the match (for “Match”) and the short and offset together (for “Offset”) are connected to port 1. These measurements are repeated on port 2.

The “Through” method involves physically connecting the two ports heads together (**Figure 2-15**) and recording the S-parameters. The “Unknown” method involves pointing the two ports together, but not physical joined, possibly with a known antenna attached to the end of each port and recording S-parameters. The “unknown” in the calibration refers to the unknown phase when a signal was sent from one port to the other through the space between.

Figure 2-15: This photo showed two VNA port heads connected together in order to perform the “Through” portion of a TOSM calibration.

Chapter 3 W band patch antenna

3.1 Overview

A patch antenna operating in the W band frequency range was examined initially. CST Microwave Studio was used to design and analyse the patch antenna. The antenna was built on a commercially available Printed Circuit Board (PCB), ABT18. Printing and etching techniques were used to modify one side of the board in order to create the "patch" structure. The substrate of the board separated this patch from the ground plate (copper-coated dielectric). The electromagnetic analysis/design, manufacture and testing of this antenna will be described in this chapter.

In order to feed the patch, a small hole was drilled through the PCB, in order to connect the patch to an input signal. A small wire was passed through the hole and soldered to the patch structure. The wire was excited with a W band signal through the other end of the wire being suspended in a WR10 waveguide with a direct connection to the VNA frequency multiplier head. This method to excite the planar antenna avoids the expense of high frequency 1 mm coaxial connectors. This was mechanically challenging and some experimentation was required to achieve good contact while preventing substantial damage to the board, isolating the ground plane and limiting any other undesired effects. This chapter will deal exclusively with these "back-fed" patch antennas. **Chapter 4** then will describe the use of coaxial connections feeding W band signal using a waveguide to coaxial adaptor on the WR10 waveguide of the VNA frequency multiplier head.

The EM measurements performed on the back-fed antennas are also outlined in this chapter with CST simulation in this development process. The farfield pattern generated in CST, was used to quantify the amount of power radiated by the antenna. Patch antennas tend to only radiate effectively over relatively small frequency bands around their resonant frequency and should have a low return power (S_{11} parameter) below -10 dB at these resonant frequencies, which could be achieved through correct design, manufacture and assembly.

As part of this development, circular and rectangular patch antennas were examined. The finalized design was manufactured by circuit board photolithography in the Experimental Physics Department. A number of limiting factors made manufacturing the antennas difficult. A major limiting factor was the size of the patch for W band frequencies. Due to the small size of the patches, only simple 2-D shapes (circles, rectangles, squares) could be accurately reproduced. Any detail on the patch smaller than roughly ~ 0.5 mm was beyond the tolerance available for the in-house manufacturing process. Several tests were performed on the manufactured antennas in the VNA lab and these results were compared to the simulated results from CST.

3.2 Circular patch antenna

A circular patch geometry (**Figure 3-1**) was considered initially and was used to test the influence of the various free parameters (patch dimensions, dielectric thickness, feeding mechanisms and feed wire offset distances). The cavity analysis, described in **Section 2.5,** was used to determine a starting point for the patch radius of the device.

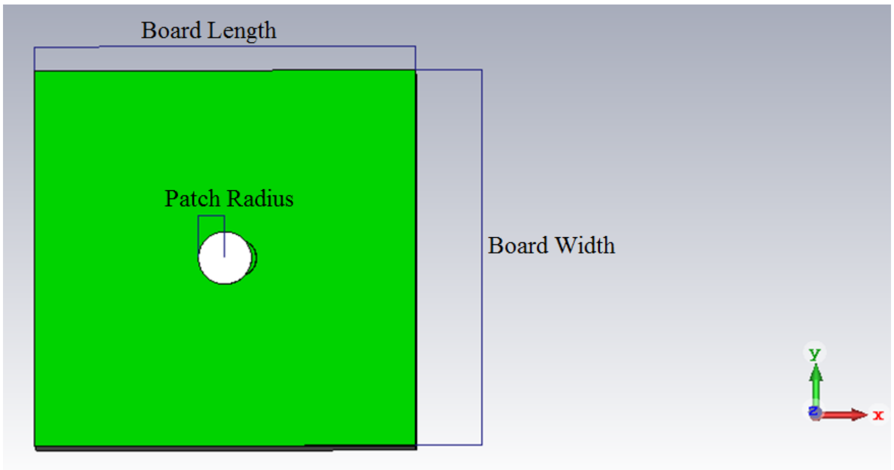

Figure 3-1a: Circular patch antenna as seen from CST, viewed from top. The white circle at the centre of the device was the patch. The green section was the exposed substrate of the PCB.

For the parameters used in this simulation, the length and width of the board in the *x* and *y* direction respectively (see **Figure 3-1a**) define the size of both the substrate and the ground plate. For an antenna with a dielectric constant of 3.3 operating at 100 GHz, the radius of the patch from **Equation (2.6)** should be 0.48 mm.

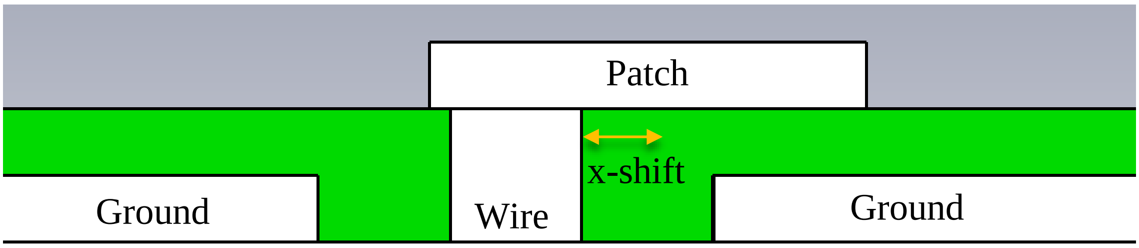

Figure 3-1b: Cross section view of patch antenna. The wire connects the patch to the power supply. The displacement of the wire along the *x*-axis relative to the centre of the device was referred to as the “x-shift” parameter. It should be noted that the choice of axis is arbitrary as moving in the orthogonal direction (the *y*-axis) or diagonally would have an equivalent effect as the patch is a circle.

The first patch geometry to be analysed was the circular patch with radius of 0.48 mm (for full list of parameters, see **Table 3-1**). The size of the circuit board supporting the patch had no obvious starting value. The board was initially set to a size of 6 mm × 6 mm as this was comparable to the size of the modified portion of the WR10 waveguide. The dielectric thickness of commercial board (0.8 mm) was a relatively large fraction of the operating wavelength (3 mm) and this may also have an effect on the antenna performance. The dielectric thickness (in the model) was initially set to 0.1 mm to ensure the approximation used in the cavity analysis model of the dielectric thickness being much smaller than the wavelength of operation.

The patch thickness was set to 0.01 mm and effects due to the finite size of the patch were ignored in this first approximation analysis. The ground plane of the antenna was set to a thickness of 0.8 mm which takes into account the metal on the PCB and the support structure underneath. The ground plane covers the entire area beneath the dielectric. The wire through the ground plate/dielectric was connected to a simulation source in the CST work environment.

Patch parameters	Value	Patch parameters	Value
Patch radius	0.48 mm	Wire coating radius	0.3 mm
Wire radius	0.1 mm	Relative electrical permittivity	3.3
Board width	6 mm	x-shift	0 mm
Board length	6 mm	y-shift	0 mm
Dielectric thickness	0.1 mm		

Table 3-1: Initial parameters used to describe the circular patch antenna based on the cavity model. The parameters for the wire are based on a small wire available in the department.

The “x-shift” parameter (**Figure 3-1b**) describes the displacement of the wire from the centre of the patch along the *x*-axis and it was important to optimise to achieve highest directivity. In CST, the wire was created such that at x-shift = 0 mm, the wire as passed directly though the centre of the patch. This parameter was increased from 0 mm → 0.5 mm in steps of 0.1 mm, which moves the wire from the centre of the patch towards the edge of the patch. Steps of 0.1 mm were chosen as this accuracy was possible to reproduce by using a micrometer stage when drilling this device (the manufacturing techniques used to create the device are described in **Section 2.4**).

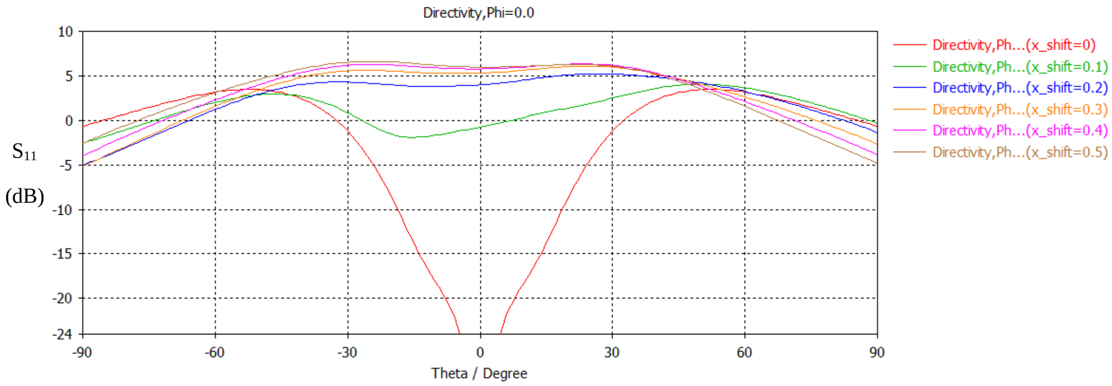

Figure 3-2a: Farfield pattern of the antenna as “x-shift” was changed.

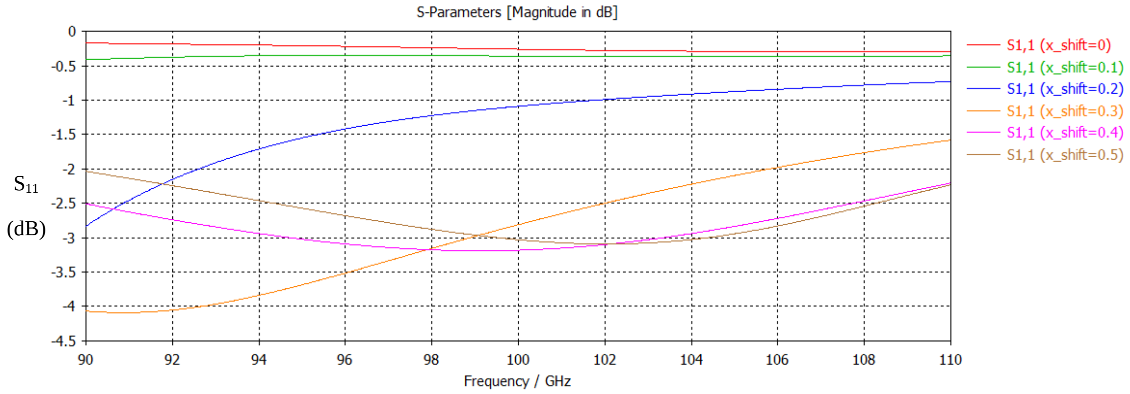

Figure 3-2b: Plot of S_{11} as the displacement of wire along *x*-axis ("x-shift") was altered.

The farfield pattern of the different antenna configurations (**Figure 3-2a**) showed that the displacement of the wire had a large effect on the directivity. When the wire passes through the central position of the patch (i.e. x-shift = 0 mm), the antenna had an extremely low on-axis directivity. The antenna had a larger directivity when the wire was offset from the centre of the device.

The S_{11} parameter (**Figure 3-2b**) of the antenna had a minimum return loss (S_{11}) at 100 GHz and this occurred when the wire was 0.4 mm from the centre of the antenna. It was clearly seen from these two figures that the worst position for the wire was directly through the centre of the antenna (i.e. x-shift = 0 mm). When the wire passes through this central position, the antenna produces a beam which had a null on-axis and two lobes radiating in different directions (**Figure 3-2a**). When x-shift was greater than 0 mm, the farfield patterns had two peaks off-axis, located at approximately ± 30°, which was not ideal. Additionally, the return loss was high, with a S_{11} parameter value of -0.25 dB, meaning that 94% of power was reflected, which was poor.

The antenna had a larger directivity and a lower return loss when the wire was offset from the centre of the patch. At the best position, when x-shift = 0.4 mm, the on-axis directivity of the antenna increases to 5.8 dBi, but this antenna still suffers from a large S_{11} of -3.2 dB at the targeted frequency of 100 GHz. This means at most only 52% of the power fed into the device was radiated.

This design was not behaving well. It would appear that other parameters, such as the patch radius and board size, may also be affecting the antenna's performance.

The effect of the radius of the patch on the antenna's performance was examined next. The radius of the circular patch was altered in size from 0.36 mm → 0.6 mm, i.e. 0.14 mm on either side of what was predicted from theory, in steps of 0.02 mm. The size of the patch radius was altered along with the wire displacement and the x-shift was also altered from 0.2 mm → 0.4 mm. This was to see if the wire displacement and the patch size were independent parameters.

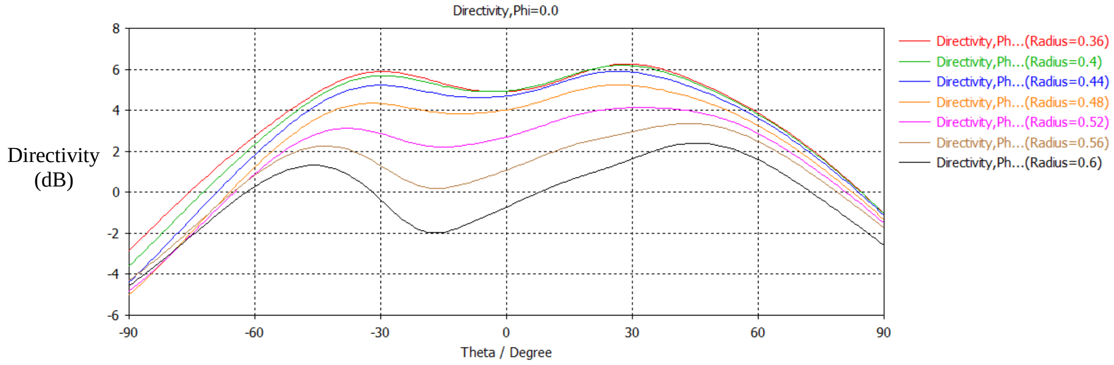

Figure 3-3a: The farfield pattern at 100 GHz of the different radii with an x-shift of 0.2 mm.

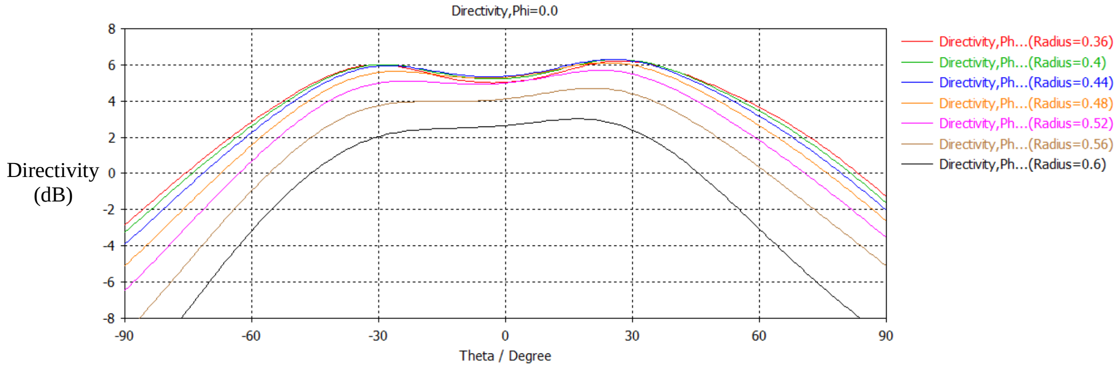

Figure 3-3b: The farfield pattern at 100 GHz of the different radii with an x-shift of 0.3 mm.

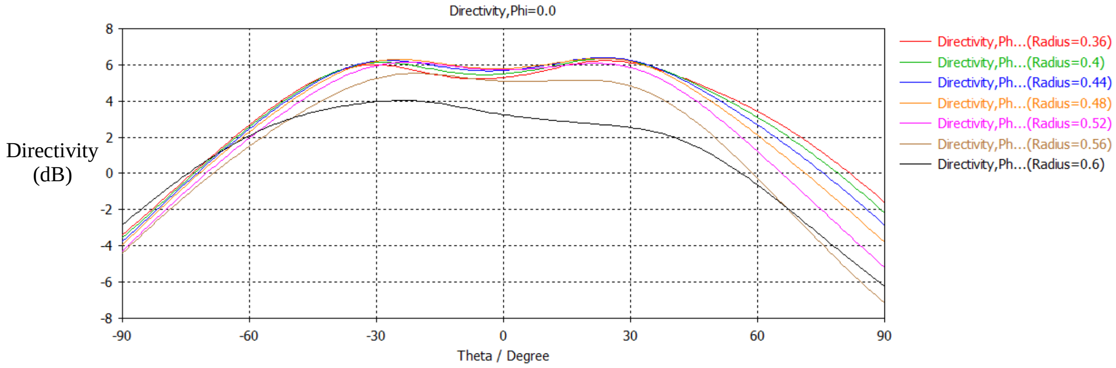

Figure 3-3c: The farfield pattern at 100 GHz of the different radii with an x-shift of 0.4 mm. The results from this test were similar to the results from **Figure 3-3a** and **Figure 3-3b.**

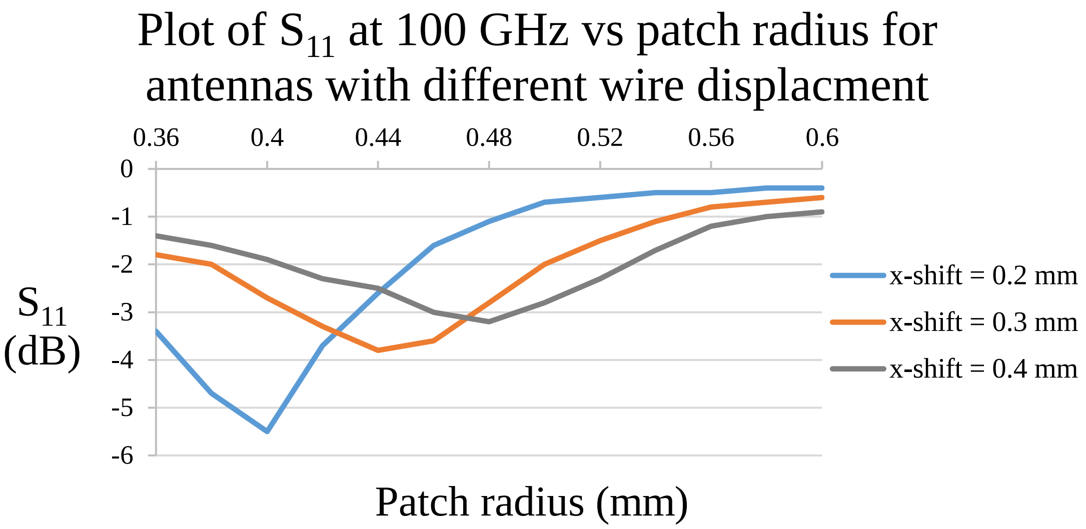

Figure 3-3d: Plot of the S_{11} at 100 GHz parameters of the antenna versus the patch radius.

The farfield pattern of each antenna in **Figure 3-3a, Figure 3-3b** and **Figure 3-3c** all show that these antennas beams had a similar double peak shape. Ideally, the farfield pattern should reach a maximum at the centre (0°) of the beam. However, the directivity of these antennas, reached a maximum at roughly ± 30° off-axis, which was not ideal. Additionally, patches with a low S_{11} parameter also tend have a corresponding high maximum directivity.

The devices with a smaller patch radius had a larger on-axis directivity than the larger patches. It was desired for the device to reach its maximum directivity on axis, (i.e. when $\theta = 0°$). All devices showed two distinct beams, indicating that the beam in not propagating along the desired axis of propagation. The directivity of the antenna was strongly depended on the patch radius.

The plot in **Figure 3-3d** showed that a small change of the patch radius greatly changes the S_{11} parameter. There was a strong relationship observed between patch size and the resonant frequency. The S_{11} parameter for these antennas was rather large as the S_{11} value was never below -10 dB (i.e. The return loss was high). The lowest S_{11} parameter was obtained when the patch radius was 0.40 mm for the antenna with an x-shift of 0.2 mm. As the x-shift value increased, the patch radius that had the minimum S_{11} parameter also increase, but the minimum value was less than it was for the antennas with a lower x-shift. This also implied that wire displacement and the patch size were not independent parameters.

The lowest S_{11} parameter was obtained for the device with the patch radius was 0.40 mm for the antenna with an x-sift of 0.2 mm. This antenna also reached an on-axis directivity of 5 dBi. The peaks of the designed antennas were not located at the centre of the beam, but rather each beam had two distinct peaks and the S_{11} parameters were above -10 dB. This design was not optimum either, so further investigation was needed to improve the characteristics.

The dielectric board size was altered to determine if this affected the antenna’s performance. The board width (along the *y*-axis) and the board length (along the *x*-axis) was varied between 3 →

12 mm. The width was kept to a constant of 6 mm when length was varied. The patch radius was fixed at 0.4 mm and the *x*-axis offset was 0.2 mm.

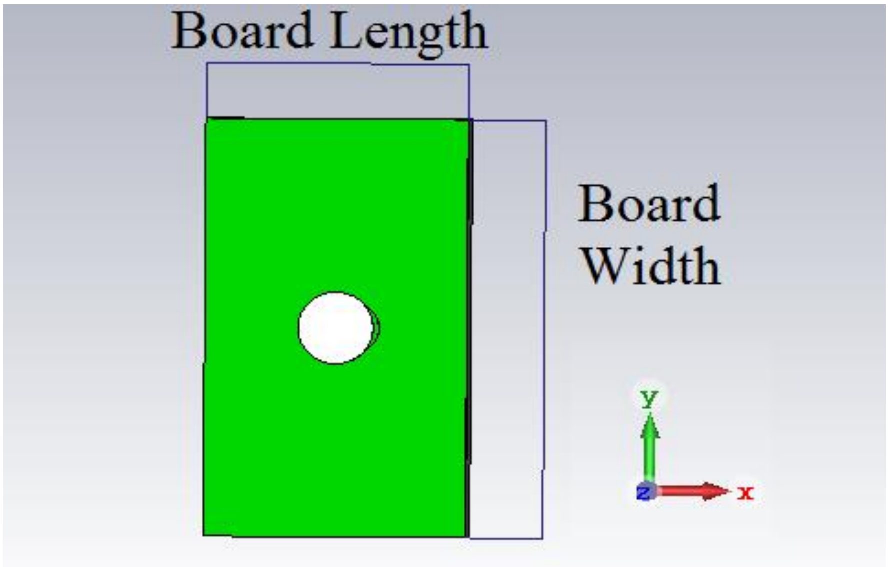

Figure 3-4a: Diagram of patch antenna detailing the axis convention used to distinguish between board length and width. The board width was the length along the *y*-axis and the board length was the length along the *x*-axis.

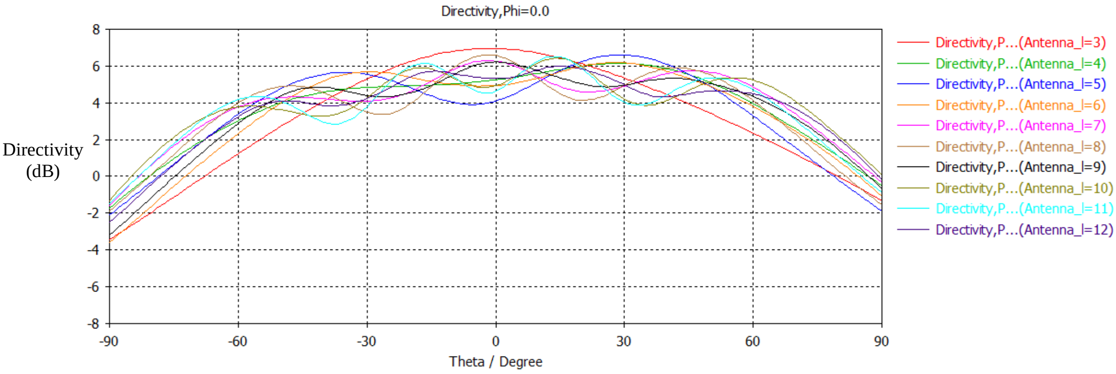

Figure 3-4b: The farfield pattern of the antenna due to altering the board length (*x*-axis).

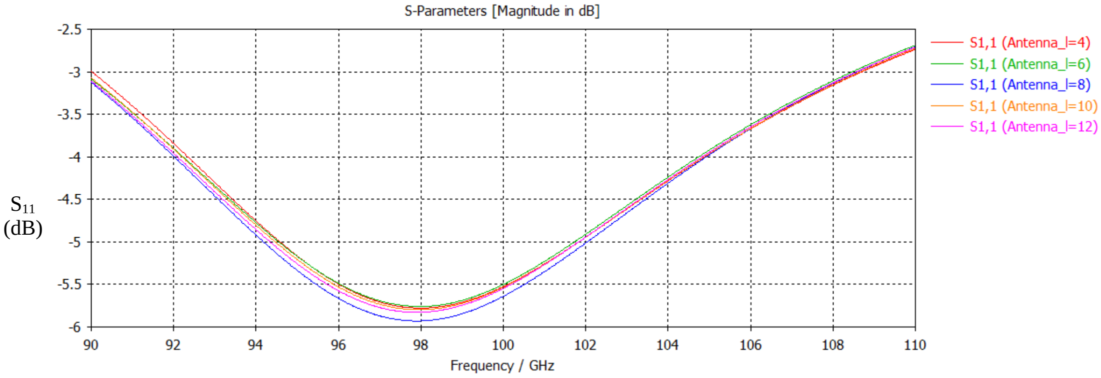

Figure 3-4c: The S_{11} of the antenna due to altering the board length (*x*-axis).

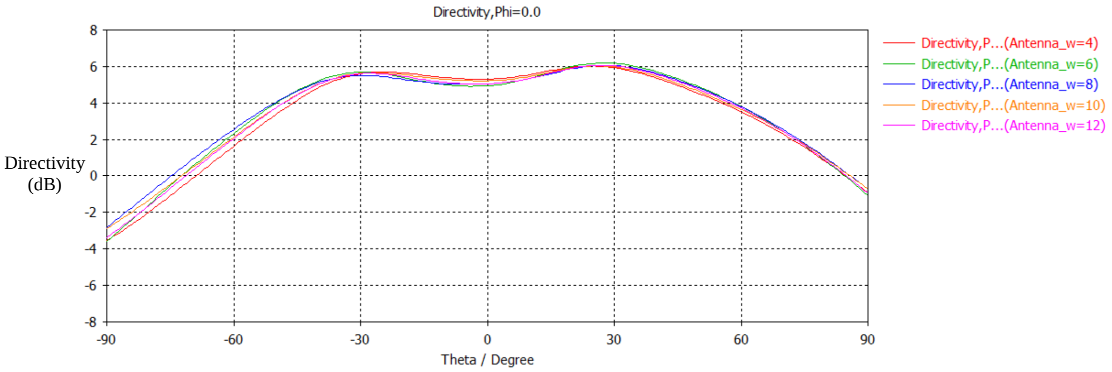

Figure 3-4d: The farfield pattern of the antenna due to altering the board width (*y*-axis).

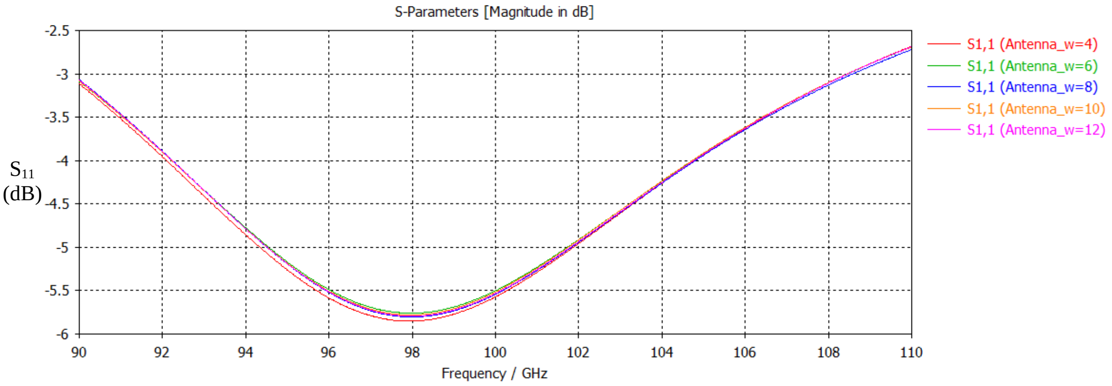

Figure 3-4e: The S_{11} of the antenna due to altering the board width (*y*-axis).

A small change in the length of the board width has a large effect on the shape of the farfield pattern (see **Figure 3-4b**). The antenna had a single on-axis peak when the board length was 3 mm (in red in **Figure 3-4b**). The farfield patterns of antennas of various sizes at 100 GHz showed that the on-axis directivity reached a maximum of 7 dBi with a board length of 3 mm and a minimum of 4.1 dBi at 5 mm. The beam shape with a board length of 3 mm was preferred, as the directivity reached a maximum at the centre. There was found to be no simple relationship between board length and directivity.

It was found from **Figure 3-4d**, that altering the width of the board did not change the overall shape of the farfield pattern, unlike altering the board length. Additionally, altering either the board length or width had only a small effect on the return loss of the antenna (**Figure 3-4c** and **Figure 3-4e**).

Altering the board size along the *x*-axis significantly affected the farfield behaviour of the antenna, but altering the board size along the *y*-axis only slightly affected the farfield pattern. This asymmetry was due to the effect of the x-shift parameter, which alters the position of the wire from the centre of the board along the *x*-axis only.

Altering the size of the board effects the S_{11} parameter by 0.4 dB (**Figure 3-4c**). The effect of altering the size of the board was relatively small when compared to the effect of altering the radius of the patch, which changes the S_{11} parameter by up to 5 dB (**Figure 3-3d**).

Each parameter tested was also affected by the other parameters, i.e. each parameter was interdependent. The critical parameters for the design of this antenna, as tested so far, were the radius of the patch, the board length and the displacement of the wire from the centre of the patch along the *x*-axis. In a series of tests, all these parameters were altered in order to optimise the overall performance.

Patch parameters	Value	Patch parameters	Value
Patch radius	0.43 mm	Wire coating radius	0.3 mm
Wire radius	0.1 mm	Relative electrical permittivity	3.3
Board width	12 mm	x-shift	0.2 mm
Board length	3 mm	Dielectric thickness	0.1 mm

Table 3-2: Parameters for idealised circular patch antenna.

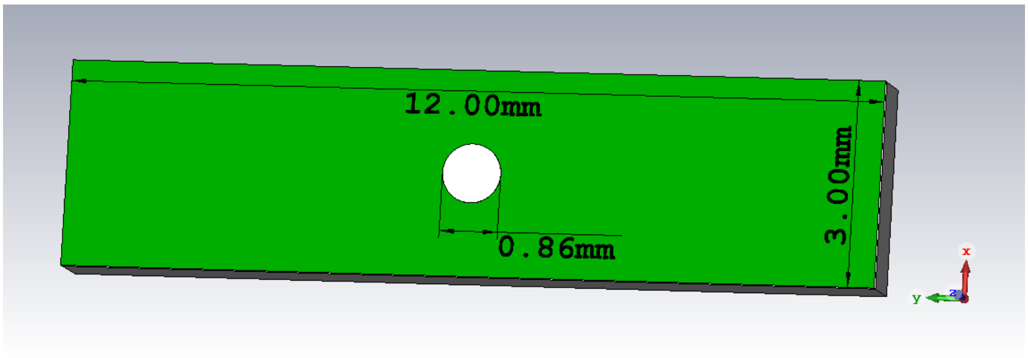

Figure 3-5a: Circular patch antenna of radius 0.43 mm as viewed in CST.

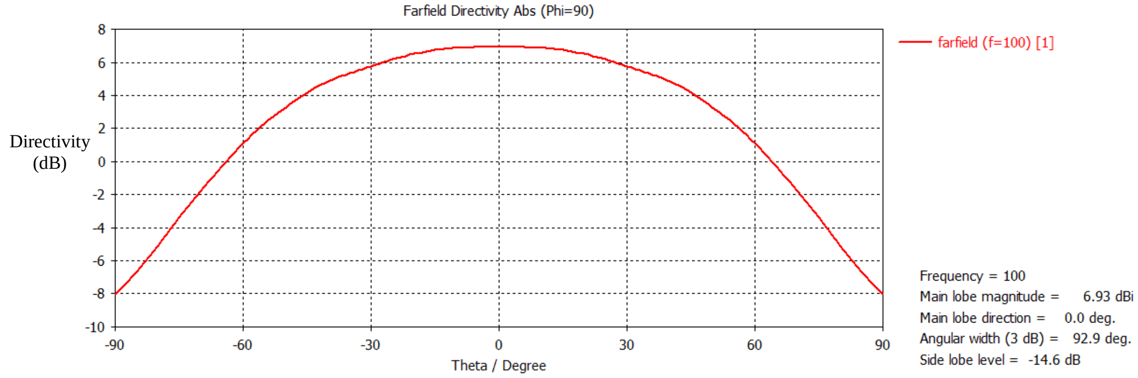

Figure 3-5b: Farfield plot of the antenna along the $\varphi = 90°$ axis (equivalent to the *y*-axis).

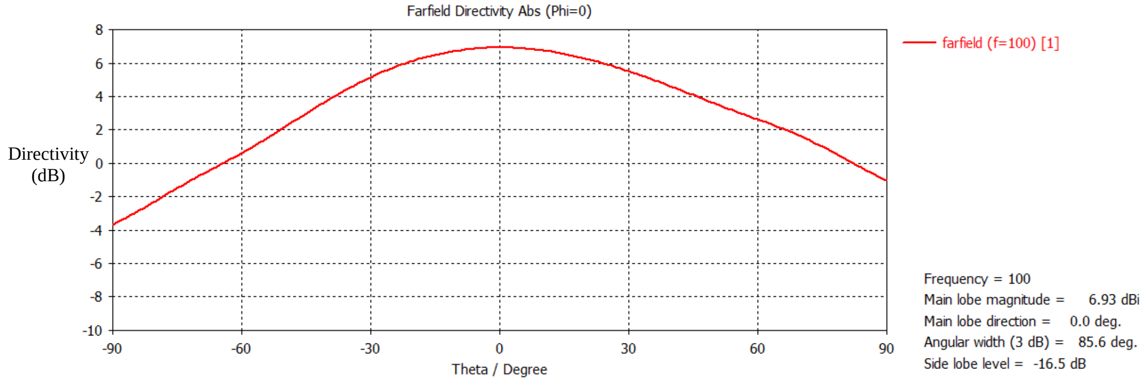

Figure 3-5c: Farfield plot of the antenna along the orthogonal $\varphi = 0°$ axis (equivalent to the *x*-axis).

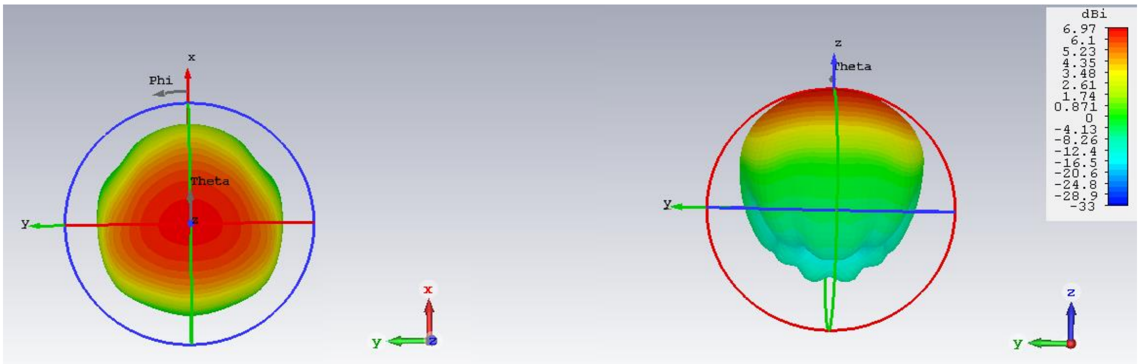

Figure 3-5d: 3-D farfield plots of the idealised antenna viewed from top (left) and side (right). The beam was propagating along the desired axis of propagation (the *z*-axis).

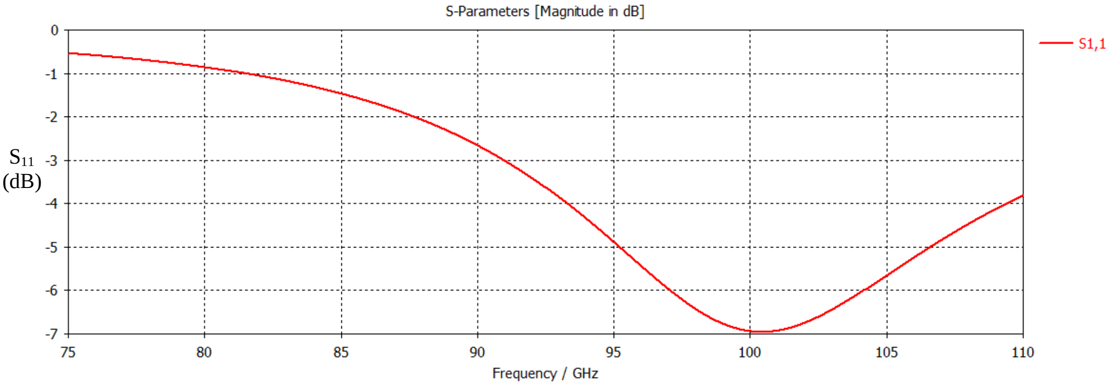

Figure 3-5e: The S_{11} parameter of the circular patch antenna.

Overall this antenna showed several favoured characteristics. The farfield pattern of this circular patch antenna indicates that the power was radiating along the *z*-axis and had a relatively large directivity in the main beam of 7 dBi (**Figure 3-5b**).

The board was longer in width (along the *y*-axis) than in length (*x*-axis) and the device had a larger maximum directivity when it had this characteristic. This was due to the asymmetry of the beam, i.e. the beam pattern was different along the *y*-axis (**Figure 3-5b**) compared to the *x*-axis (**Figure 3-5c**). This was influenced by the position of the wire feed, which was offset along the *x*-axis, but was not offset along the *y*-axis in this analysis. If the wire was offset in the y-axis, then the board would be longer in the *x*-direction. As **Figure 3-5e** shows, the S_{11} parameter of the antenna showed a sharp decrease at 100 GHz to -7 dB. This was above the desired return loss of -10 dB.

The thinnest board initially available in the Experimental Physics department had a substrate thickness of 0.8 mm. The antenna design needed to be scaled to match this available board. The effect of this substrate thickness was also examined. The substrate thickness was altered from 0.1 mm → 0.8 mm in steps of 0.1 mm. The device used the table of parameters shown in **Table 3-2,** with the exception of the substrate thickness.

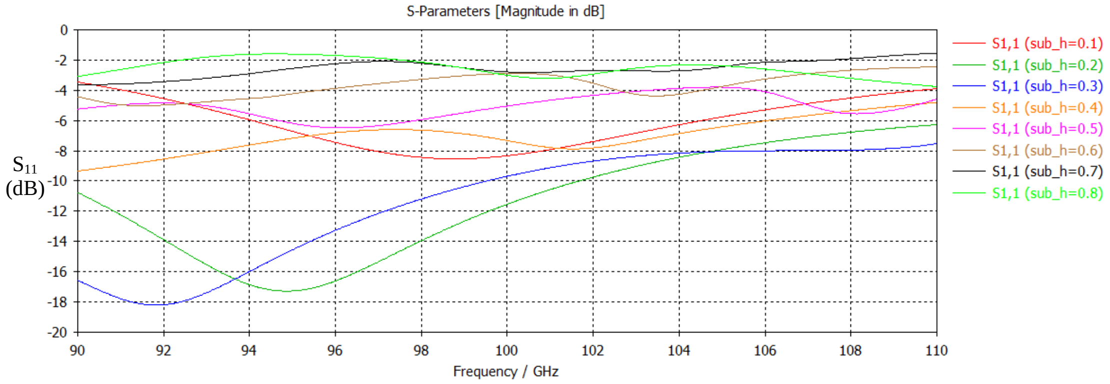

Figure 3-6a: Comparison between S_{11} parameters for different antenna geometries at 100 GHz used when examining the effect of the substrate height on the antenna's performance.

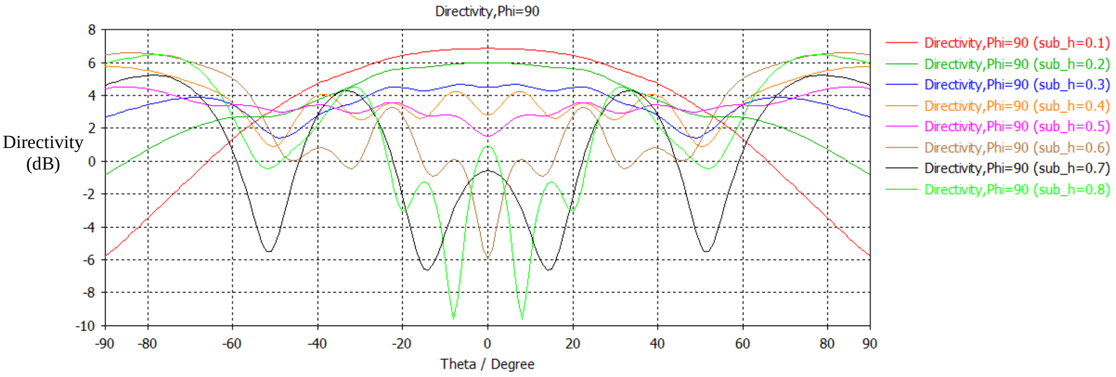

Figure 3-6b: Directivity of the antenna at 100 GHz as substrate height changes.

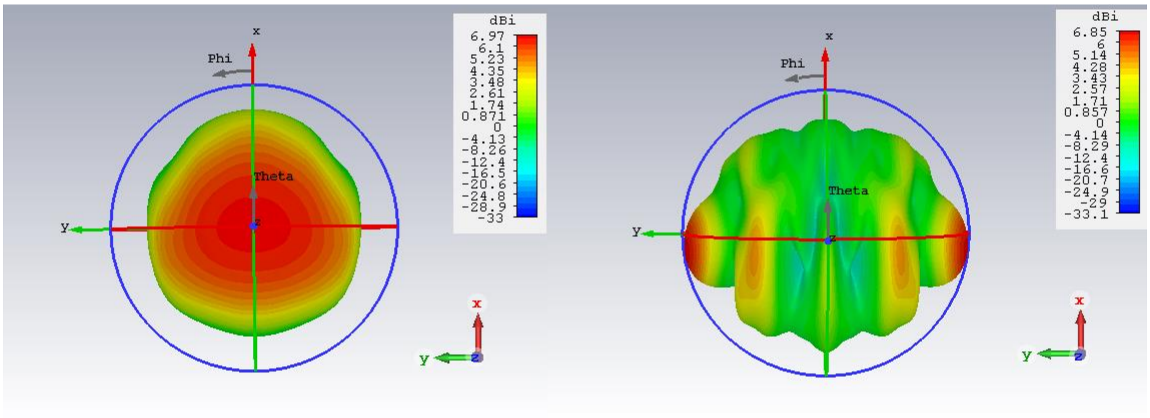

Figure 3-6c: 3-D farfield pattern of the antenna with a substrate height of 0.1 mm (left) and 0.8 mm(right).

Altering the substrate thickness affected both the S_{11} parameter and the directivity of the patch antenna. The S_{11} parameters in **Figure 3-6a** showed an initial decrease with increasing substrate thickness, decreasing to a minimum of -11.5 dB with a substrate thickness of 0.2 mm, before increasing up to -2.9 dB with a substrate thickness of 0.8 mm. The antennas with a lower dielectric height had a lower overall return loss. Devices with a substrate thickness above 0.5 mm suffer from a high return loss. The directivity of the antennas as seen in **Figure 3-6b** decreases with increasing substrate thickness. The shape of the farfield beam changes, and with a substrate height of 0.7 mm, the off-axis beam sidelobes become larger than the on-axis beam. The devices with thinner substrates had a relatively large on-axis peak in their beam pattern, while the devices with a large substrate thickness had large side lobes. The 3-D farfield plot in **Figure 3-6c** showed the presence of large undesired side lobes propagating along the *x*-*y* plane. These side lobes were larger than the beam propagating along the desired direction of propagation.

The best antenna behaviour seen in **Figure 3-5** was with a dielectric thickness of 0.1 mm, however the thinnest board available initially in our programme had a substrate thickness 0.8 mm. The beam using a board with a thickness of 0.8 mm (in **Figure 3-6c**) showed the presence of large side lobes and was not optimal. A board with a dielectric thickness of less than 0.2 mm was required for the circular patch antenna to operate more optimally at 100 GHz.

3.3 Rectangular patch antenna

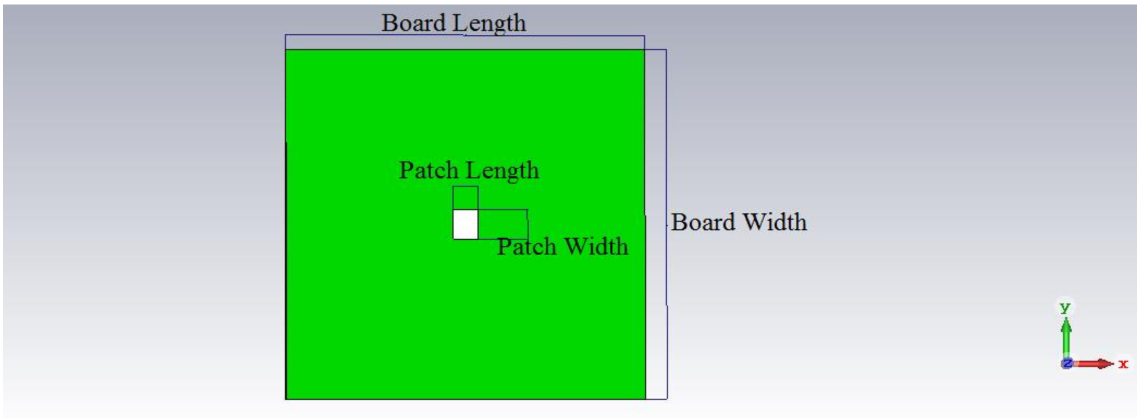

Figure 3-7: Rectangular patch antenna as seen from CST, as viewed from top.

A rectangular patch antenna was also designed and investigated. Initially the dielectric thickness, the x-shift of the feed wire and the wire parameters were set to the same values as the optimum circular antenna from **Table 3-2**. For a fair comparison between the two antenna designs, the simulated rectangular patch antenna was designed on the same PCB dimensions as the circular patch described in **Section 3.2**. This section provides a summary of the effects of changing the various parameters of the design including the position of the feed wire, the patch size and the substrate height or thickness. The first rectangular patch antenna analysed was based on the previously designed circular patch antenna.

Patch parameters	Value	Patch parameters	Value
Patch length	0.83 mm	Wire coating radius	0.3 mm
Patch width	0.9 mm	Relative electrical permittivity	3.3
Wire radius	0.1 mm	x-shift	0.2 mm
Board width	12 mm	y-shift	0 mm
Board length	3 mm	Dielectric thickness	0.1 mm

Table 3-3: Initial parameters for rectangular patch antenna based on the design on the cavity analysis method. The device had lowest return loss when the *x*-axis offset was 0.2 mm.

The cavity analysis was again used to determine a starting point for the patch size. For an antenna with a dielectric constant of 3.3 operating at 100 GHz, the length of the patch was 0.83 mm

(**Equation (2.5)**) and the width (*y*-axis length) was 0.9 mm. For the patch, the length and width were the length of the patch in the *x* and *y* direction respectively.

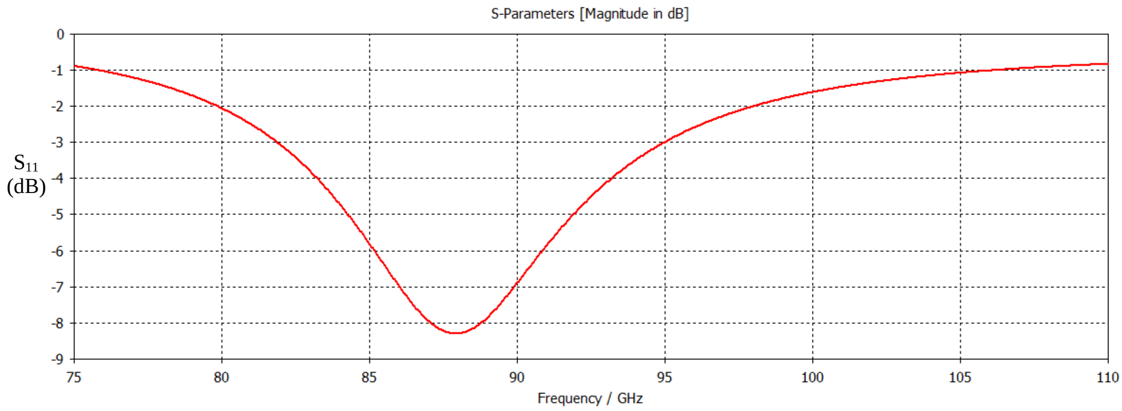

Figure 3-8a: This graph presents the S_{11} parameter of the antenna over the W band.

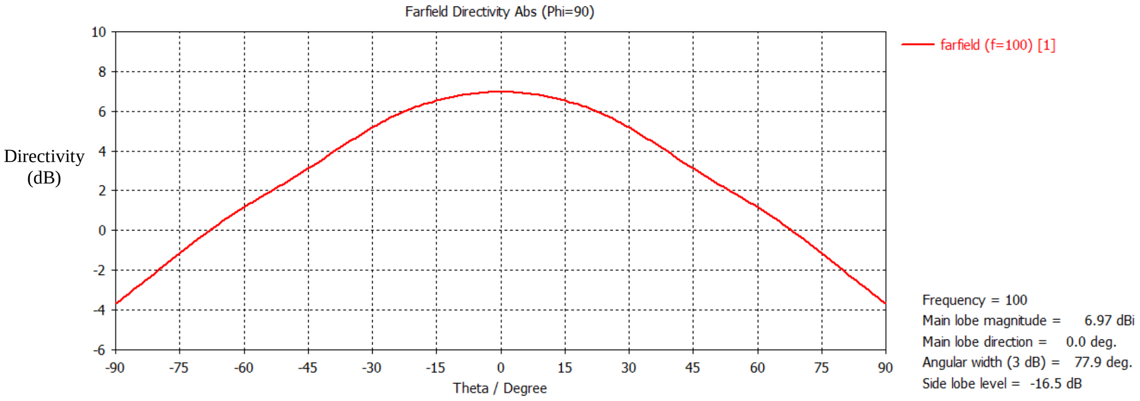

Figure 3-8b: The farfield pattern of the antenna described.

Figure 3-8a shows that the device resonated most strongly at regions around 87 GHz. The antenna reached a maximum of roughly 7 dBi at 100 GHz (**Figure 3-8b**). The beam had the desired farfield pattern characteristics, a relatively large directivity with minimised side lobes. It should also be noted that the wire offset and the patch size were not independent parameters.

The starting parameters were altered in CST to optimise towards the best performance. The first parameter analysed was the wire offset and this was tested to see if there was a different between altering the device along one axis rather than the other (x or y direction). For this test, the offset along one axis was set to 0 mm and the offset along the other axis was varied from 0 mm → 0.5 mm (see **Figure 3-10** for offset along both axes).

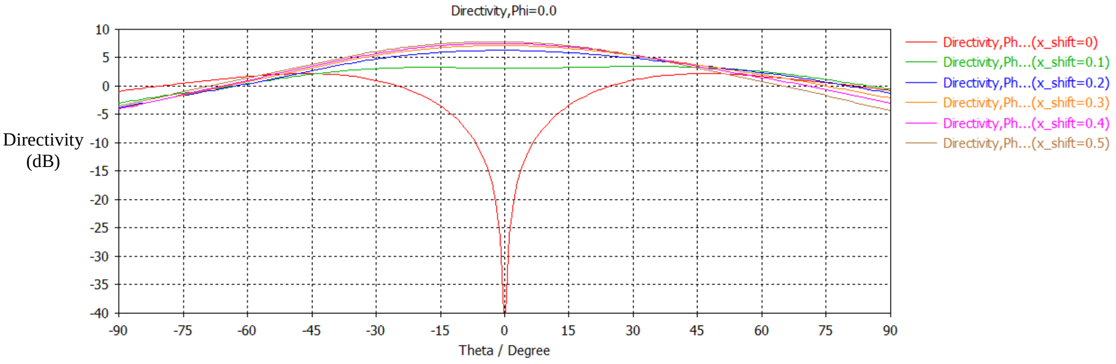

Figure 3-9a: The effect on the farfield of the beam as the position of the wire along the *x*-axis (x-shift) was altered.

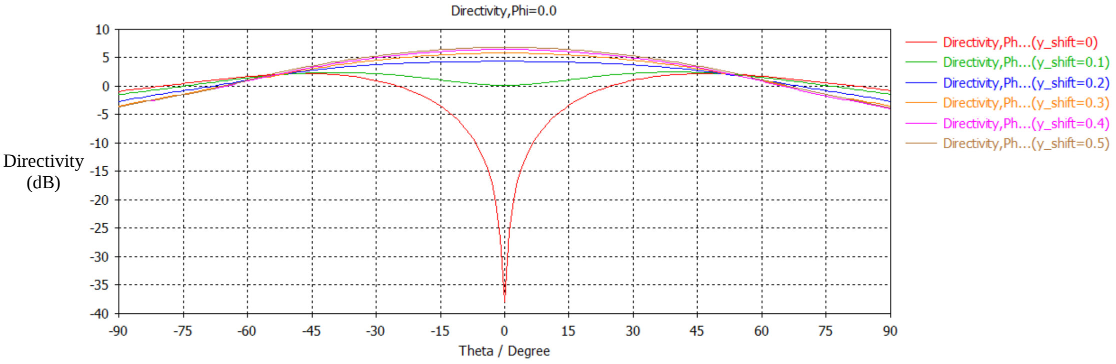

Figure 3-9b: Farfield of patch antenna at 100 GHz as the position of the wire along the *y*-axis (y-shift) was altered.

In both **Figure 3-9a** and **b**, the maximum directivity reached was ~7.5 dBi. Offsetting the device along one axis was equivalent to offsetting the device along the other axis as expected. Additionally, both plots showed the need for the wire to be offset. The antenna did not radiate power on-axis when the wire was passed through the centre of the device.

The wire could be shifted diagonally along both the *x* and *y*-axis, which is more difficult to manufacture accurately in a real device. The offset along both axes was varied from 0 mm → 0.5 mm as shown in **Figure 3-10**:

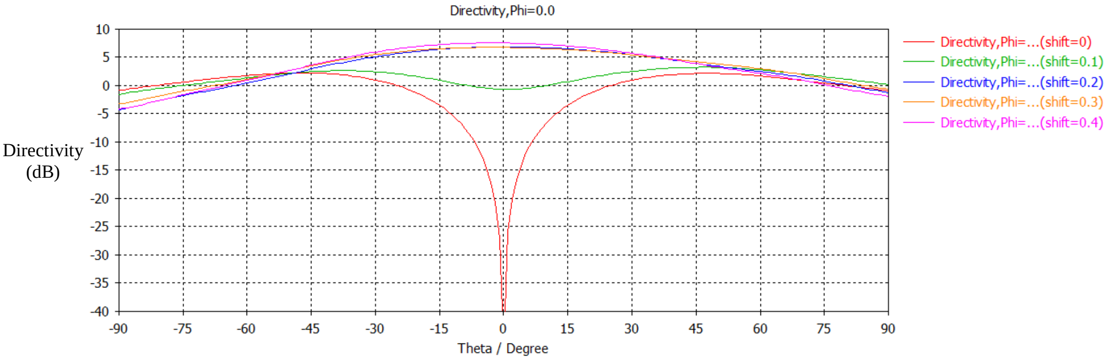

Figure 3-10: Farfield pattern of rectangular patch antenna as device is altered along the *x* and *y*-axis.

The plotted farfield in **Figure 3-10** were similar to though generated in **Figure 3-9**. The wire needs to be offset from the centre by some amount (between 0.2 and 0.4 mm, which varied depending on other parameters). However, it did not make a difference which axis the wire was offset along. For the following simulations the device will be offset along the *x*-axis only.

After determining the effects of the wire feed, the effects of the size of the patch were examined next. The patch length was altered as it was increased from 0.5 to 1 mm in steps of 0.1 mm. This changed the size of the patch in the *x*-axis direction.

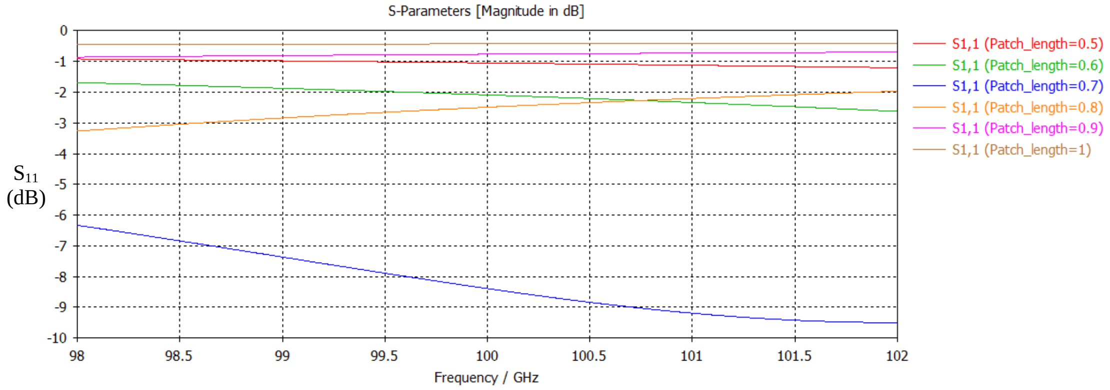

Figure 3-11: S_{11} parameters of the different antennas, arranged according to patch length.

From **Figure 3-11**, the curve of the S_{11} parameters for patches longer than 0.7 mm have a positive slope and so have a higher resonant frequency. The curves of the lengths below 0.7 mm have a negative slope and so have a lower resonant frequency. This implies that increasing the size will decrease the resonant frequency and vice versa, which was expected from the cavity model.

The minimal S_{11} parameter was found when the patch length was 0.7 mm with a value of -8.39 at 100 GHz. However, the minimum value S_{11} parameter for the 0.6 mm length antenna was -2 dB at 100 GHz. This was noteworthy as a change of only 0.1 mm in the length of the antenna could change the effectiveness of the antenna by roughly 6 dB. As a result, smaller steps sizes were then examined in order to find the patch size which has a resonant frequency of 100 GHz. The patch length was altered from 0.6 mm to 0.8 mm in steps of 0.02 mm. This alters the size of the patch in the *x*-axis direction to find a design with a S_{11} minimum at 100 GHz.

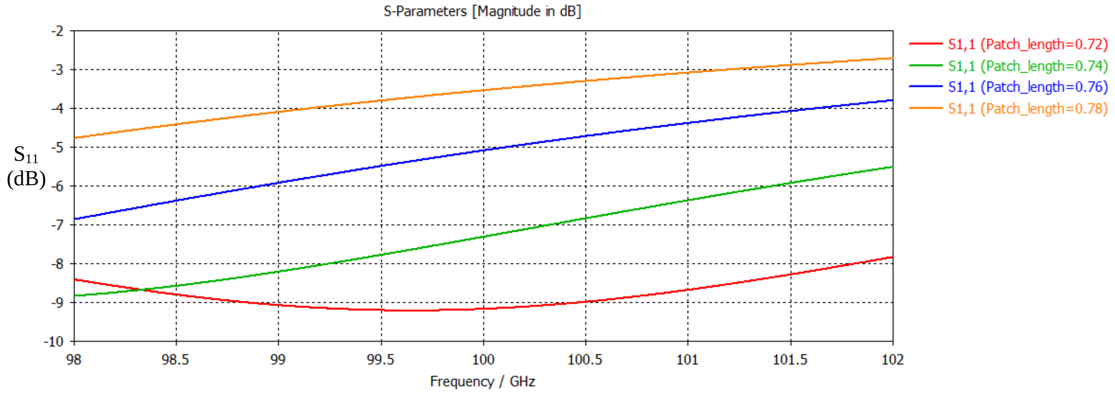

Figure 3-12a: Plot of the S_{11} parameters due to increasing the patch length from 0.7 → 0.8 mm.

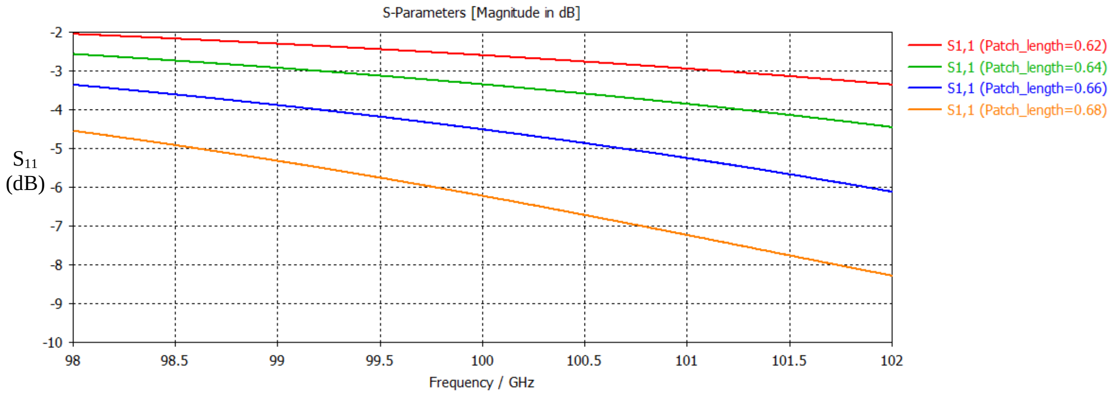

Figure 3-12b: Plot of the S_{11} parameters due to increasing the patch length from 0.6 → 0.8 mm.

From **Figure 3-12**, the minimum S_{11} parameter occurs at a different frequency for different patch lengths. A small change in the patch size had a large effect on the antenna's return loss. The same pattern holds from before in **Figure 3-11**, with patches longer than 0.7 mm have a positive slope and vice versa.

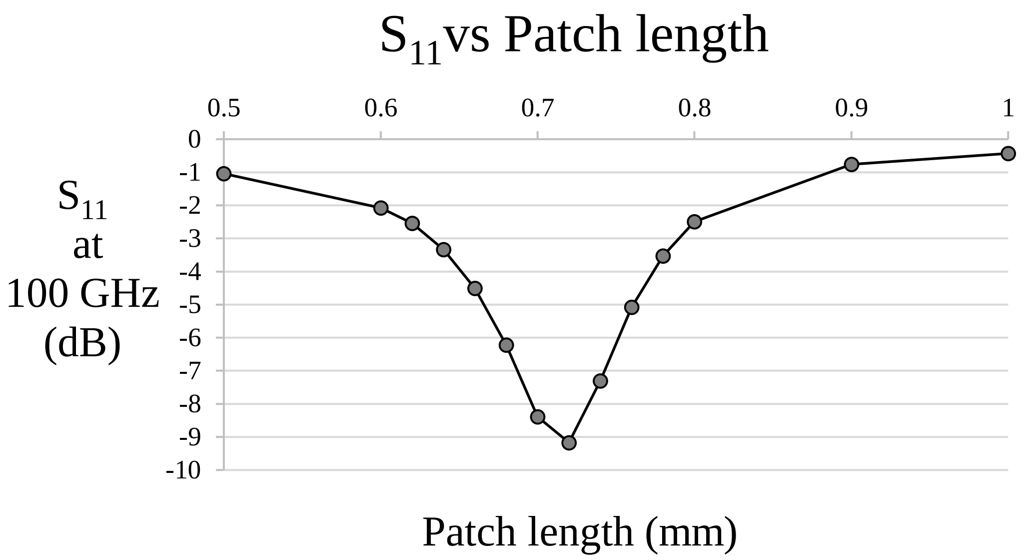

Figure 3-13: This graph showed a Plot of S_{11} at 100 GHz versus patch length.

Figure 3-13 shows a minimum value of S_{11} was reached when the patch length was 0.72 mm. The S_{11} parameter at 100 GHz was found using the graphs in **Figure 3-11** and **Figure 3-12**. This antenna was the best so far designed and the characteristics of this antenna are shown in **Table 3-4.**

Patch parameters	Value	Patch parameters	Value
Patch width	0.72 mm	Wire coating radius	0.3 mm
Patch length	0.9 mm	Relative electrical permittivity	3.3
Board width	12 mm	x-shift	0.2 mm
Board length	3 mm	Dielectric thickness	0.1 mm
Wire radius	0.1 mm		

Table 3-4: Patch parameters for the optimal rectangular patch antenna.

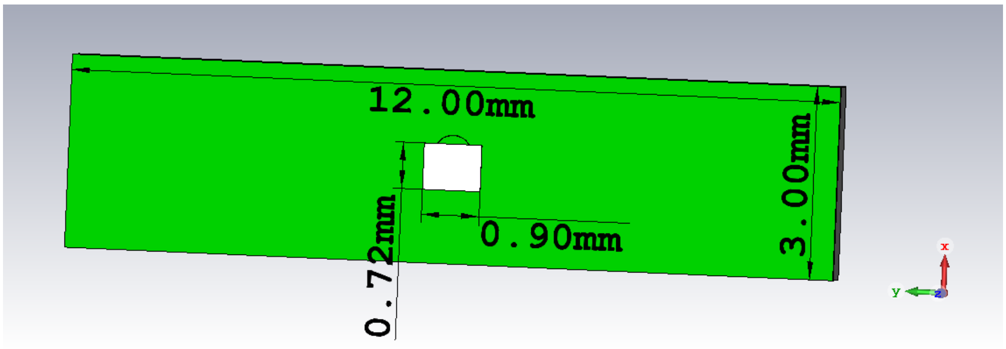

Figure 3-14a: Idealised rectangular patch antenna simulated in CST.

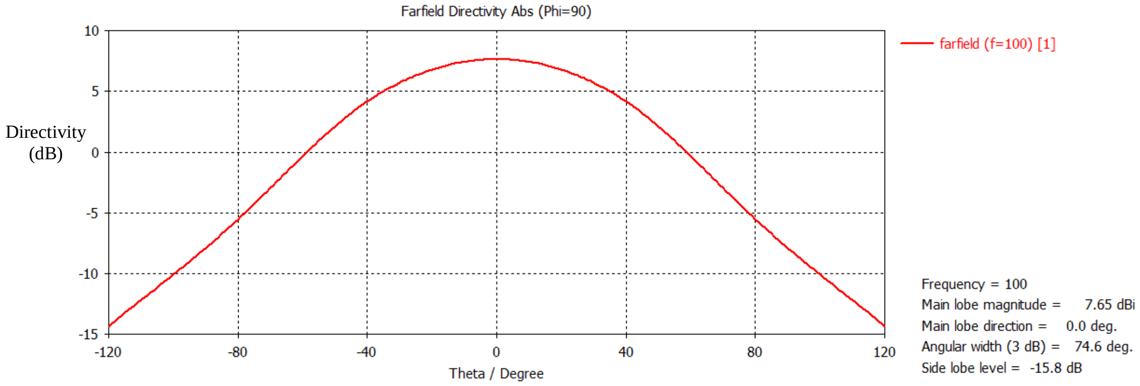

Figure 3-14b: Farfield pattern of a single patch antenna along the $\varphi = 90°$ axis.

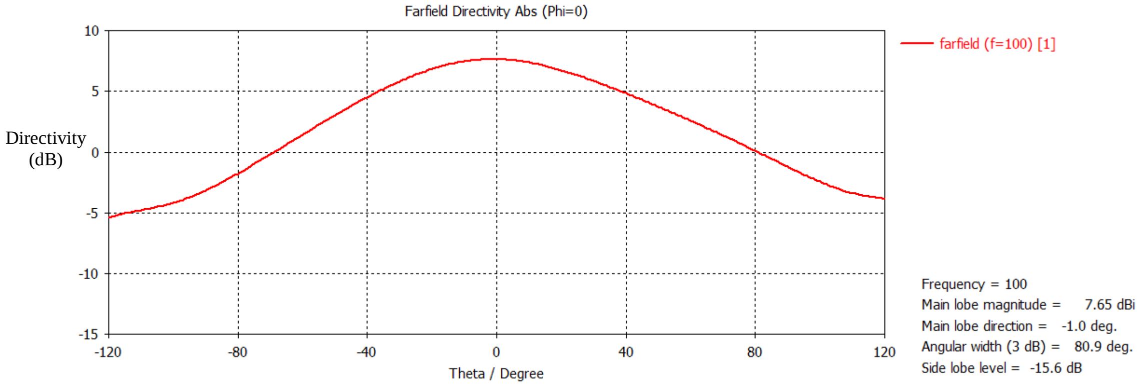

Figure 3-14c: Farfield pattern of a single patch antenna along the $\varphi = 0°$ axis.

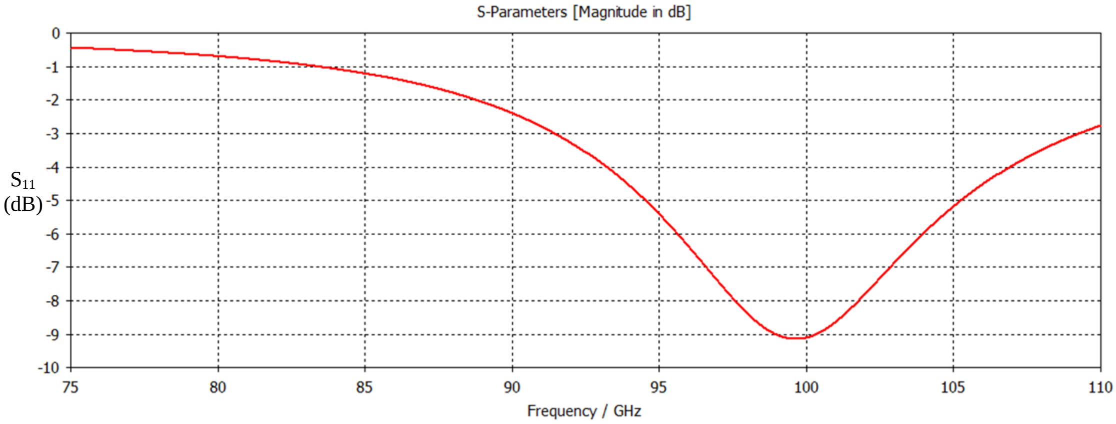

Figure 3-14d: Plot of S_{11} parameter over W band frequencies.

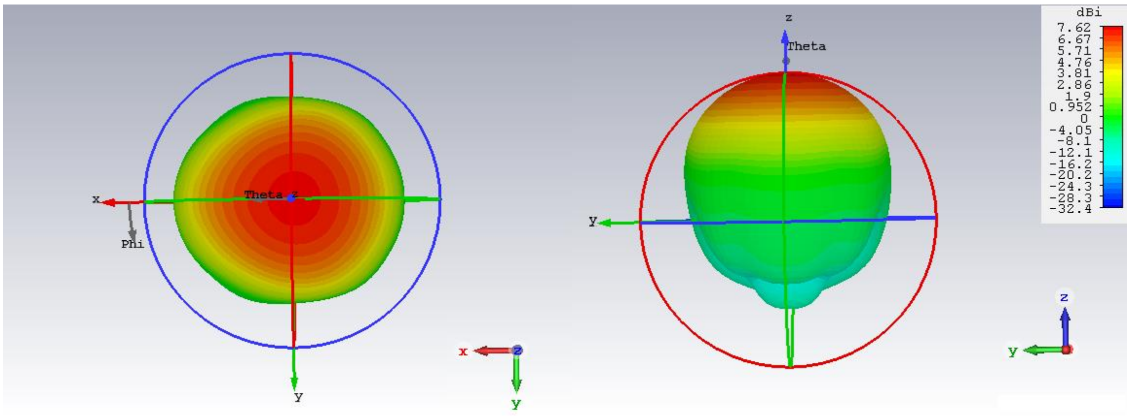

Figure 3-14e: The 3-D farfield plot of antenna from the front (left) and side (right).

Figure 3-14 showed the rectangular patch simulated in CST, with farfield plot along the $\varphi = 90°$ axis (**Figure 3-14b**), the $\varphi = 0°$ axis (**Figure 3-14c**), the S_{11} plot (**Figure 3-14d**) and a 3-D plot of the farfield (**Figure 3-14e**) at 100 GHz. This antenna had the desired farfield and S_{11} characteristics. The farfield pattern along the $\varphi = 90°$ axis showed that the antenna reached a maximum directivity of 7.6 dBi. The S_{11} plot indicated that the antenna radiated its power most efficiently at approximately 99.5 GHz.

An S_{11} parameter of -9 dB indicates that more than 87.4% of the power was radiated. The 3-D view of the antenna showed power was radiated along the positive *z*-axis as expected. As seen in the 3-D plot, the antenna was symmetric about the *x*-*z* plane, but showed a slight asymmetry around the *y*-*z* plane. The antenna reached a peak directivity of 7.6 dBi.

One interesting detail of this antenna was the asymmetry observed in the 3-D farfield pattern (**Figure 3-14e**), which was also observed for the cuts along the $\varphi = 0°$ and the $\theta = 90°$ axis. The farfield beam pattern was asymmetric in one direction, which was due to the offset of the wire along one axis.

Despite the antenna in **Figure 3-14** showing favoured characteristics, it was not possible to build this antenna as the available ABT18 PCB had substrate thickness of 0.8 mm. The effect of substrate height or thickness was also examined. The substrate height was increased from 0.1 → 0.8 mm in steps of 0.1 mm. These results can be compared to a similar test done for the circular antenna (**Figure 3-6**).

Substrate height	x-shift	Patch length	Patch width	Board length	Board width
0.1 mm → 0.8 mm	0.3 mm	0.9 mm	1.3 mm	3 mm	12 mm

Table 3-5: Geometry of rectangular antenna used for examining the effect of substrate height on the device’s performance.

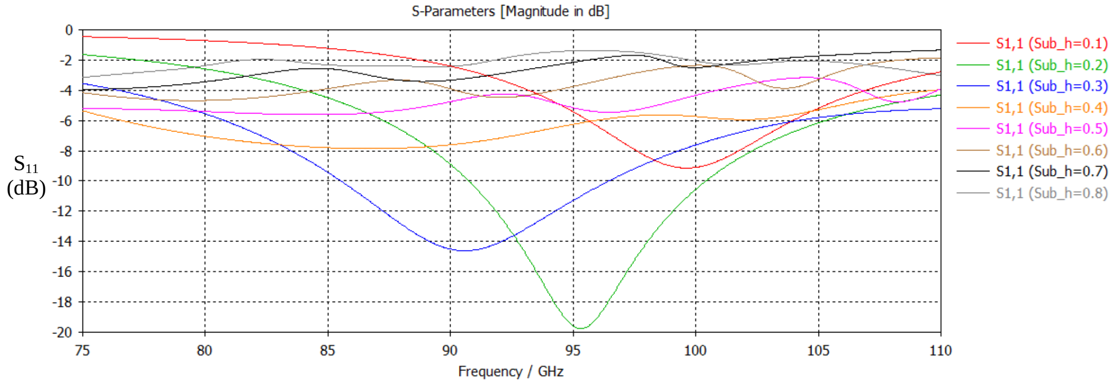

Figure 3-15a: The S_{11} parameters compared with changing substrate height.

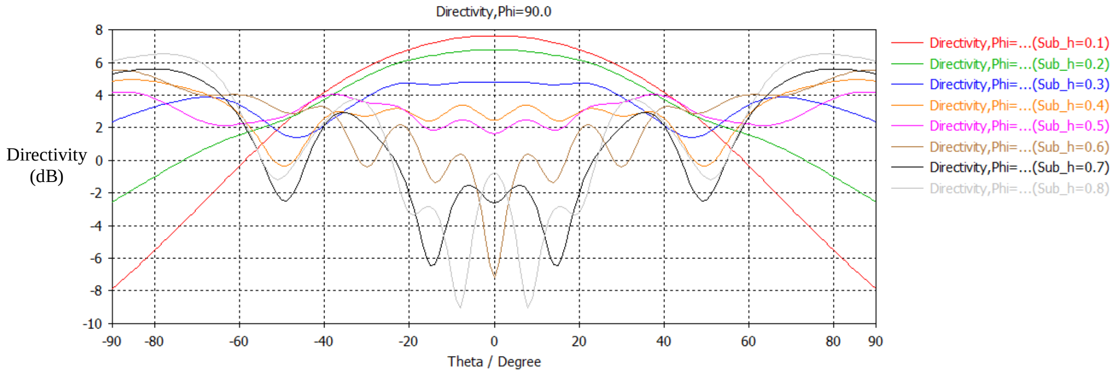

Figure 3-15b: The directivity of the antenna with changing substrate height.

The S_{11} parameters (**Figure 3-15a**) show an initial decrease with increasing substrate height, decreasing to a minimum of -10.34 dB at substrate height of 0.2 mm, before increasing up to a maximum of -1.71 dB at a substrate height of 0.8 mm. The S_{11} parameter was low at frequencies around 100 GHz for a board with a substrate thickness of between 0.1 mm → 0.4 mm.

The directivity of the antennas (**Figure 3-15b**) decreases with increasing substrate height, like the situation in **Figure 3-6**. The farfield pattern of the antennas altered significantly with substrate height. When the substrate height was 0.1 mm, the on-axis directivity was 7.6 dBi. However, when the substrate was 0.8 mm, the on-axis directivity decreased significantly to only -0.7 dBi. The smaller boards created a better beam. The patch antenna had the maximum directivity when the substrate size was 0.1 mm.

The only board available had a substrate height of 0.8 mm initially, which is shown below and results in non-optimum performance in W band. In order to verify manufacturing, coupling and testing capability this design was manufactured and its beam was measured to compare with simulations.

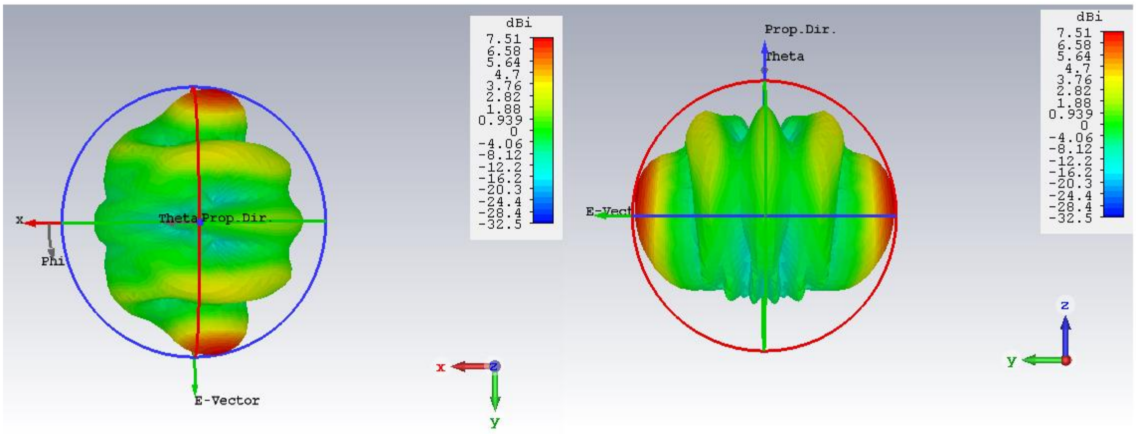

Figure 3-16: The 3-D farfield plot of the rectangular patch antenna with a substrate height of 0.8 mm, as viewed from the front (left) and side (right). This image is a combination of the same simulation generated in CST.

The farfield plot in **Figure 3-16** showed the presence of large side lobes propagating along the *x*-*y* plane. The antenna reached a maximum directivity of 3.06 dBi in the direction of the *z*-axis. This value was small compared to the size of the beam along the *x*-*y* plane, which reached a maximum of 4.8 dBi. A PCB with a thickness of 100 µm seems to be required to achieve the 'classic' patch behaviour at W band frequencies. Ideally, a PCB with a thinner dielectric needed to be sourced in order to manufacture patch antennas with better performance.

Further analysis showed that it was not possible to create a classical patch antenna using the ATB18 PCB, which could operate effectively at 100 GHz. Alternative antenna designs on this board were examined further and are presented in **Chapter 5**.

3.4 Crosstalk between patch antenna

When a collection of antennas are placed significantly close to each other, crosstalk between antennas will occur. Crosstalk is effectively the leaking or transferring of the signal from one antenna to another and, in this context, was used to refer to power from one antenna entering a neighbouring antenna and is troublesome for focal plane arrays particularly at longer wavelengths showing up as excess signal or system noise. In order to evaluate and assess the crosstalk between nearby antennas, two identical planar patch antennas were designed in the CST CAD environment. For simplicity, it was assumed that the antennas were fed a signal from the backside by an ideal port.

S-parameters were used to quantify the power entering one antenna from another and was a function of the particular geometry of the antennas and their separation. The power that leaves from port 1 and enters port 2 will be referred to as the coupling parameter or as the S_{21} parameter. The S_{11} parameter represents the power reflected back into the feed port (i.e. power lost at the input to the individual antenna). Two types of antenna arrays were considered, one group consisting of isolated antennas on separate boards and the other consisting of patches all printed along the same single dielectric base.

The two identical antennas were placed some distance apart and the S_{21} parameter at 100 GHz was simulated for different separations. The antenna created had the same geometries as one detailed previously in **Figure 3-14**. Each antenna was assumed to be connected to an ideal coaxial connection.

Parameter	Value (mm)	Description
x-shift	0.2	*x*-axis displacement of the wire from centre position
y-shift	0	*y*-axis displacement of the wire from centre position
Dielectric height	0.1	*z*-axis length of dielectric
Antenna length	3	*x*-axis length of dielectric and ground plate
Antenna width	12	*y*-axis width of dielectric and ground plate
Ground thickness	0.8	*z*-axis length of ground plate
Wire coating	0.3	Radius of the coating of coax feed
Wire core	0.1	Radius of the wire core of coax feed
Patch width	0.72	*x*-axis length of patch
Patch length	0.9	*y*-axis length of patch
Patch height	0.01	*z*-axis length of patch

Table 3-6: Parameters used measuring crosstalk between neighbouring patch antennas.

These simulations compared crosstalk without the influence of the dielectric material. When the antennas were placed in a lenslet array, the lens will need to be at least a few wavelengths wide. The patches will also need to be separated by this distance to be centred with the lens in front of them. The distance between the two antennas was varied in steps of 1 mm in the *x*-axis direction. (For the analysis along the *y*-axis see **Figure 3-21**). Antennas could also be created on the same substrate and that scenario will be detailed in **Figure 3-18**.

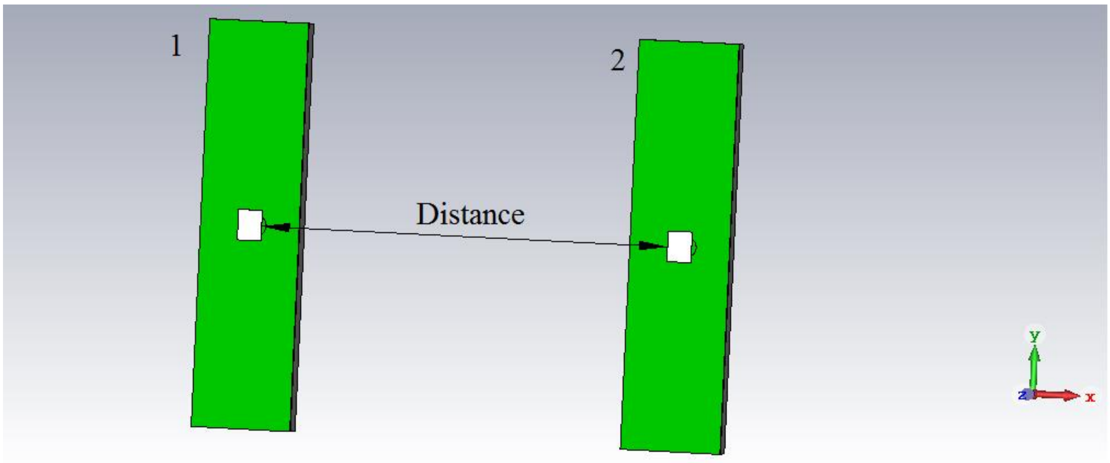

Figure 3-17a: Two identical rectangular patch antennas as viewed in CST. The patch-to-patch distance was varied along the *x*-axis. The antenna on the left was referred to as antenna 1 as it was connected to waveguide port 1 and the antenna on the right will be referred to as antenna 2 as it was connected to waveguide port 2.

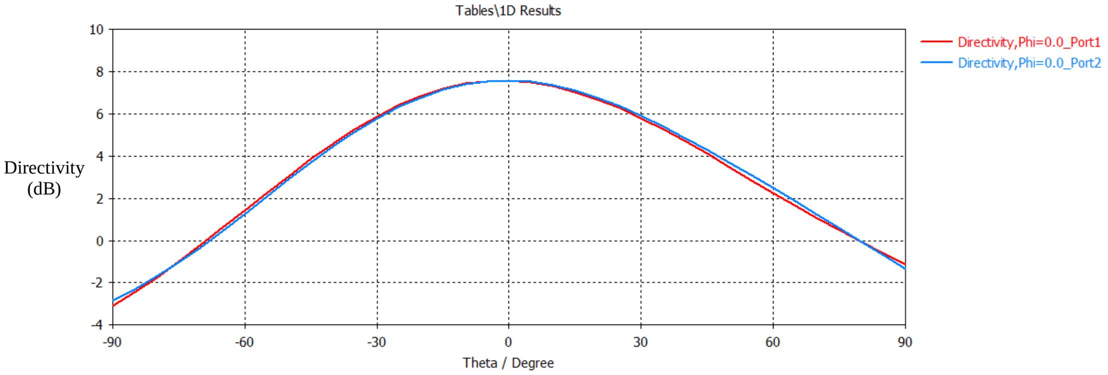

Figure 3-17b: Farfield plot of the two antennas at a frequency of 100 GHz when the devices were separated by 10 mm.

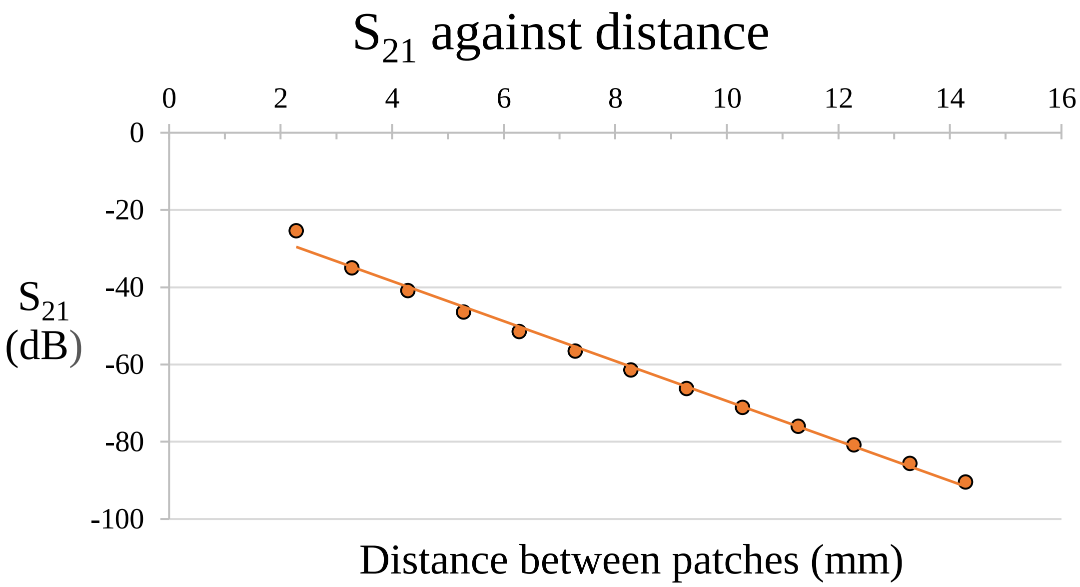

Figure 3-17c: A graph of S_{21} parameter at 100 GHz against spacing between the boards.

Figure 3-17b showed the farfield pattern of two antenna placed 10 mm apart (shown as “Port 1” and “Port 2”). Both antenna generate a similar farfield pattern as expected. The graph (**Figure 3-17c**) showed that there was a linear relationship between spacing and S_{21} in this direction. As the distance between patches increases, the crosstalk also decreases.

At the 10 mm point, under -80 dB of power was transmitted between the two antennas. This separation distance will be used as the distance for the following tests. The reason for this was that lenslets were eventually placed in front of these antennas, which will be large relative to the antennas. The lens experiments are detailed in **Section 6.3**, however, the crosstalk effects without lenslets were examined first.

In the previous simulations, the antennas were on separate dielectrics. If the patch antennas were printed onto a single circuit board this design would be easier to manufacture; however, the larger board will affect the response of the antenna at W band frequencies due to the substrate influence on the radiation characteristics. This design will be referred to as a patch array and was analysed in the following simulations (see **Figure 3-18** for diagram).

This design of the array (**Figure 3-21**) may be difficult to construct due to the small size of the board in one direction. A patch array with two patches was simulated in CST, where the patches were placed some distance apart on the *x*-axis on the same board.

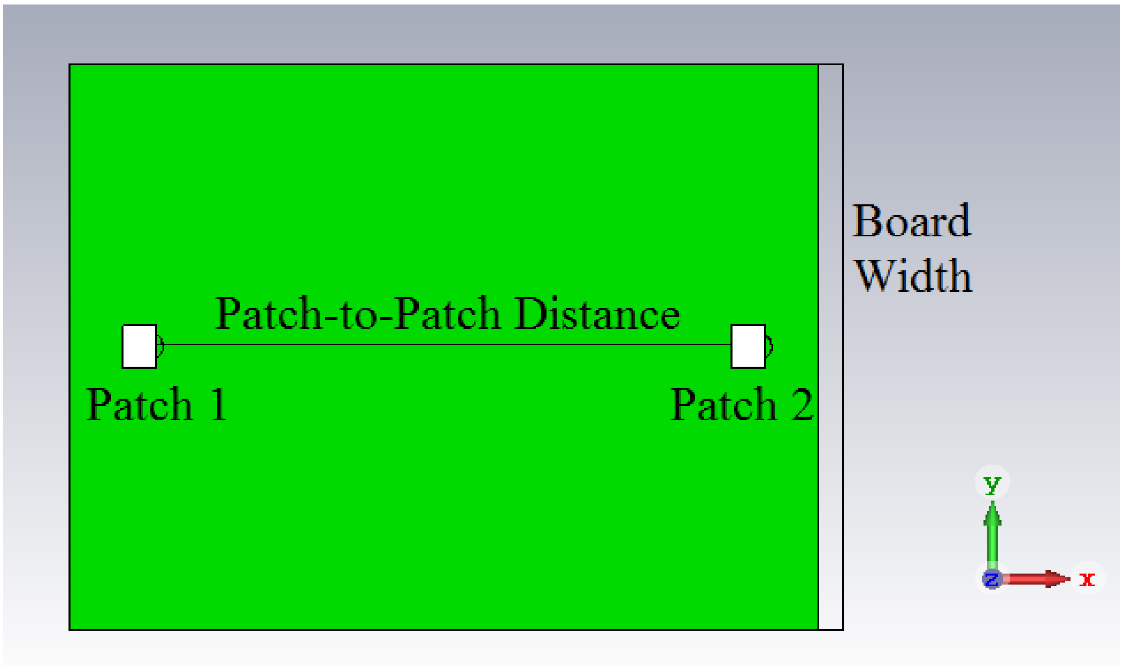

Figure 3-18: Antenna array with two rectangular patches. The same patch geometry was used in these tests as used in **Figure 3-14**.

The distance between the two patches was altered from 2 mm → 18 mm in steps of 1 mm. The following simulation monitors the effect of increasing the distance between the two patches along the *x*-axis as illustrated in **Figure 3-19a.**

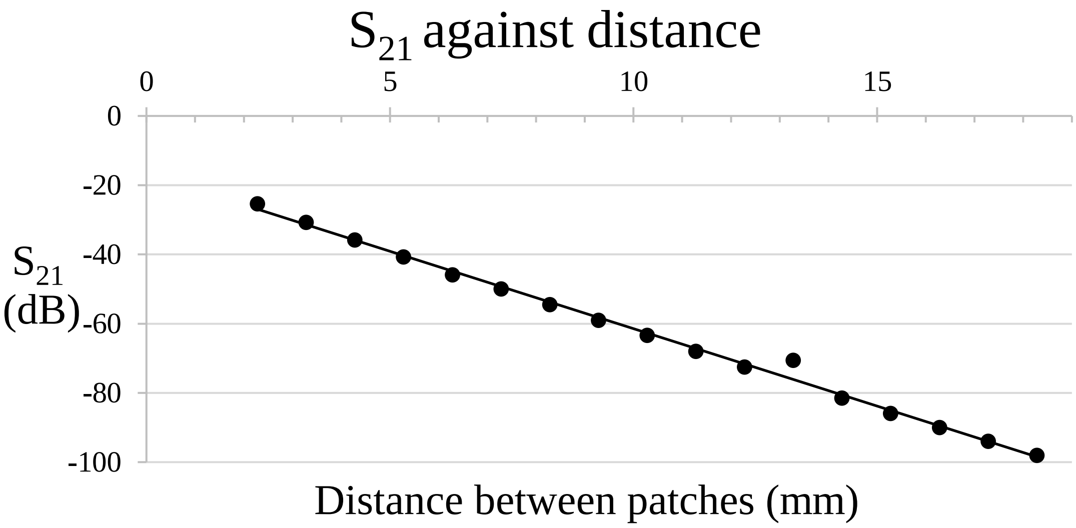

Figure 3-19a: Plot of power transferred between the two antennas against distance of separation.

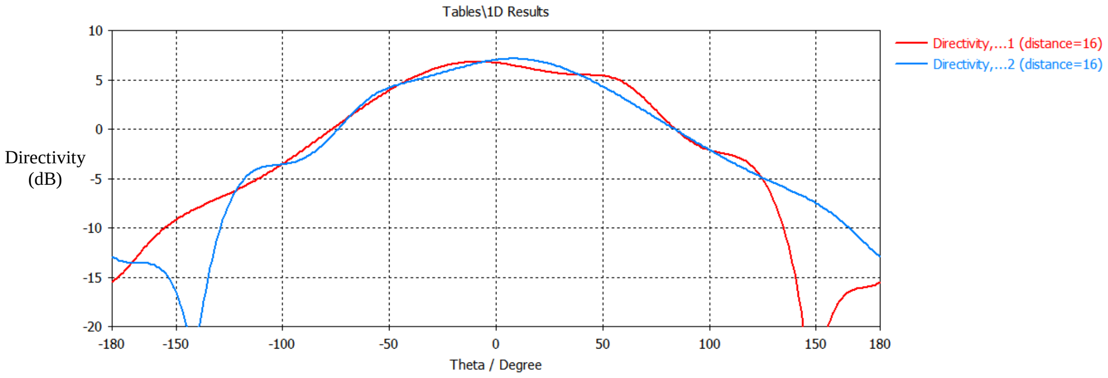

Figure 3-19b: Farfield pattern of the array, when the patch-to-patch distance was set to 10 mm.

This farfield pattern (**Figure 3-19b**) of the two patches don't match, but both do have a beam pattern that reached a maximum near the centre, but each was affected in the same manner symmetrically. The power transferred between the two antennas decreases with distance, which agrees with trend illustrated in **Figure 3-20**. The distance between the two patches in the array was increased from 2 mm → 16 mm in steps of 1 mm. As expected, the power transferred between the two antennas decreased linearly with distance between them. The antennas in an array transfers a larger amount of energy between them, when compared to a number of antennas not manufactured on a single dielectric. The PCB must also influence the transferring of energy between the two patches.

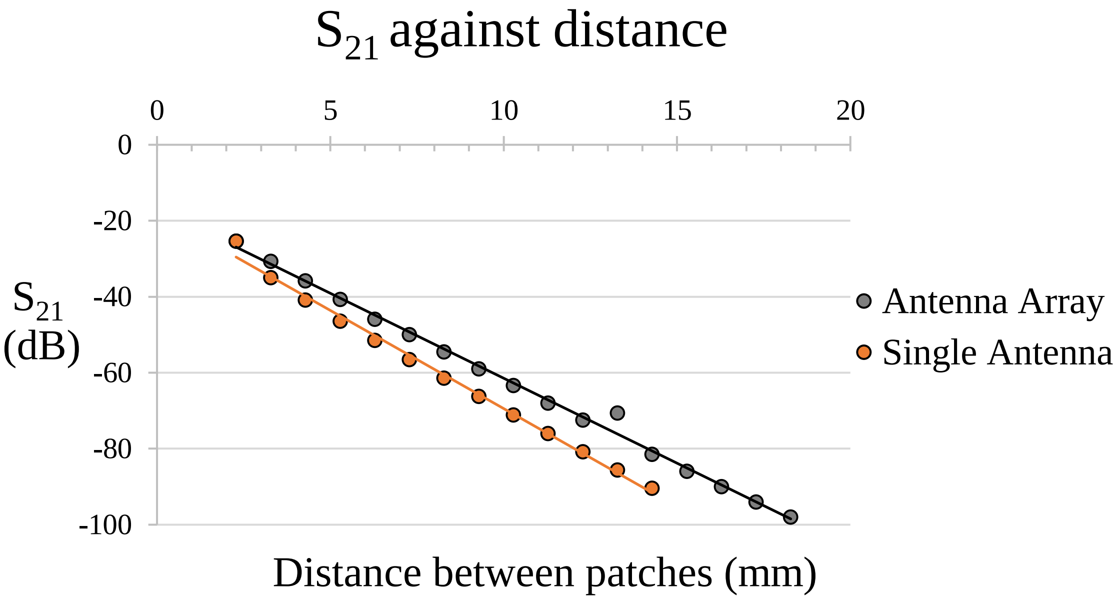

Figure 3-20: Comparison of crosstalk (S_{21}) in an antenna array and for a group of single antennas manufactured on separate boards.

There was a linear trend seen in **Figure 3-20** between crosstalk and distance. There was more crosstalk in the array design compared to the isolated antenna design as expected as more power could be transferred via the substrate. The array structure was easier to construct and there was only a relatively small increase in crosstalk between the antennas of roughly 4 dB. This increase in crosstalk could be ignored at the total crosstalk was at most -20 dB, which means that at most 1% of power was transferred between the two antennas.

Two of the antennas, with the parameters detailed in **Table 3-6**, were placed along the *y*-axis. The crosstalk and directivity of the antenna was measured as the distance between the two patches increased. Based on the results from **Figure 3-4b**, the patches should have only a small influence on each other as they were separated along the *y*-axis. The crosstalk along this direction was affected by the physical connection between the two patch antenna substrates. Farfield plots of the antennas were also taken at various separations.

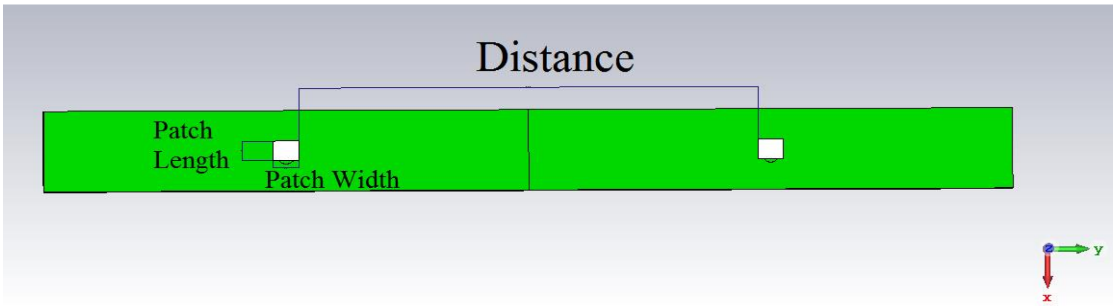

Figure 3-21a: Varying the patch-to-patch distance along the *y*-axis.

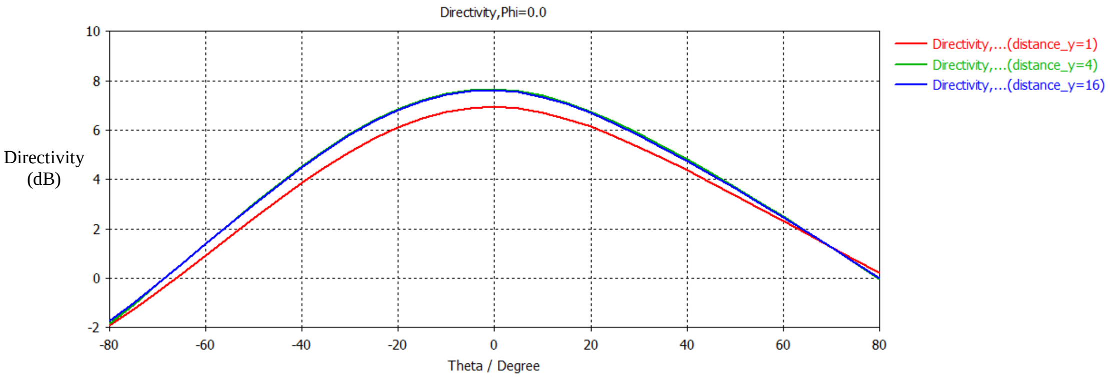

Figure 3-21b: Farfield plot of antenna, when patches were 1 mm, 4 mm and 16 mm apart.

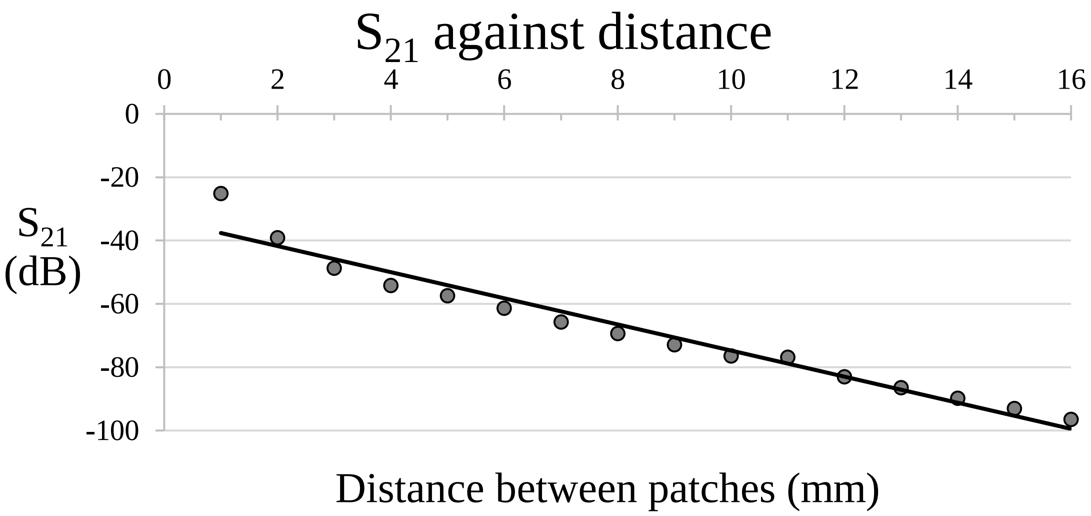

Figure 3-21c: Plot of crosstalk between antenna with distance.

The shape of the farfield pattern only changes when the patches were less than one wavelength (~3 mm) apart. When the patches were 1 mm apart, the maximum directivity of the first patch was 6.9 dBi. The maximum directivity when the patches were 4 mm apart (**Figure 3-21b**) was 7.6 dBi, which was the same when the patches were 16 mm apart. The crosstalk between the antennas when they were placed at these distances was very low (**Figure 3-21c**).

The S_{21} from the previous two simulations were plotted together in the following figure (**Figure 3-22**). The distance parameter used was the patch–to-patch distance.

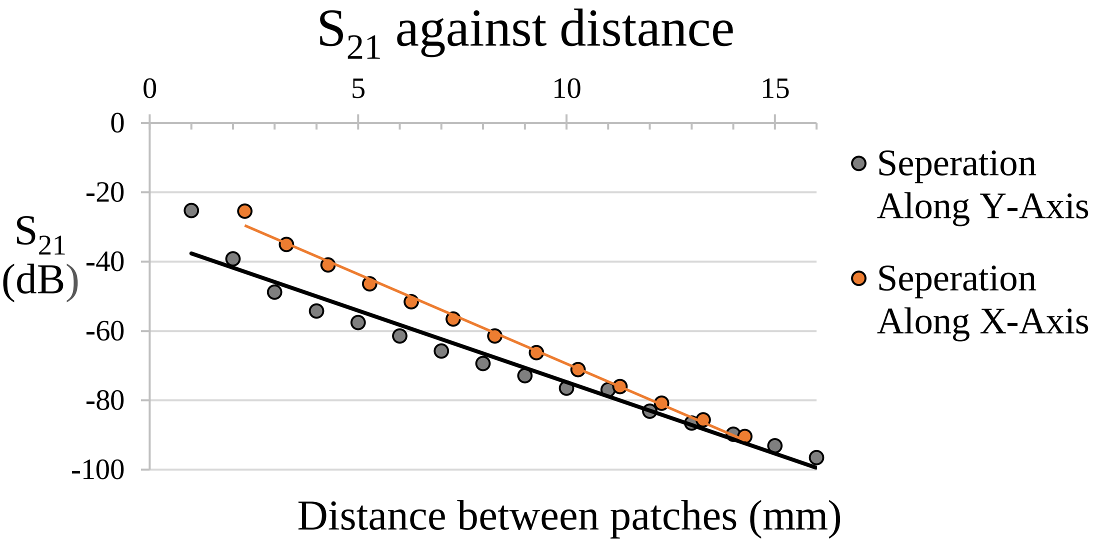

Figure 3-22: Comparison of crosstalk between the antenna along the *x*-axis and the *y*-axis versus patch-to-patch distance.

There was more crosstalk between the antennas placed along the *x*-axis compared to the antennas along the *y*-axis, which was due to the wire offset in the *x*-axis. In the previous examples, the antennas have little crosstalk between them. This might not be true if there were more than two antennas placed close to each other.

To examine the effects of multiple antennas, three identical antennas were placed 10 mm apart. The antennas were labelled 1→ 3 from left to right. The parameters of these antennas were shown previously in **Table 3-5**. This creates a 3-port sytem and so the 9 different S-parameters were recorded.

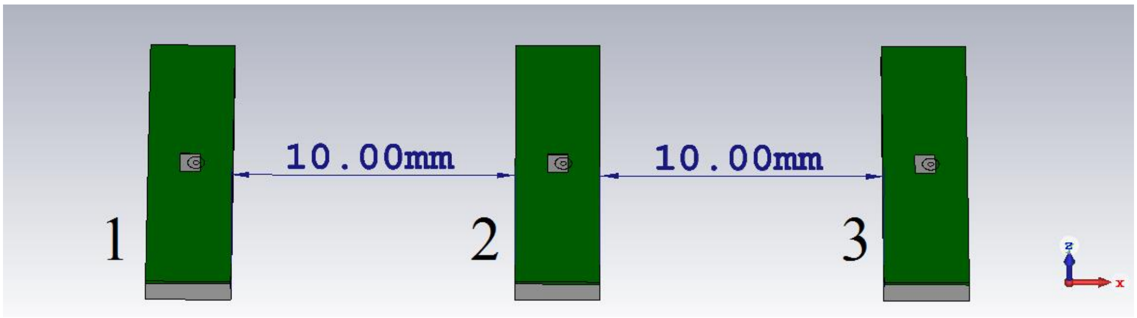

Figure 3-23a: Three identical antenna each placed 10 mm apart along the *x*-axis.

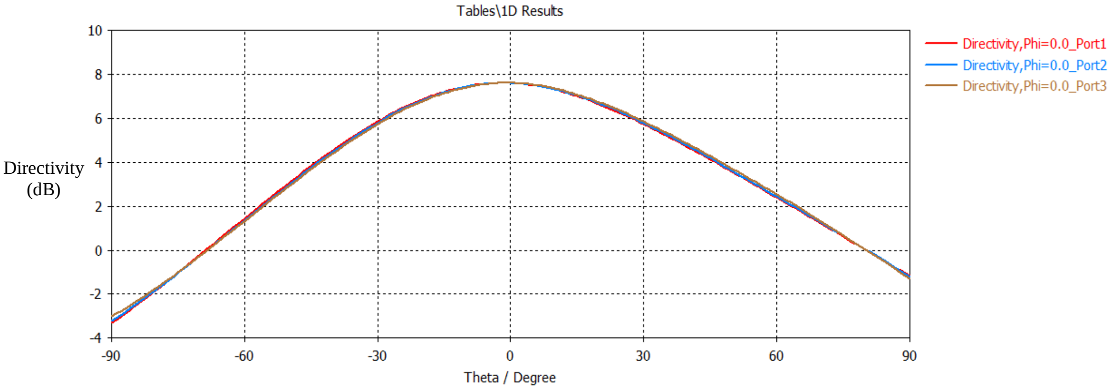

Figure 3-23b: The directivity of the 3 antennas, where each antenna was labelled according to the port it received power from.

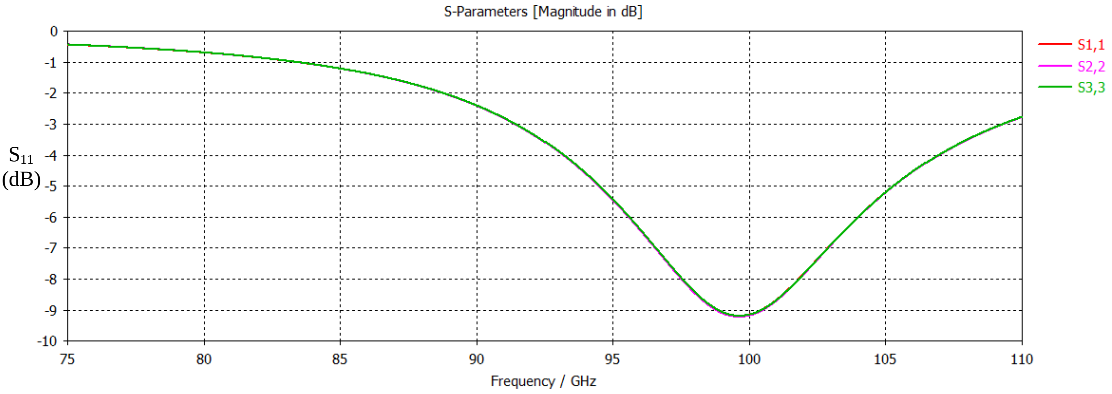

Figure 3-23c: Plot of S-parameters over the W band when the three patch antennas were placed 10 mm apart.

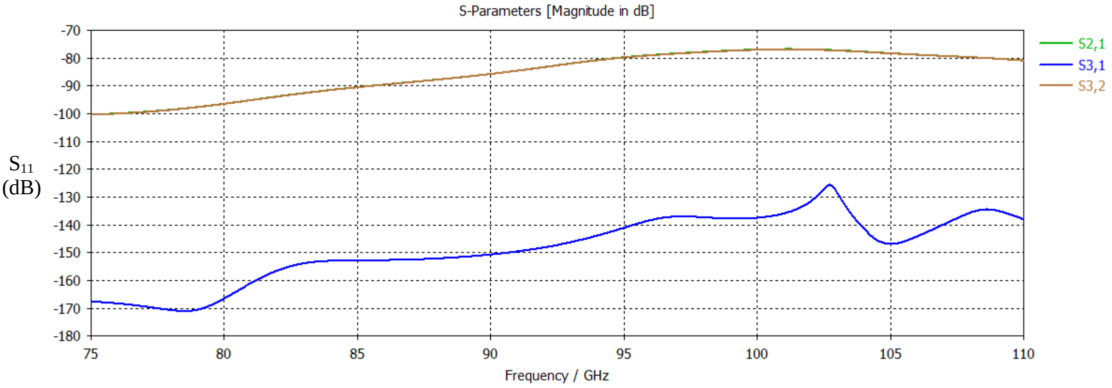

Figure 3-23d: Plot of the crosstalk (S_{21}, S_{31} and S_{32}) over W band frequencies.

The farfield pattern of these three antennas were very similar (**Figure 3-23b**), which implied that there was minimal influence on each antennas farfield pattern due to the other antennas. The S_{11}, S_{22} and S_{33} shown in **Figure 3-23c** each followed the same curve. The difference between these curves varies by less than 0.1 dB. This was expected as each antenna was identical.

The values recorded for S_{21}, S_{31} and S_{32} over the W band is shown in **Figure 3-23d**. Over this band, the S_{21} and S_{31} parameters were very similar. At 100 GHz, S_{21} was -77 dB, while the S_{32} was only 0.1 dB lower at -77.1 dB. This implies that there was an equal amount of transferred of energy between the first and second antenna and the second and third antenna. There was significantly less power entering antenna 3 from antenna 1 as expected and this crosstalk between these two antennas would be too low to measure with accuracy using the VNA.

There was a different level of crosstalk between the *x*-axis aligned antennas and y-axis aligned antennas. An array with four patches was created in CST in order to monitor the crosstalk along both of these axes. The patches were arranged into a 2 × 2 pattern and four patches were put together in the four corners of a square configuration. Each antenna was connected to a port (the 4-port system shown in **Figure 3-24**). The S_{21}, S_{31} and S_{41} were of particular interest in this simulation and were monitored as the distance between the patches was varied.

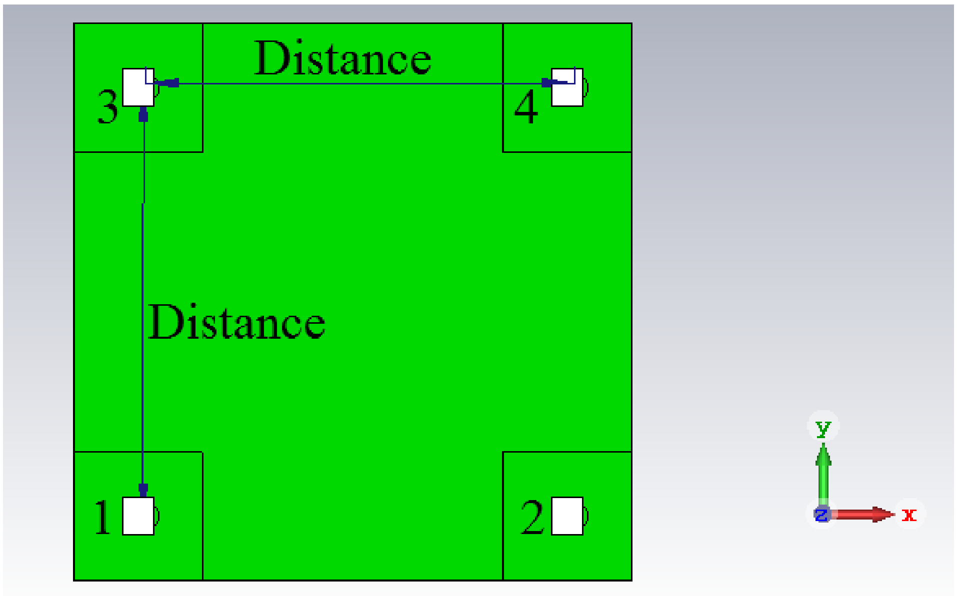

Figure 3-24a: Image of four patch antennas integrated into a 2×2 array structure. Each patch was labelled after the CST port it was connected to.

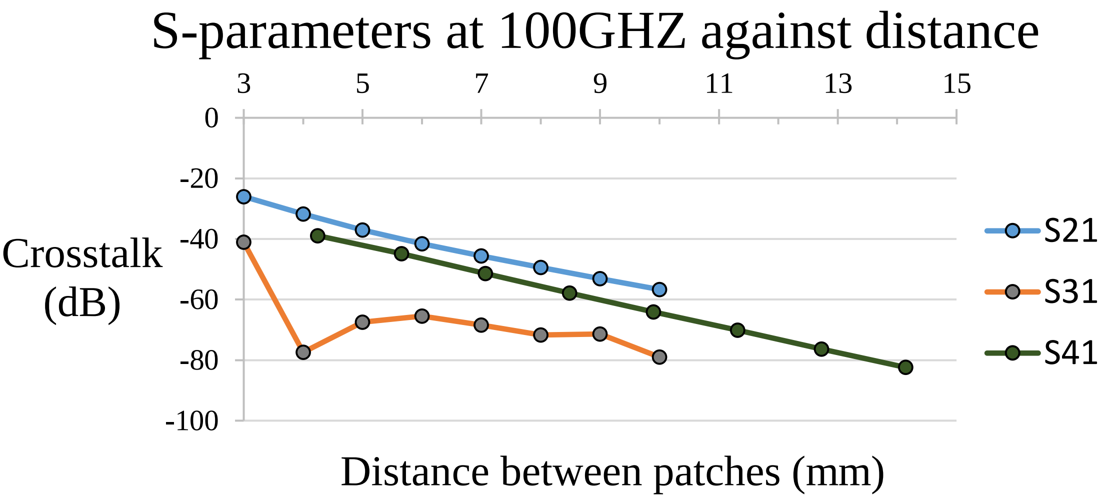

Figure 3-24b: S-parameters for each antenna in the array at 100 GHz.

Figure 3-24 showed the results from simulation test to observe the mutual coupling of four patch antenna in an array. The S-parameters were used to show how the power transfers between the patches in the array (crosstalk). The S_{21} parameter represents power leaving the first patch and entering the second port. The S_{31} parameter represents power leaving the first patch and entering the third port and the S_{41} parameter represents power leaving the first patch and entering the fourth port.

Figure 3-24b showed the effect on the S-parameters at 100 GHz with distance, i.e. The crosstalk tends to decrease with distance. The S_{21} and the S_{41} parameter decrease linearly with distance. The S_{21} was constantly larger than the S_{31}, which was unusual as patch 2 and 3 were the same distance from patch 1.

The results from the CST simulation when the patches were 10 mm apart, were examined as part of this analysis. The S_{11}, S_{22}, S_{33} and S_{44} parameters of the antenna over the W band and the farfield patterns and this distance are shown in **Figure 3-25.**

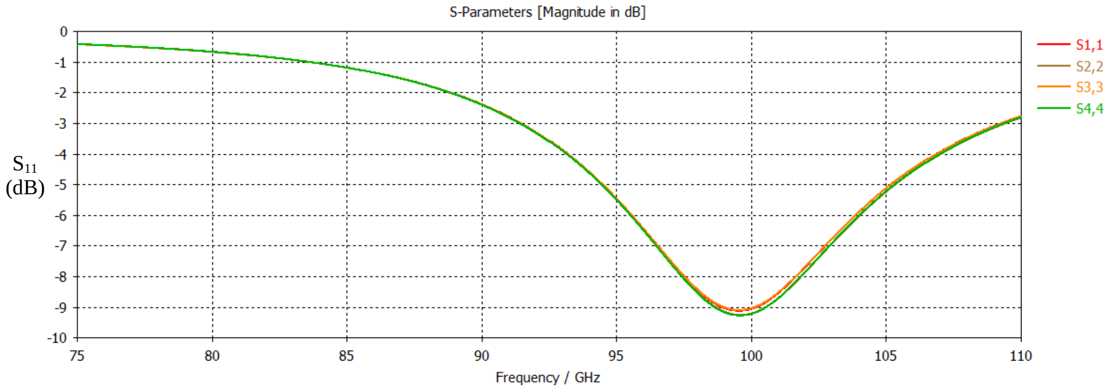

Figure 3-25a: The return loss S-parameters for each antenna in this array over W band frequencies, when the patches were placed 10 mm apart.

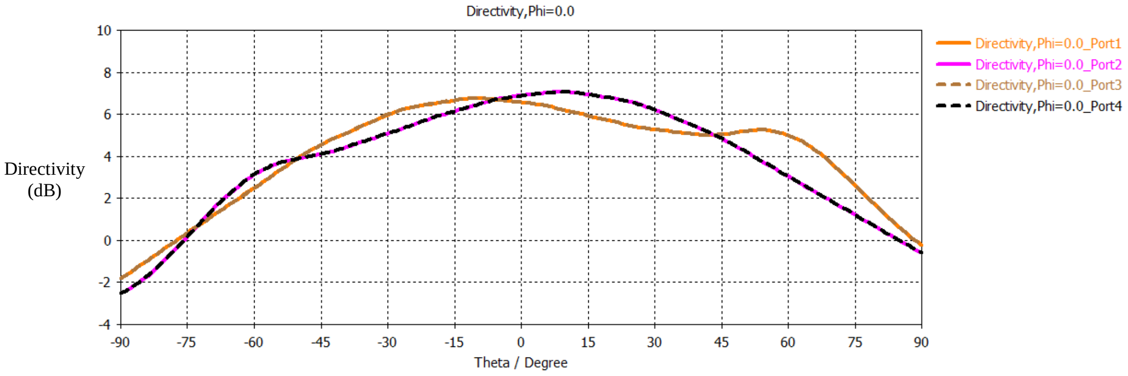

Figure 3-25b: The farfield pattern generated by each antenna in the array, along the $\varphi = 0°$ axis (equivalent to the *x*-axis), when the patches were placed 10 mm apart.

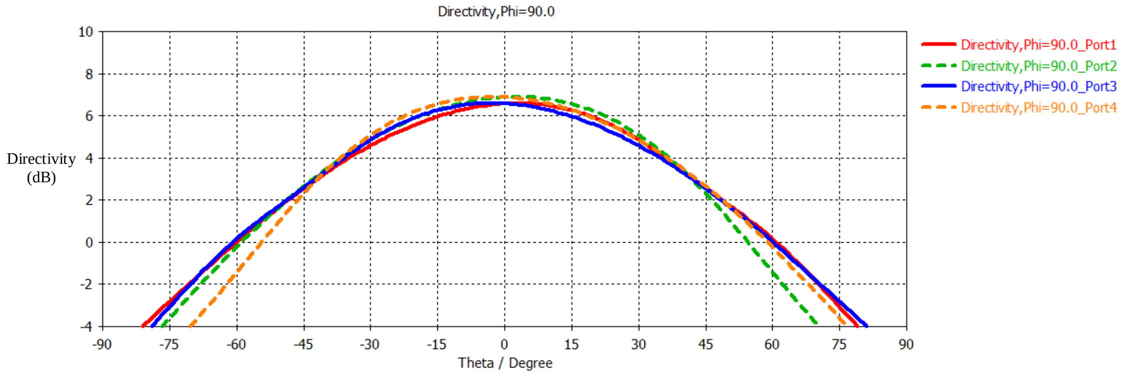

Figure 3-25c: Farfield plot along the orthogonal axis (*y*-axis).

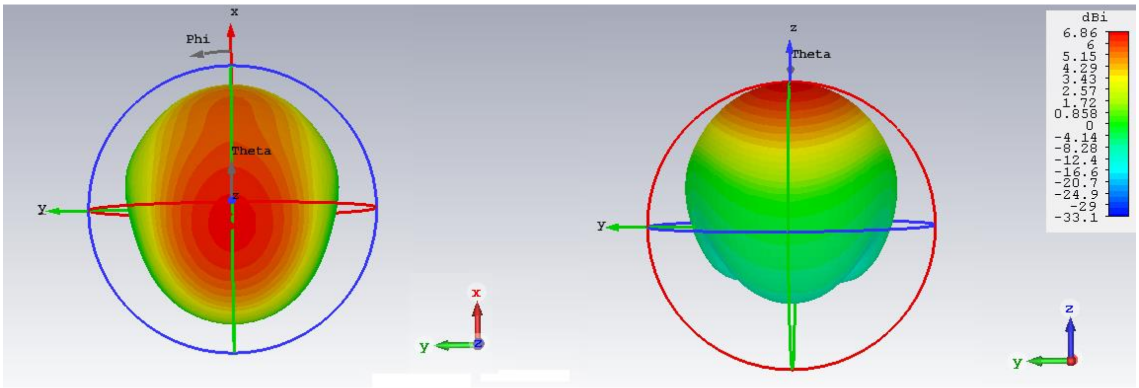

Figure 3-25d: 3-D view of the farfield pattern for patch antenna 1. The 3-D view of showed that most of the power was radiated along the desired axis of propagation (*z*-axis).

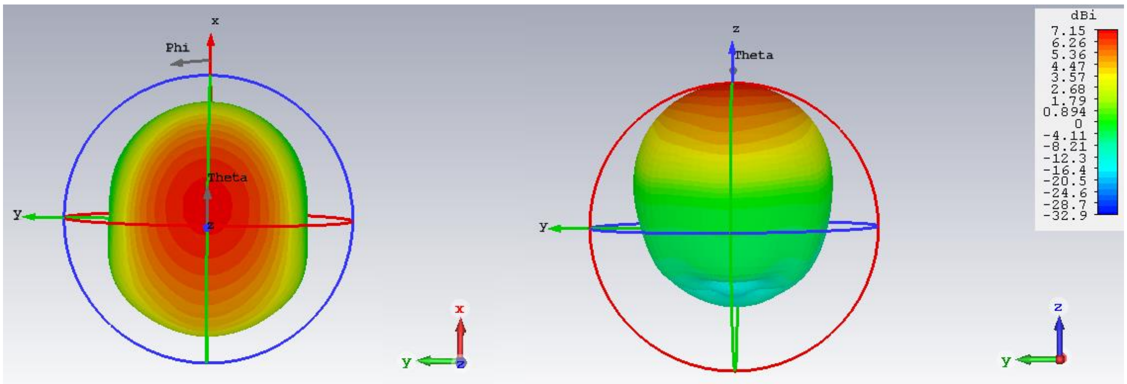

Figure 3-25e: 3-D view of farfield pattern for patch antenna 2.

The minimum S-parameter in **Figure 3-25a** for each patch were located at 100 GHz, which means that all antennas resonated at the same frequency. The return loss of each antenna was nearly identical for each antenna. This showed that having multiple patches on the same board did not affect the resonant frequency of each patch. This means that the more patches could added onto a larger board, without changing the frequencies the antenna could receive most effectively. **Figure 3-25b** shows that the farfield pattern of antenna on the left-hand side (antennas 1 and 3) were identical, as do the farfield patterns of the right-hand side antennas (2 and 4). **Figure 3-25c** shows that there was only a small difference in the beam generated by the different antennas along the *y*-axis.

The 3-D view of patch 1 (**Figure 3-25d**) and patch 2 (**Figure 3-25e**) showed that most of the power was radiated along the positive *z*-axis. However, comparing these two patches, showed that patch one radiates more power in the positive *x*-axis, while patch 2 radiates more power in the negative *x*-axis. This was noteworthy as to develop this antenna configuration, there was a shift of the wire feed along the *x*-axis, but not the *y*-axis. This seems to be affecting the symmetry of the beams in these directions. The asymmetry in the beam patterns was also the cause of the difference between the S_{21} and the S_{31} parameter from **Figure 3-25b**.

3.5 Coupling a wire feed to WR10 waveguide

When one of the back-fed patch antenna were manufactured, it needed to be feed with a W band signal and so was connected to the VNA (the power source) via a wire suspended in a modified WR10 waveguide. A waveguide section was adapted with a hole drilled into the waveguide to allow the feed wire couple radiation to the patch. CST was used to simulate and to calculate the efficiency (i.e. low S_{11} parameter) of the system and to ensure the technique could feed adequate power to the antenna (i.e. large S_{21} parameter).

A WR10 rectangular waveguide is a standard waveguide, which had an internal dimension of 2.54 mm × 1.27 mm. Additionally, there were two possible design choices for the rectangular waveguide to feed signal to the embedded wire, a closed waveguide, which terminates in a short (**Figure 3-26**) or an open waveguide (**Figure 3-30**), which opens to free-space.

A modified closed WR10 waveguide was considered first. The structure was simulated in CST's CAD environment (see **Table 3-7** for device dimensions). A wire, with an inner radius of 0.125 mm and a dielectric coating radius of 0.3 mm was fed through a hole into the waveguide wall.

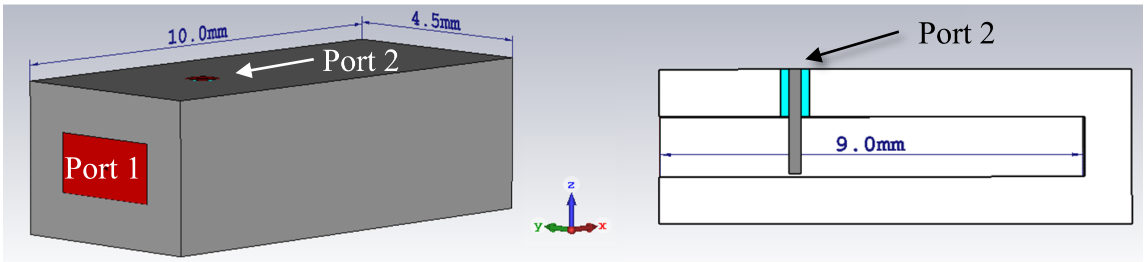

Figure 3-26: Diagram of closed WR10 waveguide as viewed from outside (left) and viewed inside (right). A port (in red), used to monitor power flow, is placed at the opening of the waveguide and at the position where the wire leaves the waveguide. Port 1 was set at the open end of the waveguide and port 2 was set at the exit point for the wire.

Internal dimensions		External dimensions	
x-axis length	2.54 mm	*x*-axis length	4.54 mm
y-axis width	1.27 mm	*y*-axis width	3.27 mm
z-axis depth	9 mm	*z*-axis length	10 mm

Table 3-7: WR10 waveguide internal and external dimensions.

The wire was placed at different positions relative to the end-wall of the waveguide. This was to determine the effects (if any) of positioning on the coupling between the wire of the antenna and the waveguide. The *x*-axis length of the waveguide was set initially to 10 mm and the wire was set to a depth of 1.2 mm inside the waveguide.

The main purpose of these tests was to determine the return loss from the waveguide and the amount of power that coupled to the wire in the waveguide. The S_{11} parameter in this case records the amount of power sent from the open end of the waveguide back through the open end of the waveguide (right to left). The S_{21} represents the power sent from the waveguide that coupled to the wire.

The wire was initially set to the closed end of the waveguide as it was moved 6 mm back from this end along the waveguide. The S_{11} parameters at the operating frequency of 100 GHz were calculated at 0.3 mm step intervals.

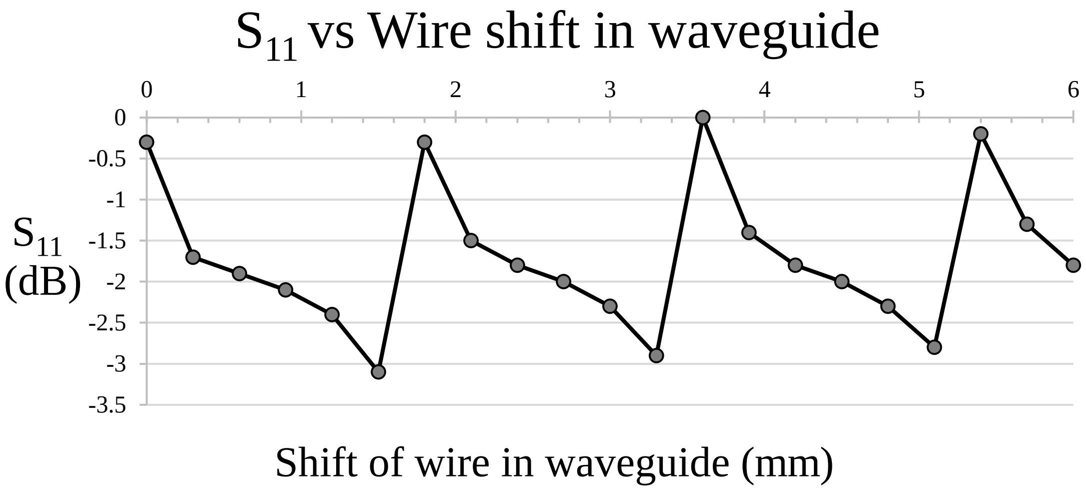

Figure 3-27: Return loss S_{11} on the waveguide as the wire is moved along the *x*-axis of the modified WR10 waveguide.

Figure 3-27 shows that the S_{11} parameter of the waveguide was low at some specific points along the *x*-axis and rises to zero at other positions. There was a large amount of reflection from the device back into the source port. The local maximum of the efficiency occurs every 1.8 mm along the *x*-axis. The behaviour of the S_{11} parameter seems to suggest some constructive and destructive interference within the waveguide.

The regions where the S_{11} parameter was at a minimum were very narrow and a change of 0.3 mm of the wire feed could increase the S_{11} parameter to 0 dB. This level of accuracy would be difficult to achieve in a practical setting. The minimum S_{11} achieved were also relatively high, only reaching 3.1 dB, which indicates that only about ~50% of the power leaves the waveguide though the antenna.

The length of wire in the waveguide should have some effect on the power transferred though the waveguide. The length of the waveguide cavity was set to 10 mm. The wire was placed at a point where the S_{11} parameter was minimized (according to the results from **Figure 3-27**). The depth of the wire was increased in steps of 0.05 mm from 0 to 1.2 mm. The range of values chosen was determined by the dimensions of the WR10 waveguide, which along this direction, had a length of 1.27 mm.

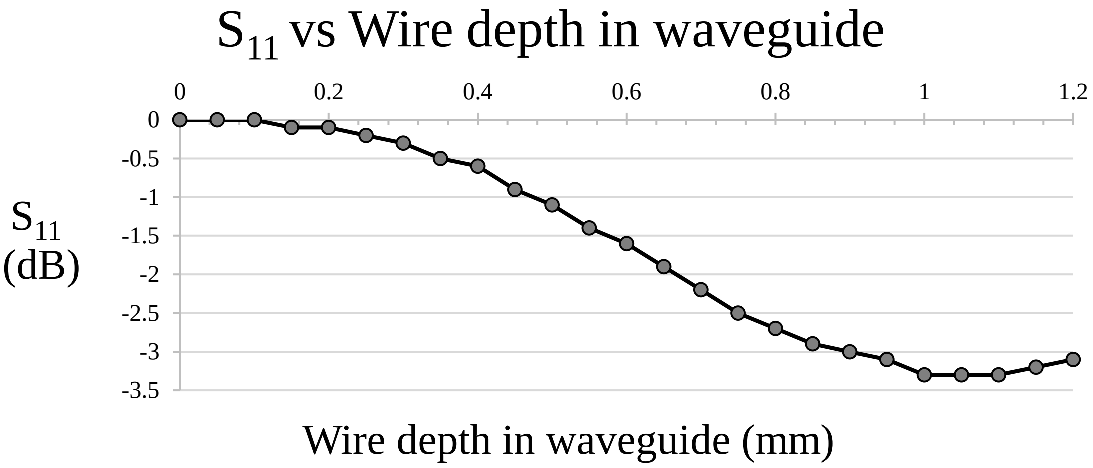

Figure 3-28: S_{11} at 100 GHz vs depth of wire in waveguide.

The minimum S_{11} parameter in **Figure 3-28** occurs at 1 mm, which was large enough to practically manufacture. The wire will need to be this long to receive the maximum amount of power in this closed waveguide. The minimum S_{11} parameter was -3.3 dB and this was still too high to be used in a realistic setting.

The effect of the cavity length on the coupling efficiency was analysed. The wire was placed at 1.5 mm from the closed end of the waveguide. The position of the wire was kept constant during the testing. The length of the waveguide was increased from 7 mm to 10 mm in steps of 0.3 mm.

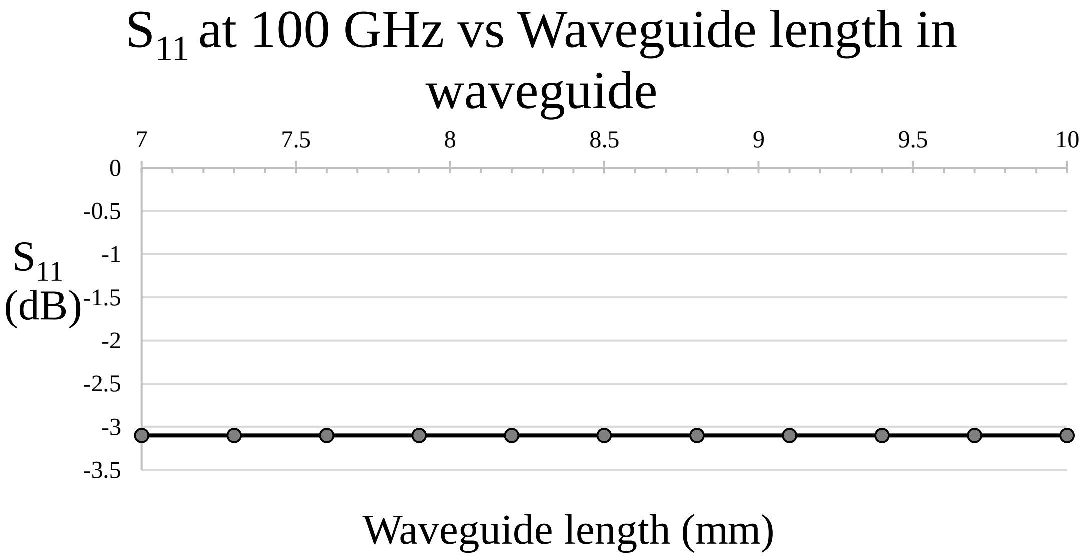

Figure 3-29: Plot of S_{11} vs waveguide length.

Figure 3-29 shows that the length of the waveguide did not appear to affect the coupling between the wire and the waveguide and the reflections in the waveguide remain high.

The previous three figures (**Figure 3-27**, **Figure 3-28** and **Figure 3-29**) show the coupling between the closed waveguide and the wire in various configurations. In each case, the S_{11} parameter (the reflection coefficient) between remains above -3.5 dB. The closed waveguide was not best suited to use to feed the antenna due to the high reflections in the waveguide and the presence of interference along the waveguide axis.

An open WR10 waveguide length was also simulated and ultimately manufactured. To manufacture accurately the waveguide had an adapter with a precisely drilled feed hole for the wire. The hole in the adapter had a 0.3 mm radius and manufactured in the mechanical workshop in the Space Research Organisation of the Netherlands (SRON), Groningen who could deliver precise machining. This device was simulated in CST as shown in **Figure 3-30**:

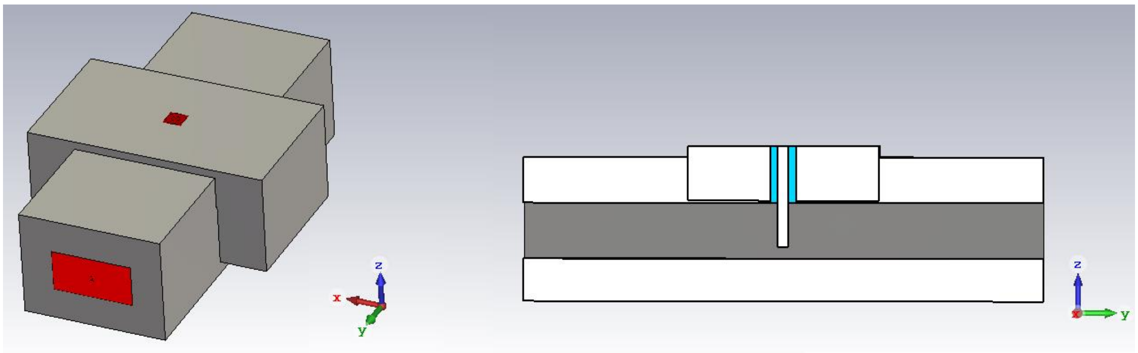

Figure 3-30: WR10 waveguide with attached holder. A port was placed at one end of the waveguide and a second was placed above the hole where the wire leaves the waveguide.

The wire was excited with a waveguide port in CST work environment. The ability of the wire and the waveguide to couple radiation was examined. The wire, with an inner wire radius of 0.125 mm and a dielectric coating radius of 0.3 mm was used. It was necessary to test at what depth the wire should be placed in the WR10 waveguide.

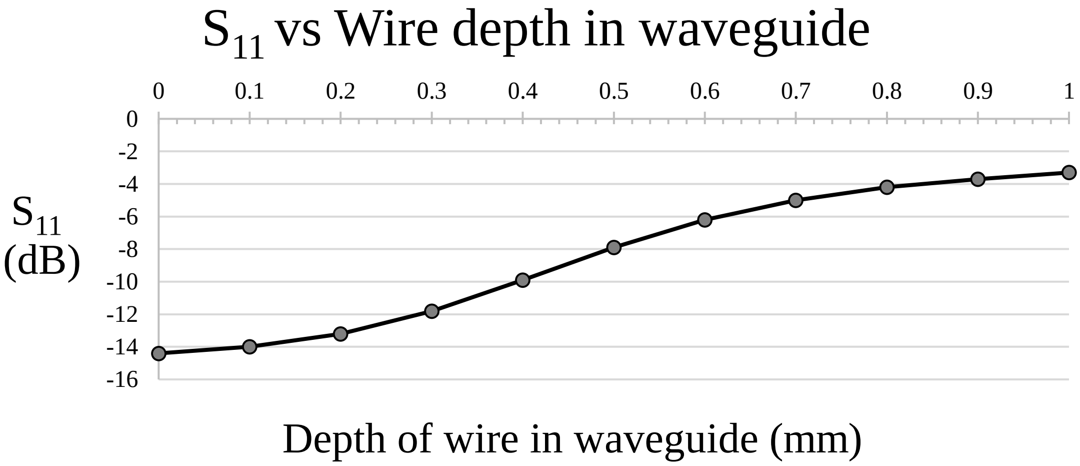

Figure 3-31a: Power reflected in waveguide with increasing wire depth.

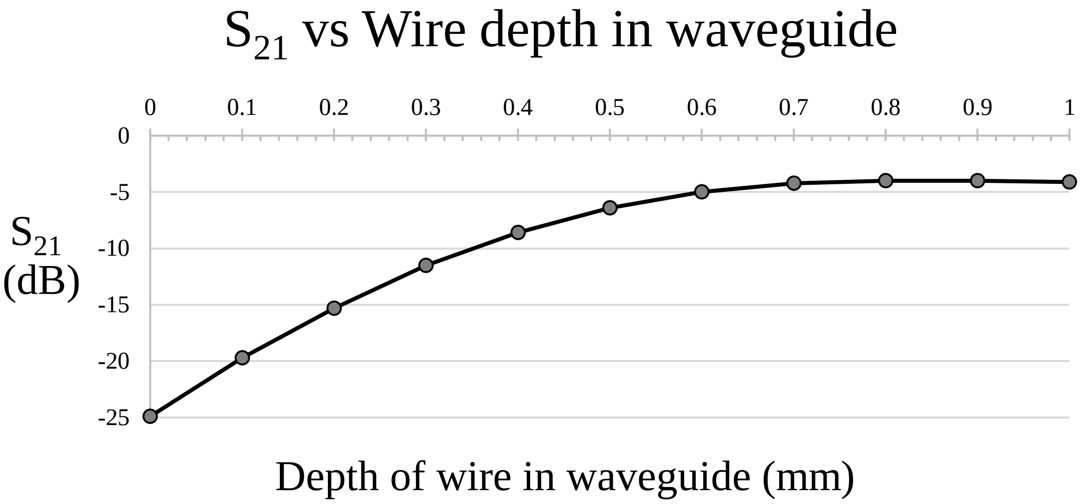

Figure 3-31b: Power sent into feed though waveguide with increasing wire depth.

Figure 3-31 showed the power reflected by the wire (**a**) and transmitted into the feed (**b**). More power was reflected back into the waveguide as the depth of wire in the waveguide was lengthened. However, the deeper the wire in the waveguide, the more power was transferred by the wire. There was a range of depths between 0.6 mm and 1 mm where the maximum power could be extracted via the wire, where reflections were also kept to a low level. Based on these two graphs, the wire should be between 0.3 mm and 0.7 mm deep in the waveguide, as at these depths more power was coupled than reflected.

As the dielectric coating on the wire was difficult to precisely remove from the metal in the lab in setting up this arrangement; it was necessary to test the effect this wire coating had in coupling power from the waveguide.

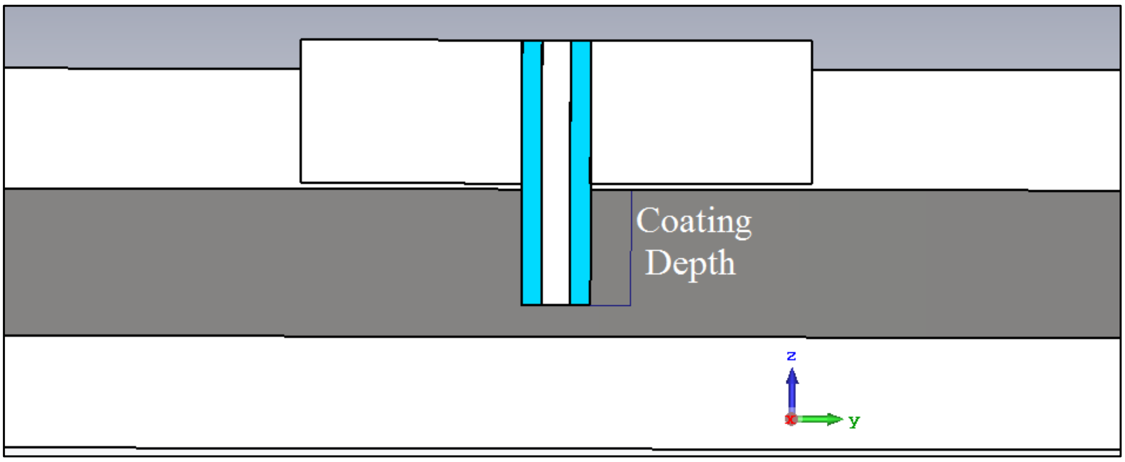

Figure 3-32a: Waveguide with dielectric coating in waveguide.

The S_{11} parameters were used to calculate how much power was coupled as the wire in the waveguide was varied from 0 mm to 1 mm, in steps of 0.2 mm. The depth of coating of the wire was varied from 0 mm up to the length of the wire, which was set to 1 mm. The power received by port 2 is shown below (**Figure 3-32c**). A value of 0 dB would indicate all the power was leaving from the waveguide.

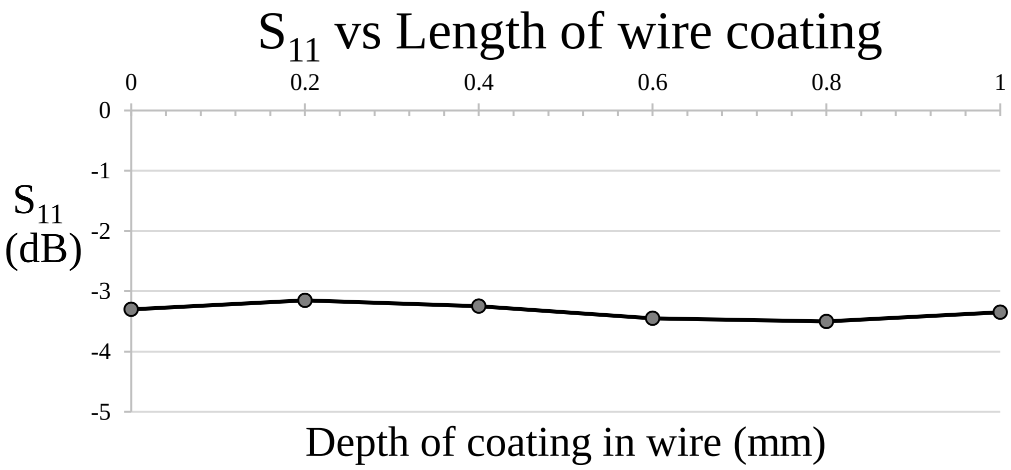

Figure 3-32b: Power reflected due to wire coating.

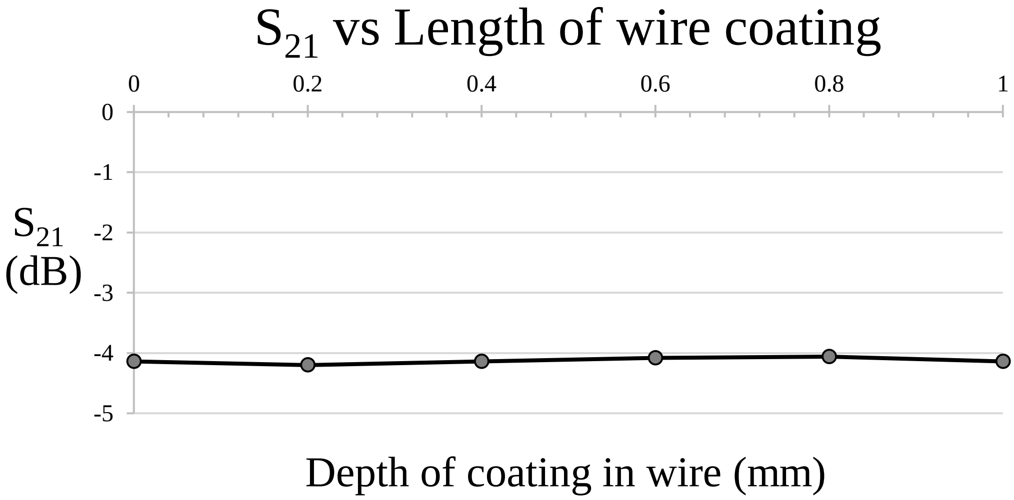

Figure 3-32c: Power transferred as depth of coating varies.

Figure 3-32 shows that the ability of the wire to extract W band power from the waveguide was not affected by the length of the wire coating. The dielectric coating was effectively transparent in this frequency range. This result makes coupling easier as the dielectric on the wire was difficult to remove accurately.

In summary, the open waveguide performs better than the closed waveguide. The reflections in the open waveguide were smaller than in the closed waveguide. Positioning the wire along the open waveguide had little influence compared to the closed waveguide, as the open waveguide had no interference effects. The open waveguide was ultimately used to feed power to the patch antenna in initial tests.

3.6 Design parameters

The circuit board geometry initially available was an ABT18 printed circuit board. This was a board with a dielectric constant of 3.3 (i.e. refractive index of 1.812). The loss tangent (0.01) and the dielectric constant were both characterised in earlier experiments using the VNA facility at a frequency of 100 GHz. The dielectric thickness defines the height of the substrate between the two copper plates and this was 0.8 mm (see **Table 3-8** for details). This value should be small relative to wavelength for the assumptions in the cavity analysis to be correct.

In order to connect the patch to an input signal, a small hole will be drilled through the PCB from the underside. The hole allows the wire to feed the patch and was then soldered to the patch. It was estimated that the position of this hole could be drilled to an accuracy of 0.1 mm along both the *x*-axis and *y*-axis relative to the patch. The wire needed to be quite small, with a radius of 0.1 mm as the patch itself was of the order of 1 mm. Additionally, the wire had a plastic coating radius of 0.3 mm.

Achieving reliable soldered connections while avoiding electrical contact to the ground plane was difficult. The shape of the patch was also altered with the solder material being deposited on the patch to achieve an electrical connection.

3.7 Manufacture of prototype patch antennas

This section will detail the development of the patch antenna described earlier, including the manufacturing process (see **Figure 3-33**), the measurement process and the results. Several prototype patch antennas were manufactured (dimensions shown in **Table 3-8**).

The patches were etched onto the PCB and to feed power into the antenna, a small wire was to be connected to the patch and connected to the modified waveguide at the other end. The radiated field was then to be detected by the other VNA head. The VNA facility effectively acted both as a source and as a detector. The results were then compared with the simulated parameters from CST.

3.7.1 Manufacturing process

The patches were etched onto the circuit board using photolithographic techniques in Maynooth's Experimental Physics Department. Several different patches of with sizes were etched onto the circuit board. Then the antennas were placed on a drill press to drill the hole to feed the wire though the substrate (see **Figure 3-34** for finished antenna). The edges of the patch were measured relative to a needle placed in the drill head to get a reference measurement. This was repeated five times in order to locate the hole position as accurately as possible. A small drill bit was used to make a 0.3 mm radius hole in the board. The debris was removed from inside the hole. A small wire with a Teflon coating was inserted into this hole. The wire was soldered to the patch using of soldering paste. Very fine sandpaper was used to remove any excess material from the patch surface.

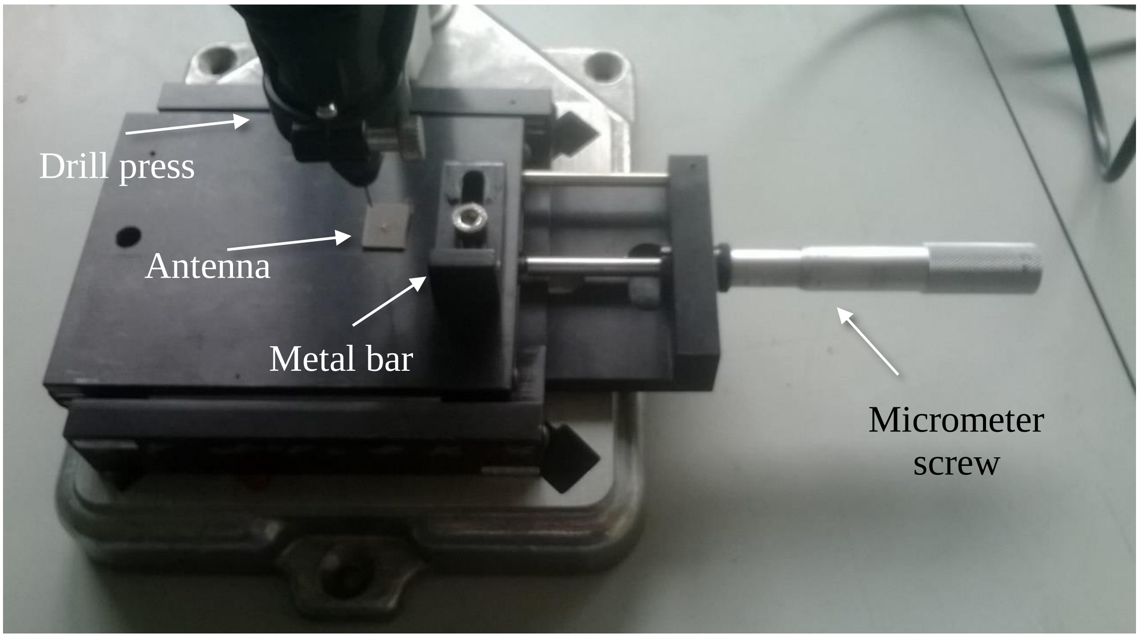

Figure 3-33: Configuration used to manufacture a hole through the patch antenna. The stand contained micrometer screw gauges, which were used to move the antenna and measure the position from the edges of the patch. The micrometer screw gauge was used to move the board accurately. The antenna also needed to be held in place using a metal bar, as a high level of accuracy was required to drill the hole in the correct spot.

A wire clipper was used to cut away excess parts of the wire. Only a small length of wire was required, between 2.4 mm → 3.3 mm length. If the wire was any longer, the wire won't fit into the modified waveguide and if the wire was any shorter, the patch and waveguide signal won't be well coupled.

Each patch was created on the same board using the same feed wire type. The electrical connections were tested using a multimeter. Of the seven patches etched on the circuit board, only 2 of the devices were electrically isolated successfully. The soldering and sandpapering process also inherently altered the shape of the functioning patches.

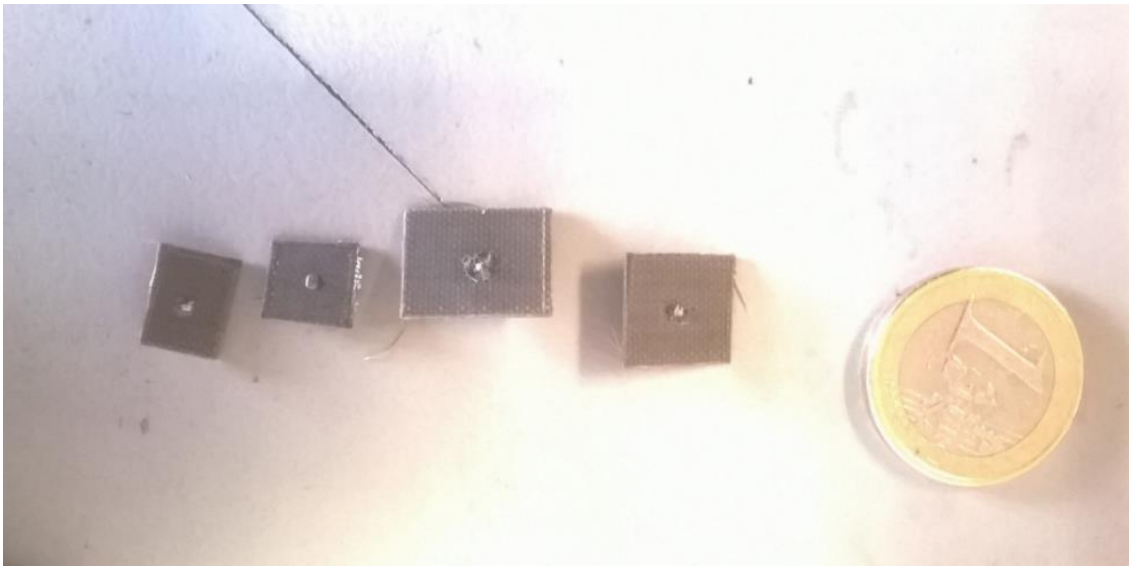

Figure 3-34: Manufactured patch antennas. The patches on each antenna have been altered during the manufacturing process. There remains a relatively large amount of soldering material on the patches, which can't be removed without severing the electrical connection. Additionally, each board had different sizes due to difficulty in cutting the size of the boards.

Patch parameters	Patch antenna 3	Patch antenna 4
Patch width	1.2 mm	1.2 mm
Patch length	0.9 mm	1 mm
Board width	11.4 mm	8 mm
Board length	12.6 mm	10.6 mm
Wire radius	0.125 mm	0.125 mm
Wire coating radius	0.3 mm	0.3 mm
Wire Offset	0 mm	0 mm
Relative electrical permittivity of board	3.3	3.3
Dielectric thickness of board	0.8 mm	0.8 mm

Table 3-8: Parameters of constructed rectangular patch antennas.

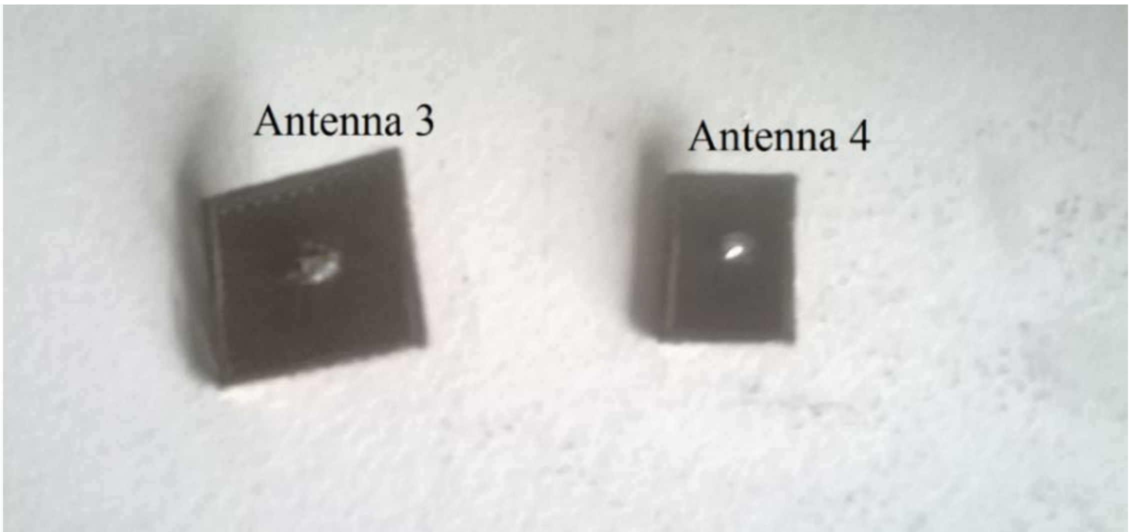

Figure 3-35: Photo of operational antennas.

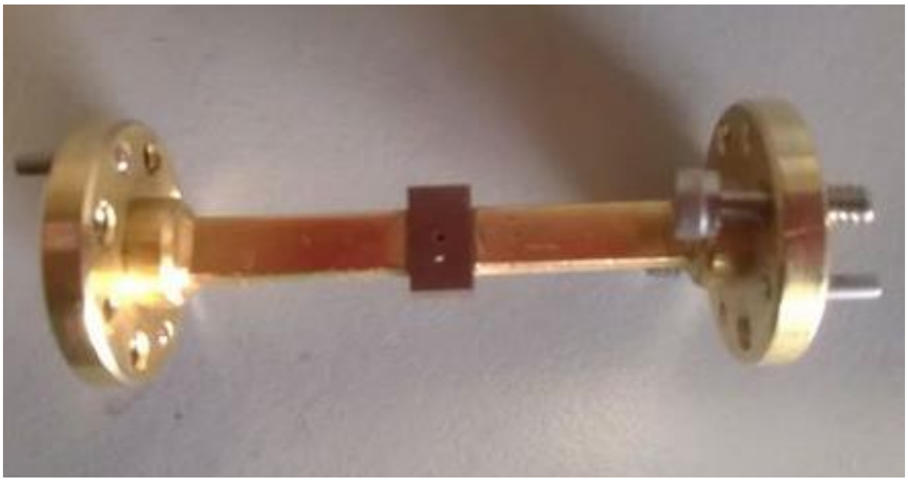

Figure 3-36: Modified WR10 waveguide used to feed a signal to the patch antenna.

The modified WR10 waveguide (**Figure 3-36**) was used to feed a signal to the patch antenna. This device was simulated in CST previously in **Figure 3-30**.

3.7.2 Testing process

The farfield patterns of the patch antennas were measured with the Vector Network Analyser, using a probe waveguide antenna as detector antenna for the signal received from the patch. The VNA was calibrated using the UOSM method (Unknown, Offset, Short Match) detailed in **Section 2.8**. The S_{11}, S_{12}, and S_{21} parameters were of interest and were recorded. A diagram of the experimental arrangement is shown in **Figure 3-37**.

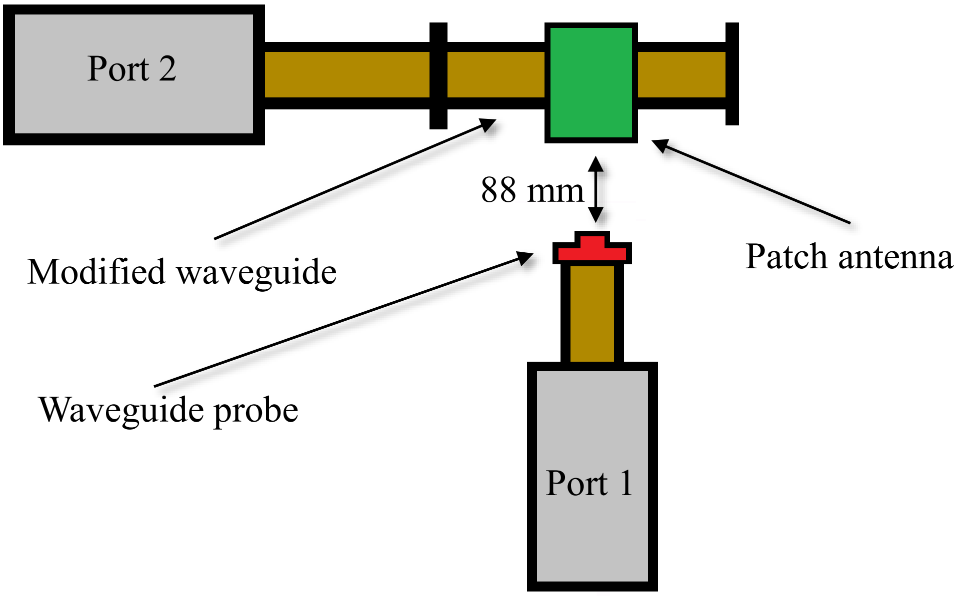

Figure 3-37a: Experimental set up to measure farfield pattern of patch antenna. Probe and antenna were seperated by 88 mm.

Port 1 was on a stand that was connected to an *x-y* scanning stages, which could move vertically and horizontally. The stage was computer controlled and an automatic scan of the antenna could be performed using a computer program. A waveguide probe was placed on port 1. The modified

WR10 waveguide was connected to port 2. The patch antennas were placed one at a time on the WR10 waveguide. The antennas were rotated to the region were the maximum signal was detected and the S-parameters of the antenna were recorded when the device was in this position. A larger S_{21} signal was detected along the horizontal direction of the device. In other words, the antennas on the 0.8 mm board mostly radiate sideways.

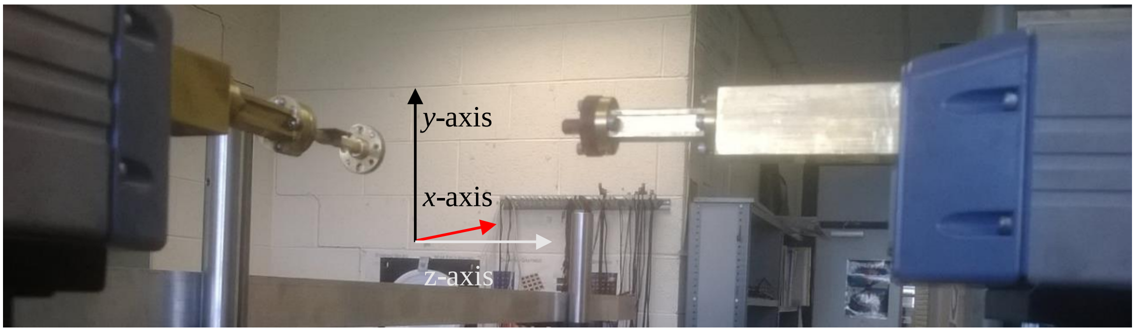

Figure 3-37b: Set up of equipment to measure patch antenna (side view). The receiving port (right) was on the scanner which could move along the horizontal and the vertical axes.

For these measurements, the *x*-axis was the horizontal axis and *y*-axis was the vertical axis. It was only possible to alter the position along the *z*-axis by moving the detecting VNA head. The antenna's field were scanned by the probe, as listed in the following figure:

	Horizontal axis		Vertical axis	
Antenna tested	Min (mm)	Max (mm)	Min (mm)	Max (mm)
Patch antenna 3	-80	80	-80	80
Patch antenna 4	-80	80	-80	80

Table 3-9: Region scanned with the VNA equipment. The distance between the antenna the waveguide probe was 88 mm. The displacement along the horizontal axis was given by h, and the displacement along the vertical axis was given by $-v$ as the vertical axis in the lab was flipped.

3.7.3 Results

The antennas were connected to port 2, so the S_{22} parameter was measured in order to find the reflections caused by the antenna, which are shown in **Figure 3-38**. Port 1 was the detector port and the S_{11} parameter was the reflection caused by the circular waveguide probe.

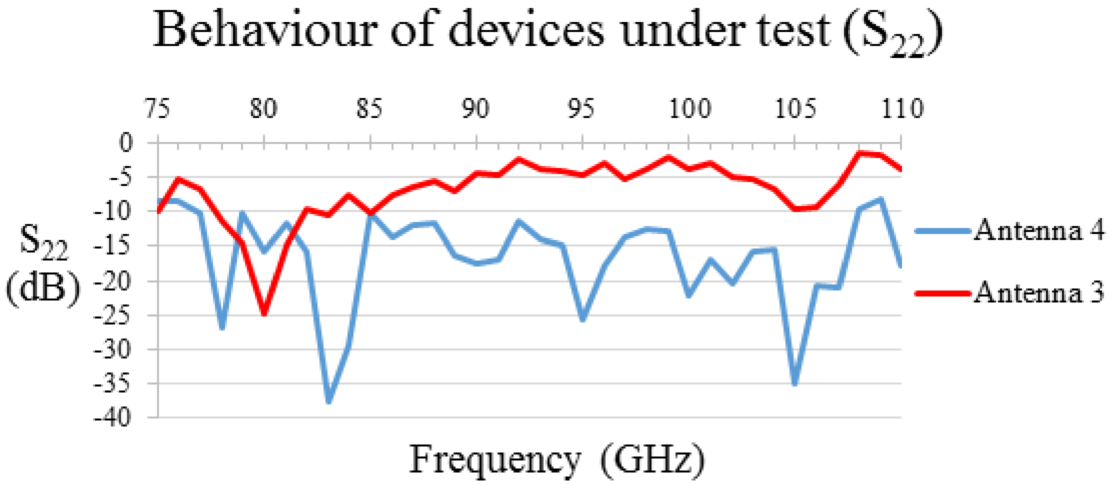

Figure 3-38: Measured S_{22} parameter (return loss) of the two patch antennas.

Patch antenna 3 showed a slight resonant structure, centred at around 80 GHz as see in **Figure 3-38**. Patch antenna 4 showed no clear resonant structure, as the S_{22} parameter (return loss) was below -10 dB for most of the frequencies measured. There was a large difference observed between the S_{22} parameters of patch antenna 3 and 4. The large difference between these two antennas was unexpected and may be a result of the difficulty in manufacturing and reproducing these devices accurately.

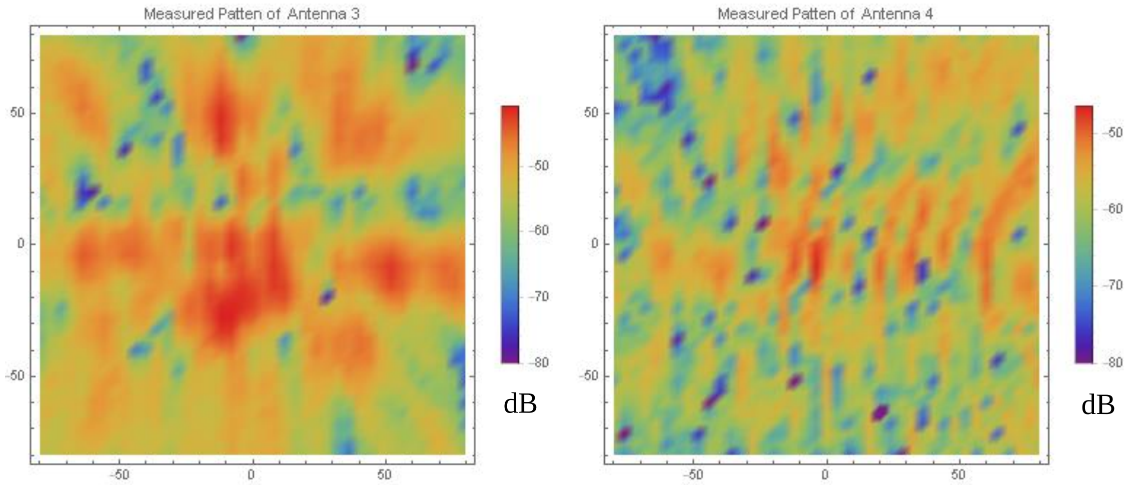

Figure 3-39: S_{21}-parameters of patch antenna 3 and 4 measured from VNA (planar scan of output field) at 100 GHz. Each scan extends from -80 mm to 80 mm along both axes.

The plots in **Figure 3-39** contained the raw data observed from the VNA. The values along each axis give the physical displacement of the detector probe in millimetres. The signal from both antennas were quite weak and there did not appear to be a region where the beam was concentrated.

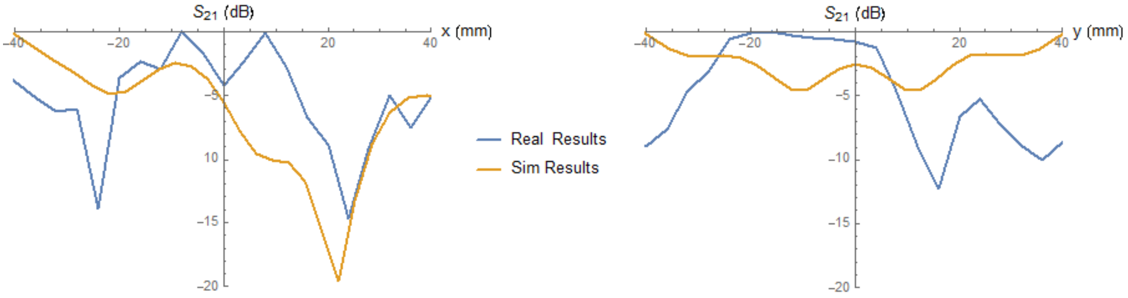

Figure 3-40: Farfield plot along the horizontal axis (left) and vertical axis (right) for antenna 3, with simulated results overlaid.

Figure 3-40 shows the normalized farfield pattern along the horizontal and vertical axes of the scan. There is poor agreement between the simulation and measured results and clearly do not agree well. This is attributed to the manufacture process altering the shape of the patches and feed wire locations slightly (i.e. general repeatability was lower than desired), leading to unreproducible results. Also, the S_{11} parameter of these designs was high, indicating that a lot of power was inherently reflected at the input side.

3.8 Conclusion

The design and development of a rectangular patch antenna at W band frequencies was described in this chapter. Two different antenna designs were simulated in CST. These circular and rectangular patch antennas were designed to create an antenna with the largest directivity possible, with minimal side lobes that minimised S_{11} around 100 GHz. From the CST simulations, a number of parameters were found that had a critical effect on the performance of the patch antennas. The displacement of the wire from the centre of the antenna, the size of the patch and the dielectric thickness all had a large effect on the antenna’s ability to radiate power efficiently. Additionally, the simulations showed that a small change (of ~ 0.1 mm) in value of any one of these attributes from their optimized values significantly altered the antenna’s performance. The size of the PCB board also effects the antenna’s performance at W band frequencies, but the effect was less significant.

A closed WR10 waveguide and an open WR10 waveguide were examined to determine which was better to couple power into a patch antenna via a wire suspended in the waveguide. The closed waveguide suffered from large internal reflections (constructive and destructive interference) with reflected power in the waveguide, which was unsuitable for feeding the antenna. Therefore, the open waveguide was the preferable feeding method to use to transfer power to the patch antenna.

The crosstalk between identical patch antennas was examined to establish the minimal crosstalk levels between the patches in the array. The S-parameters were used to quantify the crosstalk between the ports of the antennas in the array. In general, as the distance between patches increased, crosstalk decreases as expected. It was found that the crosstalk in one direction compared to another due to the asymmetry of the beam from the antenna.

The manufacture of the antenna was difficult due to the accuracy required. The accuracy required to create a patch with the correct size and with a correct wire displacement could be achieved by using conventional lab equipment. However, the substrate thickness of the available ABT18 board was 0.8 mm, which was too large for a “classical” patch antenna to be created. Antennas built with this board had a beam which radiated more horizontally along the dielectric rather than in the vertical direction as desired. A board with a smaller substrate height was required in order to create a patch antenna with optimum performance in W band. If the dielectric thickness of the board could be reduced to 0.1 mm, then “classical” patch antennas could be created to operate at 100 GHz. In this ideal case, the circular patch antenna had a lower on-axis directivity than the rectangular patch antenna. Additionally, the S_{11} parameter of the circular patch was larger than that of the rectangular patch. As the rectangular antenna performed better, all future work uses a rectangular antenna design.

Several rectangular patch antennas were constructed using the ABT18 board. The number of different issues were encountered with the manufacture of this board. The farfield pattern of the antenna did not show a region with a significant main lobe, so the beam did not appear to be radiating well. The simulation and the measured results do not agree, which could be due to the construction process altering the shape of the patches and the reproducibility of the process. Drilling a hole in the patch itself was also very destructive to a significant area of the patch. At more traditional lower frequencies, a drilled hole would be small (as the patch size is larger) and so would have a smaller effect.

Manufacturing the prototype patches for W Band was very difficult, due to the level of accuracy required, and consistent results could not be achieved. Nonetheless the ability to couple power from a short wire and feed a W band signal to a planar antenna was achieved and a weak transmitted signal was measured, which was the first W band planar antenna measurements carried out by the research group. Clearly if a more accurate manufacture and assembly technique must be developed for better repeatability. In the next chapter, the development of using coaxial cable connections to couple signal to planar structures based on the difficulty in coupling signal via a wire in a WR10 waveguide is outlined.

Chapter 4 Side-fed patch antenna

4.1 Overview

This chapter contains the design and development of side-fed W band patch antennas (a diagram is presented in **Figure 4-1**). These patch antennas were fed a signal via a microstrip line (this connection was also referred to as a planar waveguide). This planar metal strip was then coupled via a standard 1 mm coaxial connection from a waveguide-to-coaxial adaptor, which was coupled from the VNA. The work presented shows the various development stages in designing these W band planar antennas.

A board with a thin dielectric thickness relative to the W band wavelengths was required in order to create a patch antenna efficiently radiating at 100 GHz. On having difficulty with the 0.8 mm thick circuit board for quality beam patterns, the initial patch designs outlined in **Chapter 3**, two different dielectric boards were sourced. One board with a dielectric thickness of 0.4 mm and a second with a dielectric thickness of 0.125 mm were sourced externally.

This alternative coupling mechanism was tested in order to produce a practical device, which would have a low S-parameter (of less than -10 dB) and reasonable directivity greater than roughly 5 dBi. Drilling into the dielectric, as outlined in **Chapter 3**, was mechanically difficult and destructive and a better coupling solution was required. This was achieved by using the 1 mm coaxial connector and microstrip, as shown in the following figure.

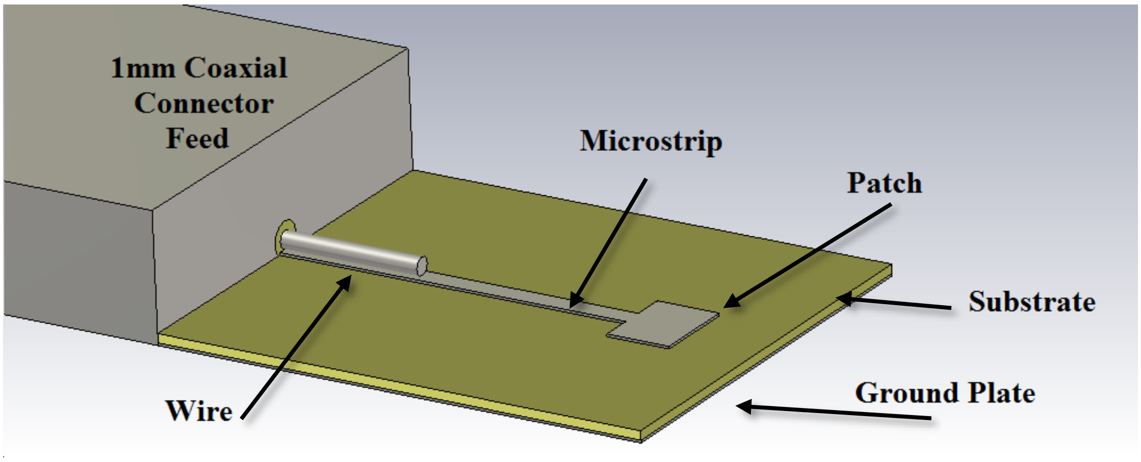

Figure 4-1: Perspective view of the side-fed patch antenna design as modelled in CST. Metallic parts are shown in grey and dielectric parts are shown in yellow.

4.2 Equipment

The first PCB board described here had a dielectric thickness of 0.4 mm, a dielectric constant of 4 and a refractive index of 2. It also had a copper coating on both sides of thickness 0.07 mm covered with photoresist. The photolithographic techniques used earlier could again be used for any antenna constructed on this board.

A second PCB with a dielectric height of 0.125 mm was also sourced. This a very specialist board and the thickness being so small (equivalent thickness to paper) makes processing very difficult. Also, as this PCB did not have a layer of photosensitive material, the photolithographic techniques used on the other boards could not be used with this PCB. The alternative technique of milling the patch shape was required.

There were two distinct coaxial connectors used during the testing process. The first device was a 1 mm coaxial connector with clamp (shown in **Figure 4-2**. The second 1 mm coaxial connector, a flange launcher (illustrated in **Figure 4-3**), was produced by Kawashima Manufacturing Co. Ltd. Both these devices were used for a similar role: to connect the antenna microstrip to the coaxial cable. 1 mm connectors are very expensive (circa €1000) and are not designed to be used multiple times with degradation of the connections over time. Due to budget constraints, only these connectors were available at the time.

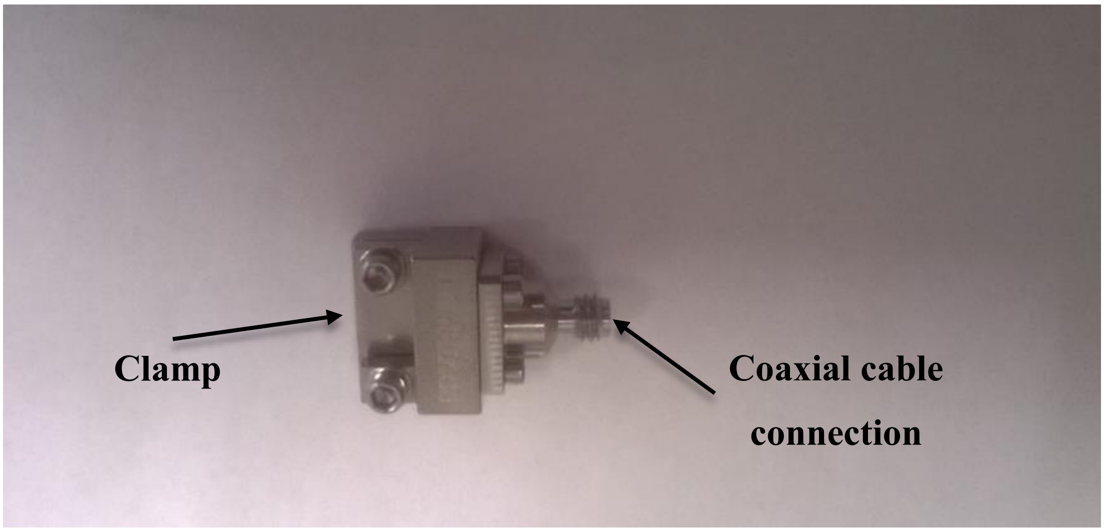

Figure 4-2: 1 mm coaxial connector and clamp used to support inset patch antenna and connect it to the coaxial cable. The antenna was slotted onto the left-hand side of the connector and held in place by the clamp. The coaxial core wire was soldered to the antenna, in order connect to the 1 mm coaxial connector line. This core wire was small enough to fit inside the 1 mm connector and had a diameter of 0.1 mm. The back (right-hand side) of the clamp was connected to a SX-12 coaxial cable.

The PCB was clamped in the gap between the two screws and these screws could be tightened to hold the antenna in place. The gap between these screws was 6 mm, which places a limitation on the size of board that could be mounted. Also, the metal structure of this 1 mm connector is mechanically large compared to the patch, so this also influences the radiation pattern. More details of the experimental arrangement are given in **Section 4.5**.

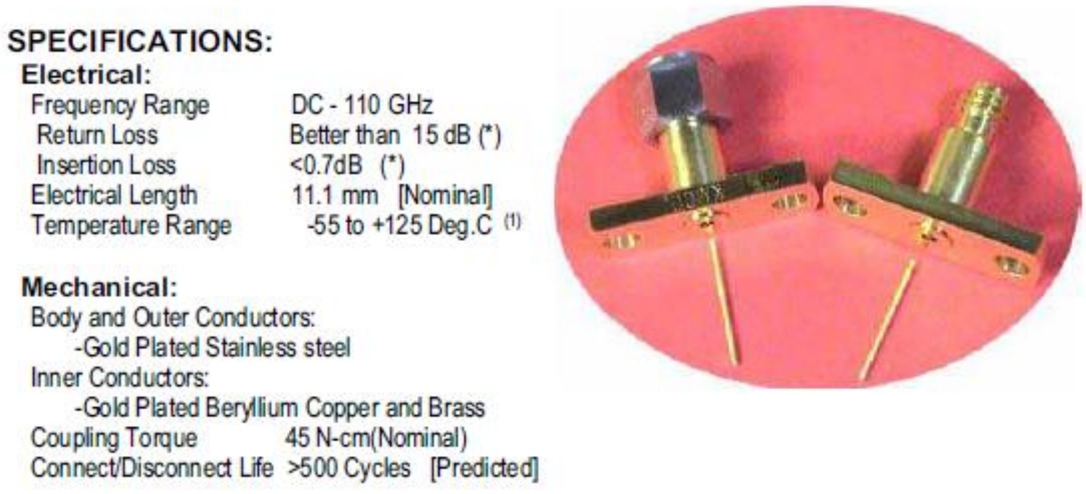

SPECIFICATIONS:

Electrical:

Frequency Range	DC - 110 GHz
Return Loss	Better than 15 dB (*)
Insertion Loss	<0.7dB (*)
Electrical Length	11.1 mm [Nominal]
Temperature Range	-55 to +125 Deg.C (1)

Mechanical:

Body and Outer Conductors:
-Gold Plated Stainless steel
Inner Conductors:
-Gold Plated Beryllium Copper and Brass

Coupling Torque	45 N-cm(Nominal)
Connect/Disconnect Life	>500 Cycles [Predicted]

Figure 4-3a: KPC100F311 flange with specifications. Credit [50]. The small core wire was solder to the antenna and the antenna was slotted into the front (flat side) of the flange. The back of the flange was twisted onto the coaxial cable.

The second connector used was a KPC100F311 flange launcher illustrated in **Figure 4-3**. This device did not have an associated clamp, which means that the antenna was mechanically free to rotate while connected electrically to the connector. However, the absence of a clamp means that mechanically the PCB board was not limited in size by the clamp.

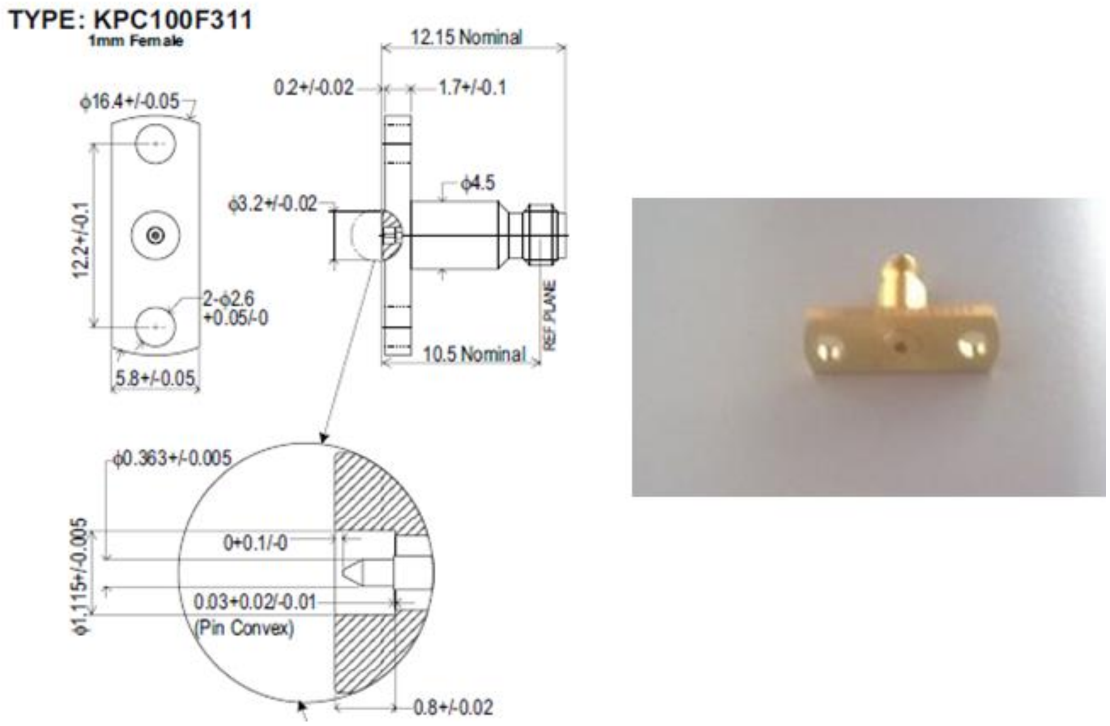

Figure 4-3b: Specifications of KPC100F311 flange launcher [50], with photo of the device (right).

Both of these devices are connected onto a coaxial cable (see **Section 2.7.3**) to feed W band signal. A SX-12 coaxial cable was used extensively during the testing of these antennas and had the specifications described in **Figure 4-4**.

Impedance	Outer conductor diameter	Inner conductor diameter	Insulator diameter	Insulator dielectric constant	Length
50 Ω	1.194 mm	0.287 mm	0.94 mm	2.1	250 mm

Table 4-1: Properties of SX-12 coaxial cable.

Figure 4-4: Photo of SX-12 coaxial cable used for W band applications in this thesis.

The coaxial cable was in turn connected onto a WR10 waveguide-to-coaxial connector (see **Figure 4-5**). Unfortunately, the SX-12 cable was needed as the 1 mm coaxial connectors and the waveguide-to-coaxial adaptor could not be connected as they both had female connection geometries.

Figure 4-5: Waveguide-to-coaxial connector (left) and H-Bend waveguide (right). Rectangular waveguides were explained in **Section 2.7.1**.

One issue, that was known before measurement, was the difficulty of VNA calibrations with the coaxial connections, as the coaxial cable lengths could not be calibrated without a calibration kit. This was not available during measurement and it would have allowed the losses and returned power to be characterised up to the end of the coaxial line. Using the waveguide calibration, the waveguide-to-coaxial adaptor, the SX-12 coaxial length and the 1 mm coaxial connections in the calibration could not be included. These objects were a source of loss and return power in the measurements described later. A 1 mm coaxial calibration kits cost approximately €25,000 and this was a prohibitive cost. As a result, the effects of the coaxial cable and connection from the device under test cannot be completely removed. A brief test was performed using the apparatus in order to estimate the effect of the connections on the final results.

4.3 Coaxial short test

Due to the non-availability of a W band 1 mm coaxial calibration kit, losses in the coaxial length were investigated by connecting a short to the end of the 1 mm coaxial connector and then measuring how much power was returned. The short consists of a small cut of the 0.125 mm PCB constructed to fit into the 1 mm coaxial connector with clamp and a wire soldered to the short (see **Figure 4-6**). This section of PCB was firstly simulated in CST to check that this device behaved like a short. This simulation explicitly assumes that the coaxial cable was perfectly lossless, as only the short in this simulation was tested.

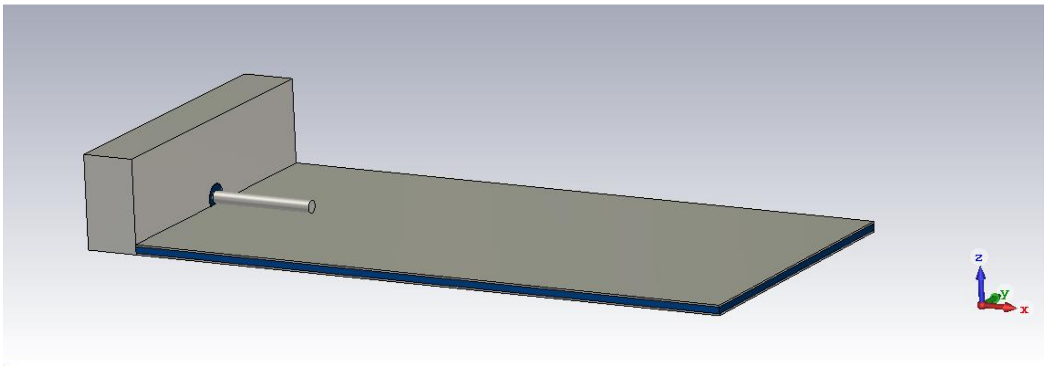

Figure 4-6a: Image of PCB short simulated from CST.

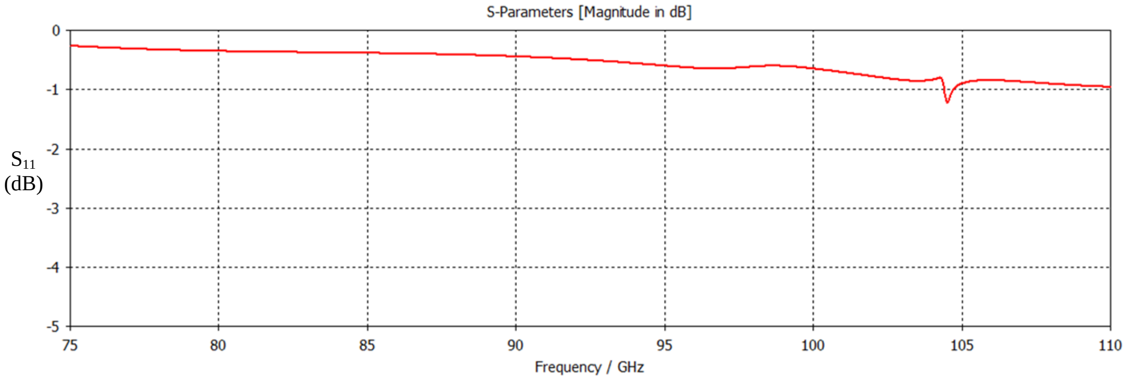

Figure 4-6b: Return loss of PCB short connected to 1 mm coaxial connector.

The high S_{11} parameter in **Figure 4-6b** indicates that most power sent though the coaxial connector will be reflected back into the port. The small cut of PCB did not behave as perfect short, but it had very high levels of return loss.

Figure 4-7a: Diagram of set up from VNA on left and close up of the short on right.

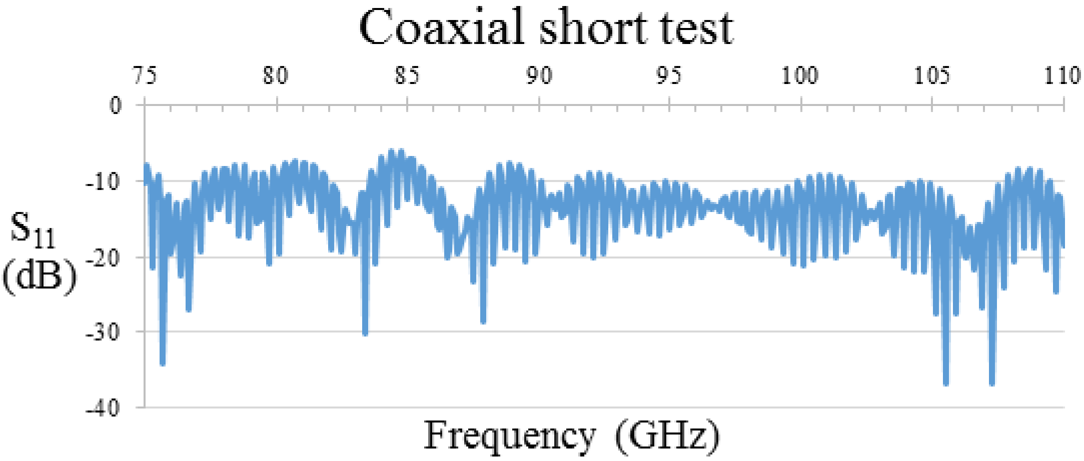

Figure 4-7b: Results from VNA using the short with the clamp and 1 mm coaxial connector.

In the physical test set up, the short was connected to the 1 mm coaxial connector, which was connected to the coaxial cable and the S_{11} parameter was measured over the W band. The results from the VNA measurement (**Figure 4-7b**) showed that the short was reflecting a lower amount of power than the −1 dB expected from a lossless coaxial cable simulation (**Figure 4-6b**). The short was reflecting about -10 dB of power on average over the W band region. To ensure that the 1 mm connector was not the issue, the test was repeated with the short connected to a KPC100F311 connector, as shown in **Figure 4-8**.

Figure 4-8a: Short connected to other KPC100F311 flange launcher.

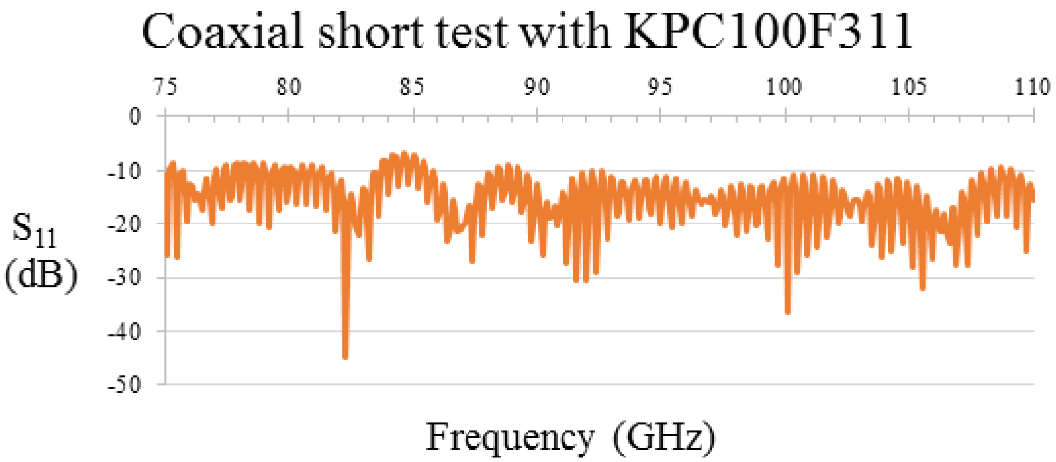

Figure 4-8b: Results from VNA using the short and the KPC100F311 connector.

The return loss S_{11} measured for the 1 mm coaxial connector and the flange launcher (**Figure 4-8b** and **Figure 4-6b**) showed similar results when each was connected to the coaxial length. Both showed an average S_{11} parameter of approximately -10 dB and both showed similar variation with frequency. These tests show that the losses were not caused by the connectors, as both graphs are the same. The loss must be caused by either the coaxial cable or by the coax-to-waveguide connector mismatch. However, without a calibration kit, it was not possible to specify which device was the actual source of these losses.

4.4 Rectangular fed patch antenna

The patch could either have a rectangular or a circular shape. The rectangular patch was chosen for the reasons explained in **Chapter 3**. The dielectric of the PCB needed to be thin relative to the wavelength. The thinnest board sourced commercially was 0.125 mm and the CST simulations were run with this dielectric thickness. Additionally, the microstrip needed to be at least 0.25 mm wide in to physically connect the microstrip to the wire of the connector with good electrical contact.

As was discussed in **Chapter 3** the antenna should work best on the thinner 0.125 mm board, but practically it is extremely thin and etching the patch shape would be difficult. If it did work well, then the design could be scaled up to the easier to manufacture on 0.4 mm board. It was also expected that the location of the microstrip feeding the patch relative to the centre of the patch would affect the beam's characteristics and this parameter was examined first. The offset of the microstrip from the centre of the patch in the *y*-axis was referred to as the "y-shift". It was expected that an offset along the *x*-axis (x-shift) will have the same effect.

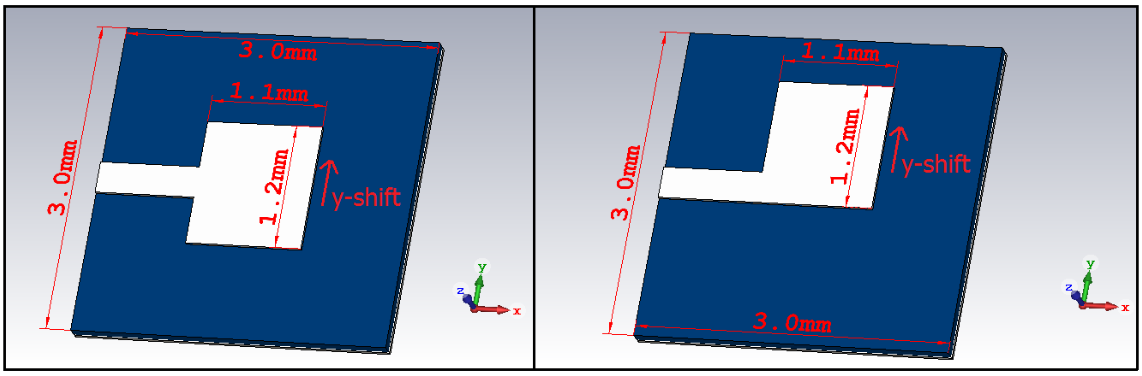

Figure 4-9: Dimensions of side-fed rectangular patch antenna, showing the effect of changing the patch's position along the *y*-axis ("y-shift"). The length and width were the length of the component in the *x* and *y* direction respectively.

The main problem found when testing this design was the position of the feed relative to the patch, shown as y-shift in **Figure 4-9**. The position of the connection between the microstrip and the patch was changed from the centre of the patch (y-shift = 0 mm) to one edge of the patch (y-shift = 0.45 mm). Altering the position of the patch relative to the microstrip changes the S_{11} parameter recorded as shown in the following figures.

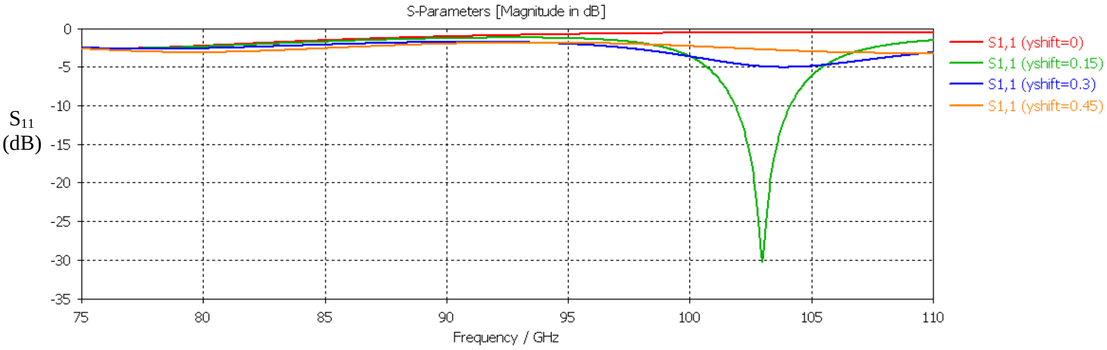

Figure 4-10a: S_{11} parameter as the position of the microstrip feed changes long the *y*-axis (y-shift).

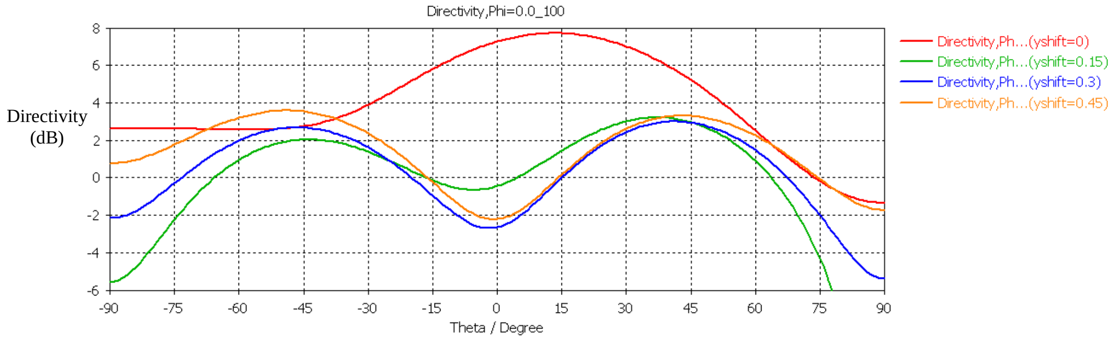

Figure 4-10b: Farfield pattern of the different antenna designs at 100 GHz.

Figure 4-10a show that altering the position of the patch slightly, alters the S_{11} parameter quite dramatically. A large reduction of S_{11} was present at a frequency of 103 GHz at 0.15 mm and the S-parameter only falls below -10 dB at 0.15 mm offset (**Figure 4-10b**). Additionally, the farfield pattern of the antenna showed that the antenna only radiates in the correct direction when the y-shift parameter was 0 mm and altering the microstrip position had made the device perform worse.

y-shift	Minimum S_{11} parameter	Directivity along *z*-axis	Problem with device
0 mm	-2.6 dB	7.3 dBi	Minimum S_{11} was too small
0.15 mm	-30.3 dB	-4.1 dBi	Directivity of *z*-axis was too small
0.3 mm	-5 dB	-9.5 dBi	S_{11} and directivity too small
0.45 mm	-3.2 dB	-9.4 dBi	S_{11} and directivity of *z*-axis too small

Table 4-2: Summary of results and collection of problems with each device examined.

The position of the microstrip-patch connection had a strong impact on the performance of the antenna. Further investigation of this design was suspended in order to investigate the inset fed patch design detailed in the following section. This design had the potential to improve the coupling and reduce the S_{11} values.

4.5 Inset patch antenna

Following on the patch antenna design outlined previously, the design of an insert patch antenna is now described. These insets should reduce the S_{11} parameter and should improve the coupling between the feeding signal line and the antenna by matching the impedance of the feedline and antenna more closely. The antenna designed in this part was best described as a side-fed inset rectangular patch antenna or inset antenna for short.

This design was based roughly on the inset patch antenna described in (M. A. Matin and A. I. Sayeed) [51]. The design described in this paper had a detailed inset cut on the patch, which was too small to accurately manufacture at W band frequencies in house.

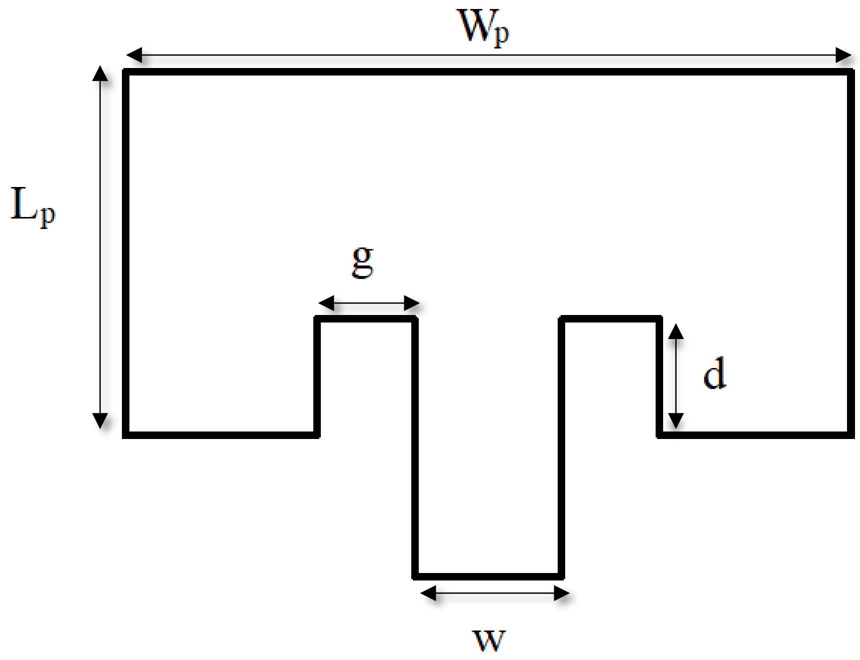

Figure 4-11: Diagram of inset patch antenna taken from M. A. Matin and A. I. Sayeed [51].

Operating frequency, *f* in GHz	10
Dielectric constant, ε_{reff}	2.2
Length of the patch, L_p in μm	9064
Width of the patch, W_p in μm	11895
Position of inset feed point, *d* in μm	3126
Width of the microstrip feed line, *W* in μm	2150

Table 4-3: Table of parameter used to create the inset patch antenna which operated at 10GHz from M. A. Matin and A. I. Sayeed [51].

To replicate this design, the insets were slanted in order to ease manufacture tolerances (see the slants introduced in the patch in **Figure 4-12**).

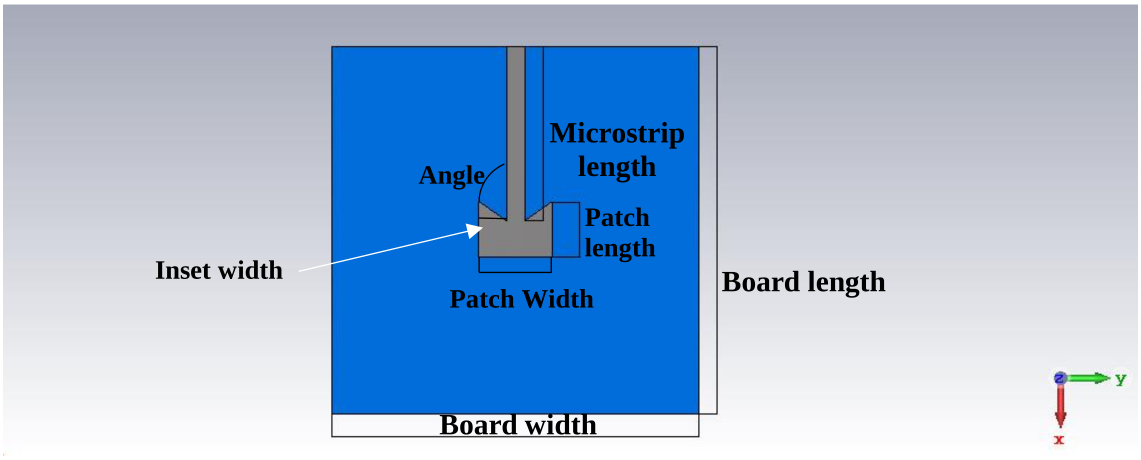

Figure 4-12: Diagram of inset patch antenna. The inset width was the distance from the edge of the microstrip to the end of the patch. Angle was the angle of inclination of the inset.

An inset patch antenna was designed on the 0.4 mm PCB (see **Figure 4-12**). This PCB had a dielectric thickness between 10% and 15% of W band wavelengths. This board may be thin enough to operate well in this range. Initial analysis began in order to create an inset patch antenna that operates optimally at 100 GHz. The antenna needed to be coupled to the 1 mm coaxial connector. As this device has an associated clamp, it places an upper limit on the board size.

4.5.1 Simulations of inset patch antenna

The microstrip width was set to 0.5 mm and the microstrip length was set to 2 mm. The patch width was set to 1 mm and the patch length was set to 0.7 mm, based on the results from the previously designed patch antennas. The size of the board was also expected to have some effect on the performance of the antennas. The dielectric thickness was set to 0.4 mm in the simulation based on the real available PCB. The patch length (along the *x*-axis) was examined first, as the patch size had a large effect on the resonant frequency of a patch antenna. The length of the patch was increased from 0.4 →1 mm in steps of 0.1 mm, in order to determine the accuracy required to manufacture this device.

Patch length	Board length	Board width	Patch width	Microstrip width	Inset length	Angle
0.4 → 1 mm	4 mm	5 mm	1 mm	0.2 mm	0.2 mm	35°

Table 4-4: Initial parameters of inset patch antenna.

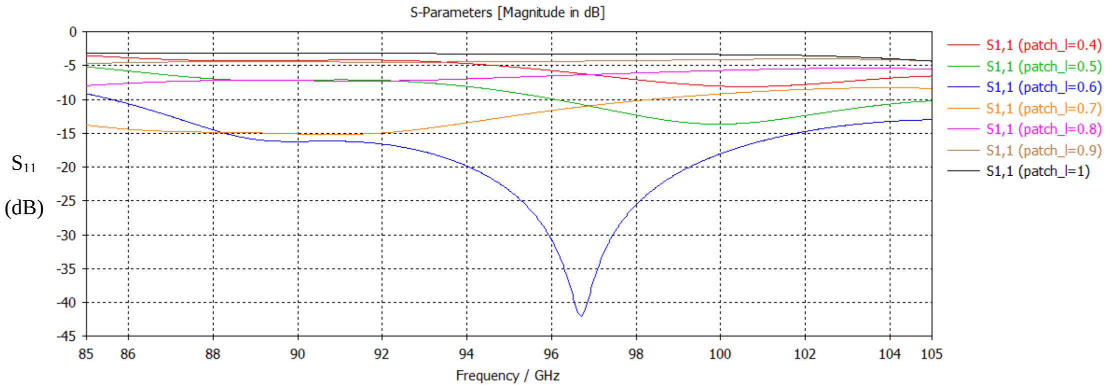

Figure 4-13a: S_{11} parameter of antennas of various patch length between 85 GHz → 105 GHz.

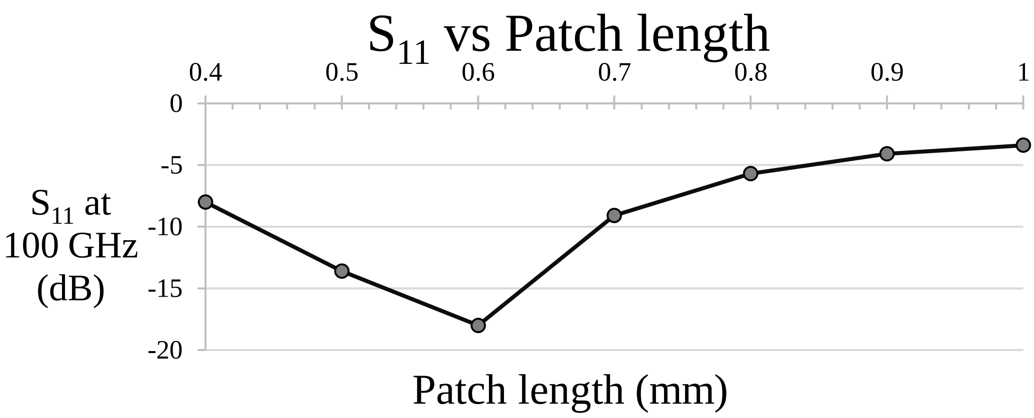

Figure 4-13b: S_{11} parameter at 100 GHz for each antenna patch length.

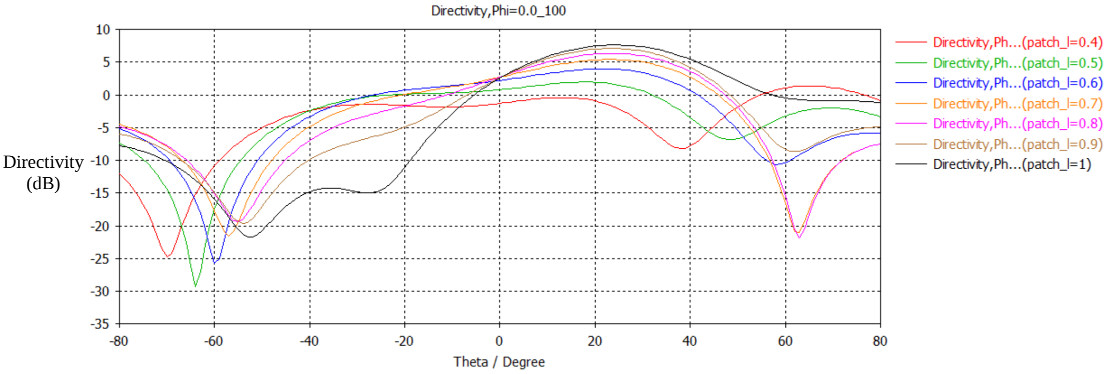

Figure 4-13c: Comparison of farfield patterns of antennas of various patch lengths at 100 GHz along the $\varphi = 0°$ axis.

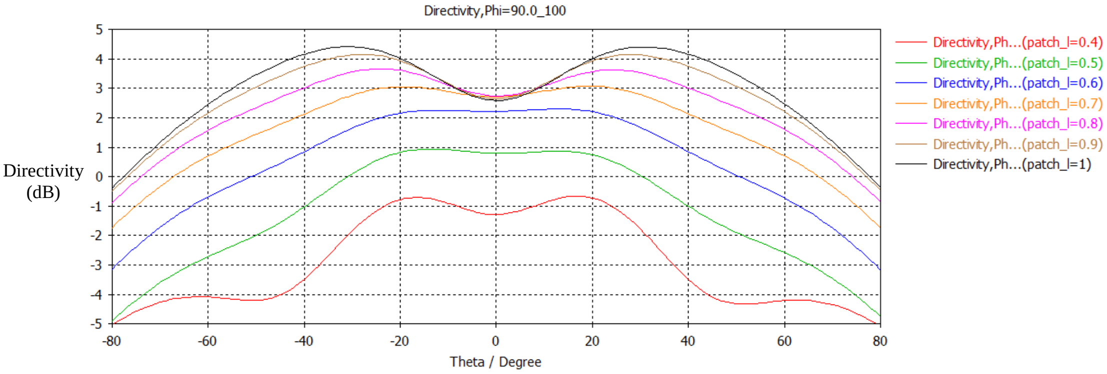

Figure 4-13d: Comparison of farfield patterns of antennas with various patch length at 100 GHz along the $\varphi = 90°$ axis (i.e. orthogonal to **Figure 4-13c**).

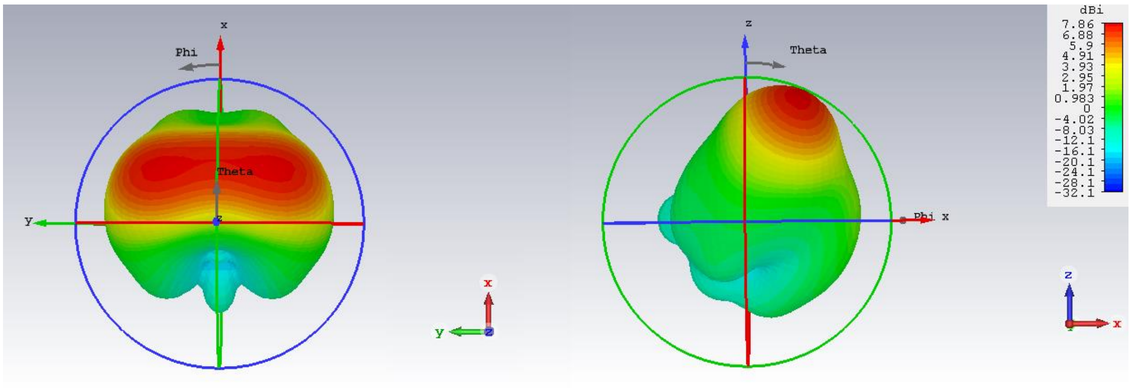

Figure 4-13e: 3-D farfield pattern for patch antenna with a patch length of 1 mm, seen from front (left) and side (right).

Figure 4-13a and **Figure 4-13**b indicates that an antenna with a patch length of approximately 0.6 mm should be resonant at 100 GHz. The farfield patterns (**Figure 4-13c** and **Figure 4-13**d) show that the antenna was most sensitive at an angle from the vertical, which was not ideal. Along the $\varphi = 0°$ axis, this offset was roughly 20° to the vertical, while along the $\varphi = 90°$ axis, the directivity had 2 peaks along either side of the centre.

Ideally, the maximum directivity should be located at 0°. The 3-D farfield pattern (**Figure 4-13e**) showed the peak directivity did not line up with the vertical and this was also true for antennas of different patch size. The strongest section of the beam did not radiate along the *z*-axis, but instead radiates at some undesired angle to the vertical.

The patch size was not causing the beam to radiate at an angle. Some other attributes of the device, such as the dielectric thickness or the microstrip line were thought to be responsible.

The effect on the microstrip on the antennas performance was also examined. The microstrip width was increased to 0.4 mm. The previous test was repeated as the length of the patch was increased from 0.4 → 1 mm in steps of 0.1 mm.

Patch length	Board length	Board width	Patch width	Microstrip width	Inset width	Angle
0.4 → 1 mm	4 mm	5 mm	1 mm	0.4 mm	0.2 mm	35°

Table 4-5: Parameters used to examine line of microstrip on inset antenna.

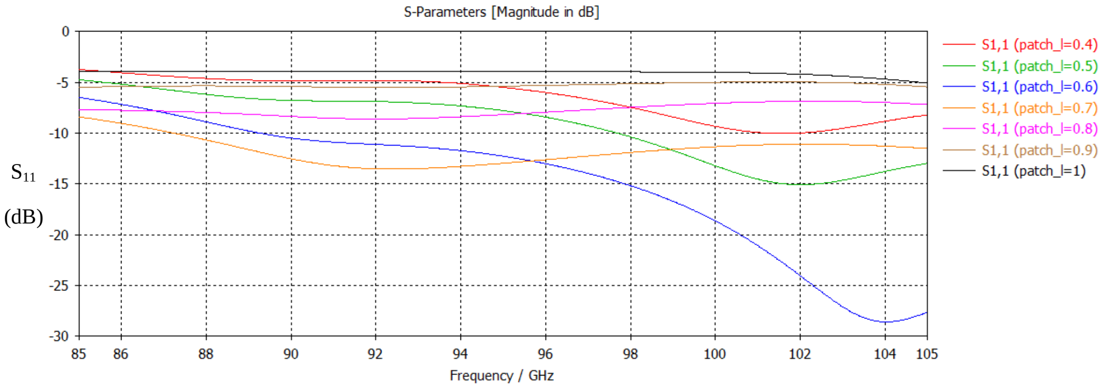

Figure 4-14a: S_{11} parameter of antennas of various patch length between 85 GHz → 105 GHz.

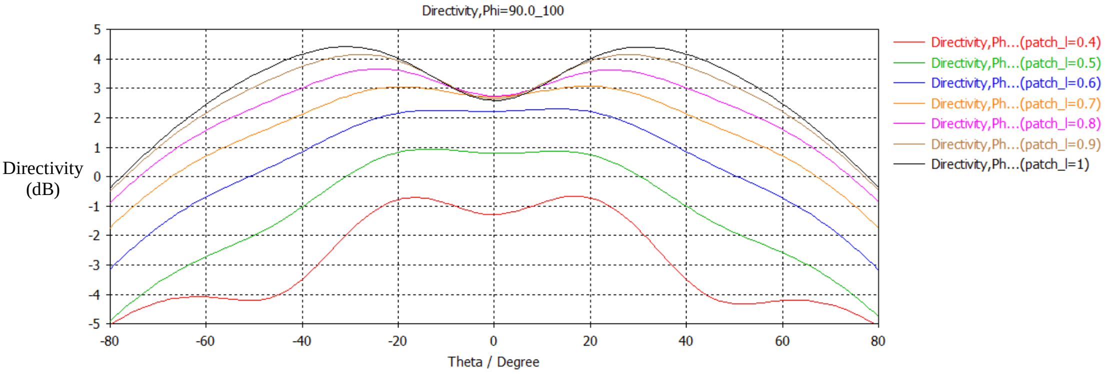

Figure 4-14b: Farfield patterns of antennas of various patch length at 100 GHz ($\varphi = 90°$ axis).

The S_{11} parameter of the antenna was very low, reaching a value of -18.6 dB at 100 GHz for a patch with a length of 0.6 mm (**Figure 4-14a**). However, the maximum directivity for the patch of length 0.6 mm was only 3.8 dBi (**Figure 4-14b**). Similarly, to **Figure 4-13d**, the different patch sizes all show a beam that radiates in two directions. The farfield patterns show that the antenna still possessed two peaks, either side of the on-axis direction. Changing the microstrip width did not affect the “tilt” on the antenna maximum directionality.

The device did not operate optimally at 100 GHz due to the “tilt” of the farfield beam. The antenna was unsuited to operate at higher end W band frequencies (roughly 100 GHz), as it appeared that a 100 GHz antenna requires a thinner dielectric, which was be examined in **Section 4.6**.

As part of these simulations, the farfield patterns at 85 GHz was also recorded and analysed. The farfield pattern generated at this frequency was generally more directive as the following figures showed.

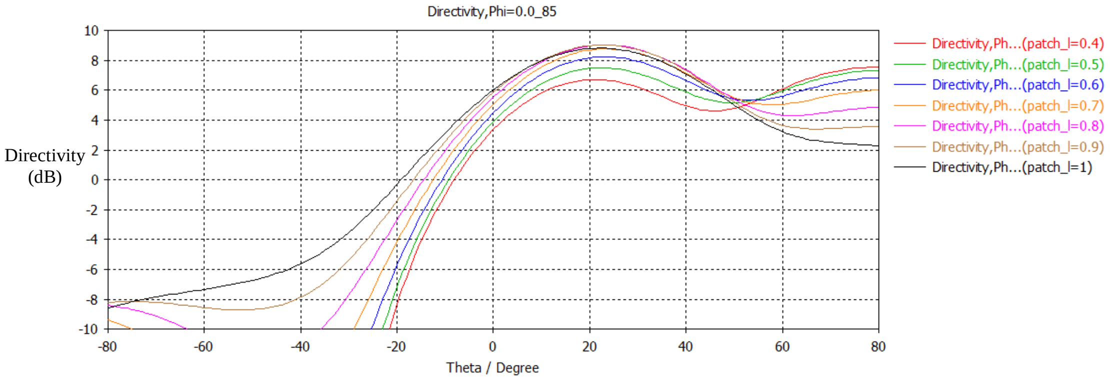

Figure 4-14c: Farfield patterns of antennas of various patch length at 85 GHz ($\varphi = 0°$ axis).

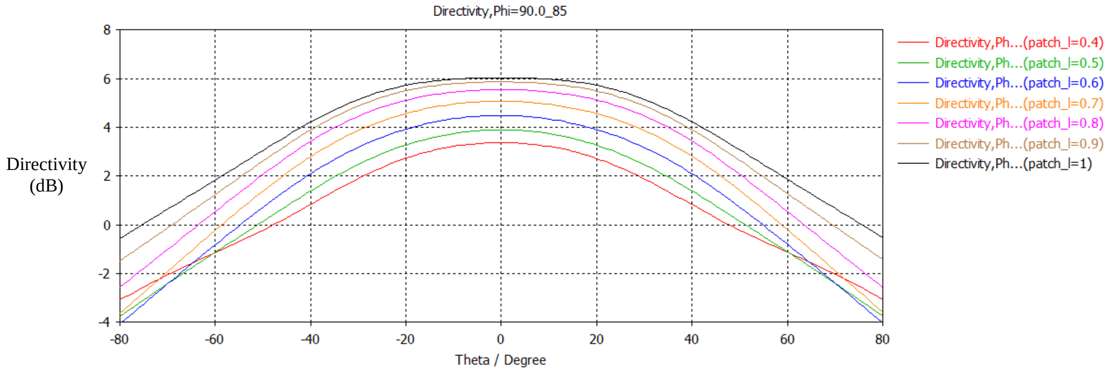

Figure 4-14d: Farfield patterns of antennas of various patch length at 85 GHz ($\varphi = 90°$ axis).

Figure 4-14c shows that the maximum directivity at 85 GHz was 9 dBi, with a patch length of 0.9 mm. However, the maximum directivity of the beam was still at a tilt of about 20° along the $\varphi = 0°$ axis.

The antenna build on this board was redesigned to operate at the lower end of the W band as **Figure 4-14d** showed promising results. Additionaly, the two-peak structure evident at the 100 GHz farfield pattern had disappeared. The following analysis was an attempt to develop an antenna to resonate at 80 GHz, i.e a low W band frequency range within our experimental capability.

The frequency range examined in CST was changed to 75 → 85 GHz and the previous test was repeated (**Figure 4-13**) as the length of the patch was increased from 0.4 mm → 1 mm in steps of 0.1 mm. Each antenna design was compared based on its ability to radiate specifically at 80 GHz.

Patch length	Board length	Board width	Patch width	Microstrip width	Inset width	Angle
0.4 → 1 mm	4 mm	5 mm	1 mm	0.5 mm	0.2 mm	45°

Table 4-6: Table of parameters for inset patch antenna operating at 80 GHz.

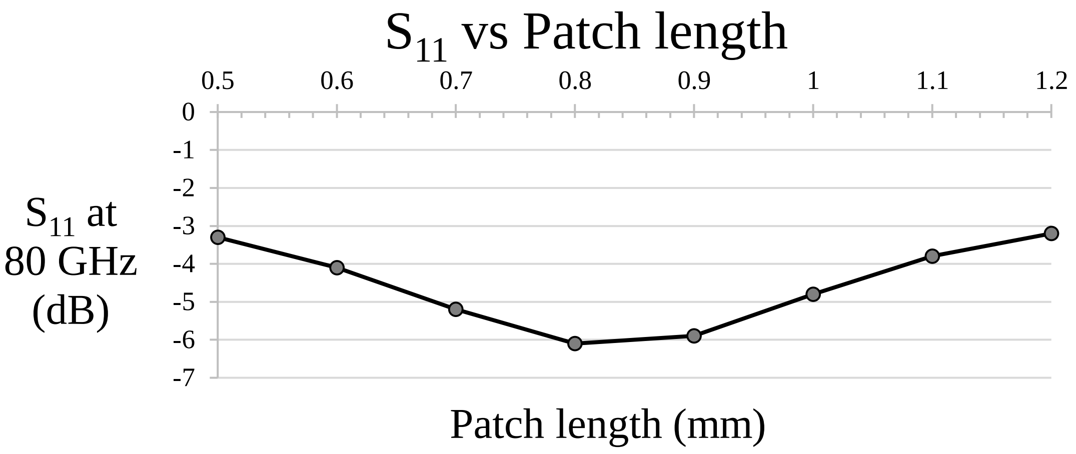

Figure 4-15a: S_{11} parameter at 80 GHz as patch length changes.

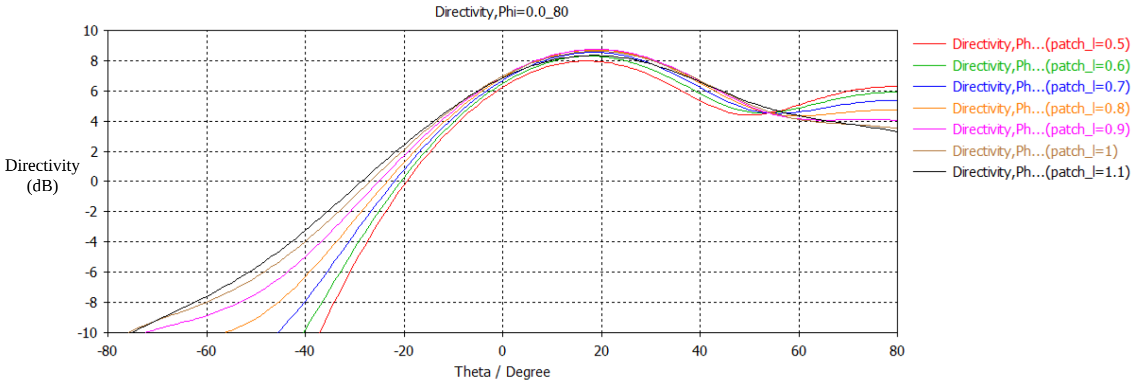

Figure 4-15b: Farfield pattern of antenna with change in patch length.

The S_{11} parameters of the antenna seen in the graph (**Figure 4-15a**) were worse than those from the antenna operating at 100 GHz (**Figure 4-13a**). The minimum S_{11} parameter for these antennas was found for patch length of 0.8 mm. The S_{11} parameter at 80 GHz for this antenna was -6.1 dB, which was equivalent to only about ~75% of the power being radiated. However, no patch length produced a S_{11} parameter below the desired -10 dB.

The maximum directivity obtained for this antenna design was for the patch with a length of 0.8 mm which had a directivity of 8.7 dB. The peak of the farfield pattern (**Figure 4-15b**) was still at an angle of about 20° from the vertical. The inset patch antenna appears to behave more like a traditional rectangular patch antenna at 80 GHz, as increasing the patch length decreases the resonant frequency. Unlike previous devices, the directivity of the device did not alter significantly with changing patch length.

The size of the board was altered to examine the effect on the antenna's performance. The board width (along the *y*-axis) and the board length (along the *x*- axis) were varied between 5 → 10 mm.

The patch was always located at the centre of the board. Varying the length of the board also alters the length of the microstrip feed. The patch length was set to 0.8 mm based on the graph (**Figure 4-15a**). The other parameters were kept the same as in **Table 4-6**.

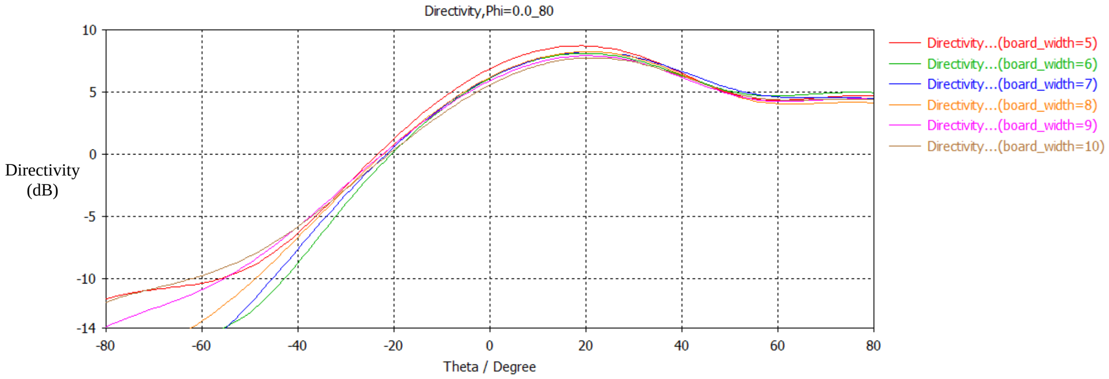

Figure 4-16a: Farfield pattern due to altering the board width (width along the *y*-axis).

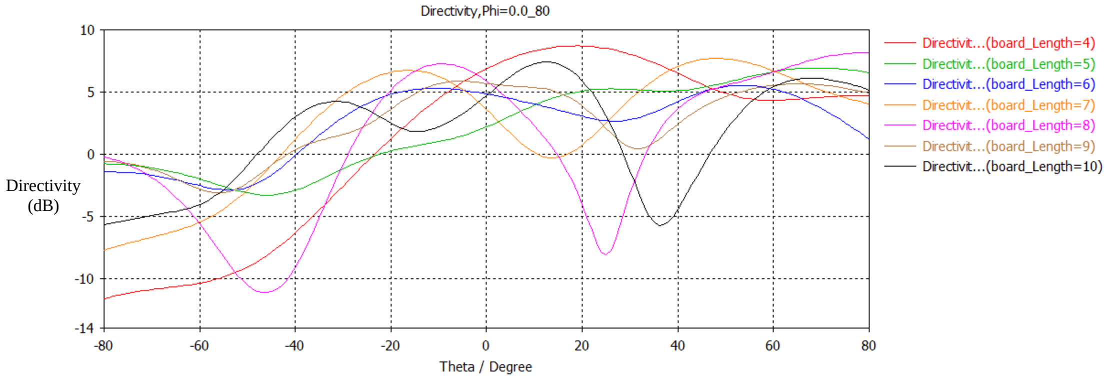

Figure 4-16b: Farfield pattern due to altering the board length (length along the *x*-axis).

Changing the width of the board (**Figure 4-16a**) had only a small effect on the farfield pattern of the antenna. The antenna still radiated at a slight angle, as seen before with the antenna operating at 100 GHz (**Figure 4-15**). The directivity decreased from a maximum of 8.7 dBi with a board width of 5 mm, to a directivity of 7.7 dBi with a board width of 10 mm.

Changing the length of the board **(Figure 4-16b**) had a larger effect on the farfield pattern of the antenna. However, there didn't appear to be a trend between board size and maximum directivity, so the larger boards were not necessarily worse than the smaller boards. This effect may be due to power radiating from the microstrip feed or the substrate. The width of the board had a relatively small effect on the S_{11} parameter and farfield pattern.

The inset on the patch antenna could also influence the farfield pattern of the antenna. The angle between the patch and the microstrip was altered from 50° to 5° in steps of 5° (see **Figure 4-12** for diagram of antenna). The farfield pattern and the S_{11} parameter was recorded as the angle was altered.

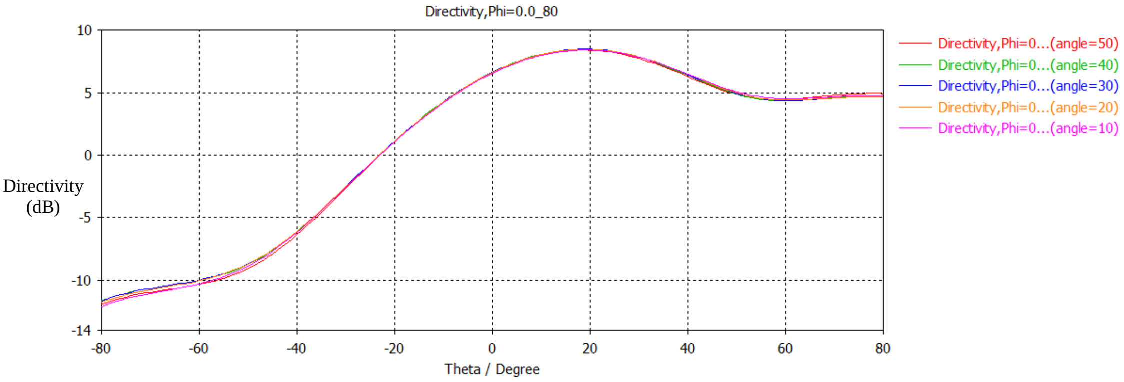

Figure 4-17a: Farfield plot of each antenna with a different patch to microstrip angle.

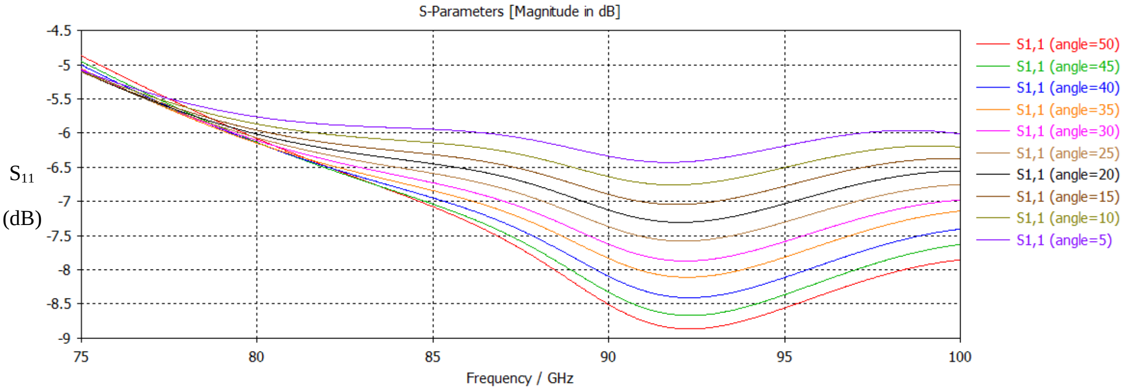

Figure 4-17b: S_{11} plot of each antenna as the angle of the inset changes.

The change in angle did not alter the farfield shape (**Figure 4-17a**). The S_{11} plot showed a gradual increase of the S_{11} parameter as the angle decreases as expected. The amount of power the device returns to the port tends to increase as the angle of the inset decreases (**Figure 4-17b**). The insets needed to be at a steep angle in order to accept power from the microstrip efficiently. Additionally, the antenna was not resonating at the desired 80 GHz, but rather between 90-95 GHz.

A 1 mm coaxial connector with a clamp was used to feed an input signal, but it was also a large metal structure relative to the patch antenna. An image of this clamp is shown in **Figure 4-2**. The size of the clamp's jaws could not be adjusted, which places a restriction on the length of the board along the *y*-axis. The effects of the clamp on the antenna's performance were simulated in CST.

Description	Value	Description	Value
Angle of cut of inset	25°	Length of microstrip (*x*-axis)	4 mm
Length of board (*x*-axis)	9 mm	Width of microstrip (*y*-axis)	0.5 mm
Width of board (*y*-axis)	7 mm	Length of patch (*x*-axis)	1 mm
Thickness of ground plate	0.035 mm	Width of patch (*y*-axis)	1 mm
Width of inset (*y*-axis)	0.5 mm	Dielectric thickness	0.4 mm

Table 4-7: Parameters used to create inset patch antenna connected to the clamp.

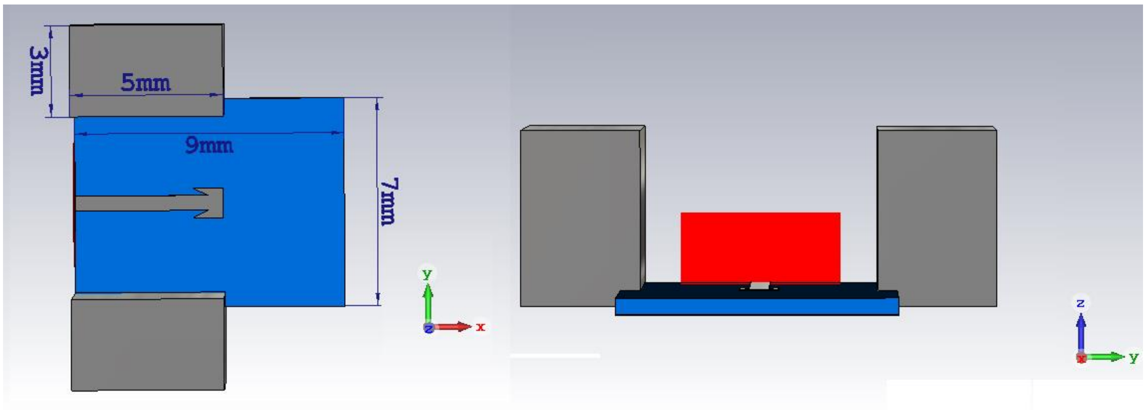

Figure 4-18a: Inset patch antenna with clamp attached as viewed from top (left) and front (right). This simulation assumes that there was ideal connection between the microstrip and the 1 mm coaxial connector.

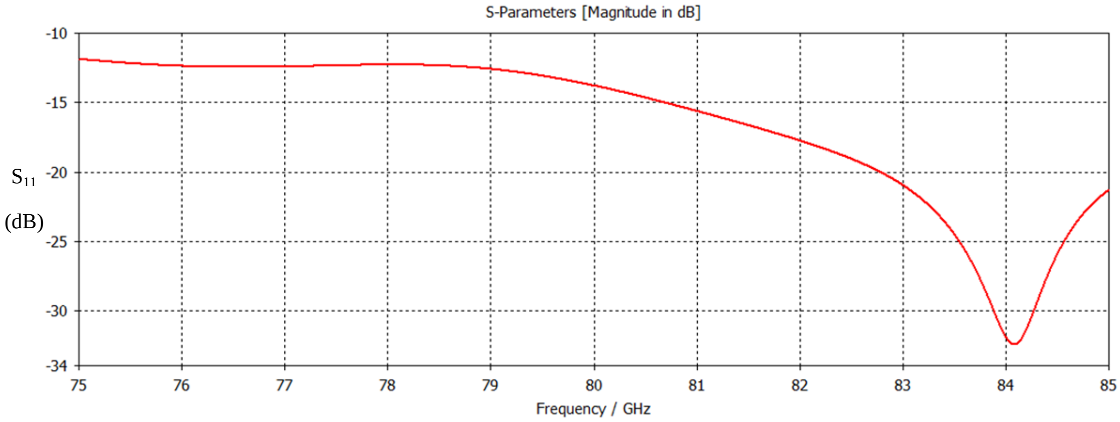

Figure 4-18b: S_{11} parameter of inset patch antenna with the clamp between 75 and 85 GHz.

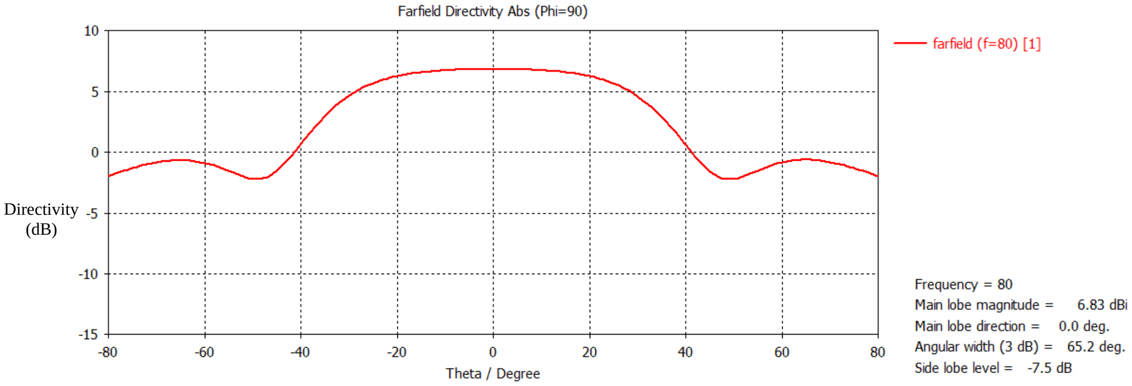

Figure 4-18c: Cross section of the farfield pattern of the antenna along the $\varphi = 90°$ axis at 80 GHz.

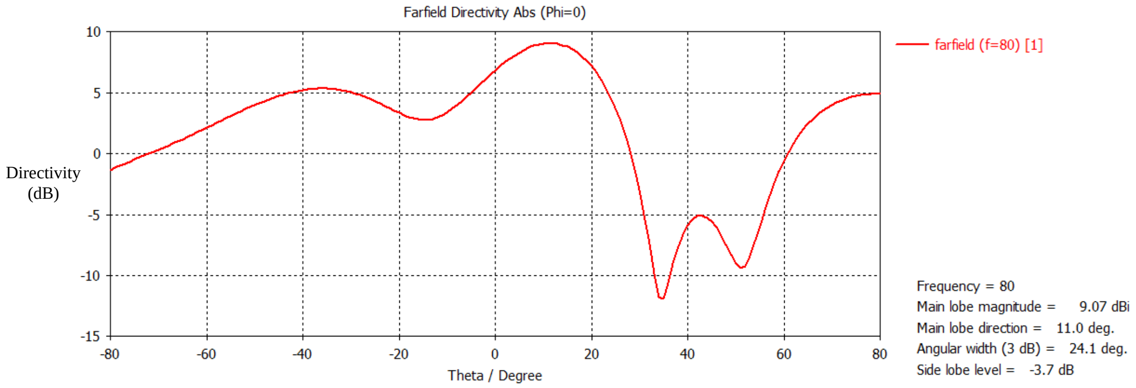

Figure 4-18d: Cross section of the farfield pattern of the antenna along the $\varphi = 0^\circ$ axis at 80 GHz.

Figure 4-18b shows that the antenna was an efficient radiator as the S_{11} parameter of the antenna was quite low and it stayed below -10 dB for the entire frequency range. The antenna was an efficient radiator as the S_{11} parameter of the antenna was quite low and it stayed below -10 dB for the entire frequency range.

Figure 4-18c and **Figure 4-18d** shows the cross section of the farfield along two perpendicular axes. When these two cuts were compared, the cut along the $\varphi = 90^\circ$ axis (**Figure 4-18c**) showed an ideal beam pattern. The beam had low side lobes and a relatively large maximum directivity along this axis. However, the cut of the farfield pattern along the $\varphi = 0^\circ$ axis (**Figure 4-18d**) showed that the beam was radiating at a slight angle to the vertical. The directivity of the beam peaks at 9.07 dB at about 10° from the centre. This slight angular tilt in the beam pattern was not ideal. This design was none the less chosen for manufacture to investigate the processes involved and to see if simulations and measurements could agree.

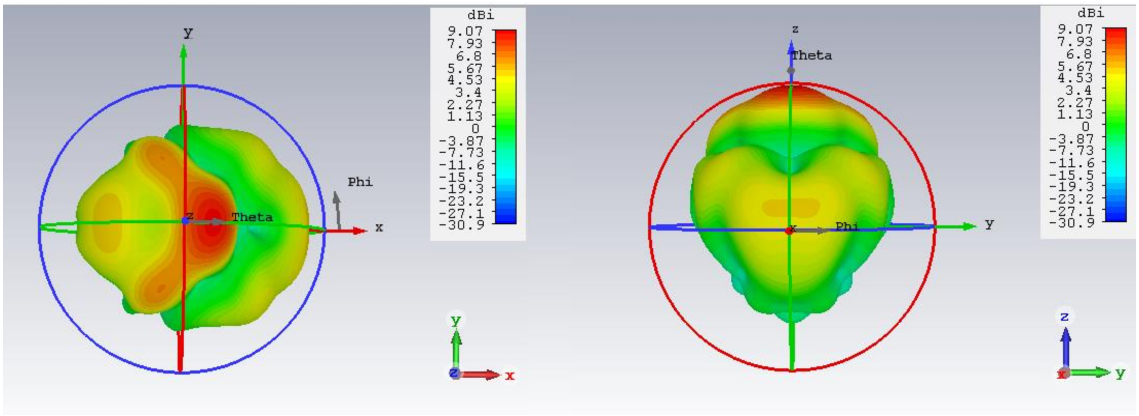

Figure 4-18e: 3-D farfield pattern at 80 GHz of the inset patch antenna with the clamp attached as viewed from top (left) and front (right).

4.5.2 Manufacture of inset patch antenna and design of connecting system

The inset patch antenna in **Figure 4-19** was manufactured using the photolithographic techniques described in **Section 2.4**. A wire was soldered onto the microstrip part of the antenna, which allows the device to be connected to the 1 mm coaxial connector (see **Figure 4-20**). The patch and microstrip feedline were etched on the PCB board which was cut down to 6 mm in length in order to fit the board into the clamp.

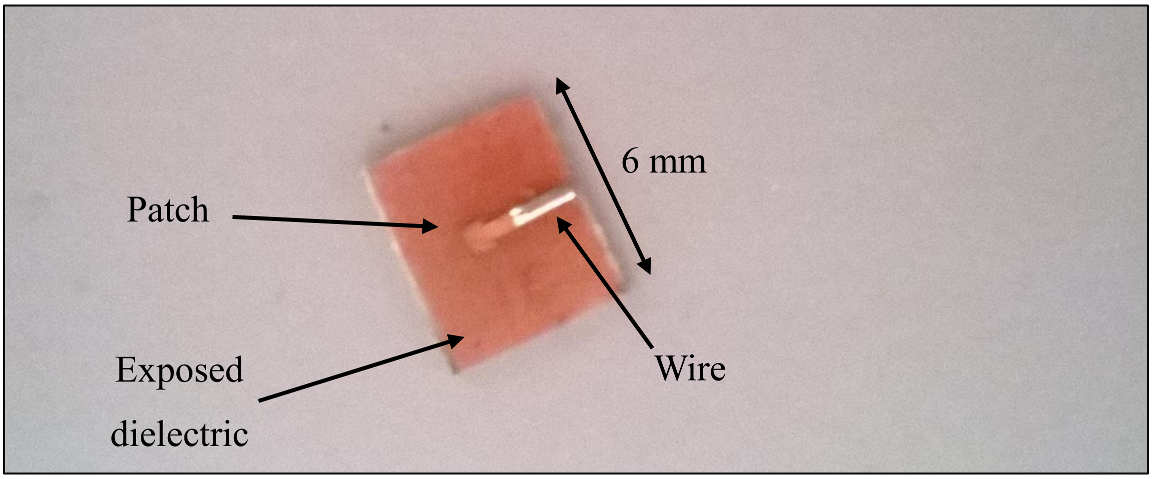

Figure 4-19: Inset patch antenna made from photolithography with high resolution mask. The patch was the pale orange-silver square at the center of the device. The bright silver part was the wire which connects the patch to the clamp (i.e. the coaxial core wire).

Two prototypes of this inset antenna were manufactured in order to test the design at W band frequencies using the VNA. The detail on the first inset patch antenna was limited due to the mask used in the photolithographic process and was referred to as "inset1". After this device was constructed, it was discovered that a higher resolution mask could be created by printing the mask using a higher resolution printer. The second inset patch antenna, referred to as "inset2", was created using this higher resolution mask, which allowed for finer detail on the antenna.

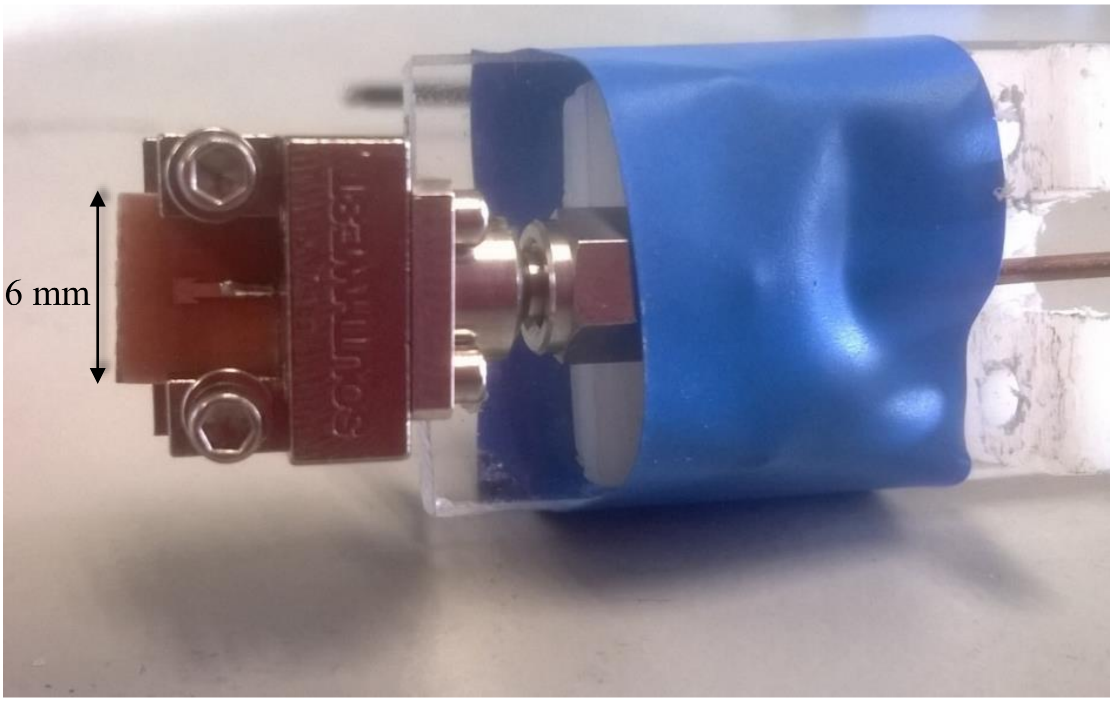

Figure 4-20: Inset patch antenna (inset2) secured in the 1 mm coaxial connector with the clamp.

The antenna was attached to the clamp that holds it in place. A coaxial-waveguide converter was connected to the VNA. Unfortunately, both the clamp and the coaxial-waveguide converter have male connectors and cannot be simply connected together. A SX-12 coaxial cable was used to connect the 1 mm coaxial connector to the coaxial-waveguide converter. Further details of the cable were described in **Table 4-1.**

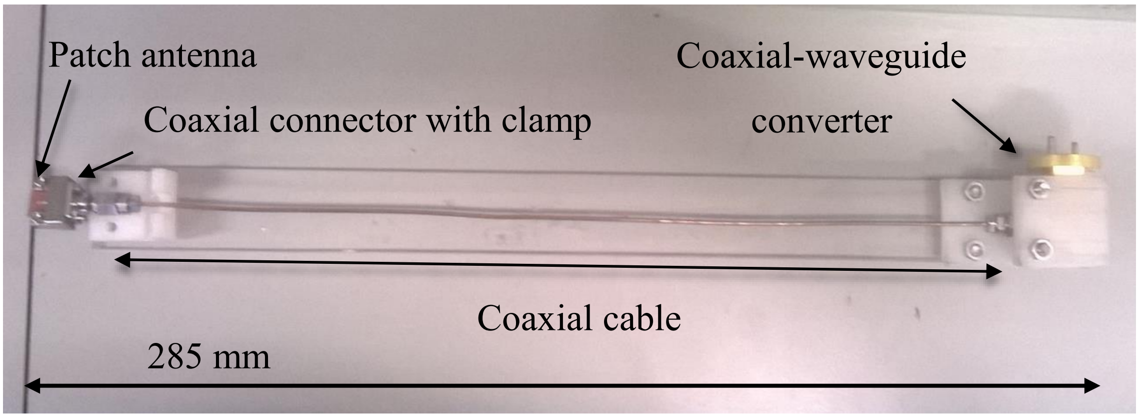

Figure 4-21: Inset patch antenna connected to feeding apparatus. The entire length was required in order to connect the 1 mm coaxial connector to the coaxial-waveguide converter.

4.5.3 Measurement of inset patch antenna

The “inset2” antenna (see **Figure 4-20** for photo of device) was set-up as shown in the following figure (**Figure 4-22**). A coaxial cable and support structure were used in this measurement (**Figure 4-21**). In order to examine the farfield of the device, a WR10 H-mode bend waveguide was used to orientate the support structure. A detailed explanation of this equipment is provided in **Section 4.2**.

The long length of coaxial cable used placed further restrictions on where the antenna could be physically placed. Additionally, the source port was connected to the VNA using short wires on the frequency extension heads and so there were physical limits to where this port could be placed. In this configuration, the probe was aligned with the front of the inset patch antenna and the antenna was 50 mm away from the circular waveguide probe detector.

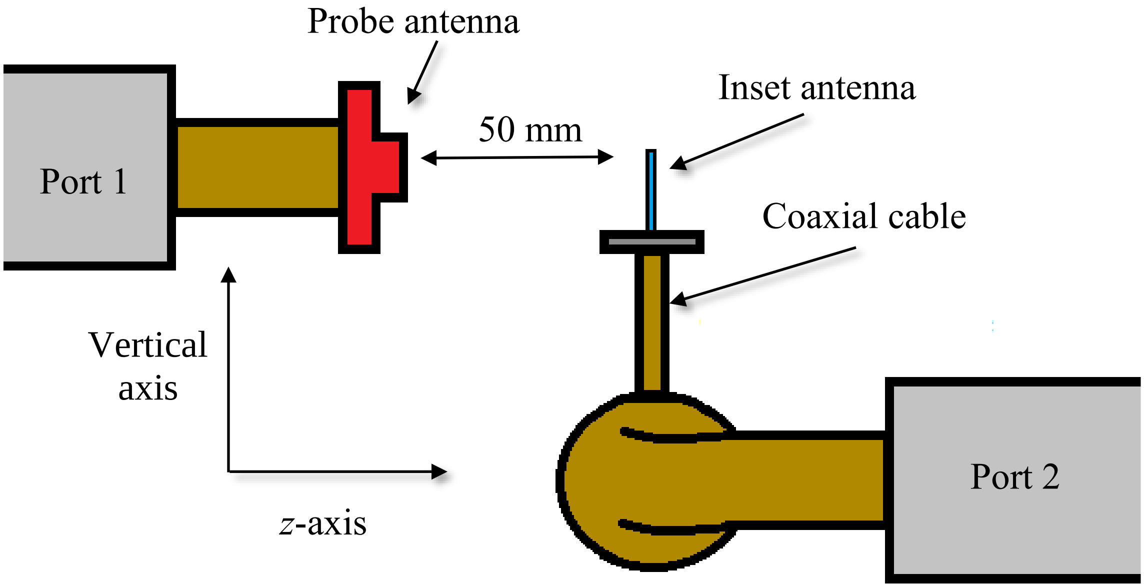

Figure 4-22: Sketch of experimental setup viewed from side. Port 2 was connected through several connectors to the antenna and was referred to as the "source port". A circular waveguide probe was placed on port 1 (referred to as the "detector port"), which was placed on the scanning rig.

The VNA was calibrated using the UOSM method (see **Section 2.8** for details on calibration). The farfield pattern of the inset antenna was scanned from -80 mm to 80 mm along both axes. The distance between the probe and the antenna was 50 mm. The following figures (**Figure 4-23a b** and **c**) detail the results of this measurement.

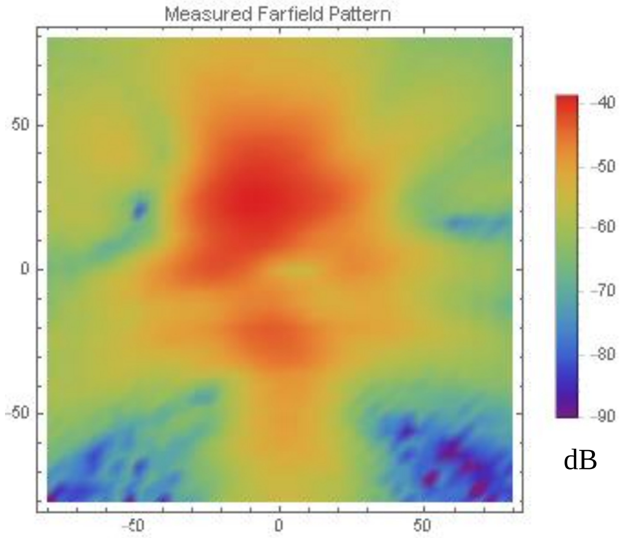

Figure 4-23a: Measured farfield pattern (S_{21}) of antenna at 80 GHz.

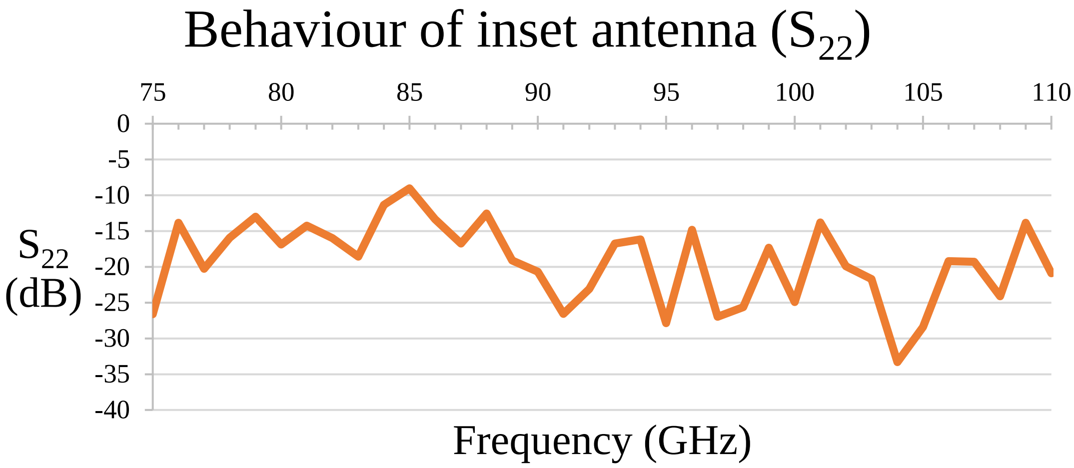

Figure 4-23b: S_{22} parameters of inset2 over the W Band.

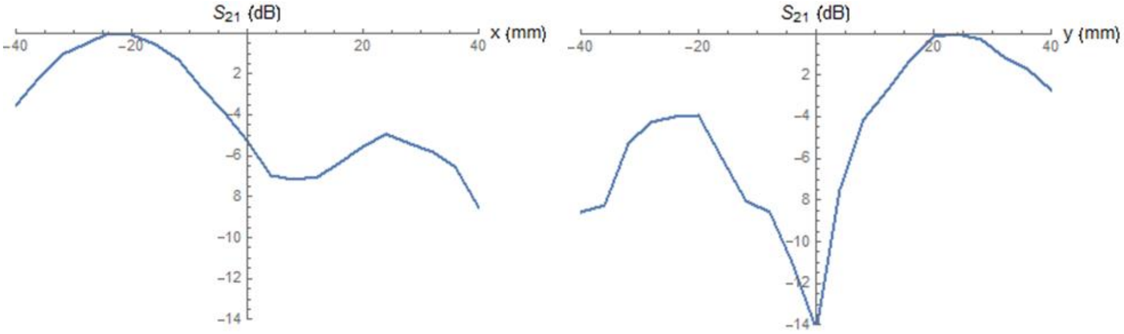

Figure 4-23c: Comparison of the antenna along the horizontal (left) and vertical (right) axis.

Figure 4-23a shows the maximum S_{21} detected was -38.7 dB. The beam of the antenna was asymmetric and split into two distinct regions around the centre of the scanned region. The beam was not propagating along the correct direction. The S_{22} parameter was low overall for this device **Figure 4-23b**. The horizontal axis cut (**Figure 4-23c** left) showed that the beam was 5 dB larger off-axis than on-axis. The vertical axis (**Figure 4-23c** right) showed a minimum value at the centre which was 12 dB weaker than the off-axis point. The large off axis measurements indicate that the beam was not aligned with the probe. These off-axis peaks reach a maximum at around 20 mm from the centre. The distances involved were too large to be due to alignment issues, instead the issue must be with the antenna's radiation pattern.

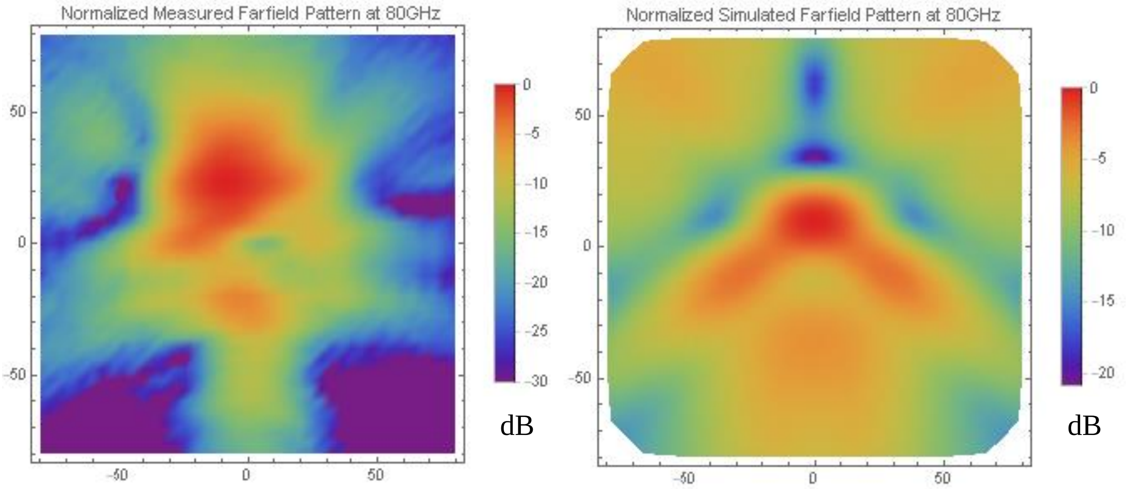

Figure 4-24: Comparison of normalized measured farfield (left) to the normalized simulated farfield (right) at 80 GHz.

The main lobe of the beam (shown in **Figure 4-24**) was located in a circle with a radius of roughly 20 mm centred at roughly at the position (-10 mm, 25 mm). The beam was radiating beam at some angle to the desired axis of propagation. The problem with this beam pattern was that the direction of the main lobe of the beam was off-centre and the centre beam was split into a stronger main beam above the centre and a weaker beam below the centre. Several issues were likely to contribute to the discrepancy – the loss in the coaxial cable leading to mismatch and standing waves between the antenna and feed and manufacture tolerances.

A new board with a dielectric thickness of 0.125 mm was sourced, which should facilitate devices to radiate at W band frequencies more efficiently. The following subsection details the development of this device on this new board.

4.6 Thin dielectric inset patch antenna

The inset antenna design described previously (**Section 4.5**) was reworked to operate on this new thinner board and will be referred to as the “thin dielectric patch antenna” (see **Figure 4-25**). One major difference in the design of this antenna was this longer microstrip that was added to reduce the influence of the clamp portion of the coaxial connector on the antenna radiation pattern.

One concern about this 0.125 mm commercial board was that the board didn’t have a photoresist layer and there was no way of applying a photoresist layer with consistent thickness within the Experimental Physics Department. However, the Electronic Engineering Department manufactured the antenna by milling the patch shape mechanically. Simulations performed in CST and then measurements of the device are described in this subsection.

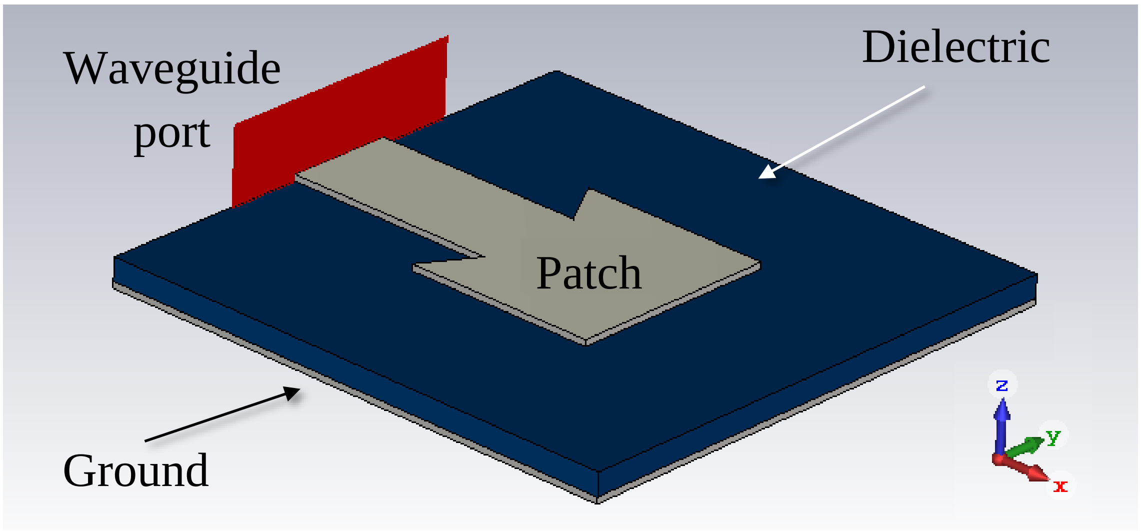

Figure 4-25: Inset patch antenna on thin (0.125 mm) PCB as viewed in CST.

4.6.1 Simulations of thin dielectric side-fed patch antenna

A series of simulations were completed in CST in order to determine the best parameters for a patch antenna. A series of simulations were performed in order to achieve a device with good radiation characteristics as detailed in the following figures.

Parameters	Value	Parameters	Value
Angle of inset	55°	Microstrip length	11 mm
Board length	6 mm	Microstrip width	0.3 mm
Board width	13 mm	Patch length	0.9 mm
Ground thickness	0.035 mm	Patch width	1.2 mm
Inset length	0.3 mm	Substrate height	0.125 mm

Table 4-8: Parameters of the designed patch antenna. A diagram of the patch as seen in CST is shown in **Figure 4-25**.

The microstrip needed to be at least 0.3 mm wide in to allow good contact physically to connect the microstrip to the coaxial connector. The microstrip length was initially set to 10 mm as from the previous tests it was observed that this length needed to be significantly longer in order to extend the patch location on the dielectric, so the patch antenna radiation pattern was removed as much as possible from the influence of the surrounding clamp of the coaxial connector.

This patch was altered in order to optimise the device to operate at 100 GHz. **Figure 4-26a → d** shows the behaviour of the antenna at W band frequencies.

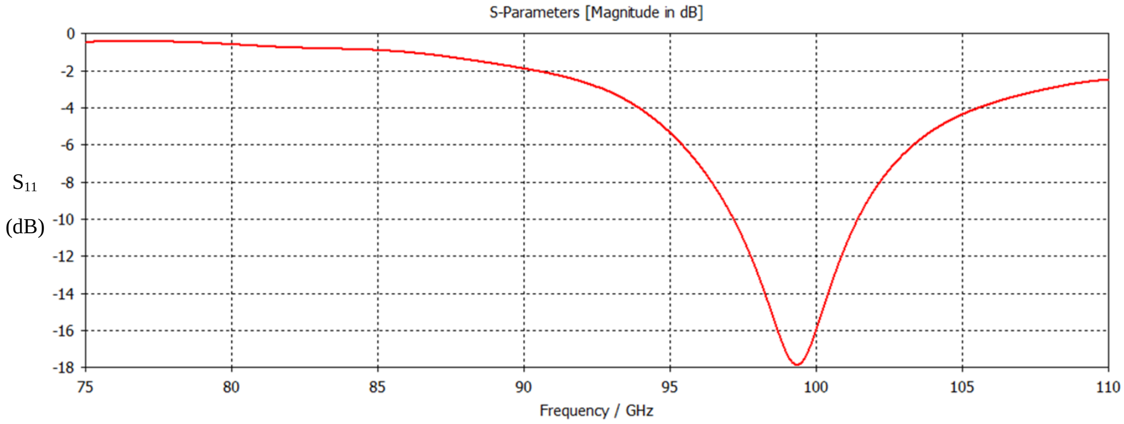

Figure 4-26a: Expected S_{11} of thin dielectric patch antenna from simulation.

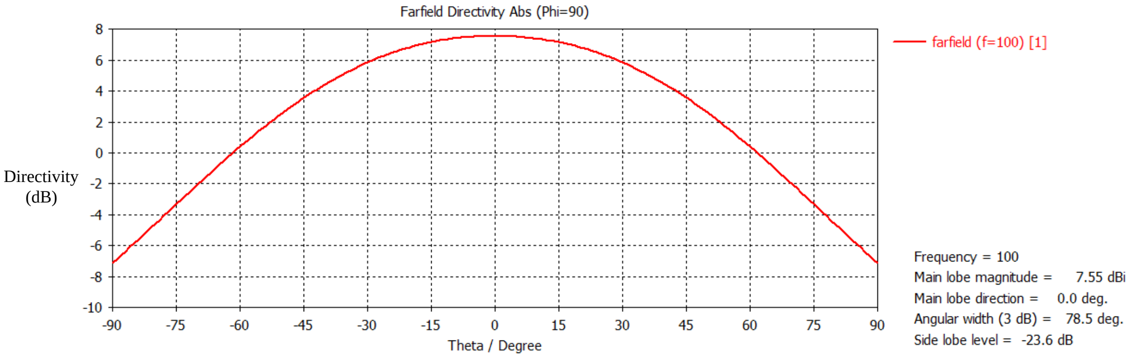

Figure 4-26b: Expected farfield pattern along φ =90° at 100 GHz from simulation.

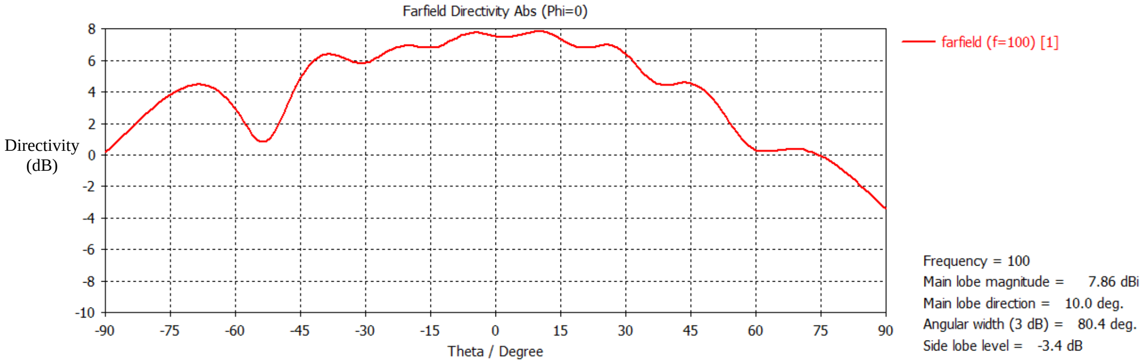

Figure 4-26c: Expected farfield pattern along φ = 0° at 100 GHz from simulation.

Figure 4-26a shows that the resonant frequency of the antenna (frequency of minimum S_{11} parameter) occur at roughly 99 GHz. The S_{11} parameter remains below -10 dB from 97 → 101 GHz, which was a large enough bandwidth to test the performance in the VNA. **Figure 4-26b** shows the farfield reached a maximum of 7.55 dBi at the centre of the main beam and has a typical Gaussian-like pattern.

The expected farfield patterns along both the φ = 90° and φ = 0° were shown in **Figure 4-26b** and **Figure 4-26c** respectfully. Along the φ = 90° axis, the farfield had the desired characteristics. However, along the φ = 0° axis, the farfield pattern was broader with irregular shape. The maximum directivity along this axis was larger (7.86 dBi) than along the orthogonal axis (7.55

dBi). This indicates that the beam was not propagating exactly parallel to the *z*-axis. The 3-D plot (**Figure 4-26d**) more clearly shows the orientation of the farfield pattern.

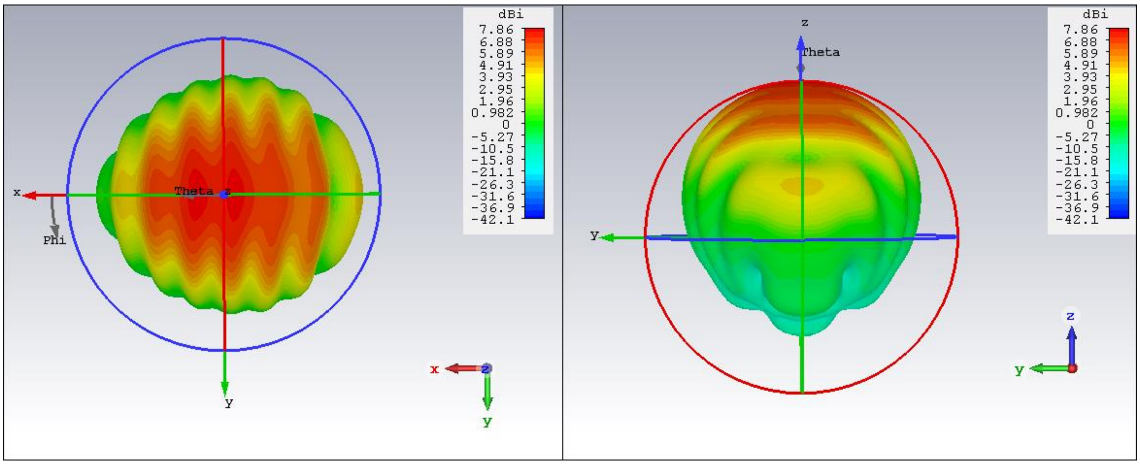

Figure 4-26e: Normalized farfield pattern from CST for the thin dielectric patch antenna at 100 GHz.

Figure 4-26d shows that the beam has several peaks or "ripples" present in the pattern on the order of 2 dB in magnitude. The beam did not have ideal characteristics, but was broadly propagating in the correct direction.

The expected farfield pattern was not ideal, but it did radiate in the correct direction. This effect was possibly due to the influence of the microstrip. The microstrip length was altered from 4 mm → 8 mm to see if the farfield was altered. It should be noted however, that simulations ignored the effect of the clamp of the 1 mm coaxial connector.

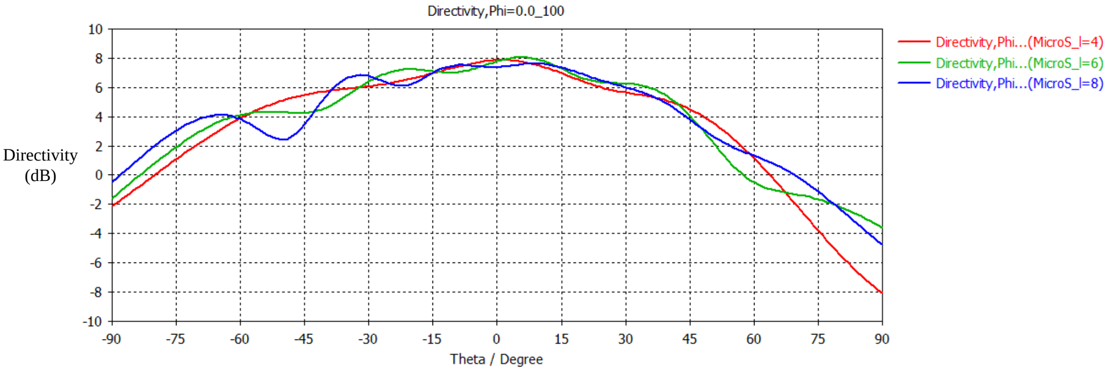

Figure 4-27a: Effect on the farfield as the microstrip length (listed as "MicroS_l" in graph) was altered.

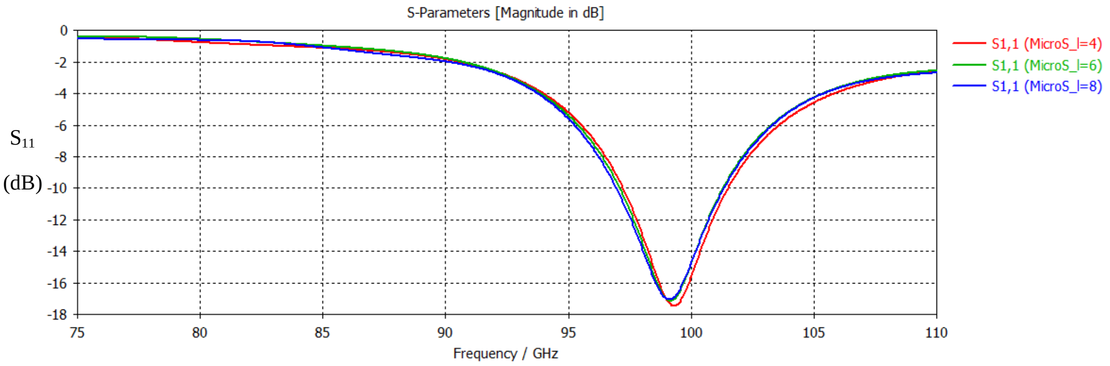

Figure 4-27b: Effect on S_{11} parameter as the microstrip length (listed as "MicroS_l" in graph) was altered.

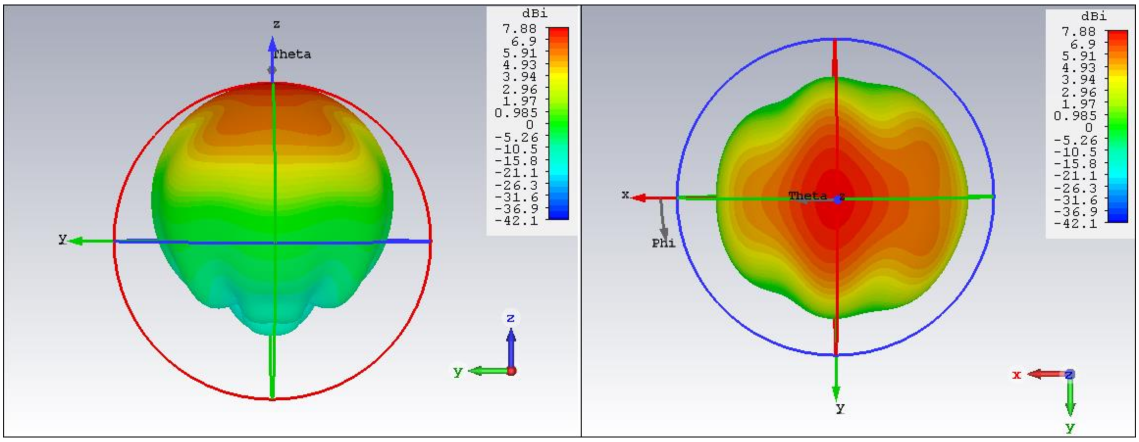

Figure 4-27c: 3-D farfield pattern of antenna fed a signal via a 4 mm long microstrip.

As **Figure 4-27a** shows, when the microstrip was long, a series of peaks, i.e. a ripple pattern, appeared in the farfield pattern. When the microstrip was small (MicroS_1 = 4 mm), the pattern rises to a peak and then decreases. As the length becomes larger more peaks appear in the farfield pattern. The return loss was almost unaffected by the change in the microstrips length (**Figure 4-27b**). The antennas with a smaller microstrip appear to perform better as shown for the antenna fed with a 4 mm microstrip in **Figure 4-27c**. There was no ripple pattern observed in this antenna. However, the previous simulations have ignored the effect of the clamp. The clamp was attached to the inset antenna of different microstrip lengths in order to determine the clamps influence.

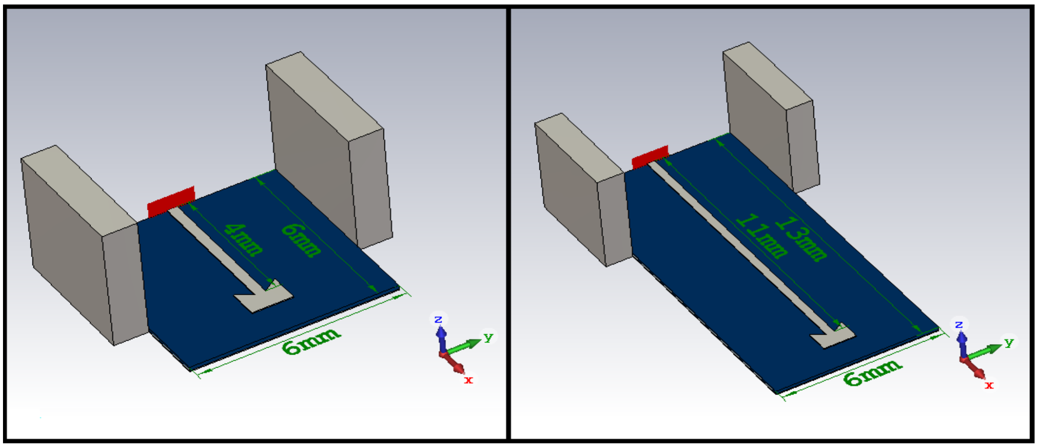

Figure 4-28a: Inset antenna and clamp with a 4 mm (left) and a 11 mm (right) long microstrip.

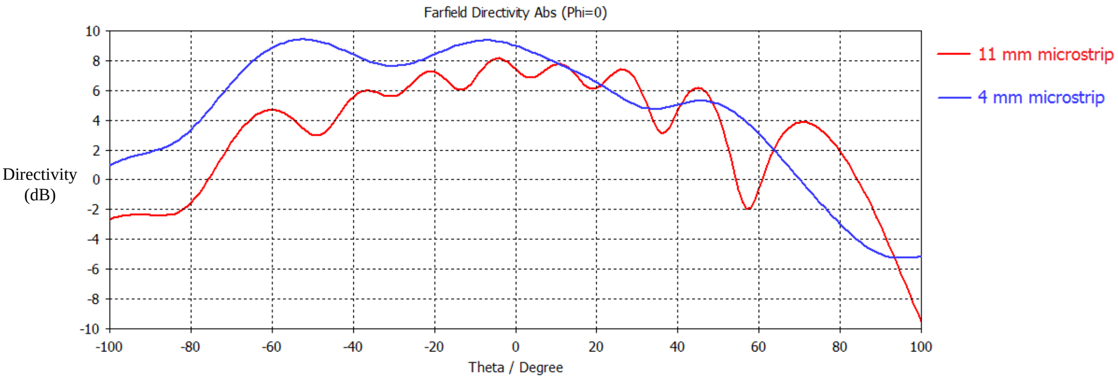

Figure 4-28b: Comparison of the farfield pattern between two antennas with different microstrip lengths, when the influence of the clamp is included.

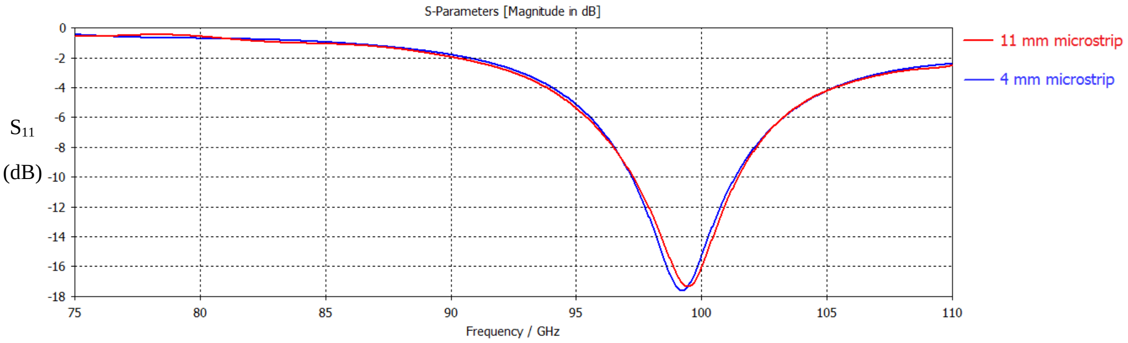

Figure 4-28c: Comparison of S_{11} parameter between two antennas with different microstrip lengths, when the influence of the clamp is included.

Figure 4-28b shows that the antenna with a shorter microstrip did not radiate on-axis. The antenna with a long microstrip contained a series of ripples, but was preferred as the beam radiates on-axis. An antenna with a shorter microstrip would perform better but, due to the clamp present, its performance decreased. The different microstrip lengths had an only slight effect on the S_{11} parameter of the antenna **Figure 4-28c**.

The inset patch antenna (the long microstrip antenna) described in **Figure 4-26** was manufactured. The device was inserted into the 1 mm coaxial connector as shown in **Figure 4-29**. The tests performed on this device are detailed in the following subsection.

4.6.2 Measurement of thin dielectric patch antenna

The VNA was used to measure the S-parameters of the antenna. The thin dielectric patch antenna was set up as previously shown in **Figure 4-22**. Again, the antenna was 50 mm away from the circular waveguide probe detector. Particular care needed to be taken when moving this antenna as it easily bends out of shape as the dielectric sheet was so thin – literally paper thin.

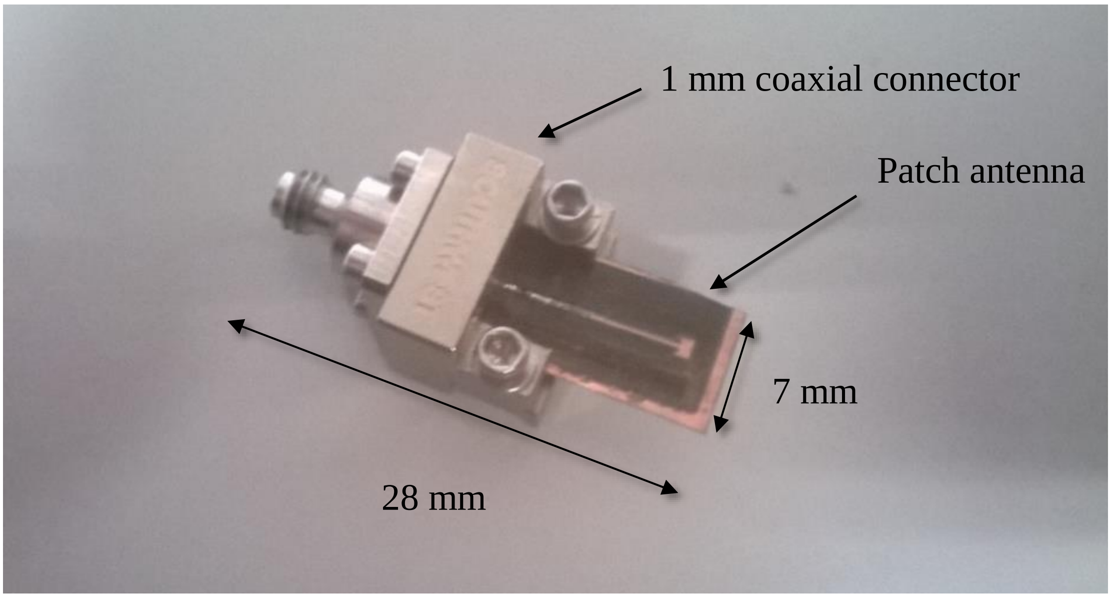

Figure 4-29: Thin dielectric patch antenna, connected to clamp. The simulations of this device are shown in **Figure 4-26**. The device was created using the milling technique which was performed by the Electronic Engineering Department in Maynooth University.

The S-parameters of the thin dielectric patch antenna were measured in the VNA. The following figures summarise the behaviour of the manufactured device.

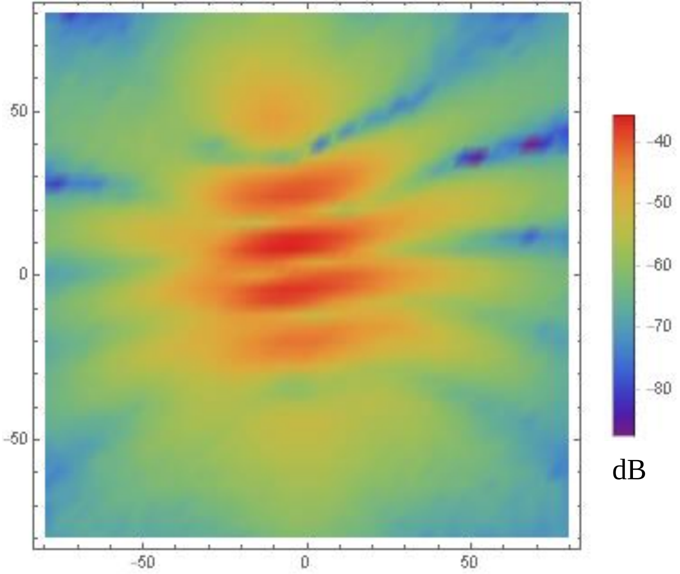
Measured S_{21} parameter from VNA

Figure 4-30: Measured farfield pattern of the thin dielectric antenna at 100 GHz, retrieved from VNA scan. The scan extends from -80 mm to 80 mm along both axes.

The maximum S_{21} parameter of the thin patch shown in **Figure 4-30** was -37.8 dB. The measured farfield radiates in the correct direction, though the “ripple” pattern expected from the CST simulation (**Figure 4-26e**) was more noticeable in this measurement. The coaxial cable or the clamp connection could be the source of the difference and the lack of calibration of the coaxial attachments remains an issue in discussing the agreement between measurement and simulation.

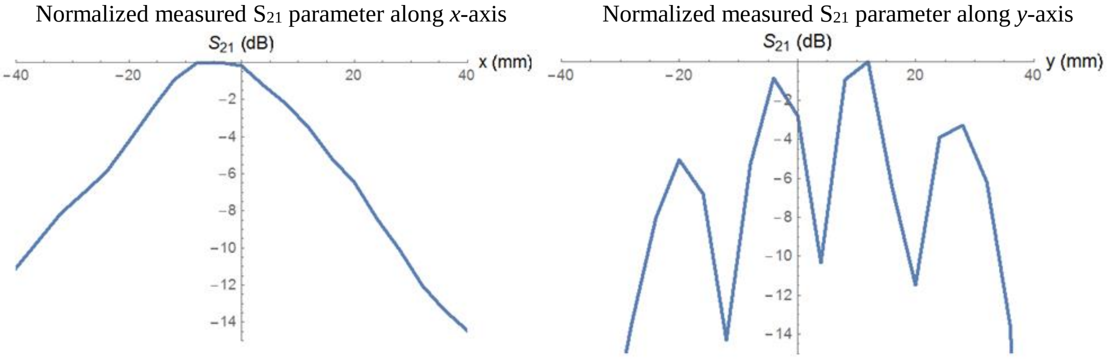
Normalized measured S_{21} parameter along *x*-axis

Normalized measured S_{21} parameter along *y*-axis

Figure 4-31: Comparison of the antenna along the horizontal (left) and vertical (right) axis.

The cross-section along the *x*-axis from **Figure 4-31** shows a directive beam, with low side lobes. However, the cross-section along the *y*-axis showed a pattern that was skewed to the right with a series of peaks. This ripple effect was also observed at other frequencies, which the following figures (**Figure 4-32a, b, c** and **d**) demonstrate.

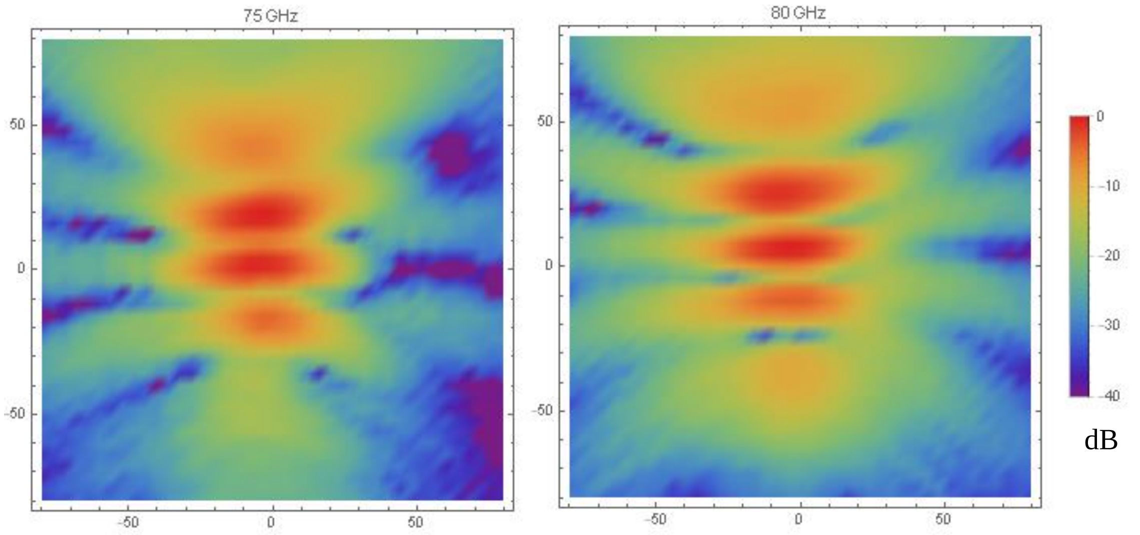

Figure 4-32a: Farfield pattern of thin dielectric antenna at 75 GHz (left) and 80 GHz (right).

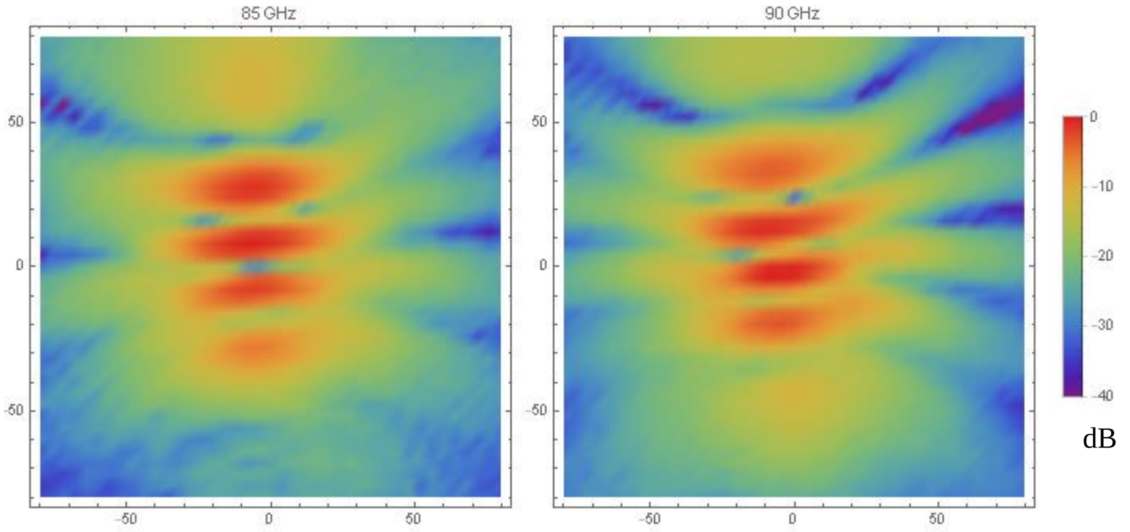

Figure 4-32b: Farfield pattern of thin dielectric antenna at 85 GHz (left) and 90 GHz (right).

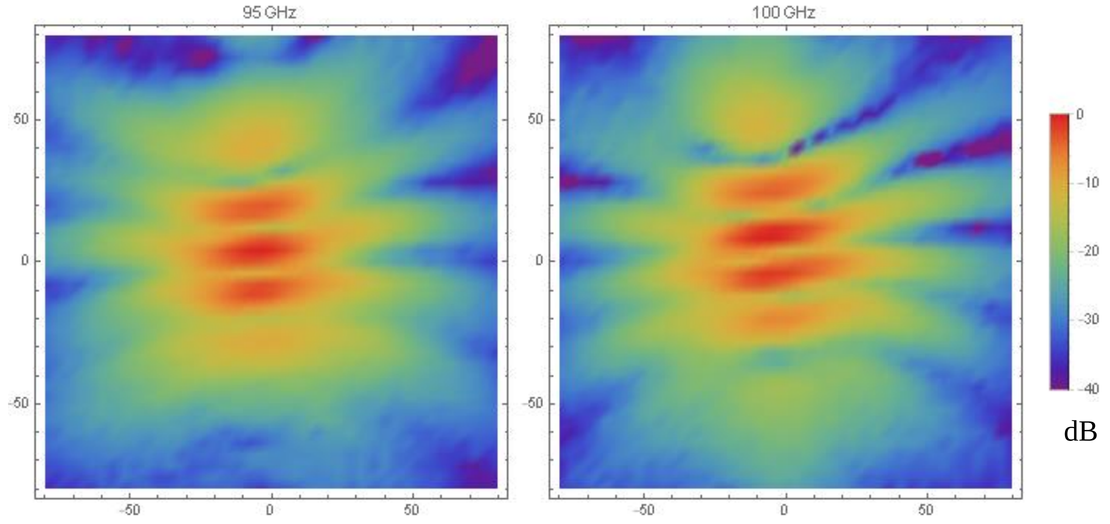

Figure 4-32c: Farfield pattern of thin dielectric antenna at 95 GHz (left) and 100 GHz (right).

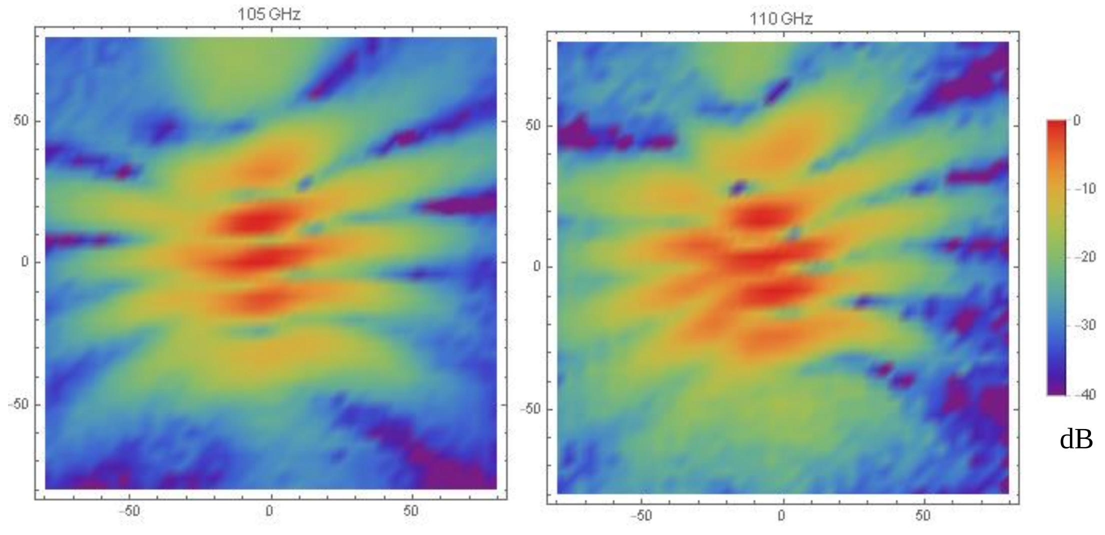

Figure 4-32d: Farfield pattern of thin dielectric antenna at 105 GHz (left) and 110 GHz (right).

Each of the farfield patterns shown in **Figure 4-32** had the same "ripple" pattern, however the exact ripple varied significantly by frequency.

The following figures show a comparison of the measured results to the simulation results. The S-parameter measured were compared to the expected values from the simulation.

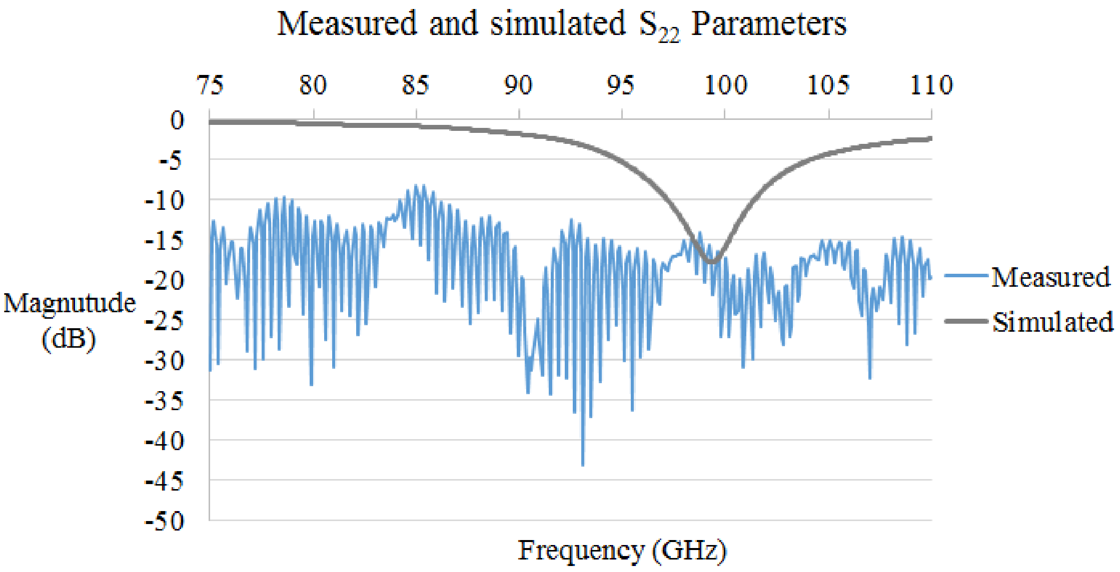

Figure 4-33: Comparison of measured and simulated S_{22} parameters. The S_{22} parameter was the return loss as the device was on port 2.

There was a large mismatch between the measured and simulated S_{22} parameters in **Figure 4-33** (equivalent to S_{11} as described elsewhere). The S_{22} parameter measured were significantly lower than what was predicted from the CST simulation and the dip at 100 GHz was not observed, as the lower levels were associated with loss in the coaxial connections.

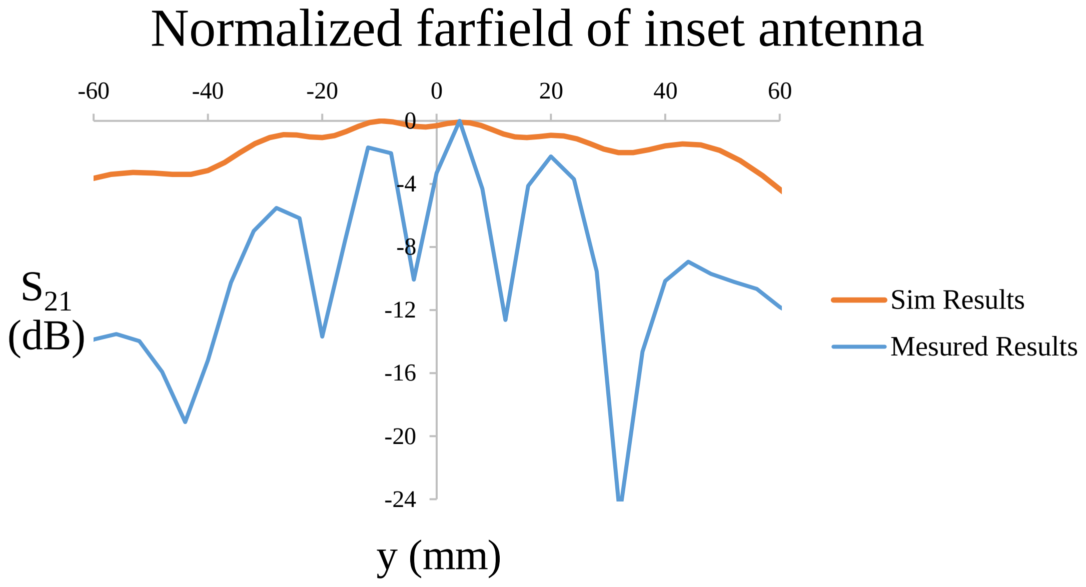

Figure 4-34a: Normalized cross-sections of real and simulated farfield patterns along the *y*-axis at 100 GHz.

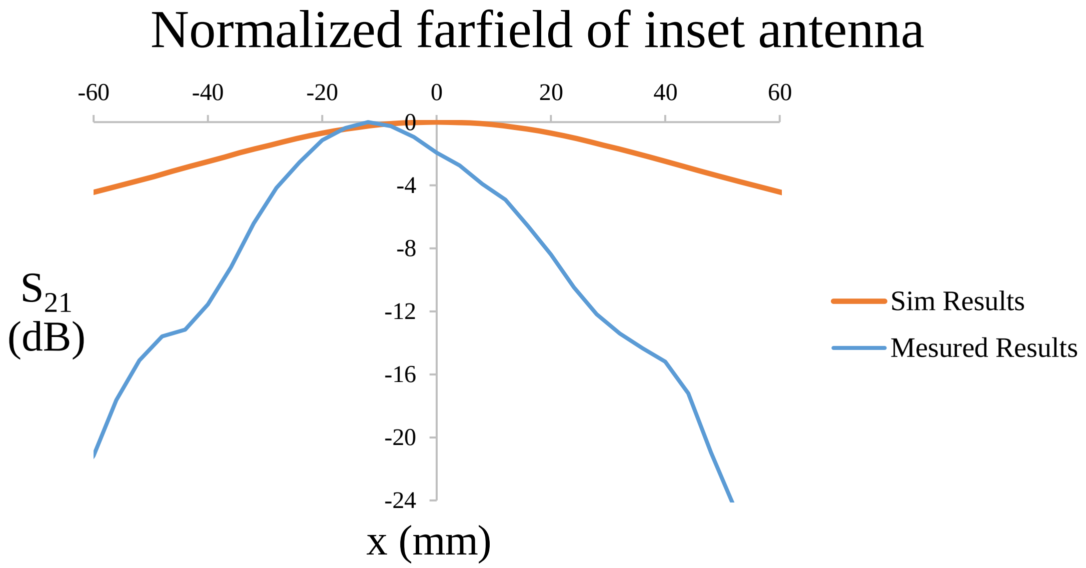

Figure 4-34b: Normalized cross-sections of real and simulated farfield patterns along *x*-axis at 100 GHz.

There was a difference between the simulated results with the measured results (**Figure 4-34**). The cut along the *y*-axis showed the beam consists of several ripples, with a relatively faint signal detected between each band. The *x*-axis cut did not show the ripple structure observed along the *y*-axis. Some ripple in the farfield pattern of the antenna was expected, but not as large as what was observed.

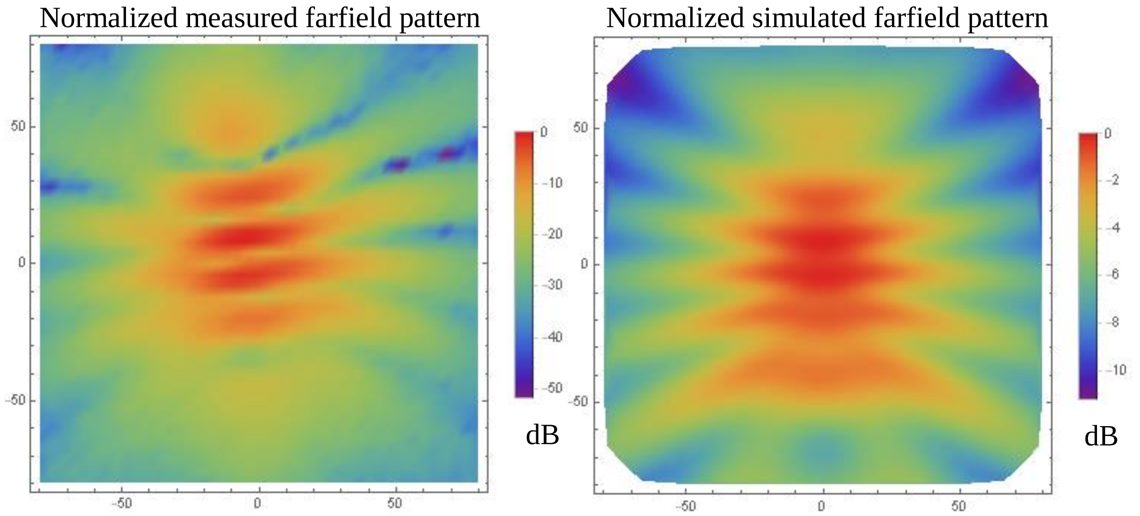
Normalized measured farfield pattern

Normalized simulated farfield pattern

Figure 4-35: Normalized measured farfield pattern (left) and expected farfield pattern from CST (right) of thin dielectric patch antenna at 100 GHz. The scan extends from -80 mm to 80 mm along both axes.

The normalized 2-D farfield pattern (**Figure 4-35**) showed the antenna radiates in the expected direction, with a similar pattern. However, the band structure along the *y*-axis was more pronounced in the measured result than was expected.

The farfield pattern of the antenna deviates from the expected farfield pattern found in CST. The measured farfield pattern was consistent with interference. The ripples were thought to be due to microstrip length, as **Figure 4-27** showed, as he ripples were along the *y*-axis, which was the same direction the microstrip feeds travel. The ripples or peaks were larger than expected in the measurements and there could also be loss or mismatch caused by a coaxial connection and cable coupling mismatch. Also, the influence of the convolution of the probe pattern in measuring the farfield pattern is not accounted for in the CST simulations.

The probe was placed at several different distances, *z*, from the antenna. to investigate if the ripples could be caused by standing waves or reflections between the probe and radiating antenna. The ripple amplitude should reduce as distance increases if that was the case.

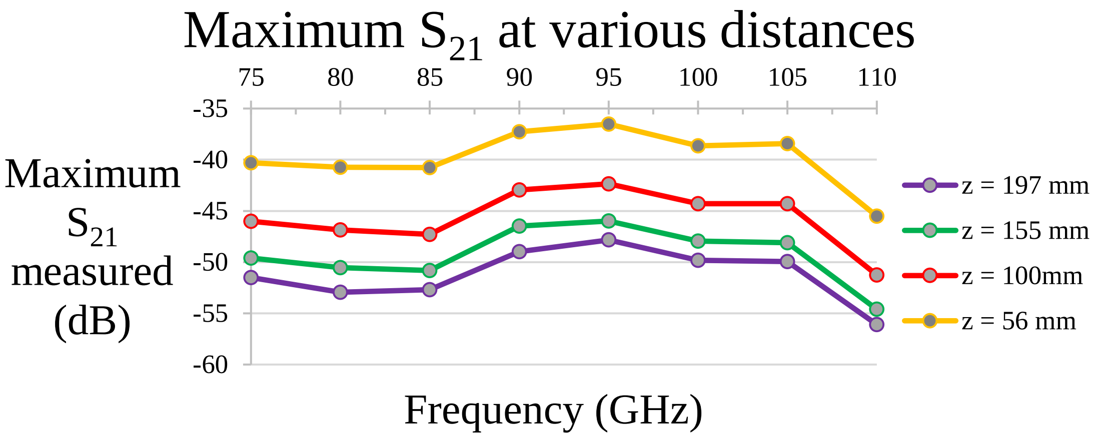

Figure 4-36a: Maximum S_{21} parameter detected at each scan distance.

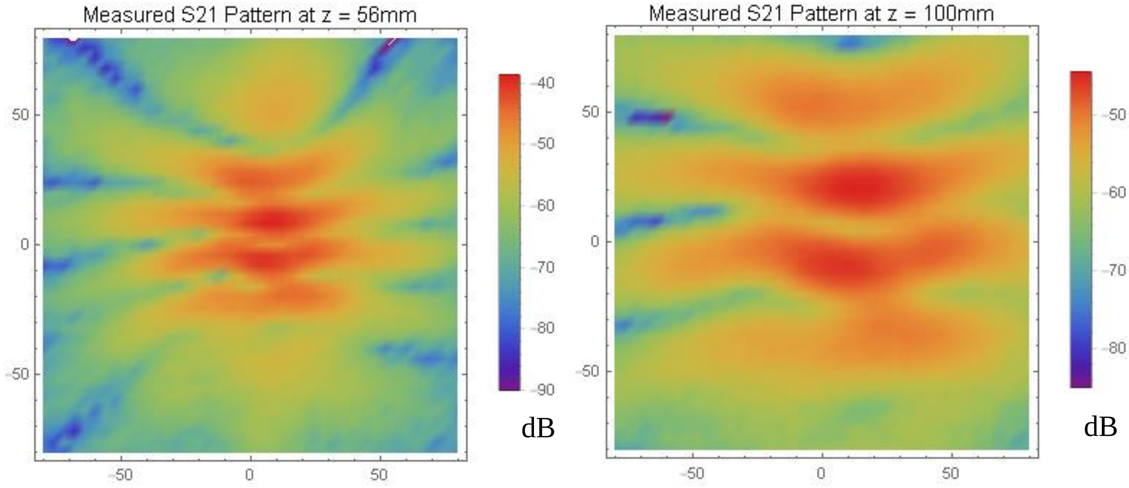

Figure 4-36b: Thin dielectric patch antenna measured at 56 mm and 100 mm.

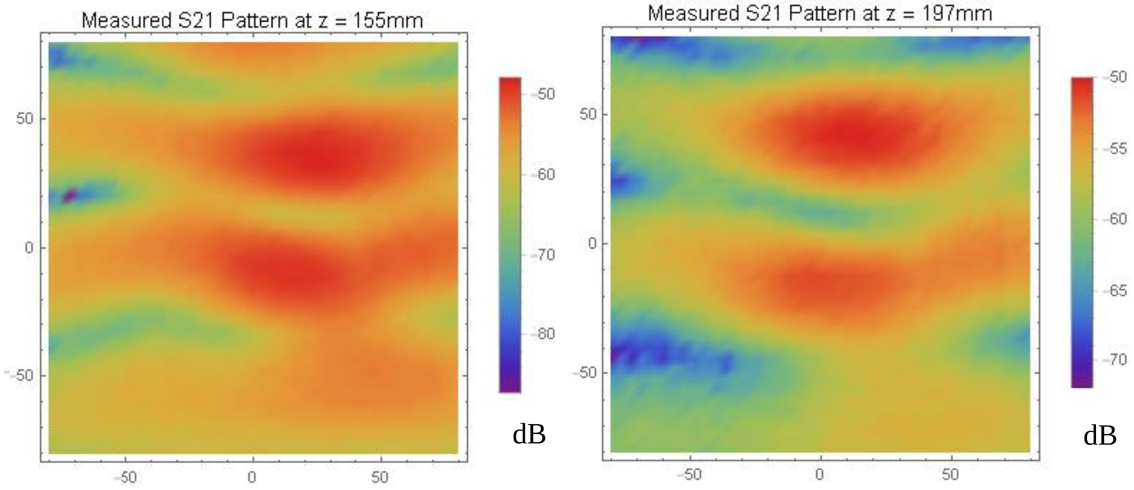

Figure 4-36c: Thin dielectric patch antenna measured at 155 mm and 197 mm. Different patterns were observed at each distance as the beam had more time to spread out.

The antenna behaves the same at each distance shown in **Figure 4-36a**, which would indicate that the ripple was not entirely caused by reflections. The ripple pattern appears in all four scans in **Figure 4-36b** and **c**, which implies that the ripple effect was an inherent property of the antenna. The measured return loss was consistently below the expected from the CST simulations (**Figure 4-33**). One possible cause of this difference was losses in the coaxial cable and waveguide to coaxial connector, which could not be calibrated out of the measurement due to no calibration kit being available.

4.7 Conclusion

The aim of the simulations was to create a side-fed patch antenna capable of transmitting a signal effectively at W band frequencies. The antennas were chosen based on their ability to create a beam with a large directivity, minimal side lobes and minimised S_{11} over this frequency band.

Side-fed refers to a patch antenna fed via a 1 mm coaxial cable connected to a microstrip line on the PCB. As a calibration kit was not available for the coaxial connections on the VNA, there was the potential that losses and reflected power that might dominate measurements. Loss in the coaxial chain was investigated using a simple PCB short, constructed in order to test the loss present in the 1 mm connections (waveguide-to-coaxial adaptor, 1 mm coax and connector element). There was a lower return loss measured compared to simulation, which implies loss of and reflection of power present in the system. However, without a calibration kit it wasn't possible to characterise the losses over the bandwidth.

A side-fed rectangular patch antenna was modelled in CST, however, this design suffered from a high coupling mismatch and irregular farfield beams. This simple design could be ruled out as a viable alternative and the more complex inset design was examined.

Inset patch antennas were designed on both a 0.4 mm and 0.125 mm thickness PCB in CST. The critical parameters for the design of this antenna design were the size of the patch, the size of the supporting board and the angle of the inset. No design could be found to allow the antenna to be built on the 0.4 mm board to operate effectively at 100 GHz with good farfield beam qualities. Instead, an inset patch antenna fed by a microstrip line was designed to operate at 80 GHz. The antenna did not operate over the entire W band frequency range as the dielectric in this board was too thick to allow the device to operate well at higher frequencies. The microstrip length had a large effect on the beam the antenna generated. The angle between the inset and the microstrip had a large effect on the S_{11} parameter of the antenna, but not the overall farfield pattern. The inset patch antennas were built on this board and tested with the VNA. The simulated farfield was different in shape from the farfield of the measured antenna and additionally the measured beam was radiating at some angle to the desired axis of propagation. These antennas did not perform as well as expected.

An inset patch antenna (operating at 100 GHz) was designed on the 0.125 mm PCB. The expected farfield patterns was rather broad and contains an unusual "ripple" over the main beam. The testing of the microstrip length showed that an antenna with a shorter microstrip did not have this ripple pattern. It can be concluded that the ripple pattern was due to the microstrip length connecting the antenna**.** However, the ripple was on the order of 0.5 dBi and was not expected to be a significant barrier the antennas performance. In the measured farfield pattern the ripple pattern expected from CST were more noticeable. The ripple effect was not caused by multiple reflections or standing waves in the measurement setup, as scanning the antenna's beam at different positions also generates the equivalent pattern. The antenna manufactured on the thin 0.125 mm PCB board radiates in the correct direction, but the detail of the beam shape did not agree with simulations overall. Measurements may be dominated by coaxial reflections which could not be calibrated out.

Chapter 5 Alternative planar antenna designs

5.1 Overview

As part of the development of W band devices, several alternate planar antenna designs were also developed in assessing different manufacturing and feeding options. This chapter details the design process of several alternate designs. Manufacturing difficulties and budget constraints place restraints on the type of devices that could be created as W band planar antennas. As the operating frequency increases, the physical size decreases. Antenna designs that function well at 1 GHz will need to be roughly 100 times smaller to operate at 100 GHz. Therefore, dimensions for a number of common designs were too small to realistically manufacture accurately.

The patch antennas designed, as discussed in **Chapter 3** and **Chapter 4**, were affected by the large size of the dielectric thickness relative to the wavelength between patch and ground plane and, at W band frequencies, requiring a very thin dielectric layer to operate in the traditional manner. Traditional patch antennas for lower frequencies were made with dielectric thicknesses between the antenna and ground plane of small fractions of a wavelength. Alternative antenna designs were examined which do not require this condition. The desired requirements for these alternative designs were the same as previous antennas: low return loss and large directivity.

Two of the PCBs available in the lab, the ABT18 and the 0.4 mm PCB, have a dielectric thickness which was significant fraction of the wavelength at W band. As observed previously, patch antennas constructed on these PCBs do not radiate in the forward direction. Instead the power flows perpendicular to the desired direction along the dielectric substrate due to its strong influence on the radiation pattern. One possible solution was to develop “endfire” antennas, which takes advantage of the flow of power along the dielectric substrate.

The remaining board, a 0.125 mm thick PCB, did not have a photoresist layer, so manufacturing required milling the antenna shape which was difficult. Additionally, the board could be easily bent out of shape in handling, so drilling holes in the board accurately was difficult.

Several potential designs were simulated in CST. Of these different designs, two were then manufactured and tested with the VNA. The different designs were detailed in the following sections

5.2 Design of endfire antennas

The patch antennas with a dielectric thickness of 0.8 mm tended to radiate horizontally along the dielectric as was observed in **Figure 3-16**. An antenna that radiates in this direction was referred to as an endfire antenna. An antenna was designed to maximize the directivity of the antenna along the plane of the PCB board. The antenna consists of a PCB, with one side being etched to form the planar antenna and director elements shown in **Figure 5-1**. A 0.8 mm substrate separates the etched front side of the antenna from the other side, which represents the ground plate through which the feed wire was placed.

The PCB board had dimensions of 10 mm × 10 mm. The green parts of the diagram were the exposed dielectric material, while the grey parts on the board were the copper in **Figure 5-1**. A copper wire connects the central element (3) to an input signal. The largest element (2) was soldered to ground in an attempt to force the antenna to radiate in only one preferred direction and as a result, the ground plate on the PCB was a necessary component of this design. The antenna was fed input power through the wire from the backside with this wire coupling power from the WR10 waveguide (**see Figure 3-30**). The designed device was referred to as the endfire antenna.

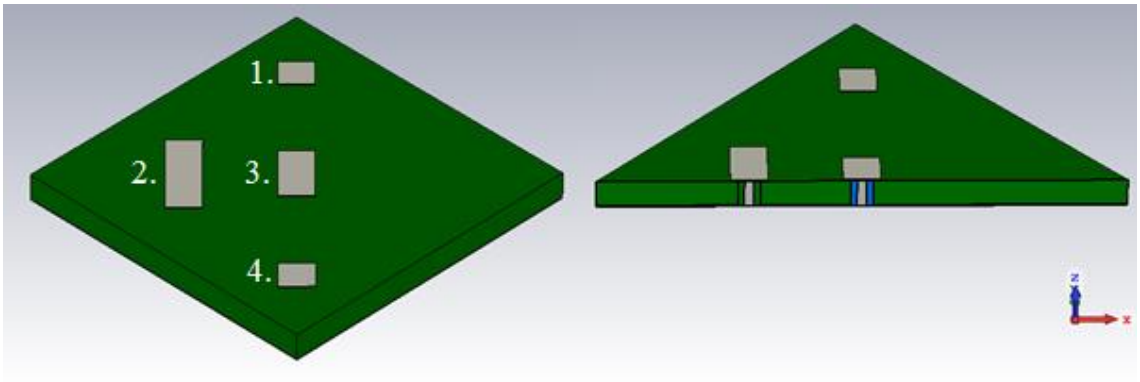

Figure 5-1a: Endfire antenna as viewed from front (left). The internal structure is shown on the right. The main direction of propagation was along the positive *x*-axis, as shown above.

The directivity of an antenna should be large this direction and low in all other directions. Due to the feeding method, only 1 of the elements in the antenna feeds power to the structure and the other elements act as directors similar to a Yagi antenna configuration.

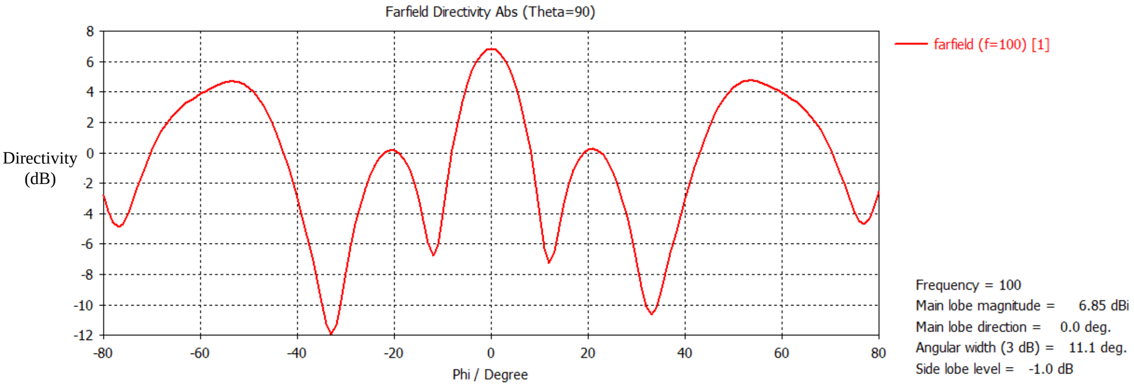

Figure 5-1b: Farfield of the endfire antenna along the horizontal axis.

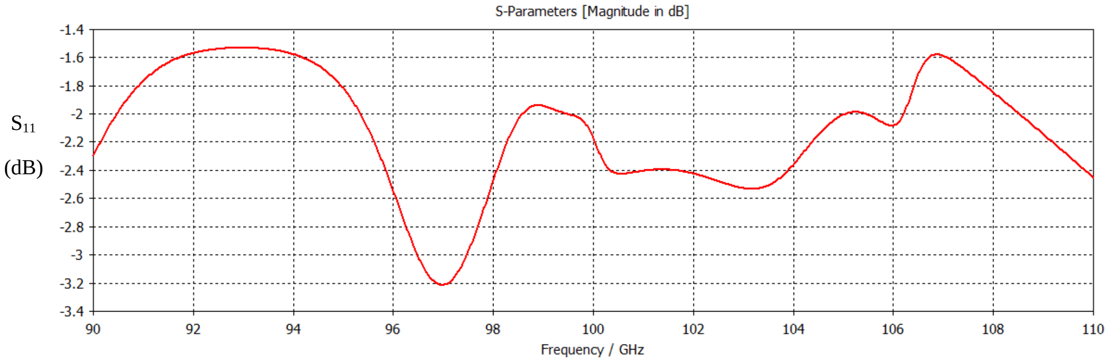

Figure 5-1c: S_{11} of endfire antenna between 90 and 110 GHz.

The antenna's farfield pattern (**Figure 5-1b**) showed a beam which was radiating strongly in several directions. The graph showed a maximum peak directivity of 6 dBi, however there were two other peaks (side lobes) present in the graph with a directivity over 4 dBi.

The S_{11} parameters of the antenna were also sub-optimal, as seen in **Figure 5-1c**. This antenna design suffers from large reflections throughout the W band frequencies. At 100 GHz, the S_{11} value was -2.2 dB, which indicates that approximately 60% of power entering the antenna will be reflected back into the device. This was the lowest possible S_{11} parameter found with this design.

The antenna was manufactured in order to test the viability of this design (see **Figure 5-2** for finished devices). The antenna shapes were etched using photolithographic techniques. A small drill was used to make a 0.3 radius hole in the centre of the middle patch (labelled patch 3 in **Figure 5-1**). A small wire with a Teflon coating was inserted into this hole. A small hole was punched in centre of the larger patch (labelled patch 2 in **Figure 5-1**). An uncoated small wire with a radius of 0.125 mm was inserted into this hole. The wires were soldered to the copper and then sandpaper was used to remove any excess material from the antenna. The electrical connections were tested using a multimeter.

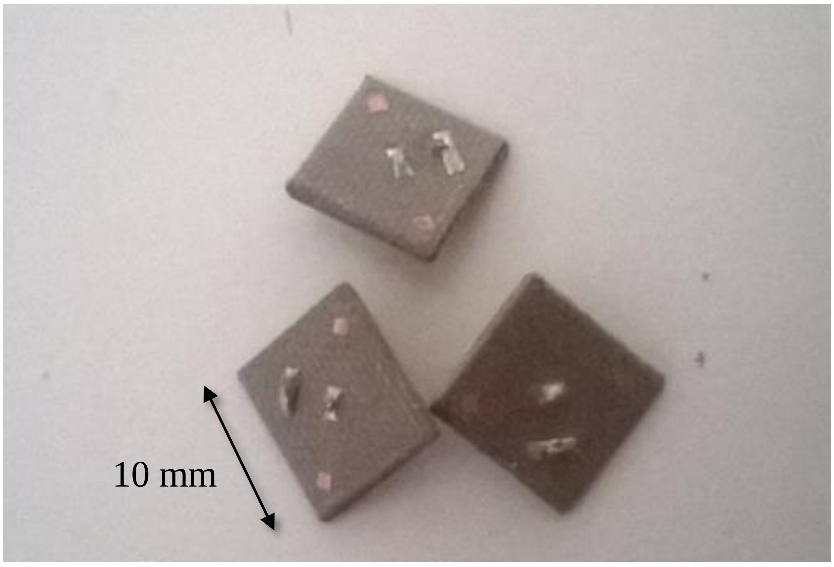

Figure 5-2: Three manufactured endfire antennas.

Of the three different endfire antennas printed on the circuit board, one was damaged in the process. The wire for this antenna did not stay in place securely after soldering. The wire from the remaining 2 antennas were placed through the hole in the modified WR10 waveguide (see **Figure 5-3**), as previously used to couple W band signal to the antenna. The two different antennas were setup in the VNA lab (configuration shown in **Figure 5-4**) and tested.

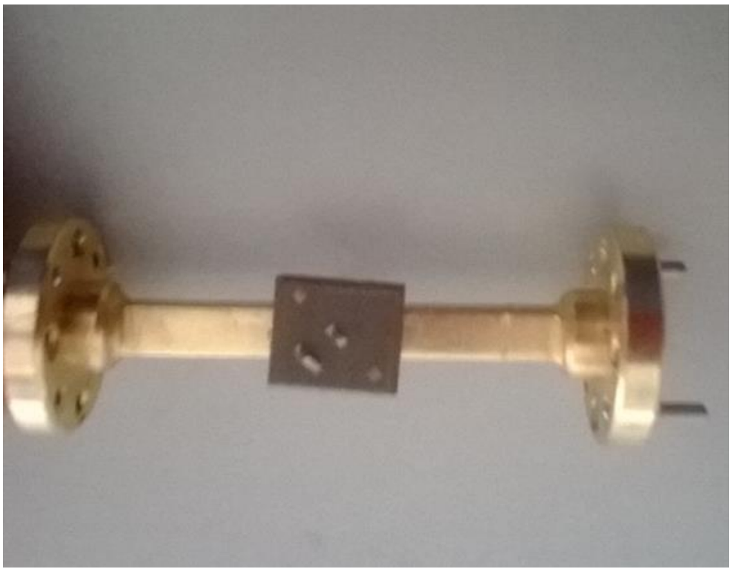

Figure 5-3: Endfire antenna mounted on modified WR10 waveguide.

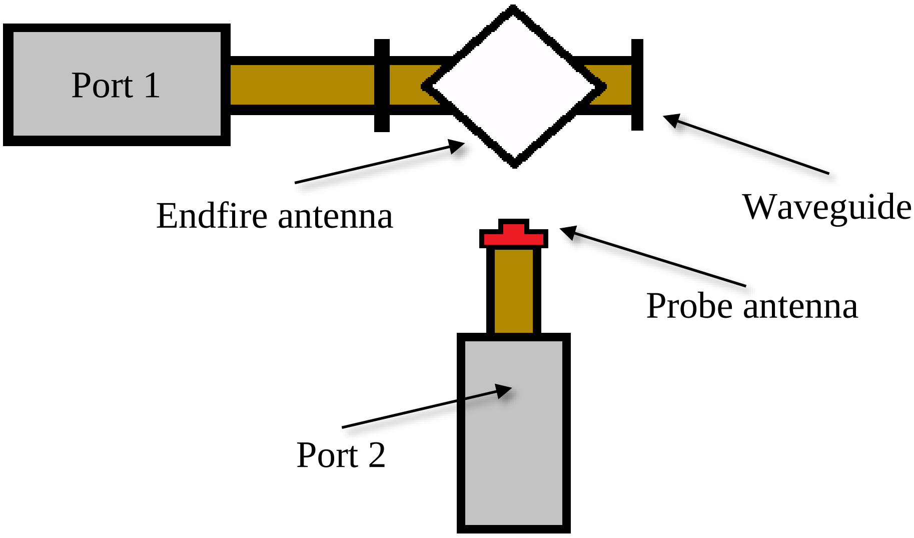

Figure 5-4: Experimental set up to measure endfire antenna. The two ports were set at 90° to each other. The modified WR10 waveguide and the endfire device were connected to port 1. A measuring probe was placed on the second port.

The antennas were tested one at a time on the WR10 waveguide. The probe was placed 10 cm from the feeding WR10 waveguide. The antenna was rotated in the WR10 waveguide until the maximum signal (S_{12}) at 100 GHz was observed. The remaining S-parameters of the antennas were recorded.

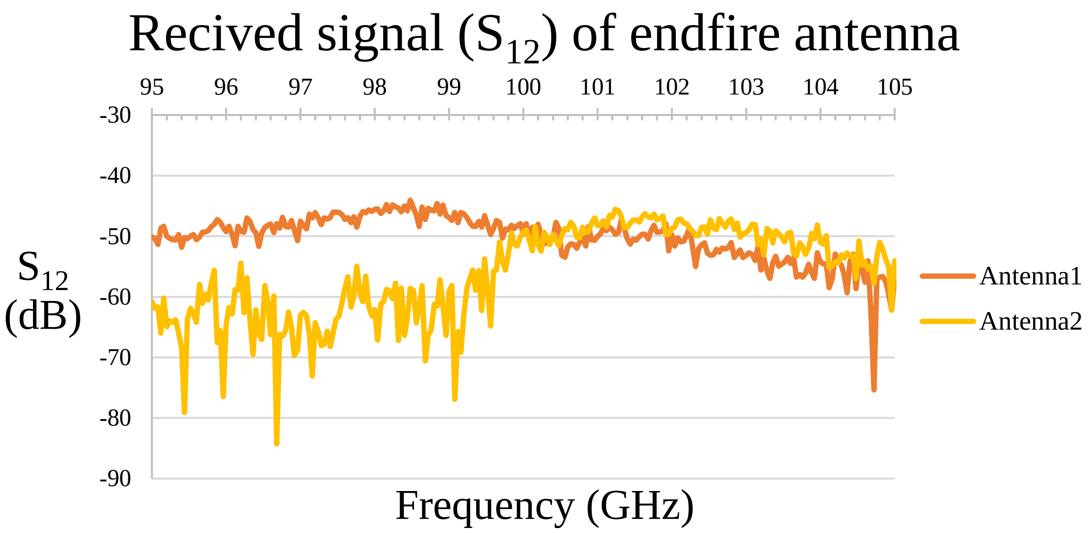

Figure 5-5a: Comparison of the S_{12} parameters between the two antennas tested.

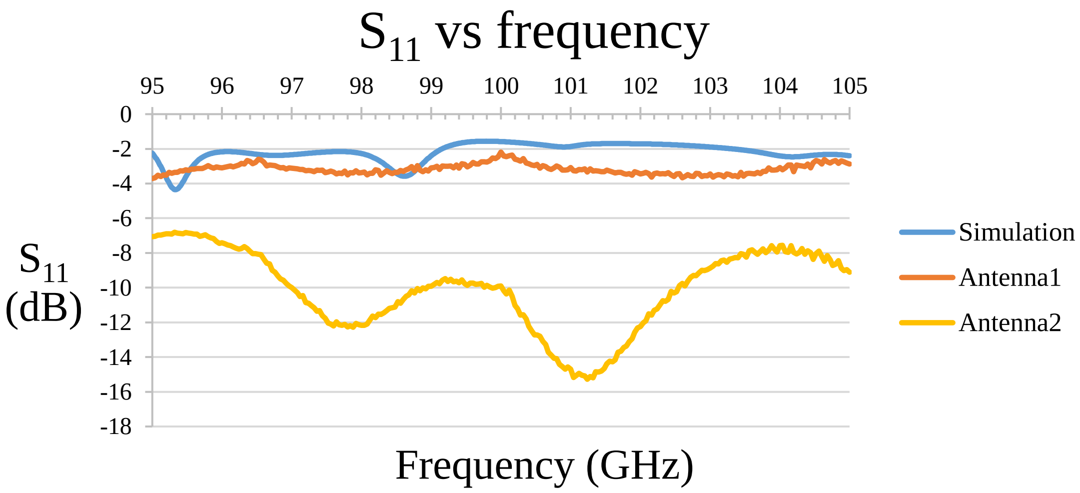

Figure 5-5b: Comparison of the S_{11} parameters of the antennas.

The first graph (**Figure 5-5a**) showed the power coupling of the two antennas over the frequency range 95 →105 GHz. Both devices show a low received signal. The received signal for the two devices should be similar, but there was a variation in the performance of the two devices.

Any S_{12} parameter below -60 dB could be considered noise, i.e. no signal was detected. Antenna 1 radiates a signal over the entire range, while antenna 2 only radiates a signal after 100 GHz.

The second graph (**Figure 5-5b**) showed the S_{11} parameter of the antennas and the expected simulation result between 95 and 105 GHz. Both antennas had a S_{11} parameter lower overall than the simulation predicted. There was also a difference in performance between the two antennas. For antenna 1, the S_{11} parameter was very large. Nowhere was the S_{11} parameter below -10 dB. Antenna 2 had a much low S_{11} parameter, which at different frequency ranges dips below -10 dB. The large difference between the two antennas was likely caused by warping of the boards during the drilling phase.

Neither antenna performs as designed. The S_{11} parameter of the antenna 2 was lower than antenna 1. However, signal from antenna 2, at frequencies below 100 GHz was equivalent to background noise. The endfire antenna was difficult to couple to the input feed wire and difficult to produce in a repeatable manner. Also, once the antenna was drilled, the shape of the radiating surface was unavoidably damaged which leads to poor reproducibility of field patterns.

5.3 Slot antenna with coaxial feed

A second antenna design was investigated, which will be referred to as a slot type antenna. This antenna design was to be constructed using the ABT18 PCB. Rather than feeding the antenna though the base, the antenna was fed from the side via a 1 mm coaxial cable. The properties of this cable have been shown previously in **Table 4-1**. In the first design incarnation, the antenna was connected directly to the end of a coaxial cable as shown in **Figure 5-6**. The plan initially was to directly connect a coaxial cable to the antenna.

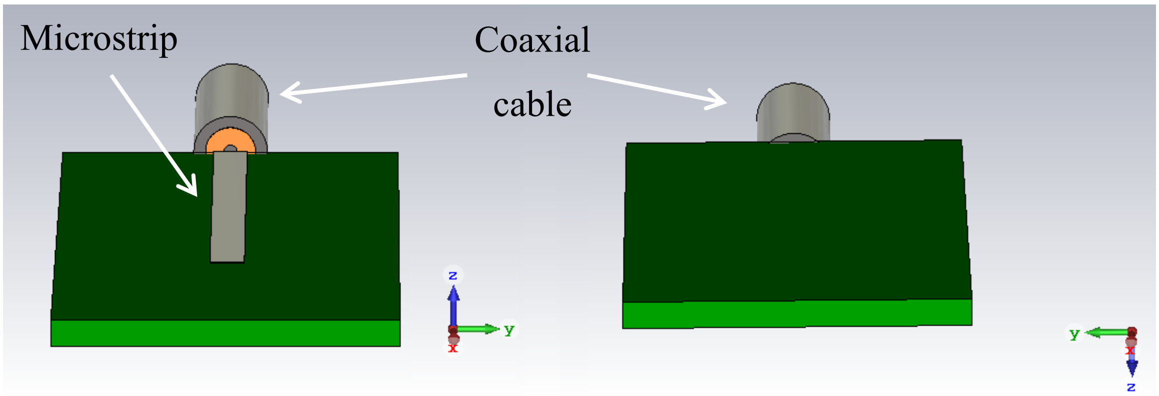

Figure 5-6: Early slot antenna design. Top view (left) and bottom view (right). The antenna went through several redesigns until a final design was chosen.

The coaxial cable was connected to the microstrip of the antenna, which was placed on top of a substrate to radiate at W band frequencies. Fundamentally, the antenna was an endfire device, which as seen in **Figure 5-6**, radiates power in the positive *x*-axis. This device was redesigned as more constrains were put in place in order to better reflect what could be created. The redesigns of this device are detailed in the following subsection, with the tests performed in the VNA detailed later in the chapter.

5.3.1 Simulation

A model of this device was setup in CST as shown in **Figure 5-6**. In CST a port was placed at the back of this cable in order to stimulate power to the structure. The cable shown in the image was 5 mm in length, however, in reality, the cable was 250 mm long (see **Figure 4-4** for image of the real cable) and the cable was reduced in size in the simulation to reduce computational overhead. It was initially planned to connect the coaxial cable directly to the antenna, via a wire similar to that on a 1 mm coaxial connector.

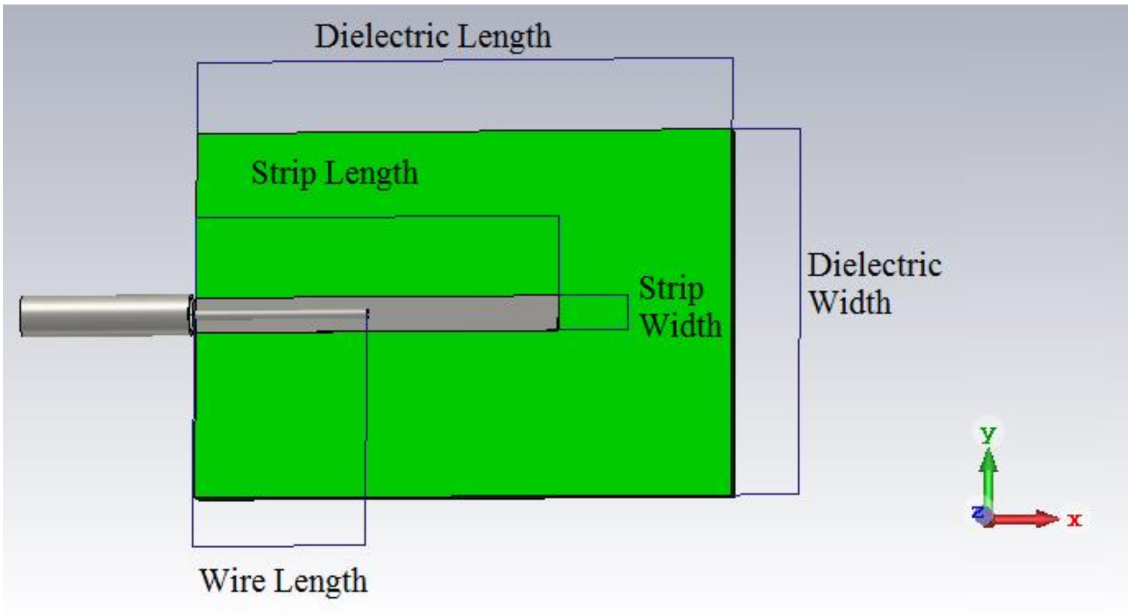

Figure 5-7a: Parameters used in design of slot antenna.

The size of the dielectric substrate, the length of the microstrip and the length of feed wire from the coaxial cable were altered. Using CST, several different parameters were varied in order to observe the performance of the device and to obtain the manufacturing tolerances required. To begin, the (*x*-axis) length of the board was altered from 5 → 10 mm in steps of 1 mm. Following on from that, the width of the board was altered from 10 →15 mm in steps of 1 mm. Additionally, the wire length was increased from 0 mm (i.e. no connection) → 5 mm. The antenna that created the most directional beam had the parameters shown in **Table 5-1**.

Antenna parameters	Value	Description
Microstrip length	10 mm	*x*-axis length of microstrip
Microstrip width	0.1 mm	*y*-axis length of microstrip
Microstrip thickness	0.035 mm	*z*-axis length of microstrip
Dielectric length	15 mm	*x*-axis length of dielectric base
Dielectric width	10 mm	*y*-axis length of dielectric base
Dielectric thickness	0.8 mm	*z*-axis length of dielectric base
Wire length	0.5 mm	Length of wire connected to microstrip
Wire radius	0.1435 mm	Radius of wire
Coaxial length	5 mm	Length of coaxial cable in the simulation

Table 5-1: Parameters used to create optimal slot antenna.

There are a few parameters that cannot be altered. The microstrip width was set to 1 mm, to allow the wire to be connected easily. The dielectric height was 0.8 mm and the microstrip thickness was 0.035 mm as the ABT18 PCB was used to create this device. The microstrip needed to be electrically connected to the coaxial cable. A small wire associated with a coax connector (see **Figure 4-3**) was available within the Experimental Physics department, with a diameter of 0.287 mm, was used to connect the microstrip to the coaxial cable.

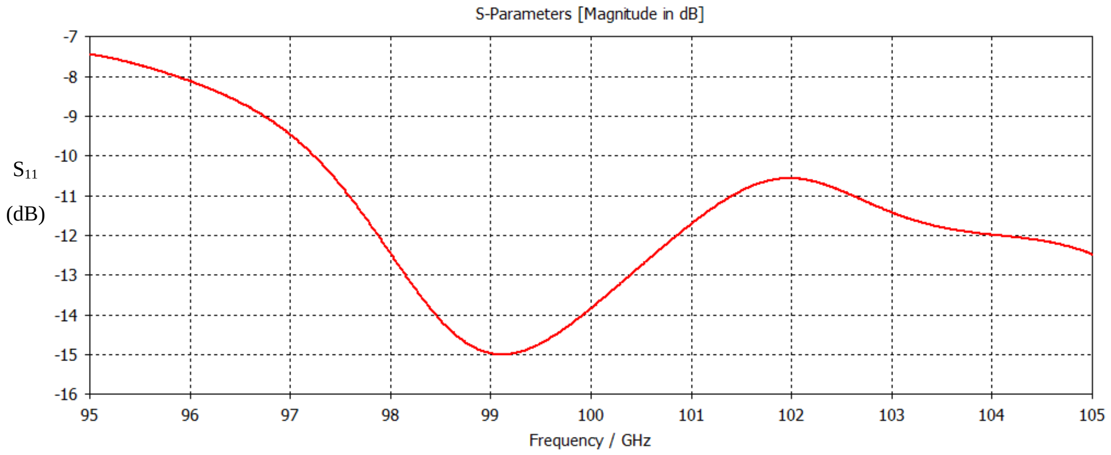

Figure 5-7b: S_{11} parameter of slot antenna fed by coaxial cable.

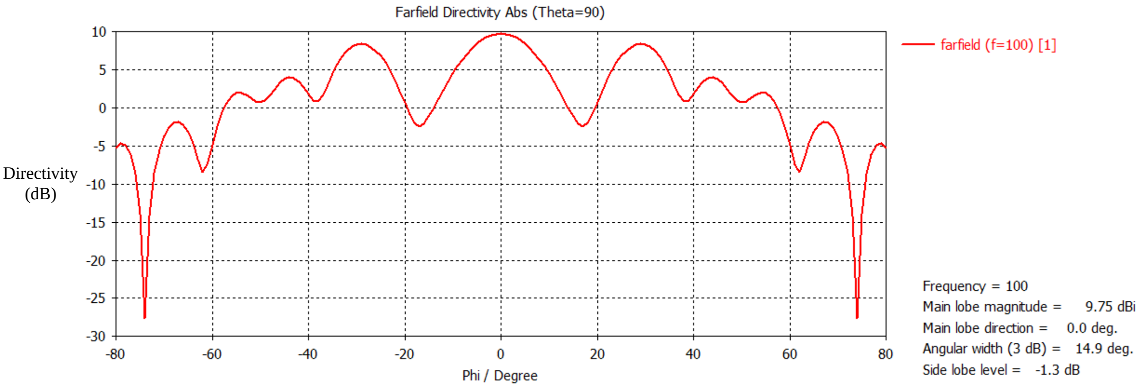

Figure 5-7c: Farfield pattern of slot antenna fed by coaxial cable.

The S_{11} parameter of the slot antenna (**Figure 5-7b**) was lower than -10 dB over a large frequency range between 97 and 105 GHz. The antenna radiates power most effectively at a band around 99 GHz. The graph also showed that the device was capable of radiating power efficiently (> -10 dB) over a large range of frequencies.

The farfield pattern of the antenna (**Figure 5-7c**) showed that the antenna reached a maximum of 9.75 dBi. The farfield pattern of the antenna had a distinct peak, but contains relatively large side lobes. This antenna had significantly less reflection than the endfire antenna.

One key feature which was redesigned was the connection between the microstrip and the coaxial cable. It was found to be mechanically difficult to connect the wire directly to the coaxial cable and instead a 1 mm flange connection was used.

The slot antenna was fed using a metallic wire attached to a flange launcher as the flange could be connected directly onto the end of the coaxial cable. A CST model of the flange was created as shown in **Figure 5-8**. The parameters used in the CST simulation of the flange were based on the specifications for the KPC100F311 (this flange had been detailed previously in **Figure 4-3**).

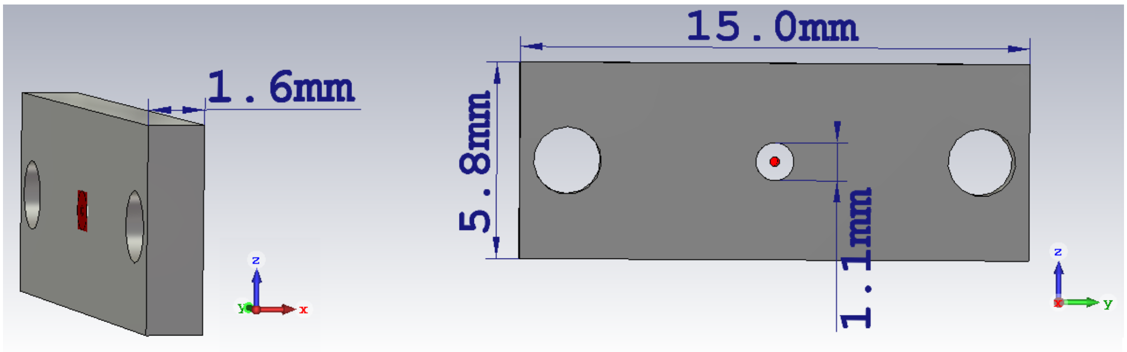

Figure 5-8: Flange connector from side (left) and front (right). The flange had an *x*-axis length of 1.6 mm, a *y*-axis length of 15 mm and a *z*-axis length of 5.8 mm. In the CST environment, the back of the flange was connected to an idealized port. The hole on either side of the device were for screws.

The flange allows for the coaxial cable and the antenna to be connected as at the centre of the flange was a dielectric cylinder surrounding a small hole, for which a wire could be slotted into. The antenna design found from the coaxial fed case (**Figure 5-7**) was connected to the flange connector and the CST model of this arrangement is shown in **Figure 5-9**. The coaxial feed used previously was replaced with this flange connector.

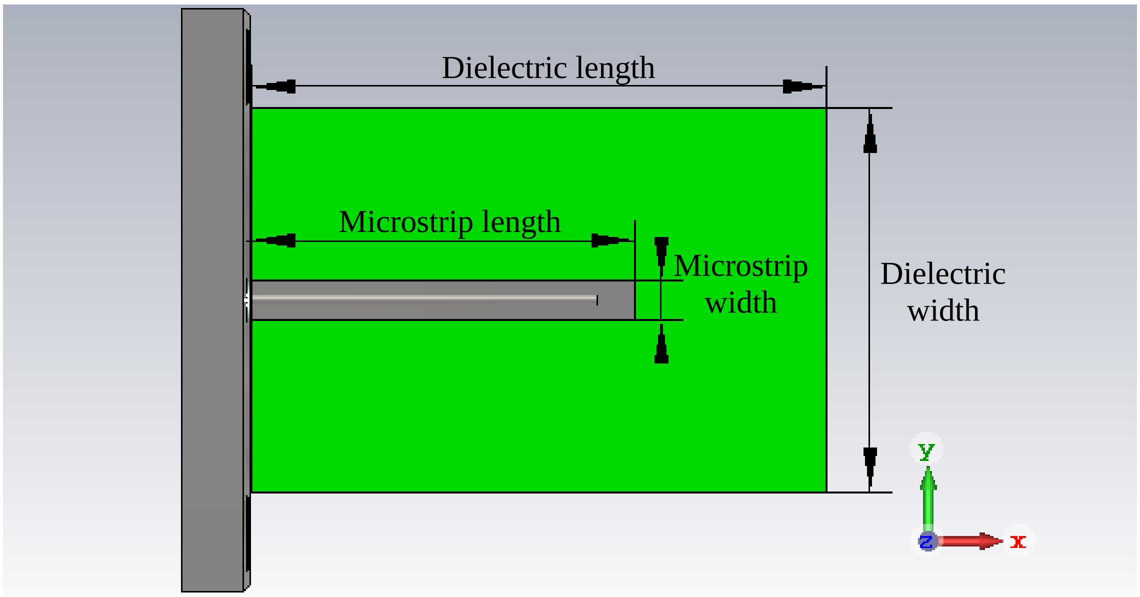

Figure 5-9: Slot antenna with flange connector viewed from the front.

The flange was attached to the board and microstrip designed previously in CST. The previous optimum parameters (**Table 5-1**) were used initially for the device.

There was a small gap between the flange and the dielectric of 0.1 mm, due to the sleeve protruding from the flange. The wire was to be soldered onto the slot and then inserted into the opening in the flange. A series of simulations were performed on this device in order to determine the optimum parameters for this device. **Figure 5-10** shows the S_{11} parameter and farfield pattern from CST.

Microstrip length	10 mm	*x*-axis length of microstrip
Microstrip width	1 mm	*y*-axis length of microstrip
Microstrip thickness	0.035 mm	*z*-axis length of microstrip
Dielectric length	15 mm	*x*-axis length of dielectric base
Dielectric width	10 mm	*y*-axis length of dielectric base
Dielectric thickness	0.8 mm	*z*-axis length of dielectric base
Wire length	10 mm	Length of wire connected to microstrip
Wire radius	0.1435 mm	Radius of wire

Table 5-2: Ideal parameters for the slot antenna fed by flange connector.

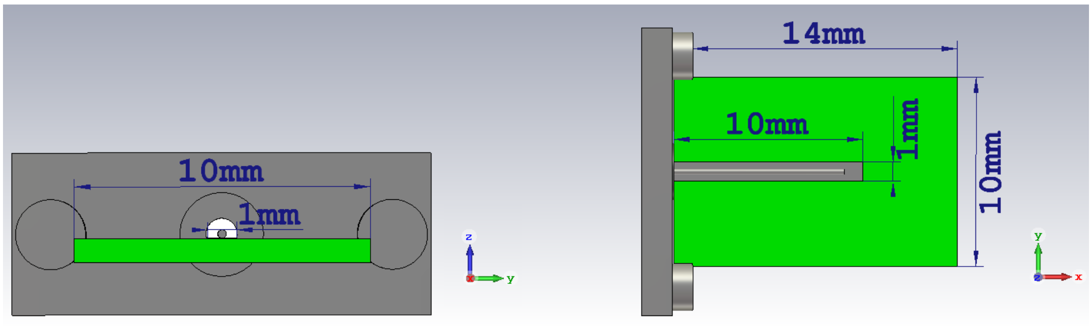

Figure 5-10a: Slot antenna as simulated in CST.

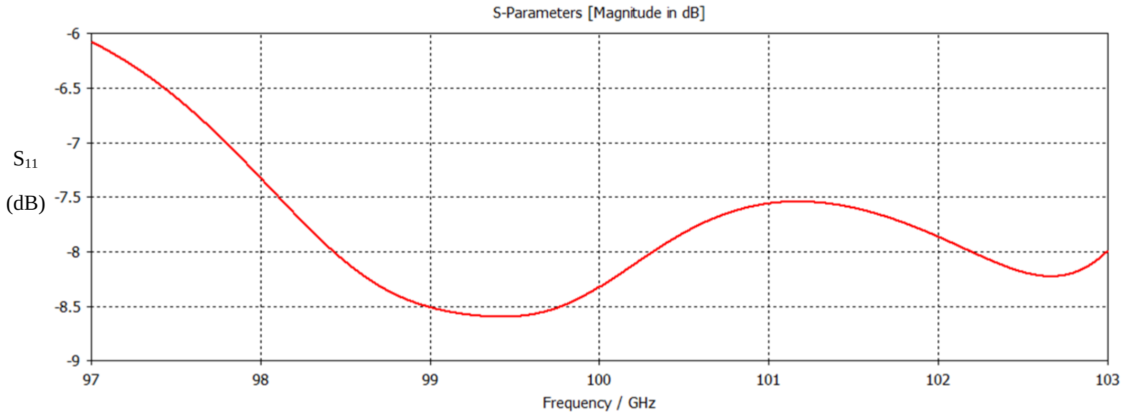

Figure 5-10b: S_{11} parameter of slot antenna design from **Figure 5-9**.

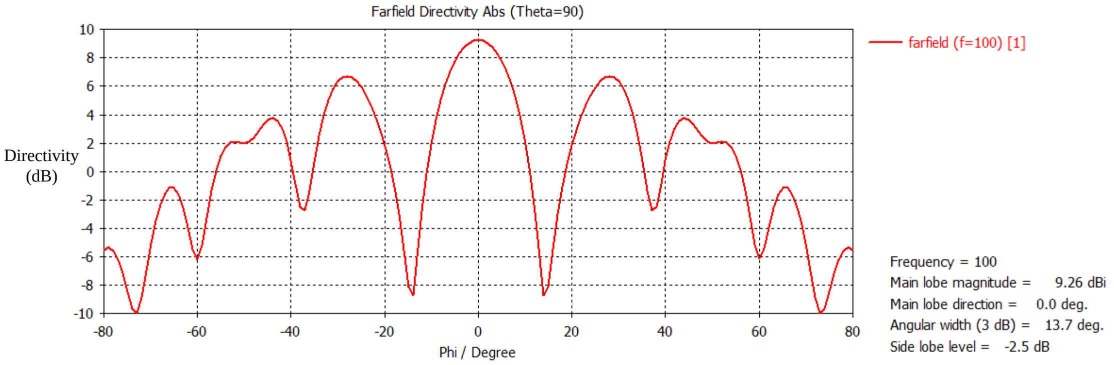

Figure 5-10c: Directivity of slot antenna along the $\theta = 90°$ axis.

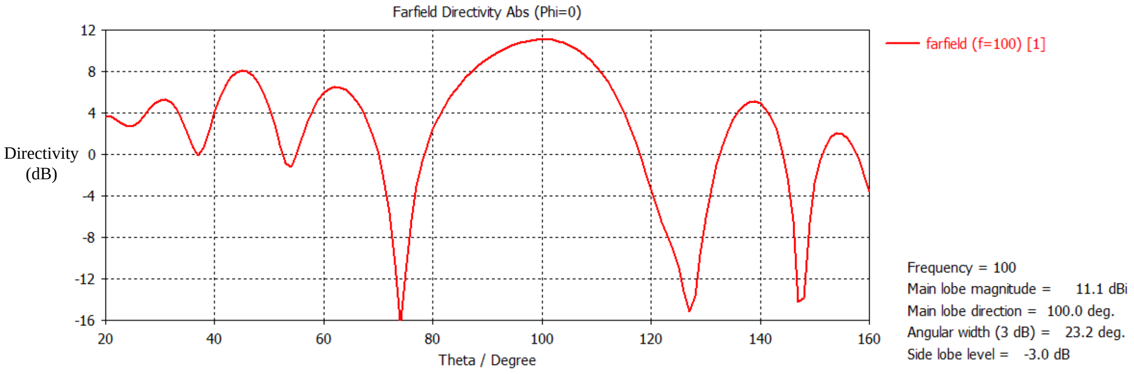

Figure 5-10d: Directivity along the $\varphi = 0°$ axis. The on-axis position of $\theta = 90°$, in this case, indicates radiating along the positive *x*-axis, which was the desired direction of propagation.

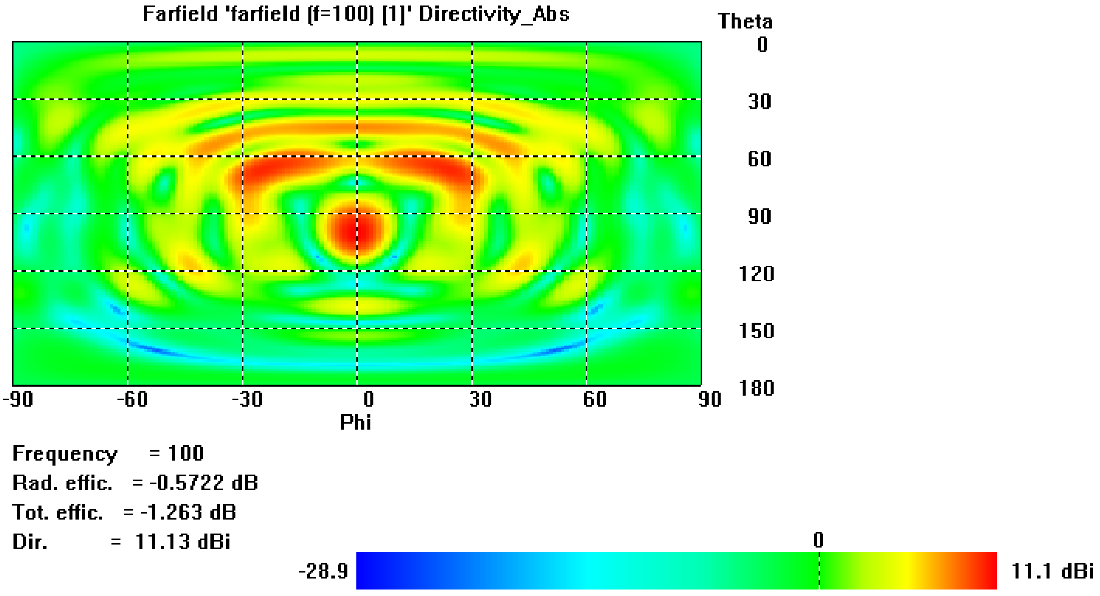

Figure 5-10e: 2-D view of the farfield generated by the slot antenna from CST**.**

The S_{11} parameter of the antenna **Figure 5-10b** was quite high, still at -8.3 dB at 100 GHz. The antenna was moderately efficient at radiating power, but a lower S_{11} would ideally be desired. A distinct peak on axis was observed in **Figure 5-10c**, which reached a maximum directivity of 9.3 dBi. As **Figure 5-10d** shows, the antenna was radiating slightly off-axis. The farfield pattern along this axis reached a maximum of 11.1 dBi at $\theta = 100°$.

The 2-D plot (**Figure 5-10e**) indicates that most of the power was radiating around the region of maximum directivity. The maximum directivity of the antenna was 11.1 dBi, which occurs at ($\theta = 100°$, $\varphi = 0°$). There were a few relatively large side lobes occurring at $\varphi = 60°$. The farfield pattern was not ideal, but it appeared to be radiating power in the correct direction. Additionally, a combination of parameters was not found which could reduce the amount or size of the side lobes.

Axis	Maximum directivity	Direction	Angular width
$\theta = 90°$	9.3 dBi	$\varphi = 0°$	12°
$\varphi = 0°$	11.1 dBi	$\theta = 100°$	23°

Table 5-3: Comparison of the directivity and the angular width along the two axes.

The antenna designed in **Figure 5-10** had several desired characteristics, as it had a moderately low S_{11} parameter and produces beam with a reasonable directivity. Overall, it was better than the previous endfire antenna examined in **Section 5.2**. Furthermore, the antenna was also relatively simple to manufacture with methods available in the lab. For these reasons this antenna was chosen to be manufactured and tested with the VNA.

The antenna needed to be held in place and a dielectric structure made of HDPE was used to hold the board and 1 mm connector securely (see **Figure 5-11a**). Metallic screws were also added to the simulation, as they will need to be introduced to connect the flange to the coax support structure. There was a cut into both the support and the board to allow for the introduction of screws.

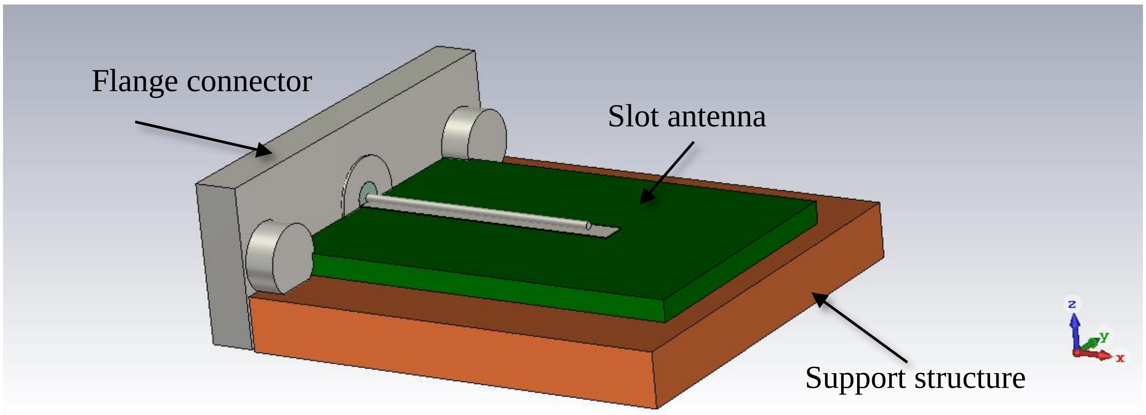

Figure 5-11a: Support structure (in orange) added to structure from **Figure 5-9.** The support structure in the simulation was initially 2 mm in thickness, 15 mm in length along both the *x* and *y*-axis. Small cuts in the support structure and in the slot antenna are required in order to insert screws to hold the flange in place.

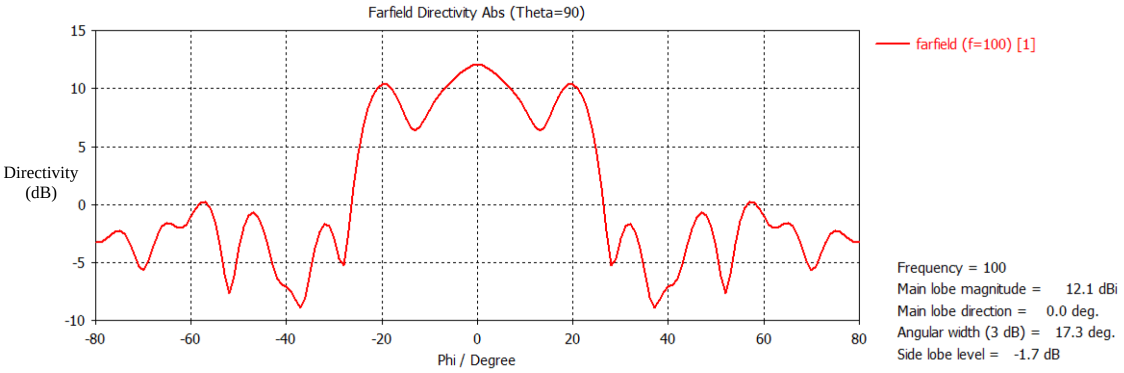

Figure 5-11b: Farfield pattern along the $\theta = 90°$ axis for the slot antenna with support structure.

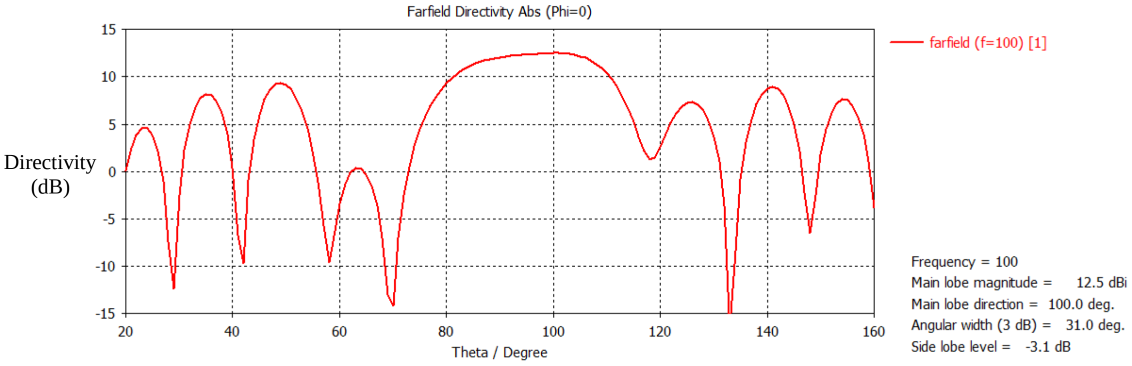

Figure 5-11c: Farfield pattern along the $\varphi = 0°$ axis for the slot antenna with support structure.

Figure 5-11b and **c** show the farfield pattern of the slot antenna with the support attached. The cut along the $\theta = 90°$ axis showed the presences of significate side lobes. There were two side lobes on both sides of the main beam that have a directivity of over 10 dBi.

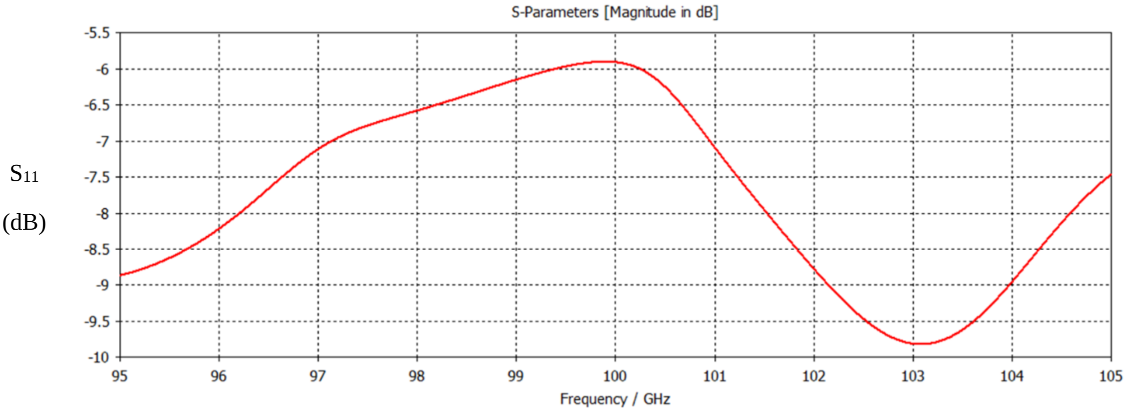

Figure 5-11d: S_{11} parameter of the antenna between 95 GHz and 105 GHz.

Nowhere in the range examined **Figure 5-11d** was there a frequency where the S_{11} parameter was below -10 dB. The antenna was not completely ideal because of this S_{11} parameter, but it still performed quite well.

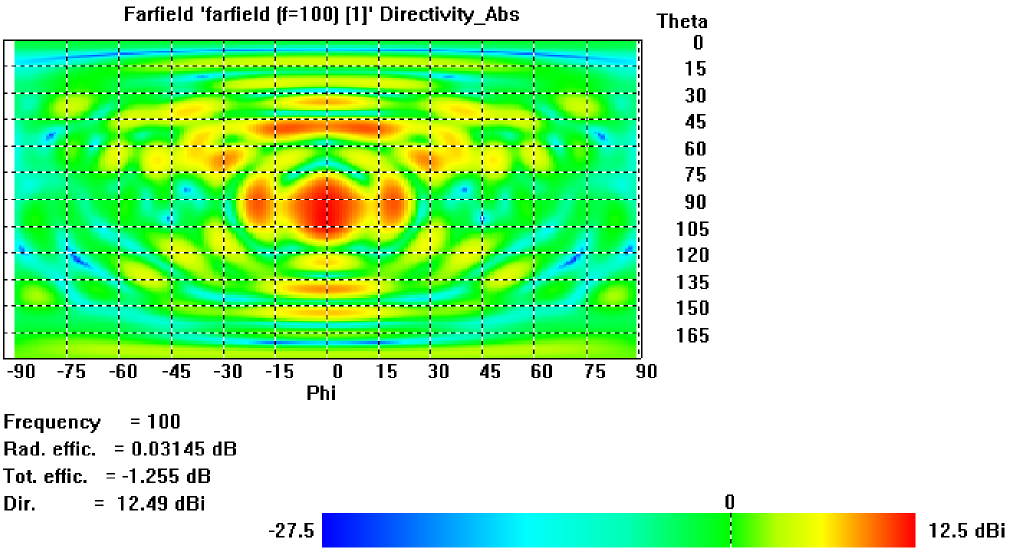

Figure 5-11e: 2-D view of farfield for the supported slot antenna.

Figure 5-11e shows that the antenna had large side lobes surround the main beam.

Axis	Maximum directivity	Direction	Angular width
$\theta = 90°$	12.1 dBi	$\varphi = 0°$	17.3°
$\varphi = 0°$	12.4 dBi	$\theta = 100°$	31°

Table 5-4: Maximum directivity along each axis and the direction of the signal in polar coordinates.

This antenna was manufactured & tested in the VNA lab. The PCB was etched using photolithographic techniques, as detailed in **Section 2.4**. The 1 mm coax connector wire was soldered onto the antenna. The sides of the board were cut to fit the device into the supporting structure.

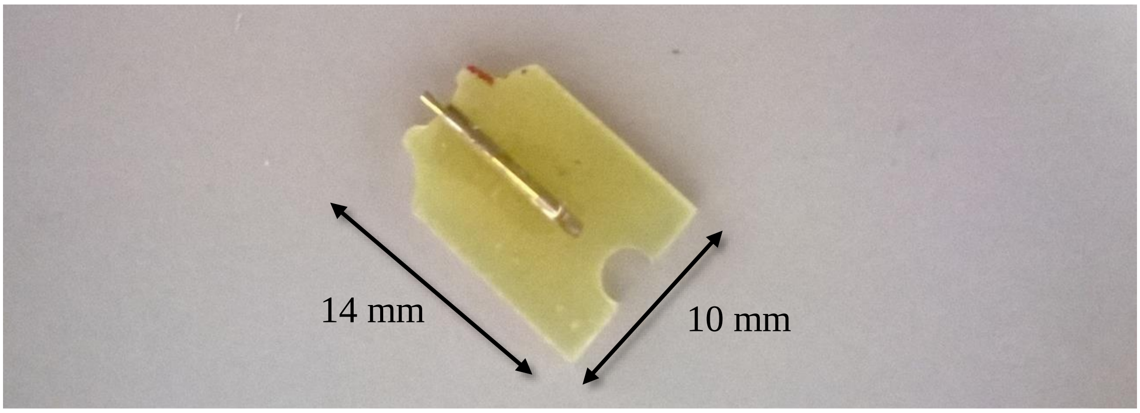

Figure 5-12: Manufactured slot antenna.

5.3.2 Test of slot antenna with supporting structure

The antenna shown in **Figure 5-12** was attached to the flange, which in turn was connected to the 1 mm coaxial cable as shown in **Figure 5-13**. This coaxial cable was connected to a waveguide-to-coaxial connector in order to connect they system to the VNA ports. A H-bend and twist waveguide were required to orientate antenna for testing. Additionally, the KPC100F311 connector was used to connect the coaxial cable to the antenna. The details and specifications of the equipment used in the experimental setup were already described in **Section 4.2**.

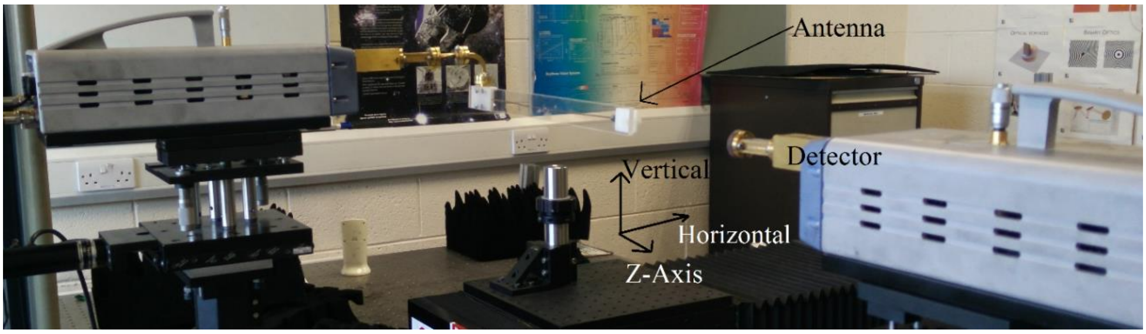

Figure 5-13: Experimental set-up to test the planar slot antenna.

As seen in **Figure 5-13**, the vertical direction was chosen to be the negative *y*-axis, right was the positive *x*-axis and the *z*-axis was the axis the power should radiate along. The distance between the front of the antenna towards the probe was 110 mm. At this distance, the pattern measured should be in the farfield. Note that this antenna was orientated differently to the previous patch antenna. Two scans of this antenna were measured after the procedural VNA calibration, as detailed in **Table 5-5**.

	Horizontal axis			Vertical axis		
Test	Min	Max	Number of steps	Min	Max	Number of steps
B1	-50 mm	50 mm	21	-50 mm	50 mm	21
B2	-135 mm	65 mm	41	-135 mm	65 mm	41

Table 5-5: Scans preformed on the slot antenna using the VNA.

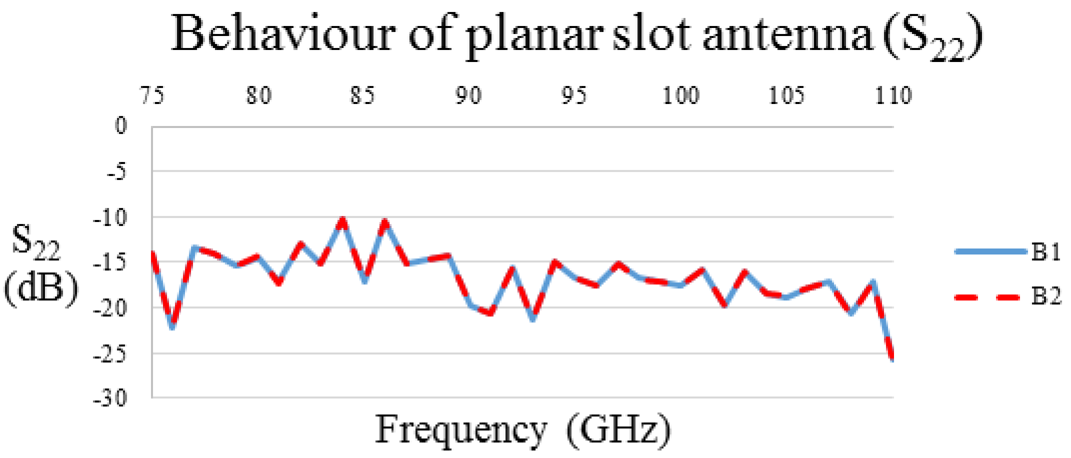

Figure 5-14a: Measured S_{22} parameter of planar slot antenna for scan B1 and B2.

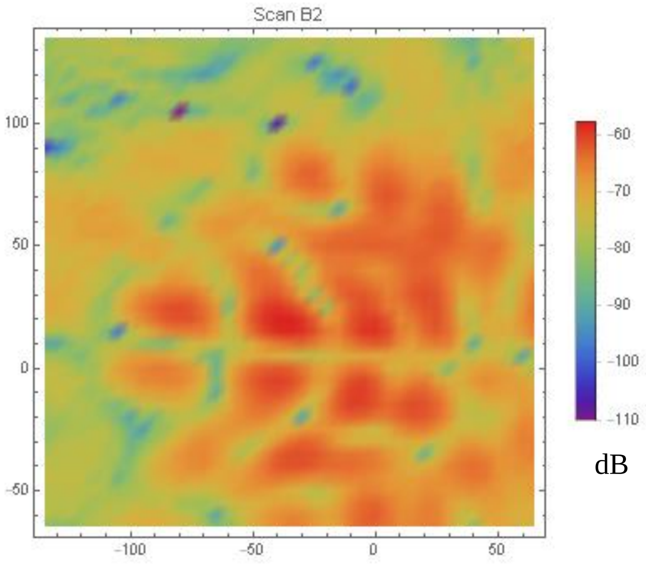

Figure 5-14b: The 2-D measured pattern of beam for scan B2.

The return loss (S_{22}) of the device was identical for both scans shown in **Figure 5-14a**. Additionally, the return loss was lower than expected from the CST simulation, as it only increases above -10 dB briefly. These low values show that very little power was reflected back into the VNA. The measured S_{21} parameter in **Figure 5-14b** varies significantly from expected and instead of these being one beam located at the centre, there were several split signals near the centre.

The following plots (**Figure 5-15a** and **b**) present the data when compared to the simulated results from CST.

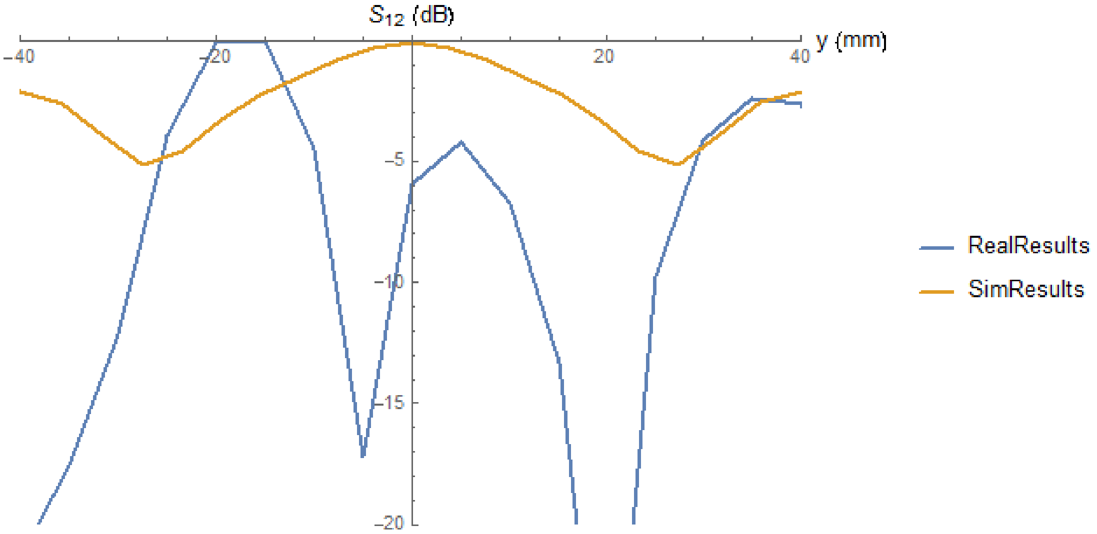

Figure 5-15a: Normalized measured results from VNA and the normalized simulated results from CST cut along the *x*-axis.

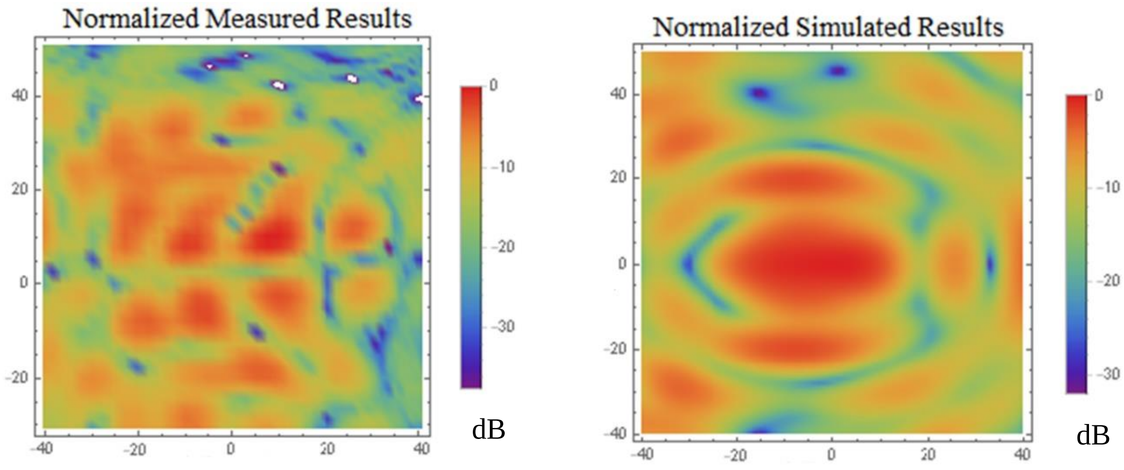

Figure 5-15b: Normalized measured results from VNA (left) and the normalized simulated results from CST (right).

Figure 5-15 shows a comparison of the results from B2 with the CST simulation. **Figure 5-15a** shows a 1-D plot of the normalized farfield along the *y*-axis and the simulation and the measured result disagree. Note that the CST plot (SimResults) was the same result from **Figure 5-11e**, but with the axis rotated to match the axis used in the VNA. The simulated and measured results were not in agreement.

Figure 5-15b shows a 2-D plot of the normalized farfield compared to simulation. The simulated and measured results clearly do not agree. Extra features are measured and are not reproduced in simulation. For comparison, the device was scanned again without the mechanical support structure to observe its influence.

5.3.3 Test of slot antenna without supporting structure

The dielectric board was removed from below the antenna and the farfield was re-measured (support illustrate in **Figure 5-9**). However, the main problem with removing the supporting dielectric was the antenna was only supported by the flange, meaning it was prone to rotating about the flange.

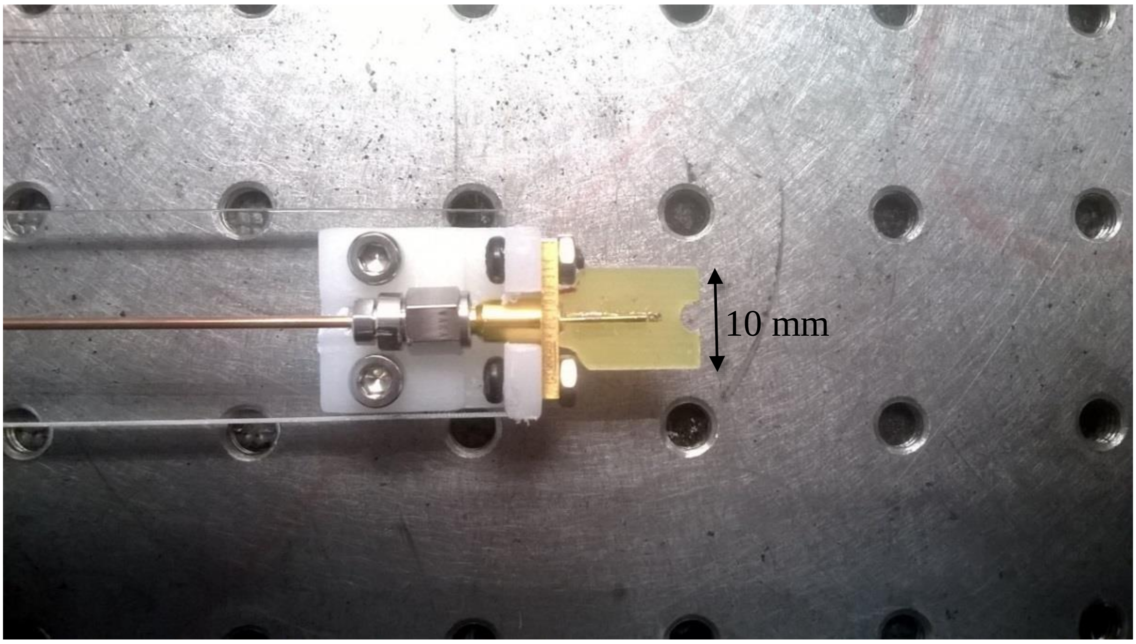

Figure 5-16a: Photo of slot antenna connected to coaxial feed.

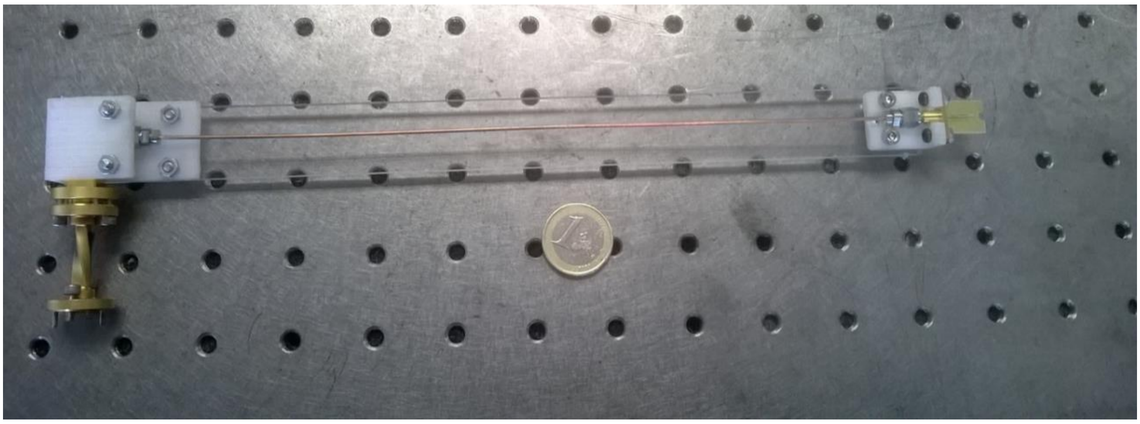

Figure 5-16b: Photo of slot antenna connected to coaxial fed. Coin added for scale.

The antenna system (as shown in **Figure 5-16**) was connected to the VNA and several scans of the antenna's farfield was performed again. The frequency scan was between 75 and 110 GHz. The number of points was reduced to 36, (point every 5 GHz). The scan size for each test is detailed in **Table 5-6**.

	Horizontal axis			Vertical axis		
Test	Min	Max	Steps	Min	Max	Steps
C1	-20 mm	20 mm	11	-20 mm	20 mm	11
C2	-80 mm	40 mm	31	-100 mm	20 mm	31
C3	-80 mm	40 mm	31	-80 mm	40 mm	31
C4	-80 mm	40 mm	31	-80 mm	40 mm	31
C5	-40 mm	80 mm	31	-80 mm	40 mm	31
C6	-40 mm	40 mm	41	-40 mm	40 mm	41
C7	-40 mm	40 mm	41	-40 mm	40 mm	41

Table 5-6: Scan size for each test performed in the VNA

The distance between the end of the antenna and the end of the probe was 55 mm. The first scan (C1) was a small scan to test if the device was radiating correctly. The following scans of the slot antenna were taken in order to ensure the antenna's beam pattern was consistent and to ensure that the antenna was properly aligned.

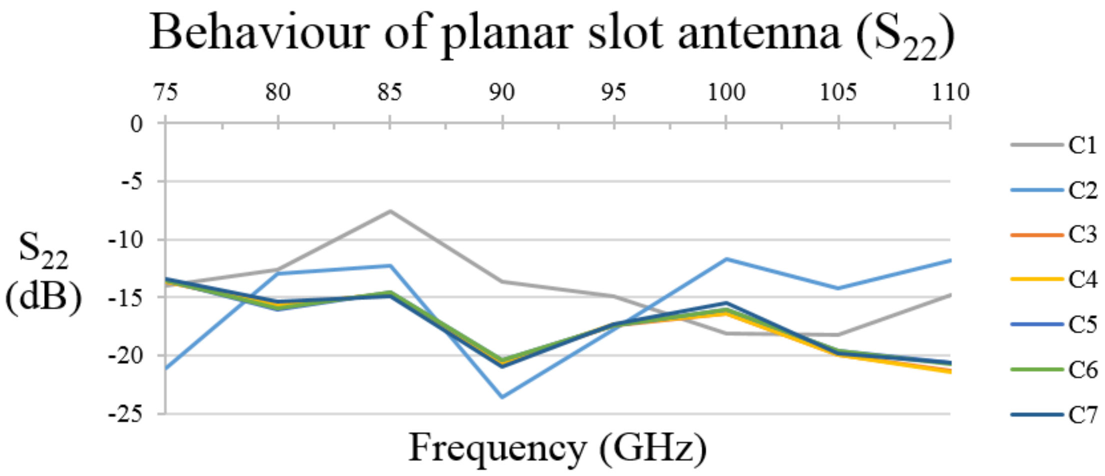

Figure 5-17: Comparison between the S_{22} parameter for the slot antenna for different tests.

These measurements were performed over a period of 6 hours. As showed in **Figure 5-17**, there was some variation of the S_{22} (the return loss) during the tests, in particular C1 and C2, which deviate from the later tests. Overall, the S_{22} parameter for the device was quite low and never exceeded -10 dB over the entire frequency range.

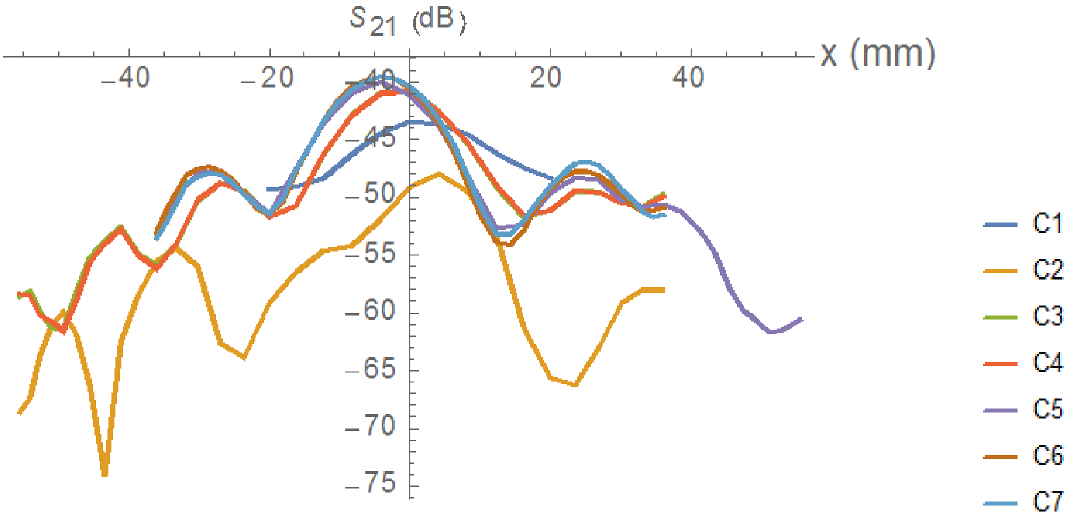

Figure 5-18: Comparison of the S_{21} parameter for the antenna, though the centre of the beam.

The previous graph (**Figure 5-18**) showed the S_{21} parameters for each scan as measured with the VNA. There was a large variation in the measured farfield patterns. The peak S_{21} was located in the centre only for some of the tests. This was due to an alignment problem with the antenna, as without any support, the antenna was prone to rotating slightly in the flange socket. The discrepancies between the scans could be attributed to changes in alignment with the detector probe. A similar farfield plot was measured in each scan, however, there was some variation which was attributed to the antenna rotating in the socket.

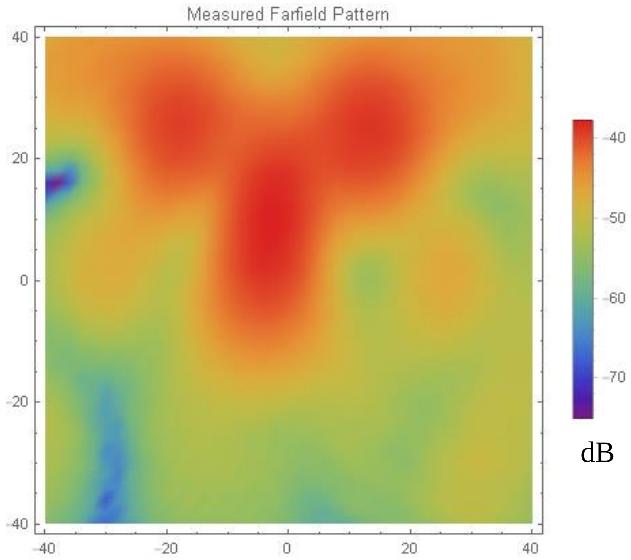

Figure 5-19a: A scan (C7) of the slot antenna as measured in the VNA at 100 GHz. The data shown was the raw data from the measurement.

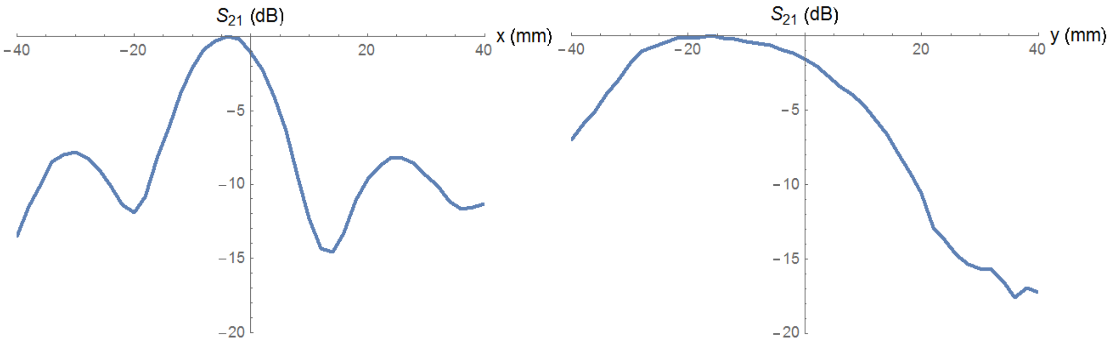

Figure 5-19b: Plot of normalized patterns along both axis for the planar antenna for test C7.

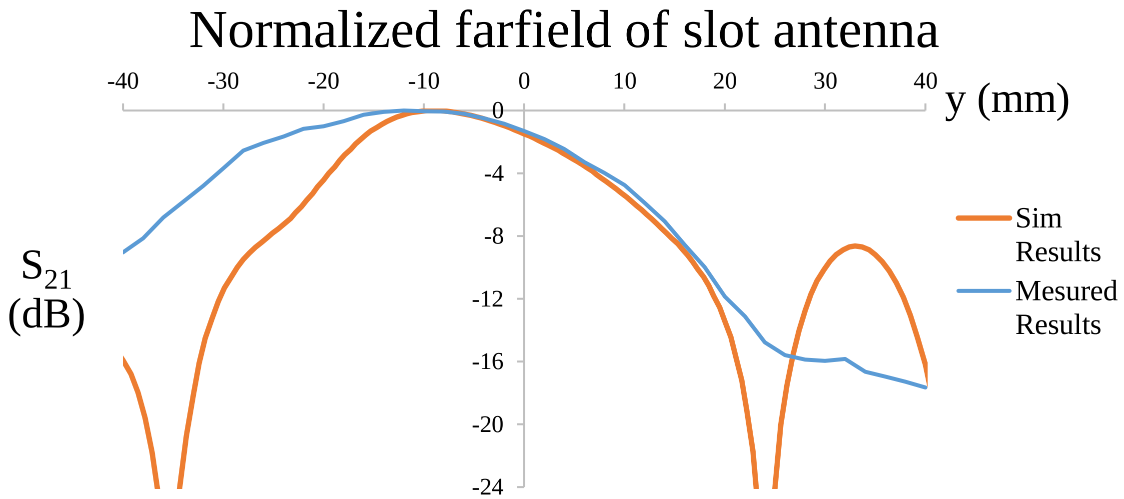

Figure 5-20a: Normalised and compared to simulation along the vertical axis at 100 GHz. The measured plot in the graph was from the S_{21} parameter from Test C7.

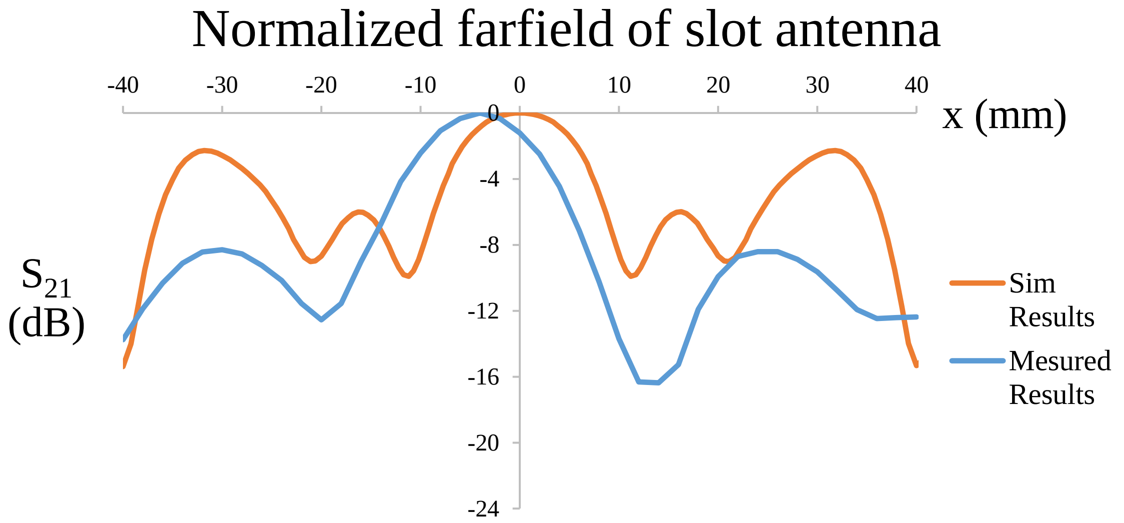

Figure 5-20b: Normalised and compared to simulation along the horizontal axis at 100 GHz. In this scan (C7), the device was aligned correctly with the probe.

Figure 5-19 and **Figure 5-20** showed a comparison of the measured farfield pattern of the antenna from the VNA with the simulated results from CST. From the measured results in **Figure 5-19a**, there was a region in the centre of the scan where the signal was strongest. There were two large side lobes present in the upper portion of the scan. The cross sections in **Figure 5-19b** shows the main lobe of the device was radiating at an angle of 20° to the *z*-axis.

In the cross section along the vertical axis (**Figure 5-20a**), the measured and simulated results have similar shapes, but the measurement was skewed more to the right. In the cross section along the horizontal axis (**Figure 5-20b**), the peak power for the measured farfield pattern occurs at roughly the same position as the simulated plot, however, the simulation predicts larger side lobes. The "offset" observed was due to the main beam of the antenna radiating at a slight angle.

The distance between the antenna and the probe detector was then altered in order to observe how the device behaved with an increased scan distance. The peak S_{21} for the antenna at various frequencies are shown in **Figure 5-21**.

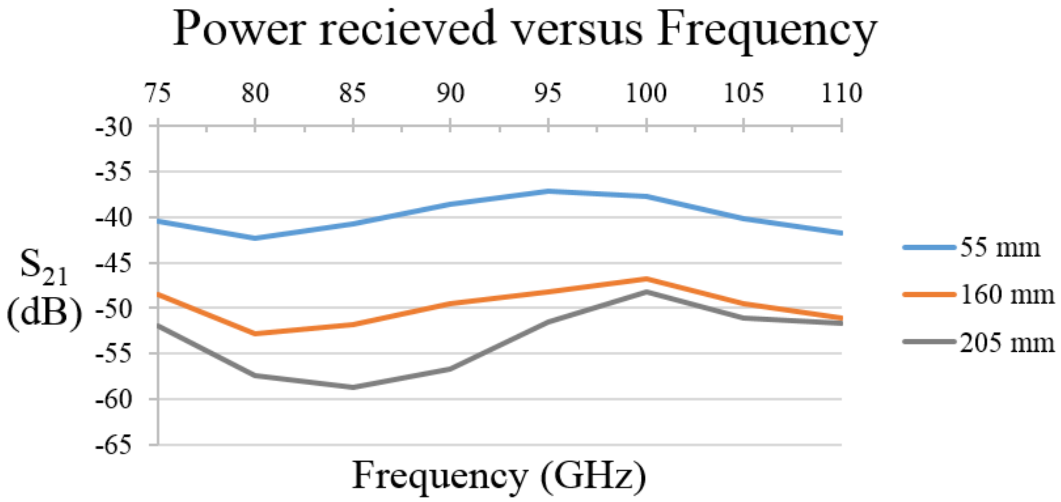

Figure 5-21: Maximum power received (S_{21}) by the slot antenna over the W band frequency range at each distance.

Figure 5-21 shows that, the greatest amount of power was detected when the antenna was closest to the receiver (55 mm) as expected and the power received from the antenna falls off with an increase in distance.

Without the support structure the measured antenna pattern is similar in characteristic shape to the simulations which is encouraging and was the best agreement found form the range of antennas measured.

5.4 Windowed metallic superstrate slot

Slot antennas are typically bi-directional devices. In [52], a superstrate was added to a slot antenna in order to force the device to radiate in one direction only. This metallic superstrate causes the electric fields from the bottom to radiate 180° out of phase with each other. The device from [52] operates at 2.45 GHz. The aim of the following simulations was to scale this design, such that it could operate at W band frequencies (see **Figure 5-22**). The device was initially scaled in size to operate effectively at 75 GHz.

Values (in mm)					
Frequency	2.45 GHz	75 GHz		2.45 GHz	75 GHz
Aperture_l	24	0.8	h2	6	0.22
Aperture_w	60	2	*mstrip_w*	2.2	0.07
Board_l	170	5.6	*Patch_l*	40	1.3
Board_w	160	5.2	*slot_l*	3	0.1
Cover_l	146	4.8	*slot_w*	120	3.9
Cover_w	150	4.9	*Y_shift*	18	0.6

PCB values	
	75 GHz
Cover_h	0.2 mm
ε_r	3
h1	0.125 mm

Table 5-7: Parameters as used in paper (2.45 GHz column) and values as rescaled for 75 GHz (in 75 GHz column). The table on the right shows the values for the available PCB.

The parameters in **Table 5-7** shows the values from the 2.45 GHz antenna scaled to 75 GHz and this antenna configuration was simulated in CST as detailed in the following figures.

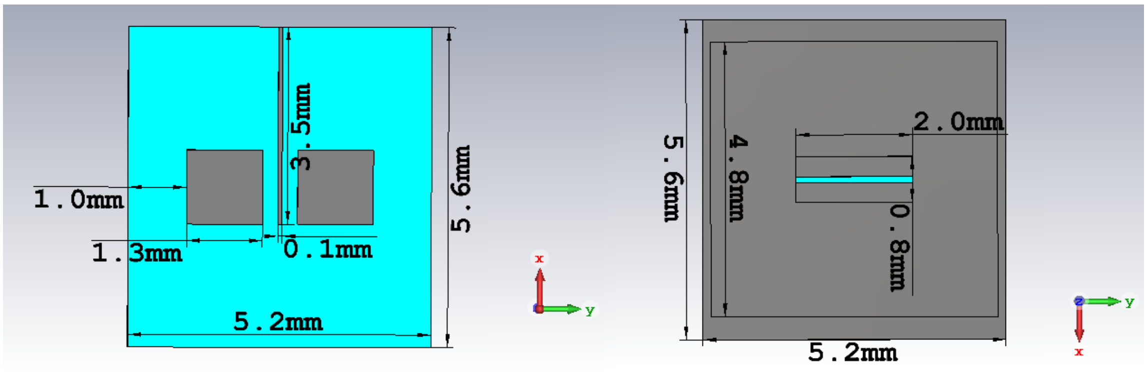

Figure 5-22a: slot antenna with parasitic patches and windowed metallic superstrate, as viewed from bottom (left) and top (right).

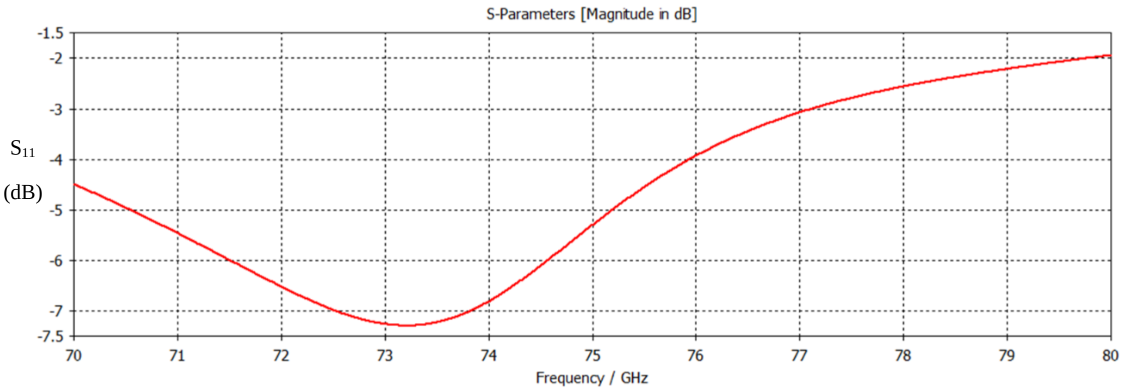

Figure 5-22b: S_{11} parameter of scaled slot antenna with parasitic patches and superstrate.

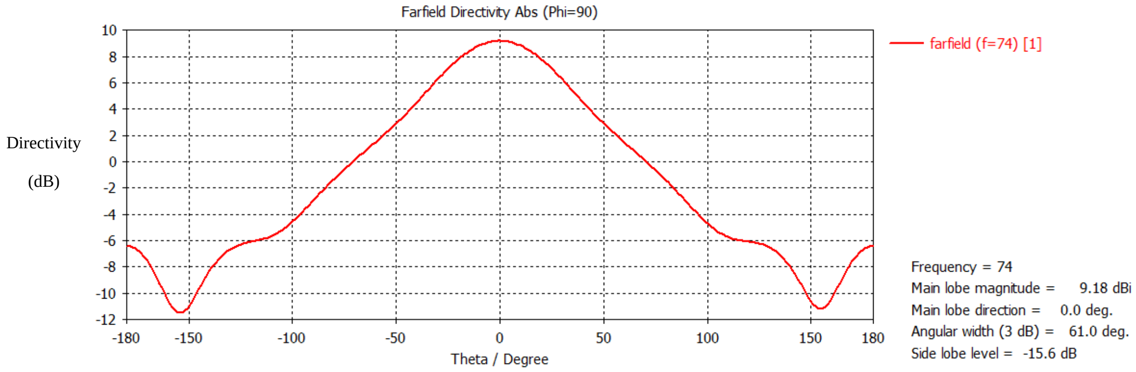

Figure 5-22c: Directivity of slot antenna with parasitic patches and superstrate.

The S_{11}, shown in **Figure 5-22b**, reached a minimum of roughly -7 dB at frequencies around 73 GHz, which was larger than the desired -10 dB. The device did not radiate power as effectively as hoped. The directivity of the antenna, shown in **Figure 5-22c,** reached a value of 9.2 dBi at 74 GHz. The large directivity of the antenna could compensate for the moderate return loss.

The main concern for manufacturing this device was the microstrip width ($mstrip\_w$), which was only 0.07 mm, was too small to reproduce accurately. The slot also had a narrow width ($slot\_w$ = 0.1 mm). Additionally, the small distance between the superstrate and the slot (shown as $h2$ = 0.22 mm), was difficult to set using conventional lab equipment. The device was difficult to manufacture with these small dimensions, but this design looks promising to operate effectively at W band frequencies.

5.5 U and E slot antennas

The U-shaped slot antennas are a hybrid between patch and slot antennas used at lower frequencies [53]. They consist of a patch antenna with a U-shaped slot cut into the patch. Patch antennas typically have small bandwidth and these U-shapes are used to increase the bandwidth of patch antennas [53]. E-shaped slot antennas [54] are similar to the U-shaped antennas in concept, but are structurally different. The patch is E shaped and fed by a coaxial line connected to the centre arm of the patch.

The values in [53] were the dimensions for the U-shaped slot antenna when it resonates at 0.9 GHz. The device was rescaled to operate at 75 GHz on a 3 mm × 3 mm section of the 0.125 mm PCB.

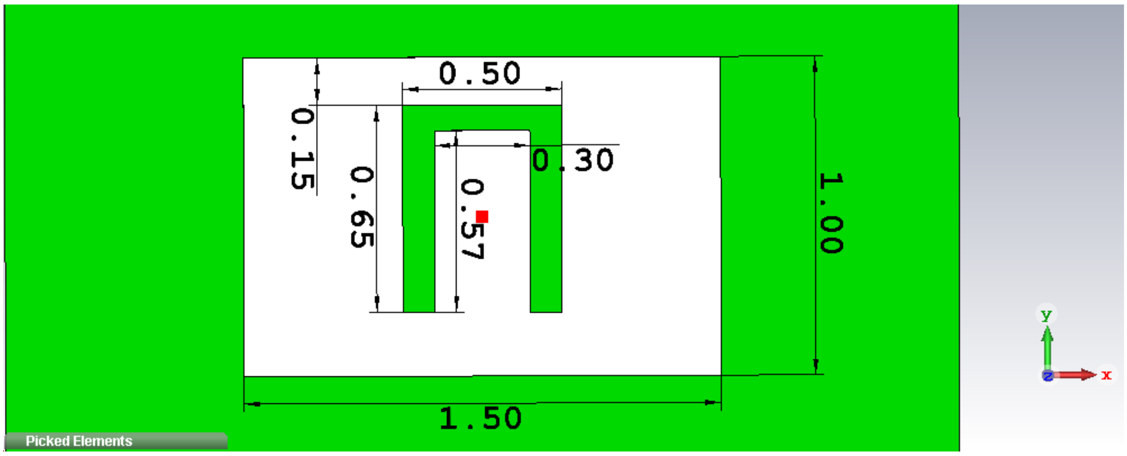

Figure 5-23a: U-shaped slot antenna operating at 75 GHz. The red dot was the centre of the patch and the location of the wire.

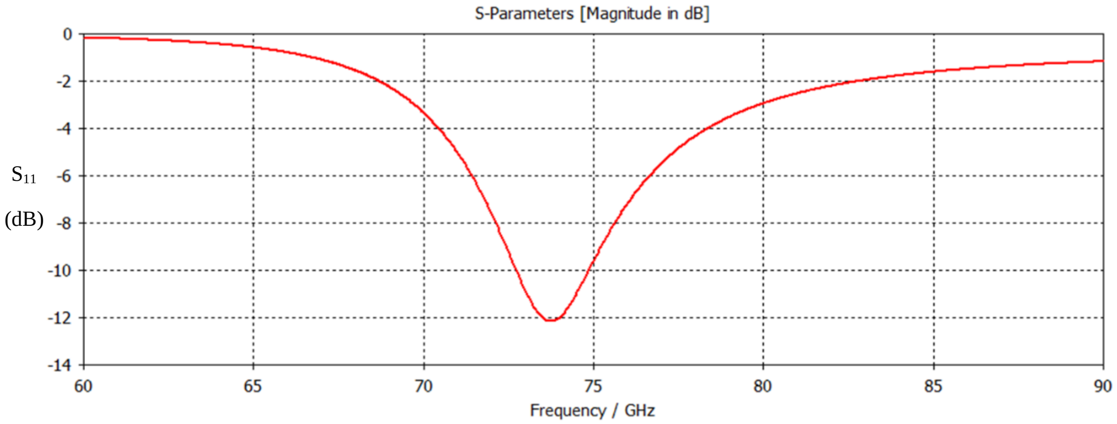

Figure 5-23b: S_{11} parameter of antenna, which reached a minimum of -12.2 dB at 73.7 GHz.

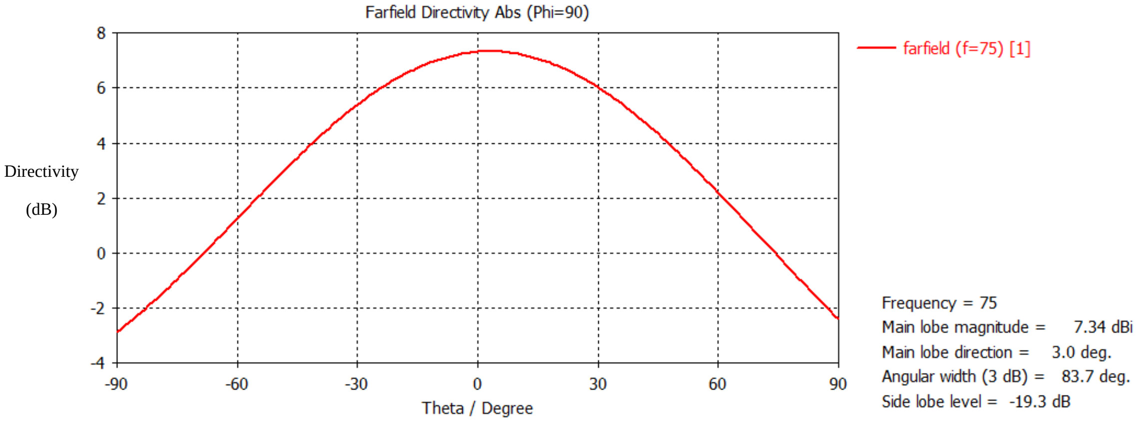

Figure 5-23c: Directivity of U-shaped slot along the $\varphi = 90°$ axis.

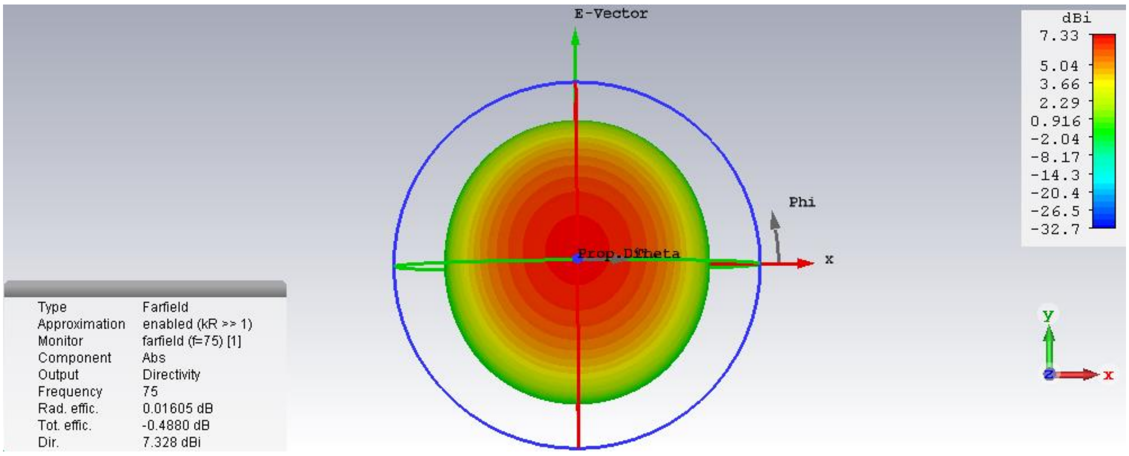

Type	Farfield
Approximation	enabled (kR >> 1)
Monitor	farfield (f=75) [1]
Component	Abs
Output	Directivity
Frequency	75
Rad. effic.	0.01605 dB
Tot. effic.	-0.4880 dB
Dir.	7.328 dBi

Figure 5-23d: 3-D farfield of U-shaped slot antenna.

The U-shape slot on the patch (**Figure 5-23a**) contains several small detailed cuts. One advantage over the patch antenna design was that the wire was fed through the direct centre of the patch, i.e. there was no need for an offset in either the *x* or *y*-axis.

The antenna

As seen in **Figure 5-23b**, the U-shaped slot antenna designed had a low S_{11} parameter (below -10 dB) and radiates power effectivly over a narrow band width between roughly 72 → 75 GHz. The antenna beam (**Figure 5-23c**) had minimal side lobes and a large directivity (7.3 dBi) at 75 GHz. The 3-D farfield of U-shaped slot antenna (**Figure 5-23d**) had good overall beam characteristics, due to it’s relatively high directivity and minimized side lobes. However, the primary problem with this design was that the dimensions of this device were below our available manufacturing tolerances.

The E-shaped design from *Yang et al* [54] was rescaled to operate at 75 GHz on a 3 mm × 3 mm section of the 0.125 mm PCB. This design deviates from the U-shaped antenna in a few important ways. The shape of the patch was clearly different (as **Figure 5-24a** shows), but the E-shaped patch was also smaller than the U-shaped patch. Additionally, the wire was offset along the *y*-axis by 0.2 mm from centre.

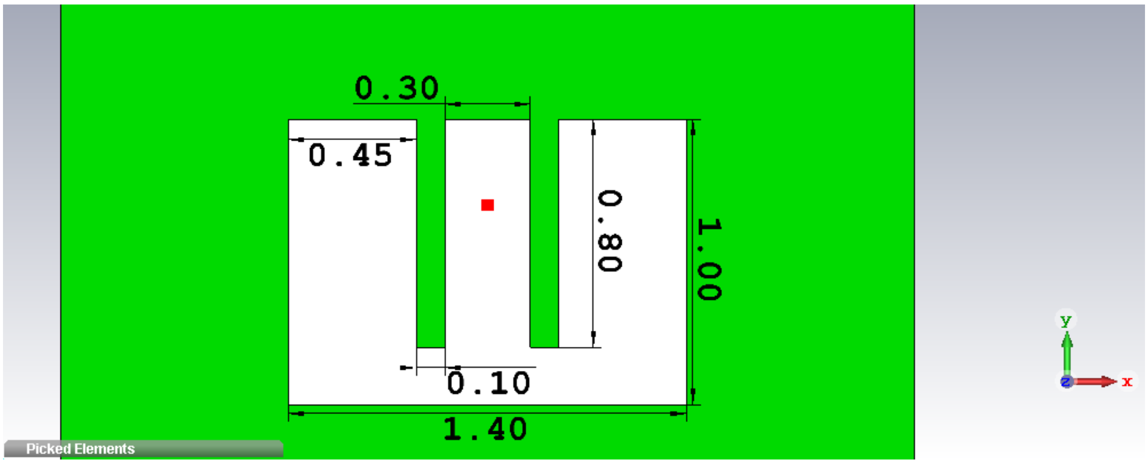

Figure 5-24a: E-shaped slot antenna viewed from top.

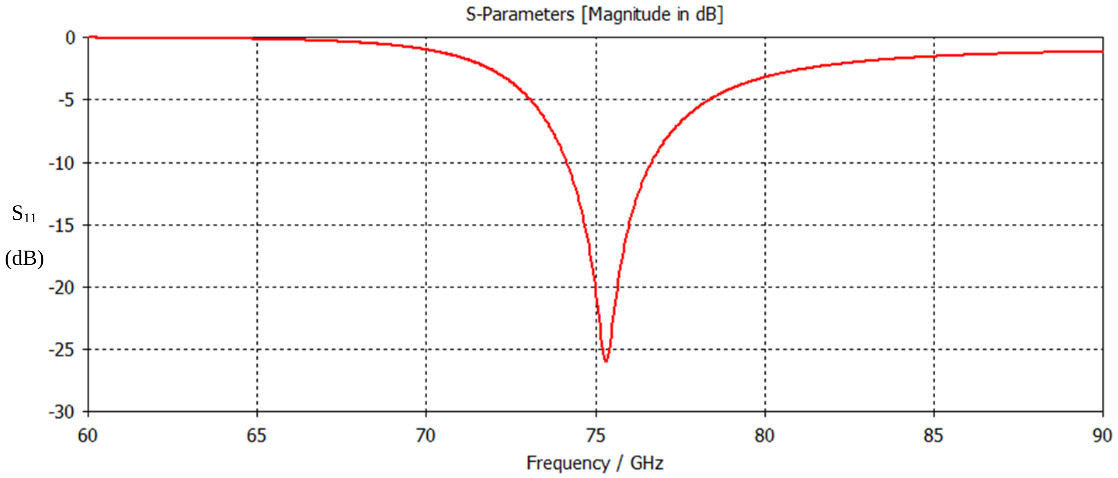

Figure 5-24b: S_{11} of E-shaped slot antenna.

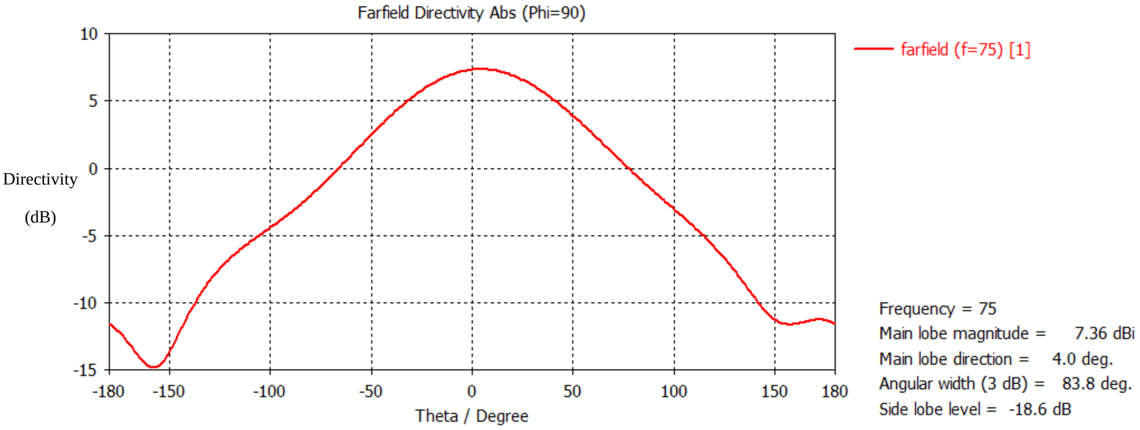

Figure 5-24c: Farfield pattern of E-shaped slot antenna.

The E-shaped patch shown in **Figure 5-24** had a number of small dimensions, but was still larger in dimension than the U-shaped antenna and should be easier to construct. The antenna also showed favourable results; the S_{11} parameter (**Figure 5-24b**)was below -10 dB between 74.1 GHz and 76.6 GHz and the directivity at 75 GHz (**Figure 5-24c**) reached 73.6 dBi. The beam was comparable to the farfield pattern of the U-shaped slot antenna. However, the patch's dimensions were below available manufacturing tolerances and so was too small to reliably manufacture with current capabilities.

5.6 Conclusion

In this chapter, several novel antennas designs (endfire, a planar slot, superstrate slot, U slot and E slot) were analysed in CST. The endfire and slot antennas were built and tested using the VNA.

Two endfire antennas were manufactured and their S-parameters were measured using the VNA. The large amount of reflections in the first antenna renders the antenna unsuitable for practical use. The second antenna did not radiate well below 100 GHz. The poor performance and the manufacturing difficulties of the endfire design render these devices a sub-optimal antenna choice.

The slot antenna designed in CST had a much lower S_{11} parameter than the endfire antenna, with an S_{11} parameter below -10 dB over a large frequency range between 97 and 105 GHz. A flange connector was used to connect the coaxial feed to the slot antenna as it was not possible to directly connect the antenna to the coaxial feed. A support board was added to hold the antenna mechanically. When tested, the antenna produced results that did not match the CST simulation. No central beam was detected, instead several peaks were seen in the beam pattern. All of the supports were removed and the antenna was placed by itself in the flange connector. The beam pattern matched the simulated results better without the support structure and a central beam pattern was generated by the antenna. However, the beam also contained two large side lobes. Without the support, the antenna was also prone to rotating in the flange, causing problems aligning the device and ensuring repeatability. The simulations did predict the presence of the two side lobes, but underestimated how prominent these side lobes would be.

Three additional interesting device designs were analysed in CST. Each of these devices were developed at lower frequencies and were rescaled to operate at 75 GHz in CST. The three devices examined in the way were: a slot antenna with parasitic patches and windowed metallic superstrate, a U-shaped slot antenna and an E-shaped slot antenna. The first of these devices was a side-fed antenna, while the other two were back-fed antennas. Each of these designs could work at 75 GHz, however each design had a low manufacturing tolerance. For that reason, neither of these devices were manufactured and tested.

The planar slot antenna device preformed significantly better than the other antennas and the previously tested patch antennas from **Chapter 3**.

Chapter 6 Lenslet design

6.1 Overview

A dielectric lenslet (small traditional lens) could be placed in front of any antenna to increase the directivity of the antenna. A collection of these lenslets could be integrated into an array of focal plane devices and, when placed in front of an array of planar antennas discussed in earlier chapters, would increase the directivity of the array as a whole. The term “pixel” in this chapter refers to a single planar antenna with a lenslet placed in-front of the antenna. In this chapter the electromagnetic/optical analysis of these pixels and the experimental measurements carried out on these devices are described. Additionally, the design steps taken to reduce crosstalk between neighbouring devices in close proximity to other pixels is discussed.

Material used for creating lenses at optical frequencies, such as glass, do not function well at millimetre wavelengths. Different dielectric materials are used for manufacturing lenses at millimetre wavelength, such as High Density Polyethylene (HDPE) or alumina, which was used for instance in BICEP3 [6]. Blocks made of HDPE were readily available and this material was proposed, as detailed later in this chapter, to develop W band lenslets. HDPE has a dielectric constant of 2.25 (an effective refractive index of 1.5) and is a rigid material that could be milled into distinct shapes, making the material suitable for lens manufacture. Additionally, the milling was within the capability of the in-house mechanical workshop at Maynooth.

The introduction of these lenses will cause part of the emitted beam to reflect back to the antenna or neighbouring antennas (crosstalk), which introduces losses to the system, thus increasing the noise or amount of reflected power detected. Therefore, lenslets should try to minimise crosstalk between neighbouring antennas if possible by reducing the amount of power being back scattered. A number of different lens geometric designs were examined using CST. Hemisphere lenses, cylindrical lenses and two different plano-convex lenslet designs were examined as detailed in **Section 6.2**.

Section 6.6 will detail the models of crosstalk simulated in CST between these lenslet fed with W band antennas. After simulating a viable lenslet design in CST, the next step was to manufacture several these designs and then measure performance with the VNA facility and those experimental results are also shown in **Section 6.6**.

6.2 Lenslet design for planar antennas

Lenslets were designed for the purpose of increasing the directivity of the antennas and it was therefore important to simulate the antenna and the lenslet in the same software. CST was the simulation software used as it could create both components and simulate their combined response. Initial testing on these lenslets assumed that an idealised rectangular patch antenna was the source of the signal on these lenslets. This patch antenna was previously optimised as shown in **Figure 3-14**. A describtion of this device is shown in **Table 6-1** below.

Parameter	Value	Description
x-shift	0.2 mm	*x*-axis displacement of the coax feed from centre position
y-shift	0 mm	*y*-axis displacement of the coax feed from centre position
Dielectric height	0.1 mm	*z*-axis length of dielectric
Antenna length	3 mm	*x*-axis length of dielectric and ground plate
Antenna width	12 mm	*y*-axis width of dielectric and ground plate
Ground thickness	0.8 mm	*z*-axis length of ground plate
Wire coating	0.3 mm	Radius of the coating of coax feed
Wire core	0.1 mm	Radius of the wire core of coax feed
Patch width	0.72 mm	*x*-axis length of patch
Patch length	0.9 mm	*y*-axis length of patch
Patch height	0.01 mm	*z*-axis length of patch

Table 6-1: Parameters used for idealised patch antenna. This antenna design was used to test the lenslets.

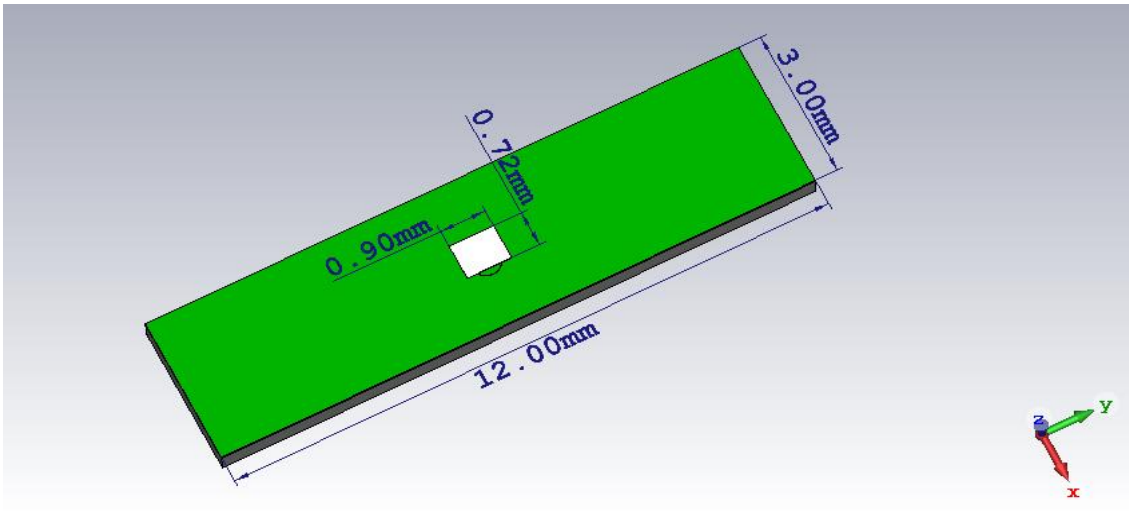

Figure 6-1: Patch antenna used with the length and width of the antenna and patch labelled. The directivity of this design was 7.6 dBi. The S_{11} parameter of this antenna at 100 GHz was -9.5 dB. So, the antenna radiates 89% of the power entering the device.

One individual antenna combined with a lenslet represents an individual pixel in an array. Different antenna designs could be used instead of the rectangular patch antenna, but only this device was considered here for testing purposes.

6.2.1 Hemisphere lens

A hemisphere lens, which consists of half sphere (a 10 mm radius) was used to focus an incoming beam onto the antenna (see **Figure 6-2** for image). A radius of 10 mm was the starting size of the lenslet, as it’s a few wavelengths wide and large enough to be manufactured.

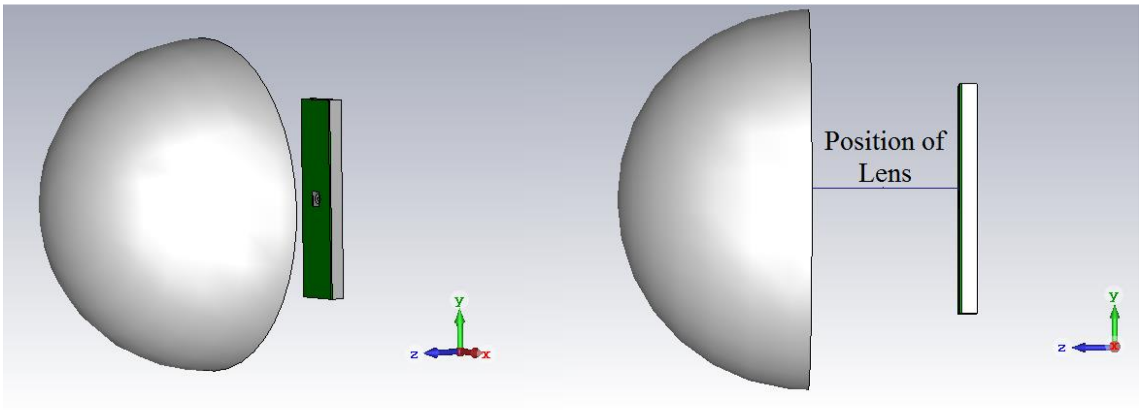

Figure 6-2: Hemisphere lens placed in front of rectangular patch antenna.

The lens needed to be placed a fixed distance in front of the patch antenna to optimally couple radiation (i.e. the focal point of lens was to coincide with the patch optically). The simulation assumes that the support mechanism had no effect on the lens performance. The position of the lens was altered from 10 mm → 4 mm in steps of 2 mm as detailed in **Figure 6-3a**. The directivity and the shape of the farfield pattern changes depending on where the lenslet was located. The goal of these tests was to find the optimal distance of the lens when coupled to this patch antenna.

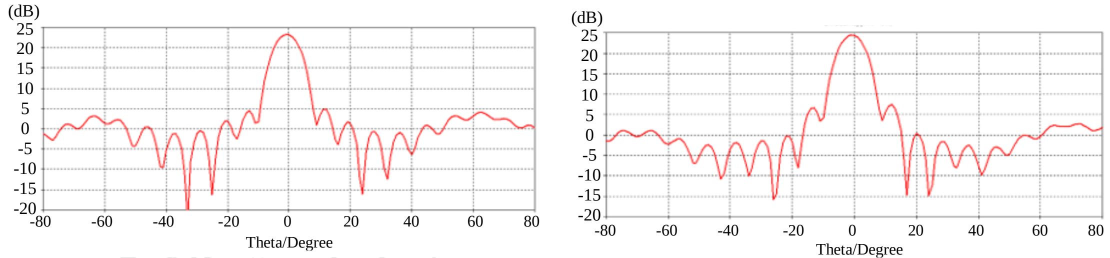

Farfield pattern when lens is placed 10mm away

Farfield pattern when lens is placed 8mm away

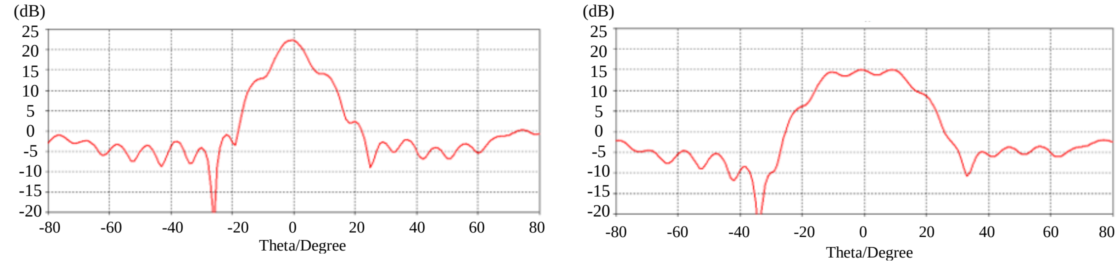

Farfield pattern when lens is placed 6mm away

Farfield pattern when lens is placed 4mm away

Figure 6-3a: Cuts of the farfield along the $\varphi = 0°$ axis when the hemisphere lenses were placed at various distances away from the antenna.

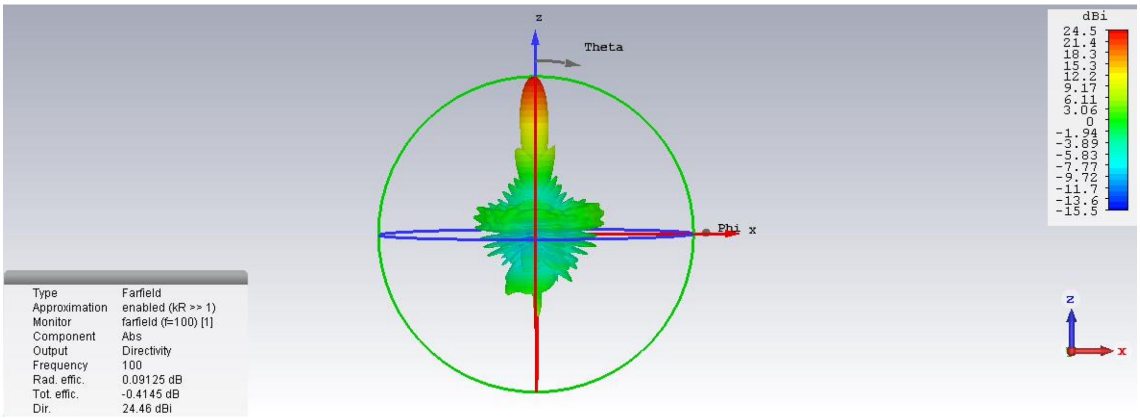

Type	Farfield
Approximation	enabled (kR >> 1)
Monitor	farfield (f=100) [1]
Component	Abs
Output	Directivity
Frequency	100
Rad. effic.	0.09125 dB
Tot. effic.	-0.4145 dB
Dir.	24.46 dBi

Figure 6-3b: The farfield pattern of hemisphere lens placed 8 mm from the antenna.

As **Figure 6-3a** shows the position of the lens was critical to the pixel's performance, as a slight change of 2 mm altered the on-axis directivity by up to 3 dBi. The hemisphere lens in **Figure 6-3b** was an excellent design that had an extremely large on-axis directivity. The directivity of the beam was increased from 7.6 dBi without the lens to 24.4 dBi with the lens; over a 16 dBi increase. The side lobes in the farfield pattern were extremely small relative to the main beam, reaching only 4.1 dBi. The lens performs best when placed 8 mm from the antenna. If the position of the lens was moved slightly a few millimetres away from the focus, the maximum directivity of the lens decreased. The position of the lens could be altered up to 4 mm from its focus, before the beam's directivity reduced to below 15 dBi.

The hemisphere lens allows the pixel to have a high directivity. However, this lens cannot be efficiently placed into an array of these antennas (using only circular packing ratios). More novel designs will need to be considered that will allow more pixels to be integrated into an array by truncating the sides of lens. However, the hemisphere lens could be considered as a benchmark case for comparison.

6.2.2 Cylindrical and elliptical cylindrical lenses

The cylindrical lens designed consists of half a cylinder (see **Figure 6-4**) and the elliptical cylindrical lenslet consisted of half a elliptical cylinder (see **Figure 6-7**). These lenses provide an interesting solution, as one large cylindrical lens could couple to many antennas in a linear array along a single axis.

The cylindrical lens design was examined first in CST, as this design was the easier one to manufacture. The lens was initially set to a radius of 10 mm and the length of the lens along the other axis was set to 10 mm to compare to the hemisphere lens of the same radius (**Figure 6-3**).

Lens length	Lens position	Lens radius
10 mm	10 mm	10 mm

Table 6-2: Parameters used for cylindrical lens design.

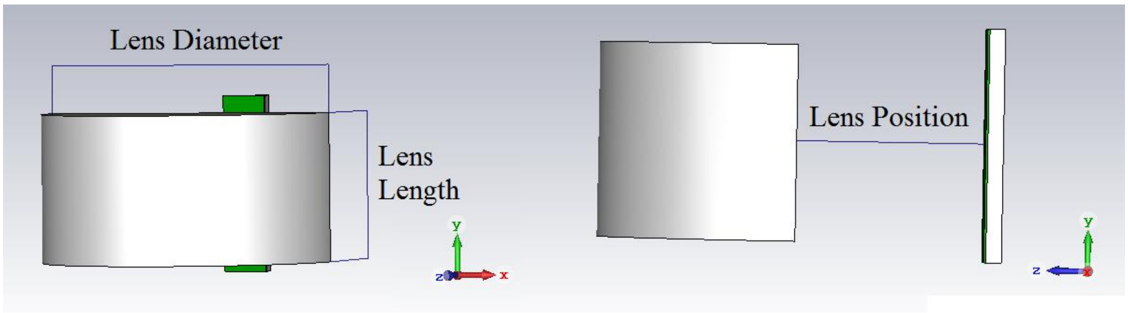

Figure 6-4a: Cylindrical lens placed along *y*-axis.

In order to test the performance of the cylinder lens, it was placed 10 mm from the patch antenna, as this was found to be optimal distance of the lens relative to the patch antenna to maximise directivity. The flat ends of the lenslet point towards the *y*-axis.

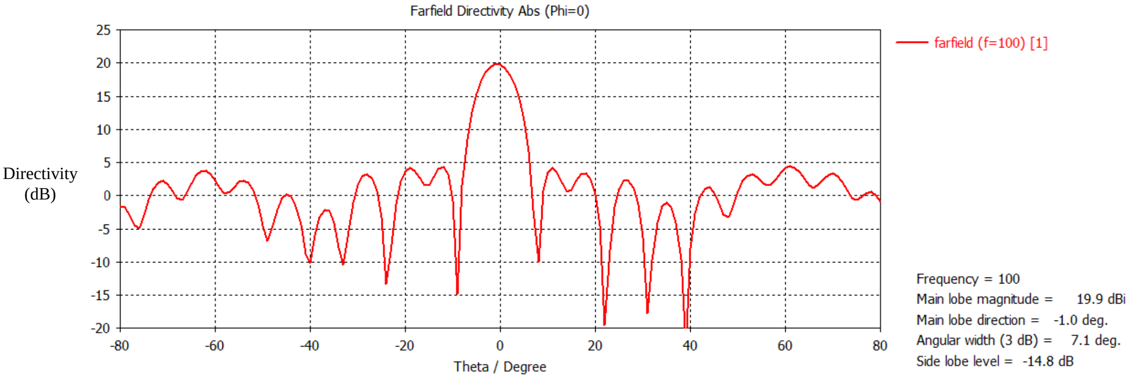

Figure 6-4b: Farfield pattern of patch antenna with cylindrical lens along φ = 0° axis.

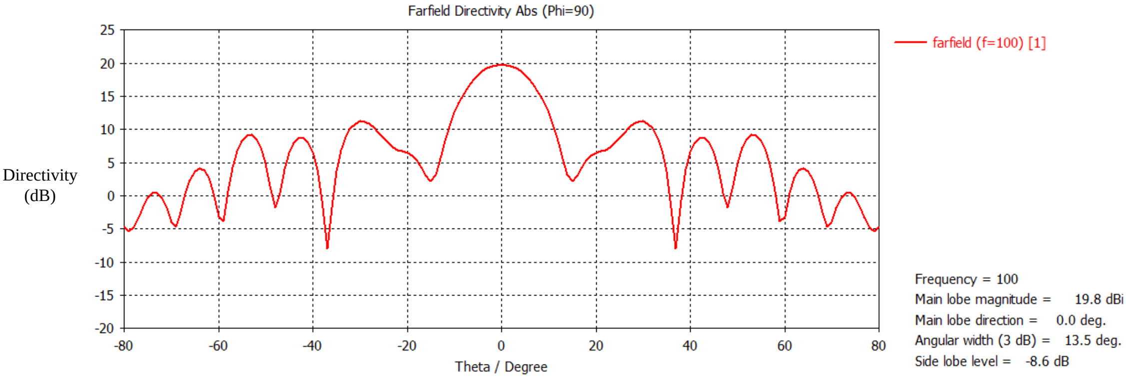

Figure 6-4c: Farfield pattern of patch antenna with cylindrical lens along φ = 90° axis.

The lens reached a maximum directivity of 19.8 dBi along the centre of the farfield beam along the φ = 0° axis in **Figure 6-4b**. The orthogonal axis shown in **Figure 6-4c** had larger side lobes.

For the lens to work in an array, the lens needed to cover more than one patch antenna. The effect of lenslet length on the antennas performance was tested. The lens length was increased from 6 → 14 mm along the *y*-axis in steps of 2 mm to investigate the effect that different size cylinders had on directivity.

Lens length	Lens position	Lens radius
6 → 14 mm	10 mm	10 mm

Table 6-3: Parameters used during testing of the cylindrical lens design.

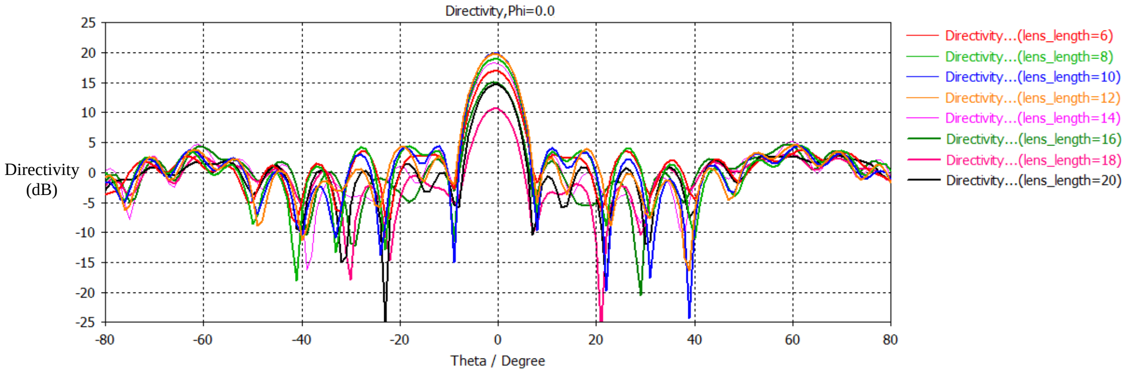

Figure 6-5: Farfield beam pattern due to lenses of different length.

Lens length (mm)	6	8	10	12	14	16	18	20
Directivity (dBi) @ 100 GHz	16.9	18.9	19.8	19.7	18.2	14.9	10.6	14.9

Table 6-4: Directivity of pixel due to lens length.

As **Figure 6-5** shows, the size of the lens did affect the directivity, which was expected, as different lenses had different foci. However, the side lobes caused by the lens were relatively small, regardless of the lens' size.

The beam from the patch antenna was asymmetric also, so the orientation of the lens may change the farfield pattern of the antenna. The lens was rotated 90°, such that the flat ends of the lens were aligned to the *x*-axis. The lens in **Figure 6-6** was placed 10 mm from the antenna.

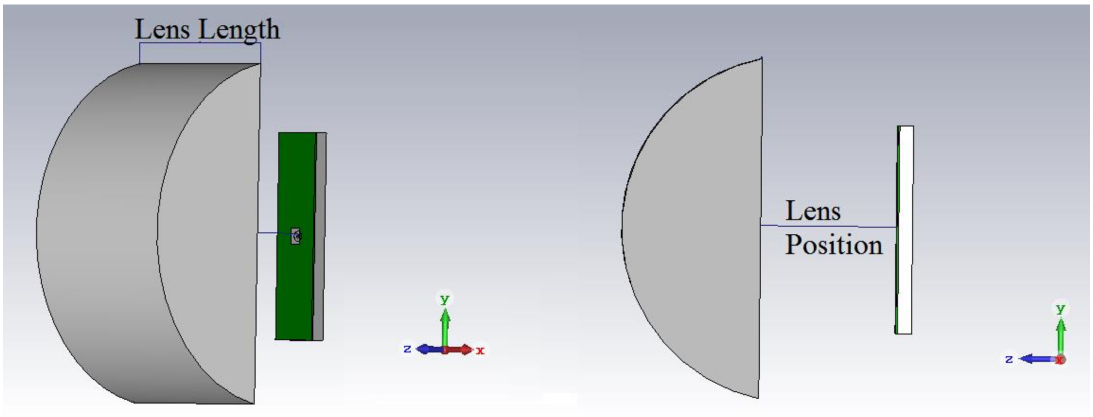

Figure 6-6a: Cylindrical lens placed parallel to the *x*-axis.

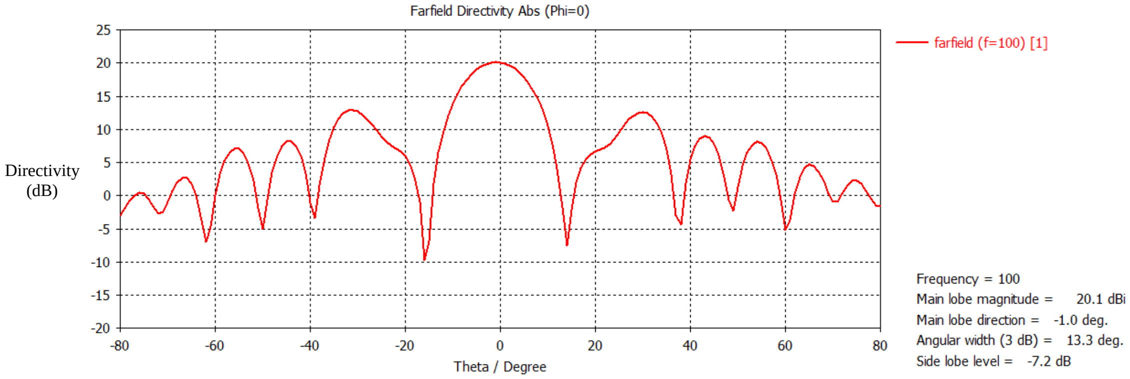

Figure 6-6b: Farfield pattern cut along the $\varphi = 0°$ axis of patch antenna with cylindrical lens.

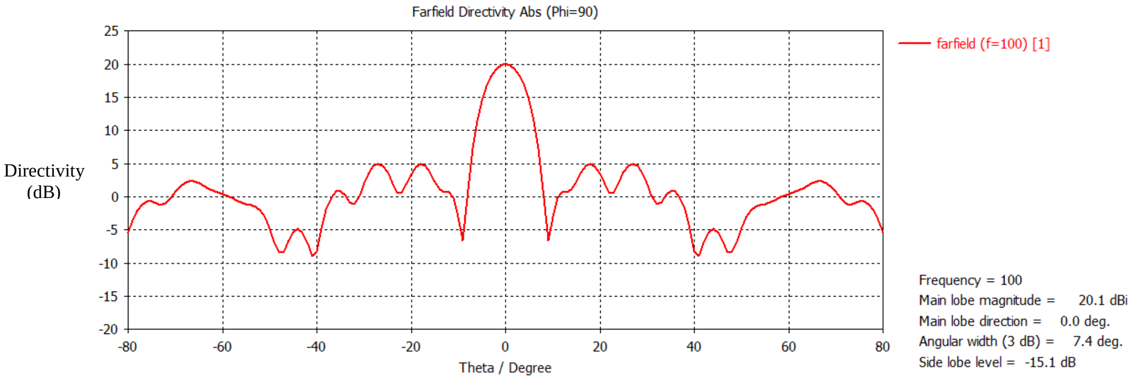

Figure 6-6c: Farfield pattern cut along the φ = 90° axis of patch antenna with cylindrical lens.

The maximum directivity of the antenna with the *x*-axis (**Figure 6-6b**) was 20.1 dBi, which was larger than when the lens was aligned with the *y*-axis (**Figure 6-4b**). Also of note, when the lens was rotated 90°, the farfield patterns also rotated 90°. The φ = 90° cross section of the farfield for the lens placed along the *y*-axis **(Figure 6-4c**) matches broadly with φ = 0° cross section of the farfield for the lens placed along the *x*-axis (**Figure 6-6b**). Both designs gave good farfield patterns and either could be used in a laboratory setting.

An elliptical cylindrical lens was also considered as shown in **Figure 6-7**. An elliptical cylinder describes a cylinder with different radii along each axis. The sides of the lens were cut to allow for multiple lenses to be placed side by side.

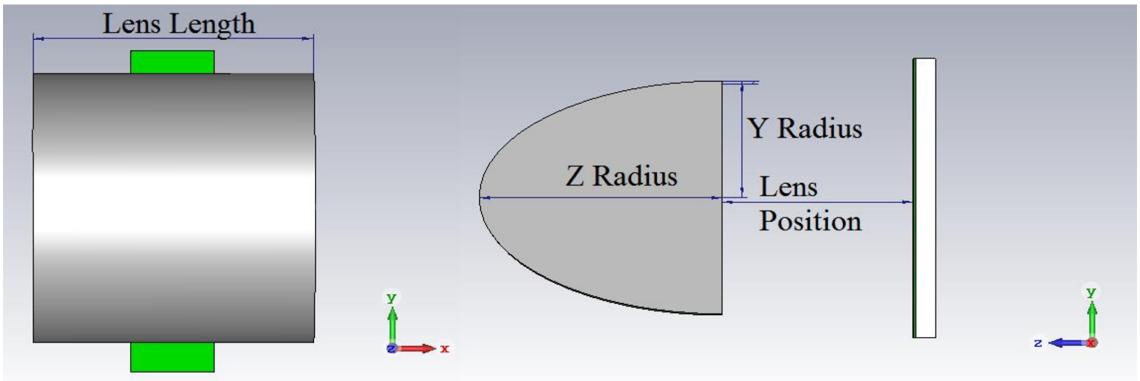

Figure 6-7: Elliptical cylindrical Lens viewed from front (left) and from side (right).

The y-radius was set to 8 mm in order to distinguish this lens from the cylindrical lens. The lens length parameter was increased from 4 → 14 mm in steps of 2 mm (results shown in **Figure 6-8**). This type of lens could possibly be manufactured to an accuracy of less than 0.5 mm. This test determined the effect the lens length had on the focal length of the lens. The distance the lens was placed in front of the antenna would need to be altered to find the true focus for the lens.

Lens length	y-radius	z-radius	Lens position
4 mm → 14 mm	8 mm	10 mm	8 mm

Table 6-5: Testing parameters for the elliptical cylindrical lens.

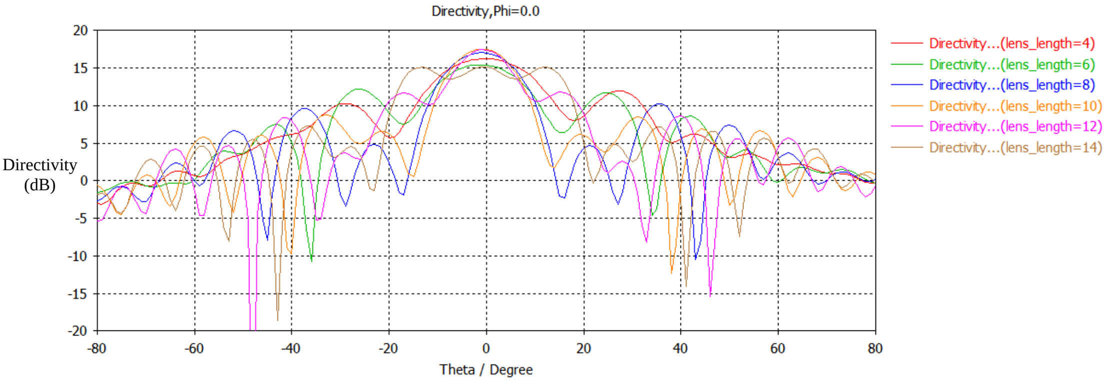

Figure 6-8a: The directivity in the φ = 0° axis as the lens length changes from 4 mm to 14 mm.

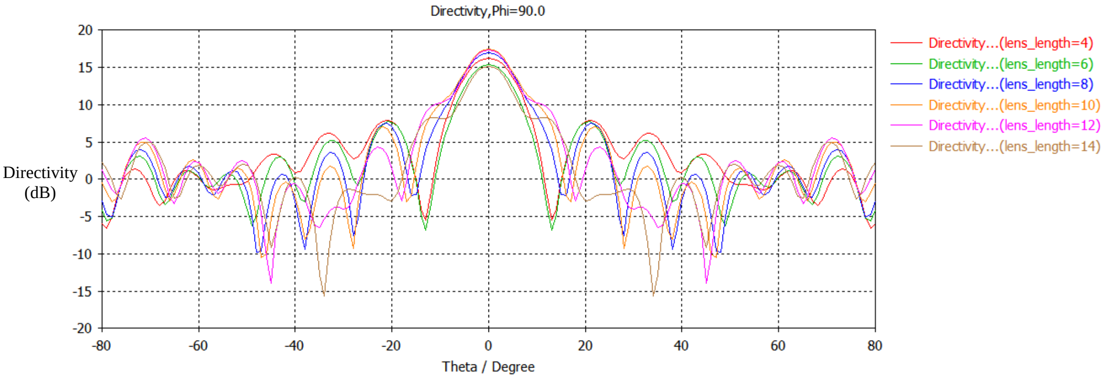

Figure 6-8b: The directivity in the φ = 90° axis as lens length changes from 4 mm to 14 mm.

Lens length (mm)	4	6	8	10	12	14
Max directivity (dBi)	16.2	15.4	17	17.4	17.4	15.1

Table 6-6: Table of maximum directivity for each lens length.

The maximum directivity for antenna with a lens length of 4 → 12 mm was found at the centre for the φ = 0° (**Figure 6-8a**) and the φ = 90° axis (**Figure 6-8b**). This direction corresponds to the positive z-axis. The larger lenses perform better than the smaller lenses. However, the lens with a lens length of 14 mm had two large side lobes in the farfield pattern, which was not ideal. The lenses with 10 and 12 mm lengths had the highest directivity of 17.4 dBi. The focus of the elliptical cylindrical lens was changing when the lens size was altered.

The radius of the elliptical lens also effected its directivity. The focus was found for an elliptical cylindrical lens with a y-radius of 5 mm.

Lens position	y-radius	z-radius	Lens length
1 mm → 10 mm	5 mm	10 mm	10 mm

Table 6-7: Parameters used to create and test the elliptical cylindrical lens.

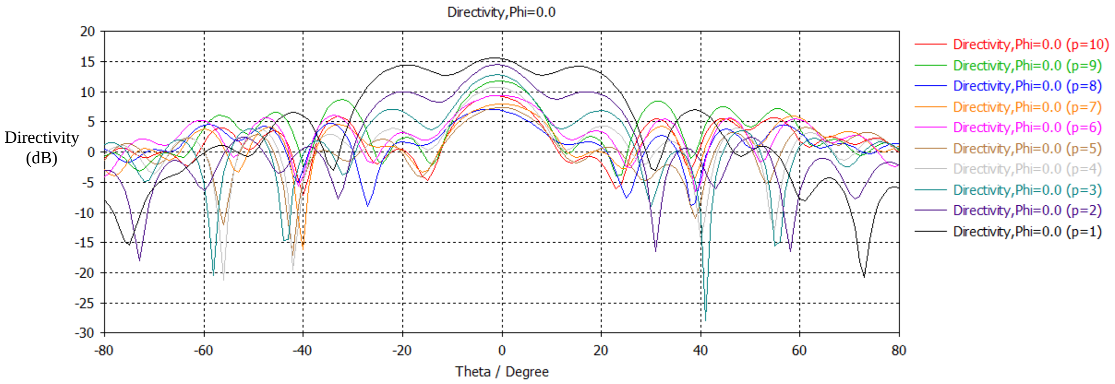

Figure 6-9: Directivity for the lenslet along the φ = 0° axis as the position of the lens was moved from 1 mm to 10 mm.

The largest directivity for **Figure 6-9** was found when the lens was 1 mm away from the antenna. The maximum directivity of this elliptical cylindrical lens was lower than the maximum found with the hemisphere lens and the cylinder lenses. The elliptical cylindrical lens was not considered further as a possible design choice.

6.2.3 Plano-convex lens

The plano-convex lenslets were similar to the hemisphere lens, but the sides of the lens were cut vertically to make the circular edge square, to potentially allow for multiple lenses to be joined together more efficiently. There were two variations on this lenslet design. The first plano-convex lens designed (shown in **Figure 6-10**) had flat vertical side faces. The second lens design, a cut was made at some angle to this flat side. This lens design creates what was called a truncated plano-convex lens (or truncated lens for short) discussed later in **Section 6.2.4**.

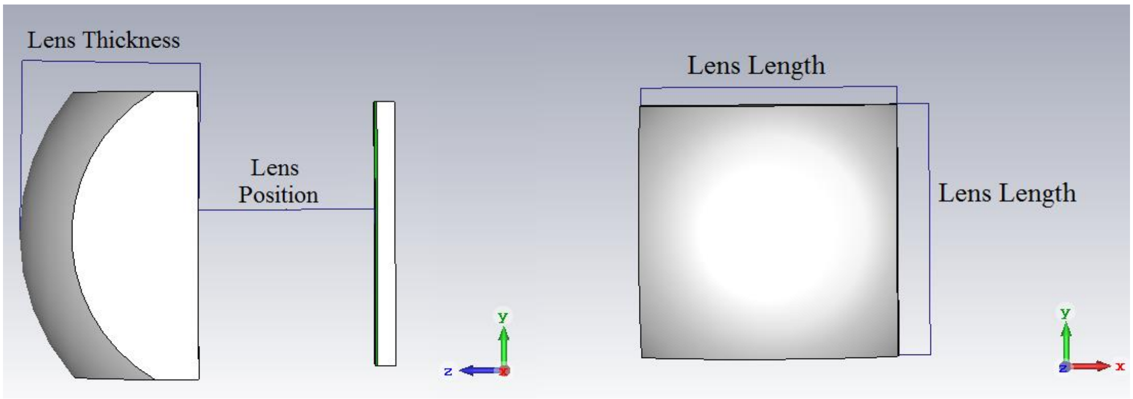

Figure 6-10: Plano-convex lenslets with the parameters used to specify its size. The thickness of the lens was the distance from the flat side to the centre of the curve.

To create these plano-convex lenslets, the sides of the hemisphere lens were cut along the *x*-*z* plane and the *y*-*z* plane. This type of design was referred to as a plano-convex lens. The lens length was the physical size of the lens along both the *x* and *y* axes. The lens thickness was the length of the lens along the *z*-axis.

The effect of the size of the lens on the pixel's performance was examined first. The thickness of the lens was initially set to 10 mm (results presented in **Figure 6-11**). The lens length could have a maximum value of 14 mm as above this value and with this thickness, the cuts created a shape than was no longer square. The position of the lens was initially set to 8 mm based on the previous test result from **Figure 6-3e**.

Lens length	Lens position	Lens thickness
10 mm → 14 mm	8 mm	10 mm

Table 6-8: Parameters used to analyse plano-convex lenses.

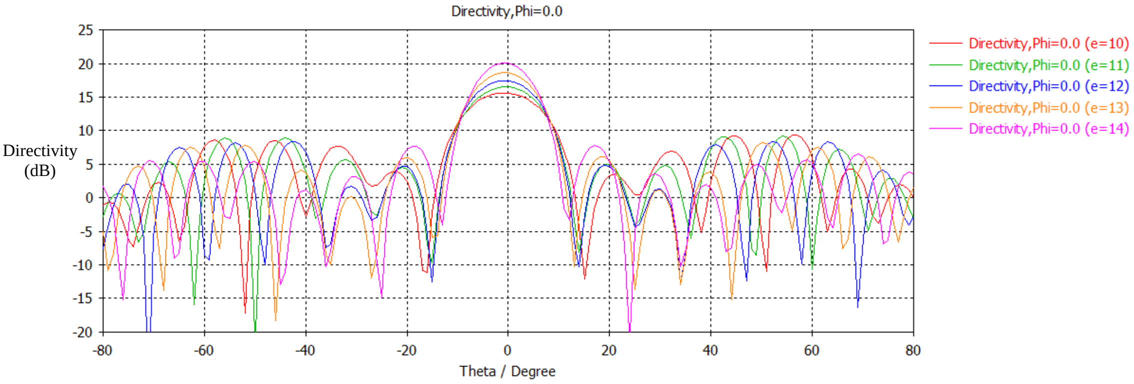

Figure 6-11: The directivity in the $\varphi = 0°$ axis as "lens length" (written as 'e' in the legend) changed from 13 mm → 10 mm.

Lens length (mm)	14	13	12	11	10
Max directivity (dBi)	20	18.7	17.4	16.5	15.6

Table 6-9: Maximum directivity of pixel observed with lens length. The larger lenses tended to have larger directivity.

The farfield patterns (**Figure 6-11b**) along the $\varphi = 0°$ axis showed that the directivity of the beam increases with length. The main beam of the pixel was on-axis for each lens length. The larger lenses have a larger on-axis directivity. Smaller lenses have lower directivity than larger lenses. The lens with a length of 14 mm performs best and produces a good symmetric farfield pattern, with a maximum directivity of 20 dBi. The plano-convex lens was not as good as the hemispherical lens, which had a maximum directivity of 24.4 dBi. This was due to the larger size of the hemispherical lens. A full comparison after the device was further optimised will be shown in **Figure 6-18.**

The larger lenses perform better, so lenses with edges greater than 14 mm may perform better. However, these larger lenses were no longer square (see **Figure 6-12a**) and when packed together, they created filling factor gaps in a potential lenslet array.

Lens length	Lens position	Lens thickness
14 mm → 19 mm	8 mm	10 mm

Table 6-10: Parameters used to test the effects of altering lenslet size.

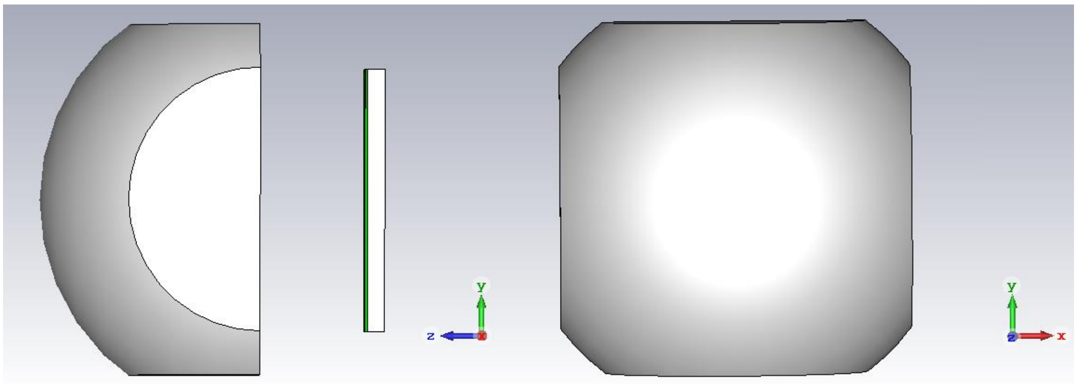

Figure 6-12a: Plano-convex lens with a lens length of 16 mm shown here. The lenslet will be inefficiently packed together due to its curved edges.

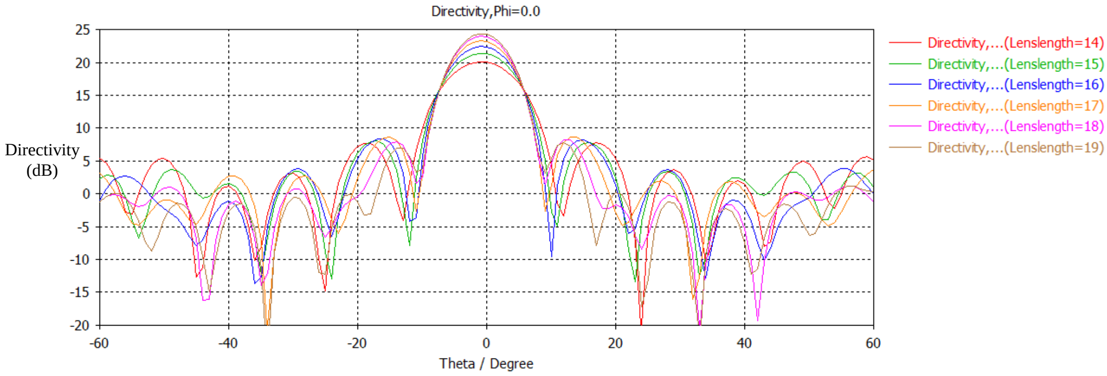

Figure 6-12b: The effect of changing lens length (written as "Lenslength" on the legend).

Lens length (mm)	14	15	16	17	18	19
Directivity (dBi)	20	21.3	22.4	23.2	24	24.3

Table 6-11: Directivity for pixel with each lens length.

Figure 6-12 shows the larger plano-convex lenses examined. All of these lenses were not exactly square in shape and have some curvature around the edges (see **Figure 6-12b**). The directivity reached a maximum for a lens with a length of 19 mm. The larger lenses produce higher directivities, but the lenses could prove to be difficult to integrate into an array due to their circular shape.

The plano-convex lens performs a little worse than the hemisphere lens, and the smaller plano-convex lenses performed worse than the larger lenses. This might be due to a change in the effective focal length of the lens or a reduction of focusing area.

The lenses that performed second best in **Figure 6-12** (the 13 mm side size lens) had its position altered relative to the patch to check if it was possible to increase the directivity. The position of the lens was altered from 3 → 12 mm in steps of 1 mm in order to find the optimum focal distance of the plano-convex lens.

Lens position	Lens length	Lens thickness
3 mm → 12 mm	13 mm	10 mm

Table 6-12: Parameters of lens used to find the correct focus for the pixel.

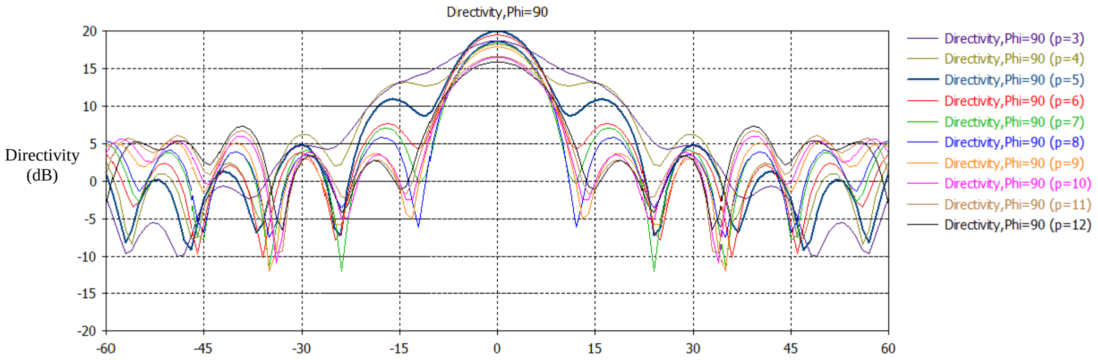

Figure 6-13: The directivity in the $\varphi = 0°$ axis as the lens position (written as 'p' in the legend) changed from 3 mm to 12 mm.

Position of lens (mm)	3	4	5	6	7	8	9	10	11	12
Max Directivity (dBi)	18.7	18.3	20	19.6	18.6	18.6	17.9	16.5	16.7	15.9

Table 6-13: Maximum directivity with lens position.

The farfield pattern of the above design (**Figure 6-13**) reached a maximum directivity of 20 dBi, while the directivity of the hemisphere lens was 24.4 dBi. The maximum directivity was found when the lens was at 5 mm from the patch. The plano-convex lens had a lower directivity than the hemisphere because it was smaller than the hemisphere lens and the patch antenna used in the pixel had a wide beam pattern.

6.2.4 Truncated plano-convex lens

An array of pixels composed of plano-convex lenses will introduce some crosstalk (reflection) between each antenna. In order to reduce crosstalk, some techniques to minimise reflections were investigated. At the sides of each lens, a cleave at an angle relative the *x*-*z* plane and the *y*-*z* plane was introduced (see **Figure 6-14**). This lens design created a truncated plano-convex lens that was referred to as the truncated lens for shorthand.

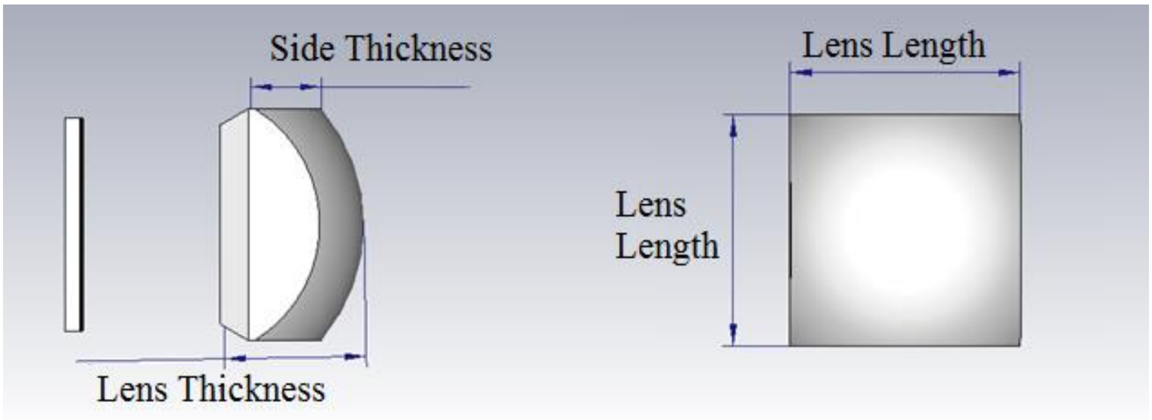

Figure 6-14a: Truncated lens pixel design. Side view with patch antenna on left and front view on right.

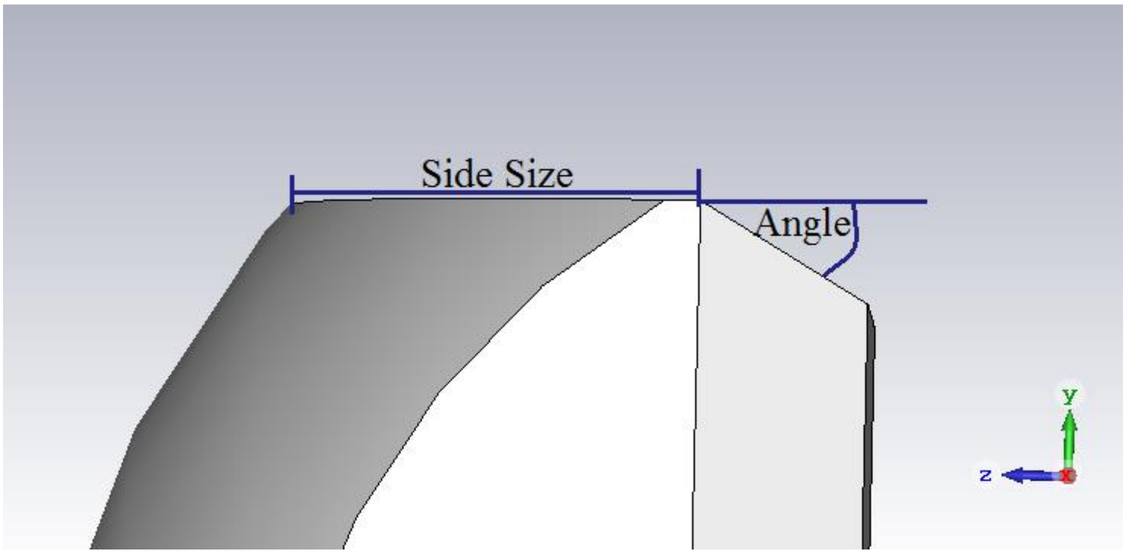

Figure 6-14b: The angle of cut used in the truncated lens design. This angle was the same for both the *x-z* plane and the *y-z* plane.

The last plano-convex lens analysed from **Figure 6-13** was used as the starting point to test this lens design. Due to the cuts on the lenses, the effective focal length of the lens may have changed. A 10 mm thickness lens was placed 8 mm from the patch antenna (see **Figure 6-15b** for simulation setup). The position was changed from 8 → 2 mm in steps of 2 mm, in order to find the optimum focal distance of the lens.

Lens position	Lens thickness	Side size	Lens length	Angle
8 → 2 mm	10 mm	5 mm	13 mm	30°

Table 6-14: Parameters for truncated lens. The distance between the lens and the patches surface was varied in order to find the focus

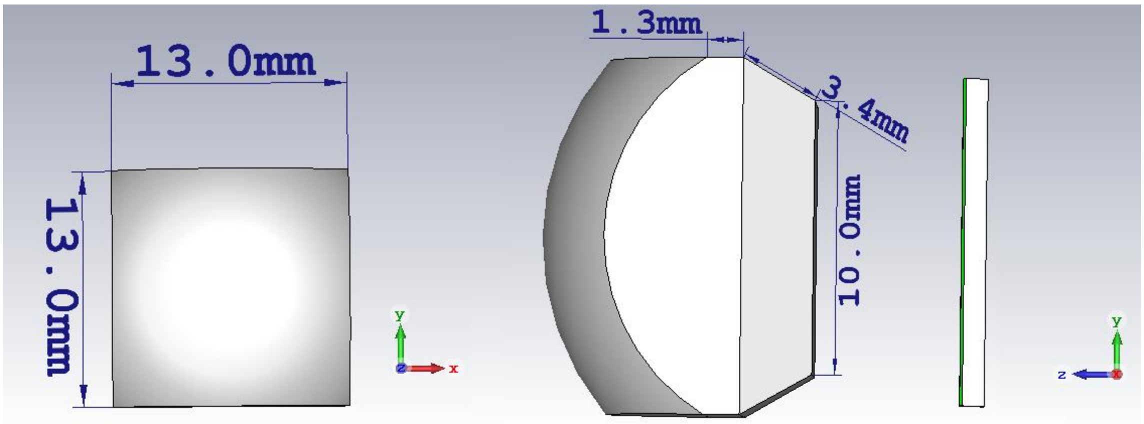

Figure 6-15b: Truncated lens with a lens thickness of 10 mm placed in front of patch antenna.

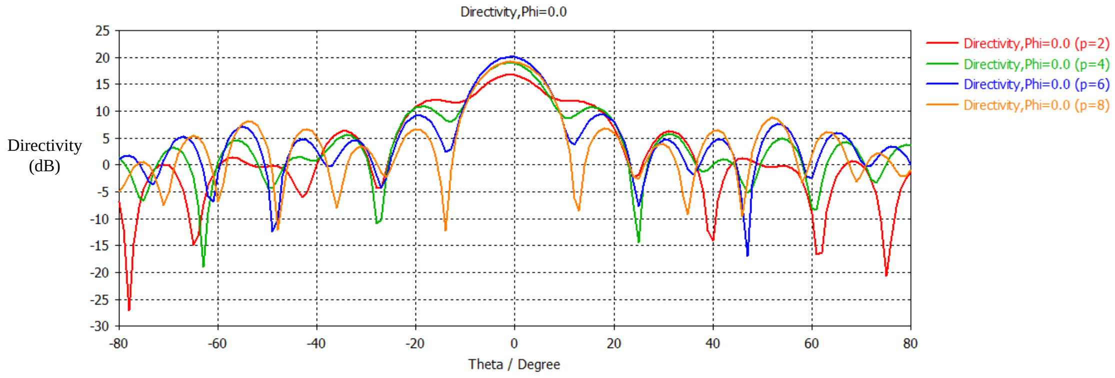

Figure 6-15c: Farfield pattern of the antenna due to the position of the truncated lens when placed at various positions.

The previously designed lenslets (**Figure 6-15c**) produce a good farfield pattern, but it was more difficult to manufacture due to the additional angular cuts. The peak directivity of 20 dBi was comparable to the max directivity found in the cylindrical lens and the plano-convex lens. The thickness of the lens was increased from 10 →19 mm to determine the effects of the lens size (as detailed in **Figure 6-16**). The lenses were all placed 4 mm away from the antenna, as this was the focus for the 10 mm lens.

Lens thickness	Lens position	Side size	Lens length	Angle
10 mm → 19 mm	4 mm	Lens thickness/2	13 mm	30°

Table 6-15: Parameters used to test a truncated lens of varying lens thickness placed in front of patch antenna. The side length of each lens was set to half of its lens thickness.

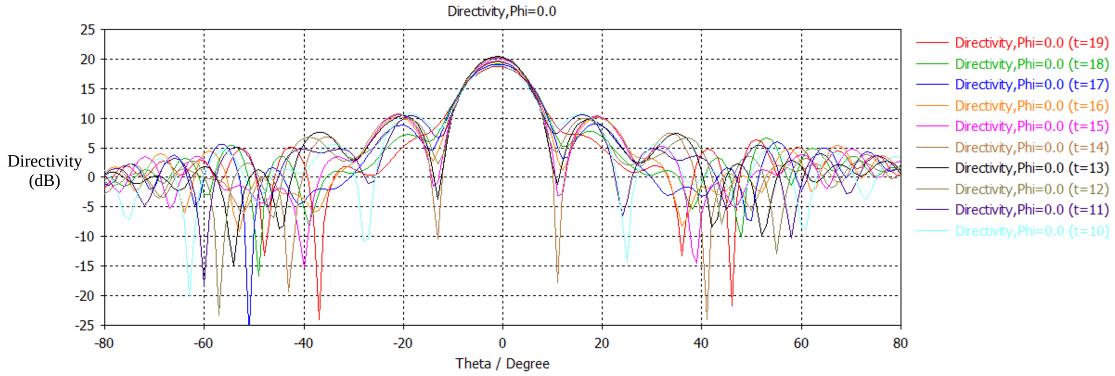

Figure 6-16: Truncated lens of different sizes.

Lens thickness (mm)	19	18	17	16	15	14	13	12	11	10
Max directivity (dBi)	18.7	19.2	19.4	20	20	20.3	20.3	20.1	19.5	18.9

Table 6-16: Maximum directivity for each sized lens.

The different lenses shown in **Figure 6-16** have similar farfield patterns with the maximum directivity always located on axis. The maximum directivity ranges from 18.7 dBi to 20.3 dBi.

One reason for the difference in the directivity of the lens was that the position of the effective focus changes. In **Figure 6-17**, the lens was increased in size to 19 mm and the position of the lens was altered from 2 → 8 mm in steps of 2 mm, to examine if the focus position of the lens was different for this lens design than the previous lens (**Figure 6-15**).

Lens position	Lens thickness	Side thickness	Edge length	Angle
2 mm→ 8 mm	19 mm	9.5 mm	13 mm	30°

Table 6-17: Parameters used to create truncated lenslet with a lens thickness of 19 mm placed in front of rectangular patch antenna.

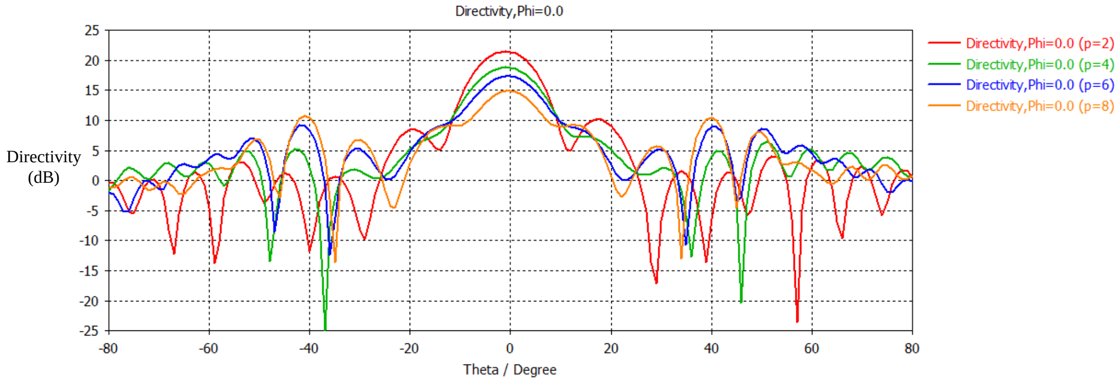

Figure 6-17: Farfield pattern of the antenna due to the position of the truncated lens.

The maximum directivity in **Figure 6-17** was 21.4 dBi and this was found when the lens was 2 mm from the antenna.

The directivity of this lens was larger than both the maximum directivity of both the cylindrical lens (**Figure 6-6**) and the plano-convex lens (**Figure 6-13**), but smaller than the hemisphere lens (**Figure 6-3**). This lens will be used to measure crosstalk as it was large enough for the cuts to be milled accurately and produced a farfield pattern with a large maximum directivity.

Four different lens designs have been examined and the farfield patterns of these different lens types are compared in **Figure 6-18**:

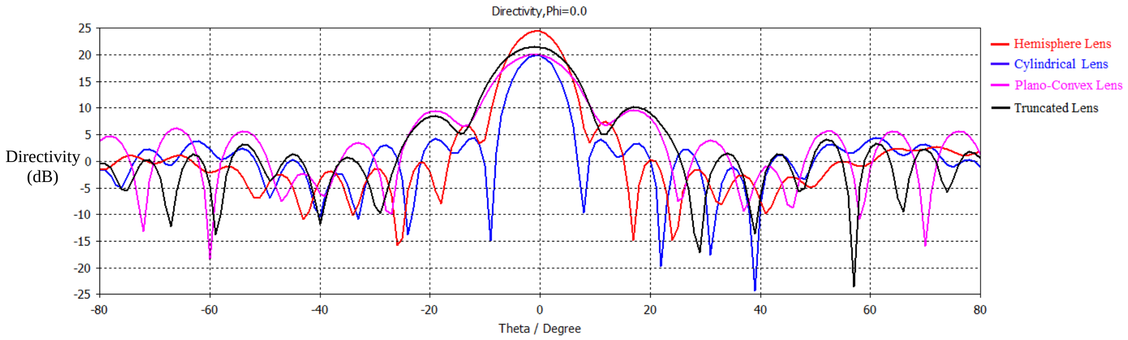

Figure 6-18: Comparison of 4 lenses placed in front of patch antenna at 100 GHz. Each lens had a unique farfield pattern and were not designed to be equivalent.

	No Lens	Hemisphere lens	Cylinder lens	Plano-convex lens	Truncated lens
On-axis directivity	7.6 dBi	24.3 dBi	19.8 dBi	20 dBi	21.4 dBi

Table 6-18: Comparison of maximum directivity for different lens types.

	Hemisphere lens	Cylinder lens	Plano-convex lens	Truncated lens
Radius	10 mm	10 mm	10 mm	10 mm
Position	8 mm	10 mm	5 mm	2 mm
Lens thickness	10 mm	10 mm	10 mm	19 mm
Lens length	-	10 mm	13 mm	13 mm
Side length	-	-	-	9.5 mm
Angle	-	-	-	30°

Table 6-19: Parameters used to create each lens. Lens thickness was the *z*-axis length of the lens and lens length was the *x*-axis and *y*-axis length of the lens.

The main result from **Figure 6-18** was that each lens had increased the directivity of the patch antenna to similar levels. Further optimisation could be carried out to improve and optimise the directivity of each design, but this analysis was not included here. All of these lens designs would be acceptable in many applications where in general, larger lenses were preferred for easier manufacturing.

6.3 Crosstalk analysis with plano-convex lens

For practical array systems, planar antennas are regularly used with small lenses or lenslets to add directionality the system. The crosstalk between identical antennas, with the addition of the lens array, was also investigated. Crosstalk in this context was used to describe the power reflected between neighbouring elements.

The purpose of designing the truncated lens (with angled cut sides) was to reduce the crosstalk between neighbouring antennas. The plano-convex pixel was compared to this truncated plano-convex lens in order to determine if the truncated pixel was worth developing.

In order to compare with previous tests, the same patch antenna (**Figure 3-14**) was used in these comparison tests. Only crosstalk along the *x*-axis was measured as this axis had a larger degree of crosstalk due to the asymmetric beam pattern of the patch antenna, which was previously observed when testing these devices in **Figure 3-22**.

A new plano-convex lens was designed (shown in **Figure 6-19a**), in order to have an accurate comparison between the plano-convex and the truncated lenslet designs. The following figures are a summary of a plano-convex lens used to reduce the crosstalk with in the array.

Position of lens	Radius	Lens length	Lens thickness
2 mm	10 mm	13 mm	13 mm

Table 6-20: The parameters used to create the lens are also shown. This lens design was based on the results from **Figure 6-13**. The lens was made longer to make it the same size as the truncated lens.

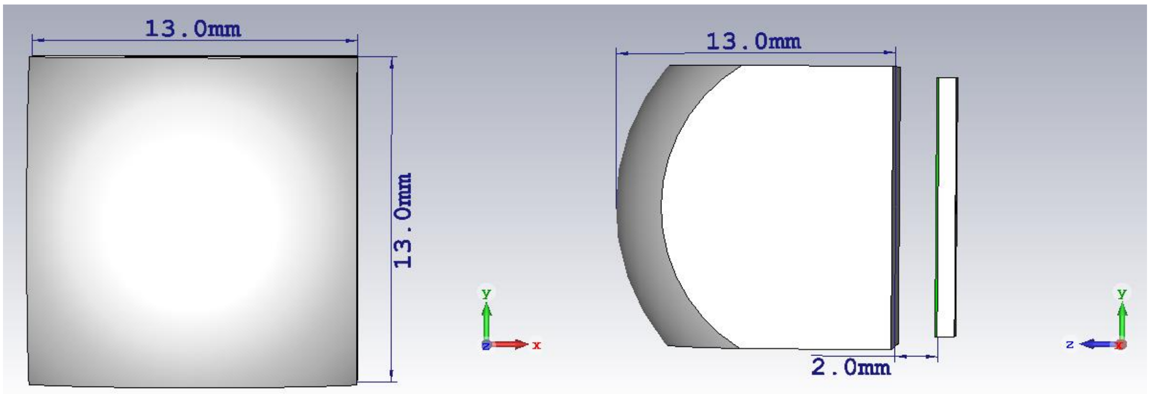

Figure 6-19a: Plano-convex pixel as viewed from front (left) and side (right).

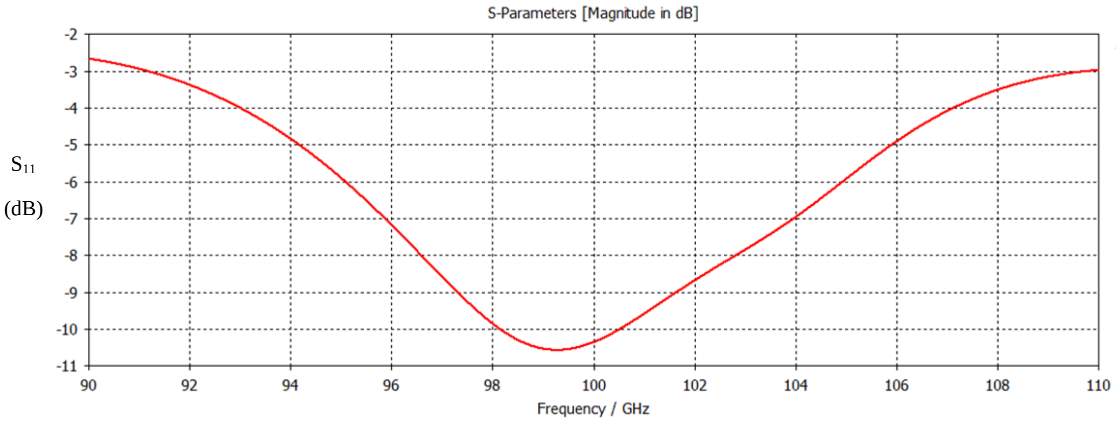

Figure 6-19b: S_{11} parameter (return loss) of the plano-convex pixel between 90 GHz → 110 GHz.

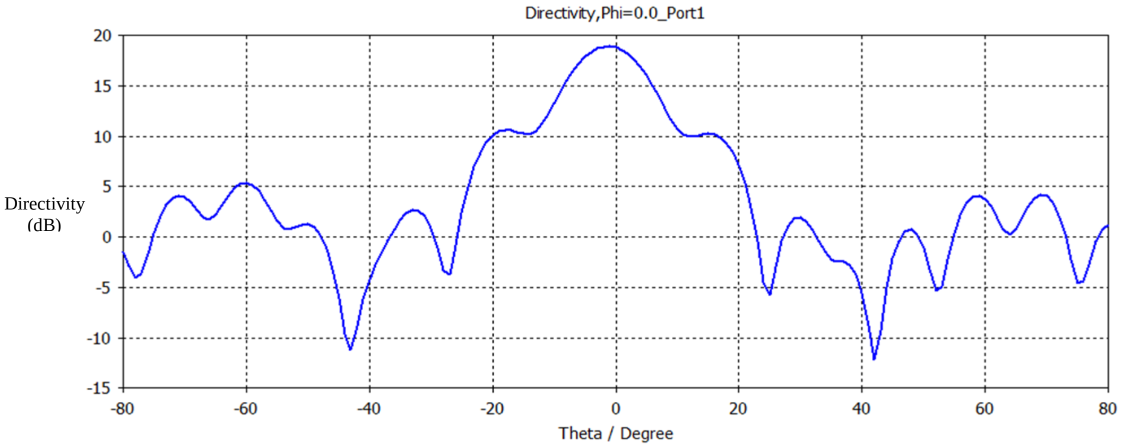

Figure 6-19c: Plano-convex pixel directivity at 100 GHz.

The S_{11} parameter in **Figure 6-19b** showed that the plano-convex pixel radiates its power best at frequencies between roughly 98 GHz → 100 GHz. The maximum directivity (**Figure 6-19c**) of this plano-convex lens design was 18.8 dBi at 100 GHz.

The truncated lenslet was designed in order to reduce crosstalk between neighbouring antenna in array using the cleaving illustrated in **Figure 6-20a**. More detail on this lens design is found in **Figure 6-15**.

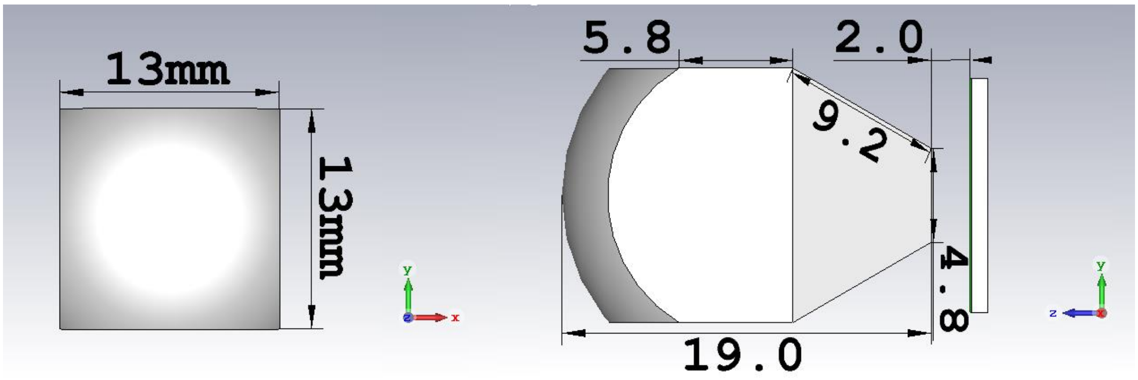

Figure 6-20a: Truncated lens with a lens thickness of 19 mm placed in front of patch antenna. Front view on left and side view on right.

Position of lens	Radius	Lens length	Thickness	Angle	Size length
2 mm	10 mm	13 mm	19 mm	30 °	9.5 mm

Table 6-21: Parameters used to create truncated lenslet.

The maximum directivity of this truncated lens design was 21.4 dBi.

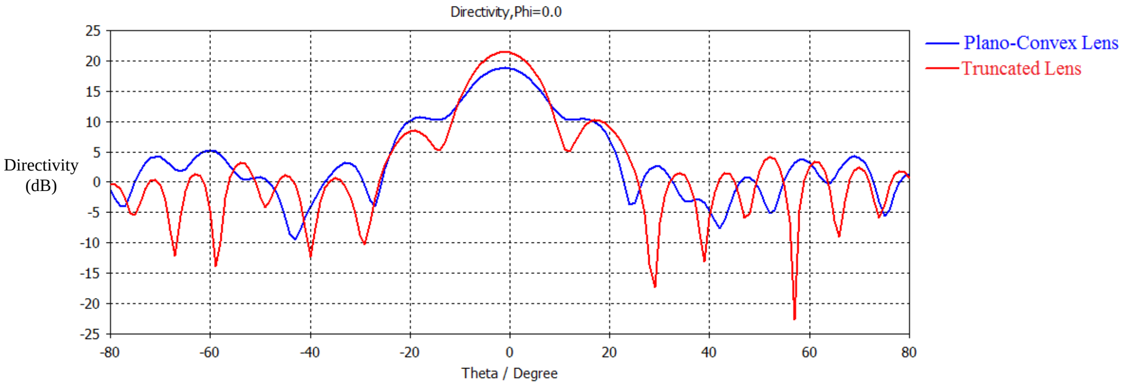

Figure 6-21: Comparison between the farfield generated by the plano-convex and truncated design.

The farfield in **Figure 6-21** shows the directivity of the truncated lens was larger than the maximum directivity the plano-convex lens.

6.3.1 Crosstalk in a 2 × 1-lenslet array

The 2 × 1-patch antenna array was analysed using the patch antenna in **Figure 3-18**, with the distance between the patches set to 13 mm. The patches were printed on the same substrate in this simulation. Both designs had a lens length of 13 mm. The two wires connected to the patches were placed 13 mm apart so that the lenses could be placed in front of the patches, without leaving any space.

Patch length (along *x*-axis)	Patch width (*y*-axis)	Wire offset along *x*-axis	Wire offset along *y*-axis	Wire-to-wire distance	Substrate thickness
0.9 mm	0.72 mm	0.2 mm	0 mm	13 mm	0.1 mm

Table 6-22: Parameters for creating 2 × 1 patch antenna.

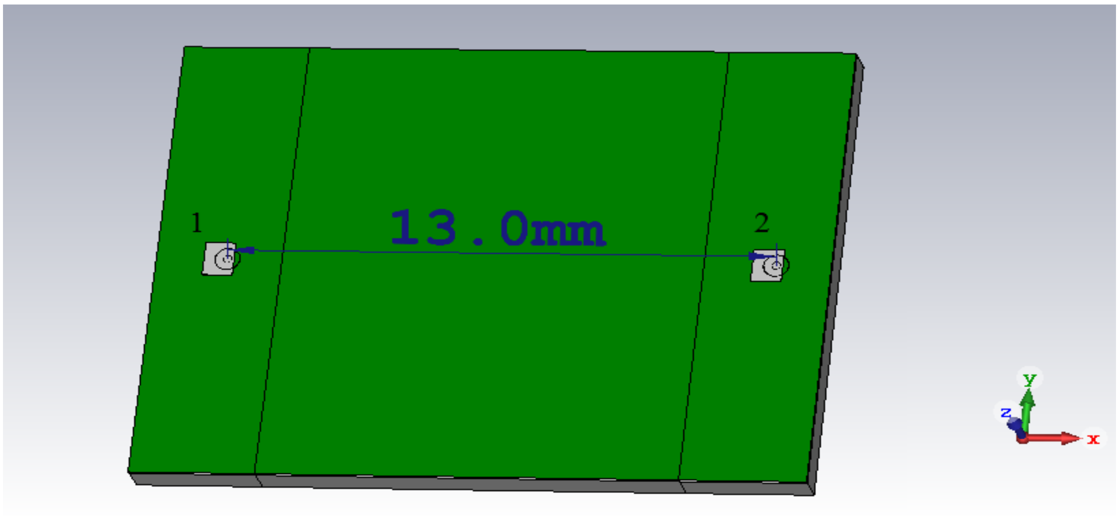

Figure 6-22a: Diagram 2 × 1-patch antenna array. Patch 1 was connected to port 1 and port 2 was connected to port 2.

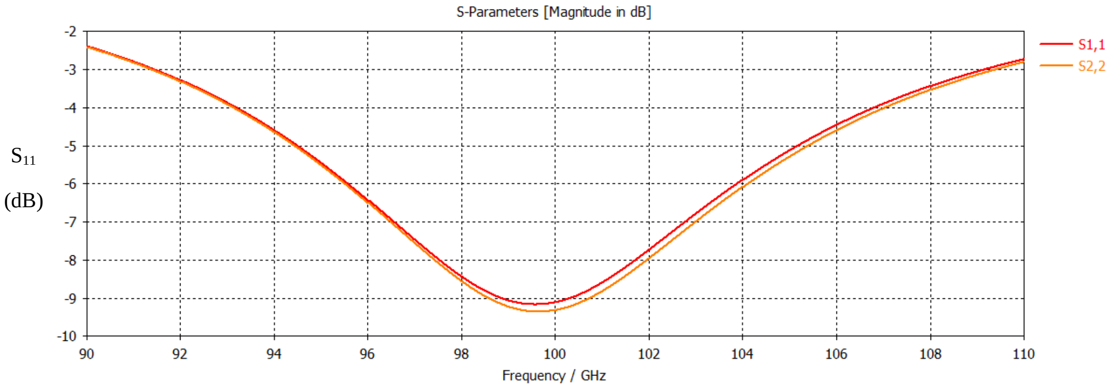

Figure 6-22b: S_{11} and S_{22} parameters of 2 × 1-patch antenna array between 90 GHz and 110 GHz. S_{11} was the return loss for antenna 1 and S_{22} was the return loss for antenna 2.

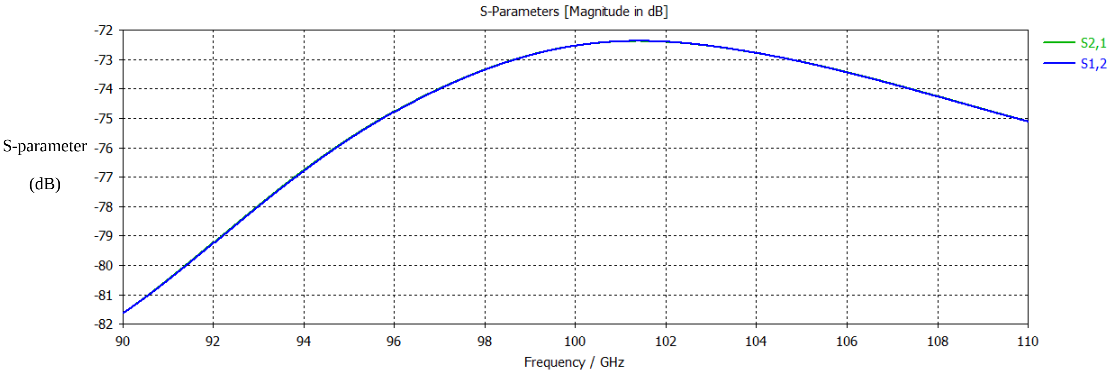

Figure 6-22c: S_{21} and S_{12} of 2 × 1-patch antenna array between 90 GHz and 110 GHz. S_{21} was crosstalk from patch 1 to patch 2 and S_{12} was crosstalk from patch 2 to patch 1.

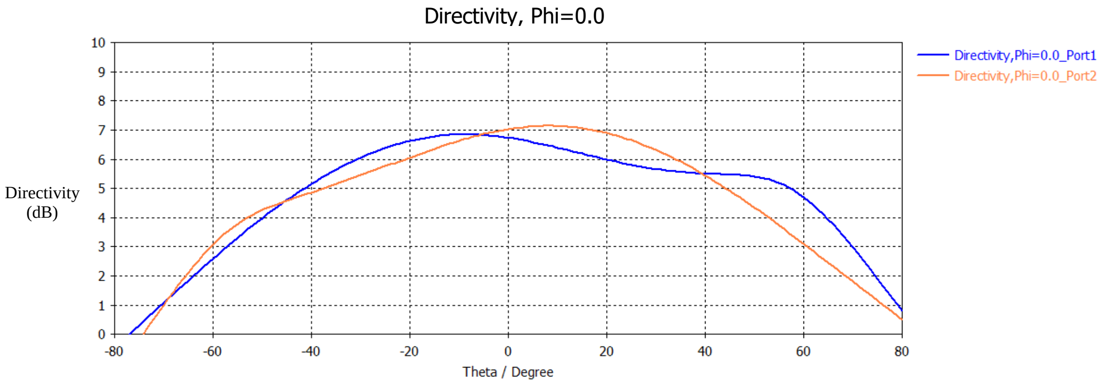

Figure 6-22d: Farfield beam created by patch 1 (port1) and patch 2 (port2).

Figure 6-22b and **Figure 6-22c** shows the S-parameters over the frequency range 90 →110 GHz behaved as expected for identical antennas operating in an array. Both of the minimums of these parameters were located at 100 GHz, which indicates that both patches were resonant at this frequency. At 100 GHz, both the S_{21} and S_{12} had a very low level of crosstalk of -72.5 dB. The S_{21} and S_{12} were shown to be identical over this frequency range, which means that an equal amount of power passes from patch 1 to patch 2 (S_{21}) as passes from patch 2 to patch 1 (S_{12}). However, **Figure 6-22d** shows the farfield pattern created by patch 1 (port1) and patch 2 (port2) were different when compared to each other due to the positioning of the patches. The cause of the difference was due to the position of the patches relative to each other. The antenna on the left (patch 1) was more sensitive to signals on the left than the antenna on the right and vice versa.

The plano-convex HDPE lens was placed in front of the antenna array described previously and **Figure 6-23b** describes the results of this CST simulation (see **Figure 6-24** for test performed with truncated lenslets).

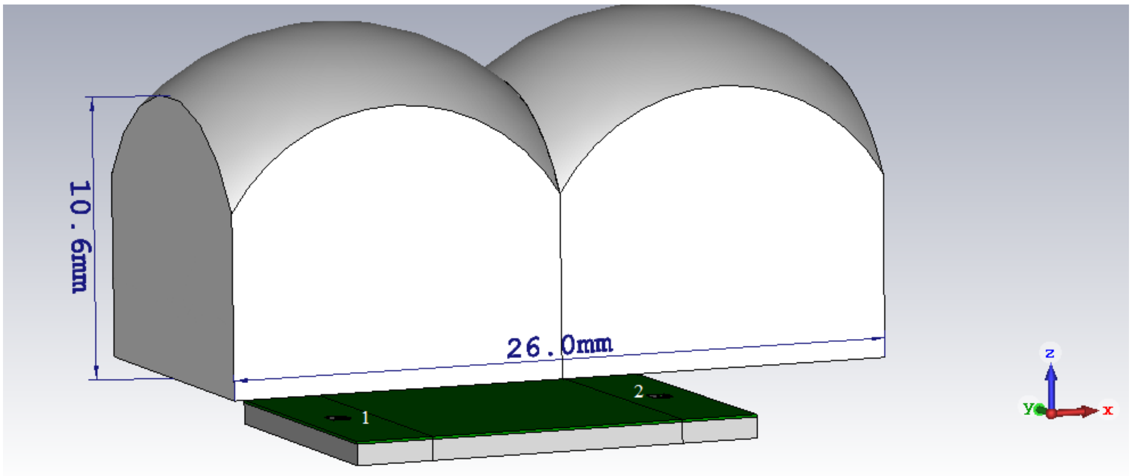

Figure 6-23a: Two patch antennas with plano-convex lenses placed in front (2 × 1-plano-convex lenslet array). The geometry of the system was shown in **Figure 6-23a**, with pixel 1 located on the left and pixel 2 located on the right. The pixels were labelled according to the ports they were connected to.

The patches were located on a single substrate. This was to allow for easier comparison between the plano-convex and the truncated lens.

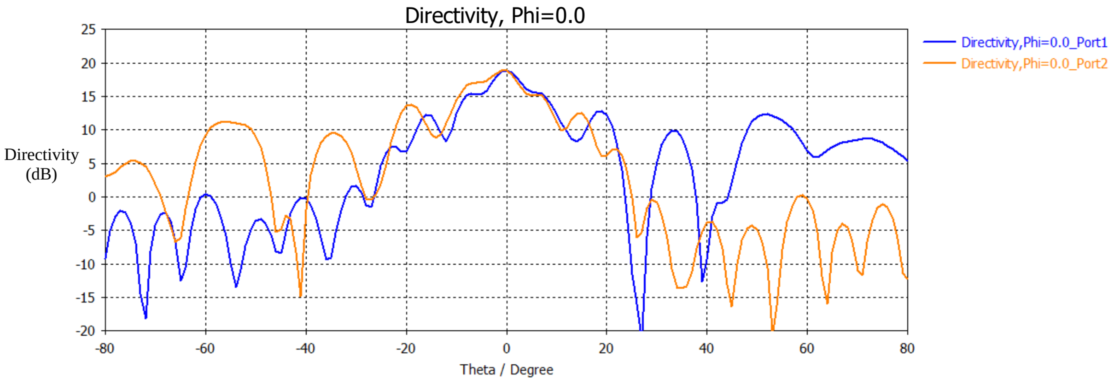

Figure 6-23b: Farfield pattern of the two pixels placed 10 mm apart, in a 2 × 1-plano-convex lenslet array with antenna 1 in blue and antenna 2 in orange.

The beam patterns of antenna 1 and 2 were asymmetrical and large side lobes were observed in both beam patterns (**Figure 6-23b)**. Both antenna in the graph have a large directivity of 18.9 dBi and 18.8 dBi. The main lobe had an angular width of 11.5° and 11.1° for patch 1 and 2 respectively. This farfield pattern had three major side lobes. For the first pixel, three side lobes appear on the right side, but not on the left side and the largest had a directivity of 12.7 dBi. These side lobes were most likely due to power reflected by the lens, back to the second patch and radiating through the second lens.

A similar effect was observed in the farfield pattern of the second antenna which appears to be a mirror image of antenna 1 beam pattern rotated about the $\varphi = 0°$ axis. The largest of the three side lobes for the second antenna had a maximum directivity of 13.7 dBi.

The plano-convex lenses were replaced with the truncated plano-convex lenses and the following figure (**Figure 6-24**) details the CST simulation.

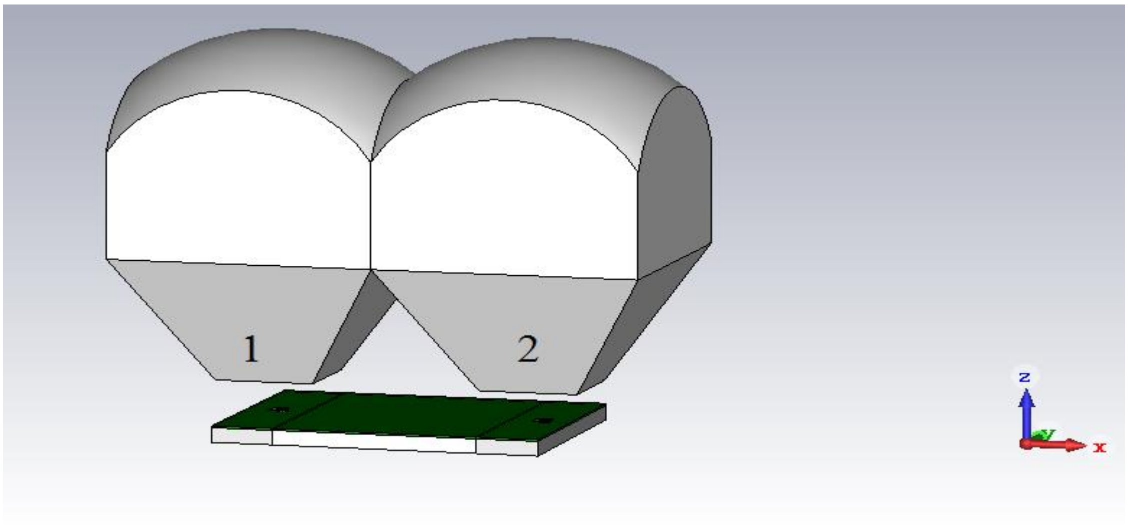

Figure 6-24a: Two truncated lens pixels with pixel 1 on left and pixel 2 on right.

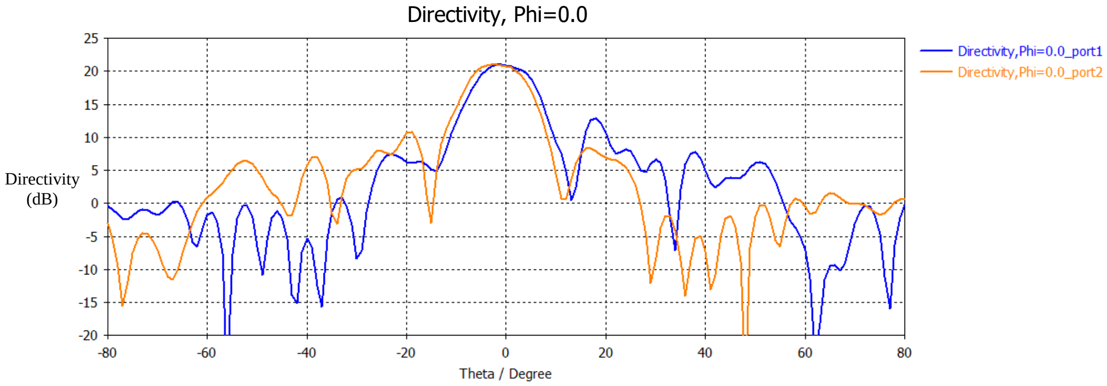

Figure 6-24b: Farfield pattern of the 2 × 1-truncated lenslet array.

There was a strong similarity between the farfield patterns generated by the plano-convex and the truncated lens pixel. The plano-convex farfield pattern (**Figure 6-23b**) and the truncated convex farfield pattern both shows that the beam pattern of the second antenna was a mirror image of pixel 1's beam pattern. Both of their beam patterns peak at the centre of the graph and both beam patterns have small side lobes.

In the following summaries, the farfield pattern and the S-parameters from the truncated lens array (**Figure 6-24b**) were compared to the results from the bare patch array (**Figure 6-22**) and the plano-convex pixel array (**Figure 6-23**).

	Pixel	Directivity at 100 GHz
No lens	1	6.7 dBi
	2	7 dBi
Plano-convex lens	1	18.9 dBi
	2	18.8 dBi
Truncated lens	1	20.9 dBi
	2	20.8 dBi

Table 6-23: Comparison of the directivity of two antennas placed 10 mm apart, with no lens pixel (**Figure 6-22e**), plano-convex lens pixel (**Figure 6-23b**) and truncated lens pixel (**Figure 6-24b**).

	No lens	Plano-convex lens	Truncated lens
S_{11} (dB) at 100 GHz	-9.1	-10.4	-9.9
S_{21} (dB) at 100 GHz	-72.5	-32.1	-50.6

Table 6-24: Comparison of the S-parameters for different lens types at 100 GHz. The plano-convex lens pixel result was from **Figure 6-23**, the truncated lens pixel result was from **Figure 6-24** and the "no lens" result was from **Figure 6-22**.

Table 6-23 compares the results from different lenslet simulations. The truncated lens the directivity of both patch 1 and patch 2 was increased by the introduction of the lenses. The slight difference in directivity measured was due to the different positions of the patch antennas.

Table 6-24 compares the S-parameters between the two patches at 100 GHz. The crosstalk (S_{21} parameter) between the patches increased with the addition of the lenses. The plano-convex lens increased crosstalk more than the truncated lens. With the truncated lens placed in front of the antenna array, less power from antenna 1 reflects into antenna 2 as desired.

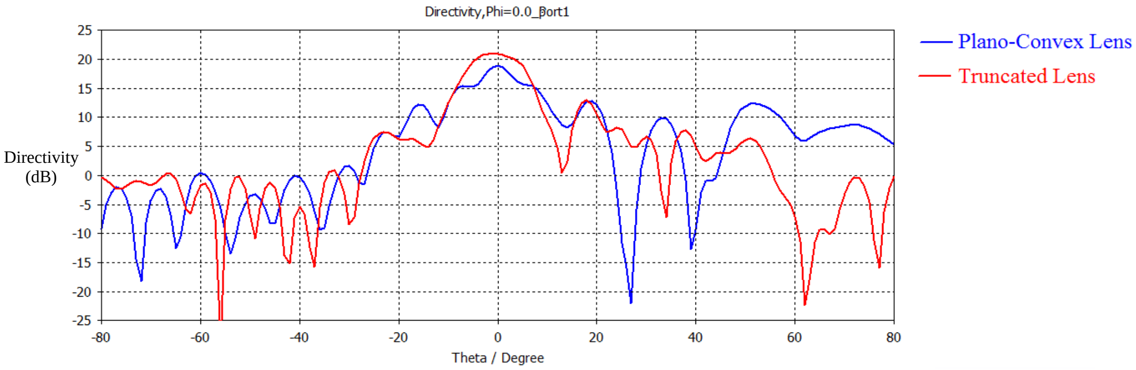

Figure 6-25: Comparison of farfield pattern generated by the rectangular patch antenna, when the plano-convex lenses (**Figure 6-23b**) and truncated lenses (**Figure 6-24b**) were placed in-front.

The farfield patter in **Figure 6-25** shows that with the plano-convex lens, the antenna generates several large side lobes, the largest of which had a directivity of 12.3 dBi, located between 45° and 60° from the centre. With the truncated lens, this side lobe was reduced in size to about 6 dBi. The truncated lens had a more directive beam than the plano-convex lens.

For this 2 × 1 patch antenna setup, the truncated lens performs better than the plano-convex lens. As well as reducing crosstalk, the truncated lens also increases the directivity over the plano-convex lens. The crosstalk in a larger antenna array will also need to be tested, to see if the truncated lens will always perform better.

6.3.2 Crosstalk in a 3 × 1-lenslet array

Patch antennas and lenses were combined in order to create a 3 × 1 pixel array. Each patch was spaced a distance of 13 mm apart. These antennas were all created on the same PCB and were labelled 1 → 3 along the positive *x*-axis. The power transferred between the three pixels was analysed in order to evaluate the crosstalk from one pixel to another.

This system was a 3-port system, as there were three antennas in the structure (see **Figure 6-26a** for diagram). Nine different coupling S-parameters were recorded in the simulation as well as the directivity of each antenna. Of particular interest was the S_{31} and S_{13} parameter, i.e. the crosstalk between antenna 1 on the left and antenna 3 on the right. The effects on crosstalk due to the plano-convex lenslets were examined first (see **Figure 6-27** for test using truncated lenslets).

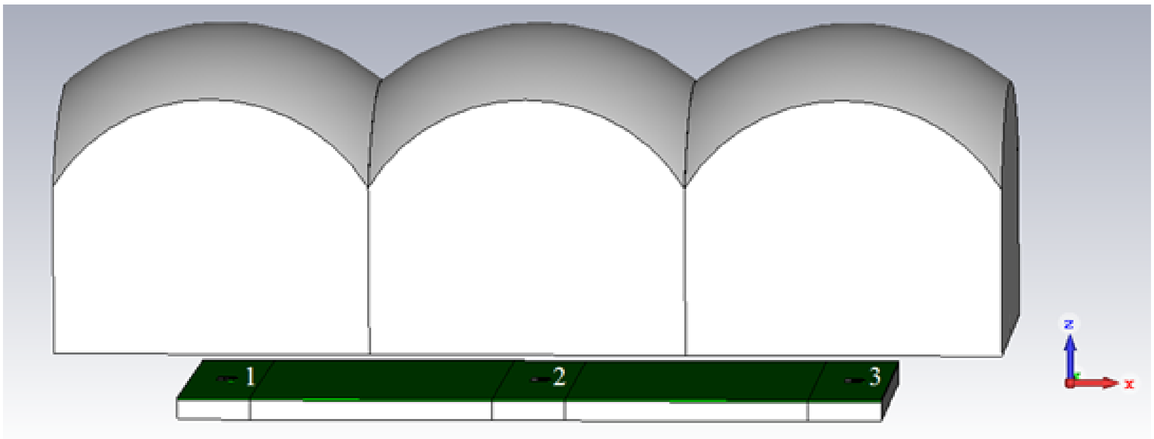

Figure 6-26a: 3 × 1-plano-convex pixels. This is a 3-port system containing 3 identical patch antennas.

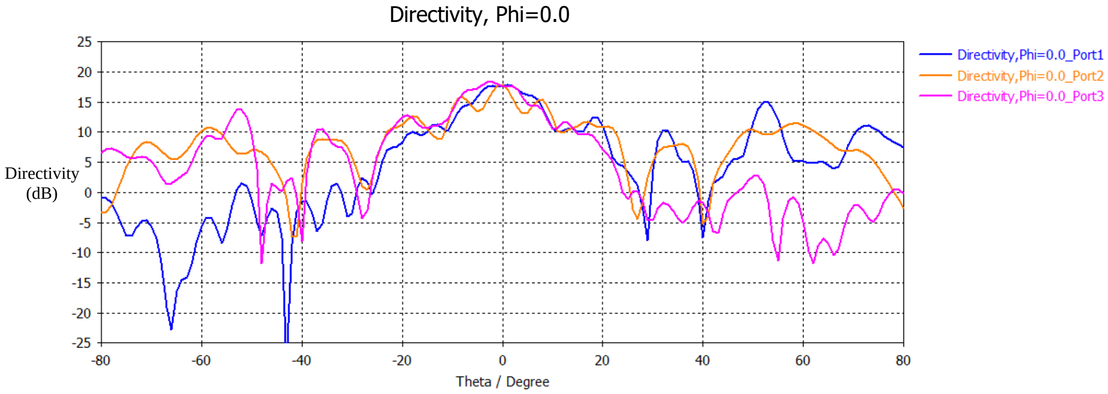

Figure 6-26b: The directivity of pixel 1, 2 and 3 for the 3 × 1-plano-convex lens array.

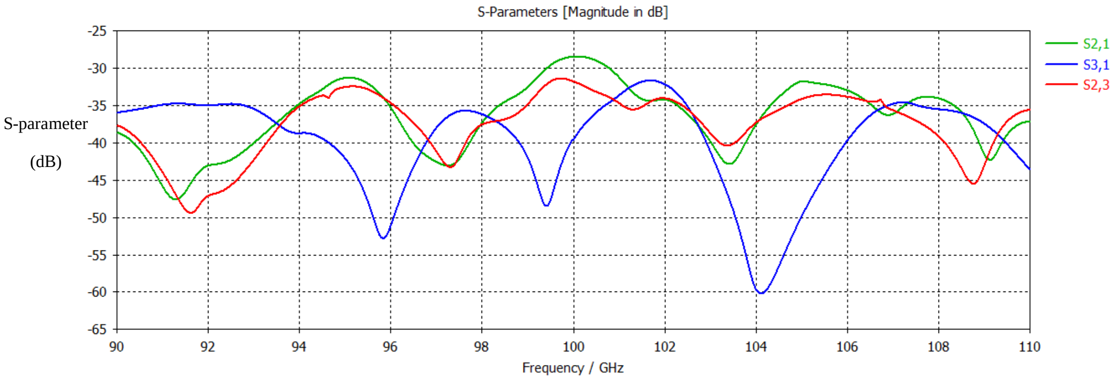

Figure 6-26c: S-parameters of the pixels over a section of the W band frequency range.

The three pixels were arranged from left to right (as seen in **Figure 6-26a**). In **Figure 6-26b** the pixel on the far left (pixel 1) had an increase in directivity on its right-hand side, but not on the left-hand side. In other words, the side with a neighbouring lenslet had an increase in side-lobes. A similar effect was seen for the pixel on the far right (pixel 3), which had an increase of directivity on its left-hand side. The pixel in the centre (pixel 2) had side lobes on both sides. This result would suggest that the lenses affect the directivity of the neighbouring patches by increasing the size of the side-lobes.

The crosstalk due to the truncated plano-convex lens array was also examined, as detailed in the following. Once again, the pixels were labelled 1→ 3 along the positive *x*-axis.

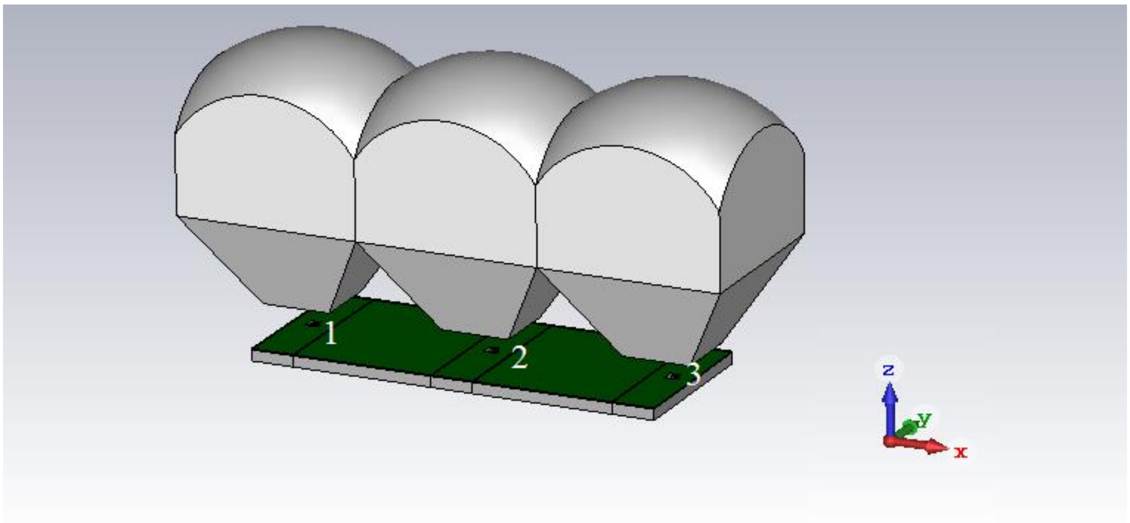

Figure 6-27a: Truncated lenses placed in front of 3 × 1 patch antenna array.

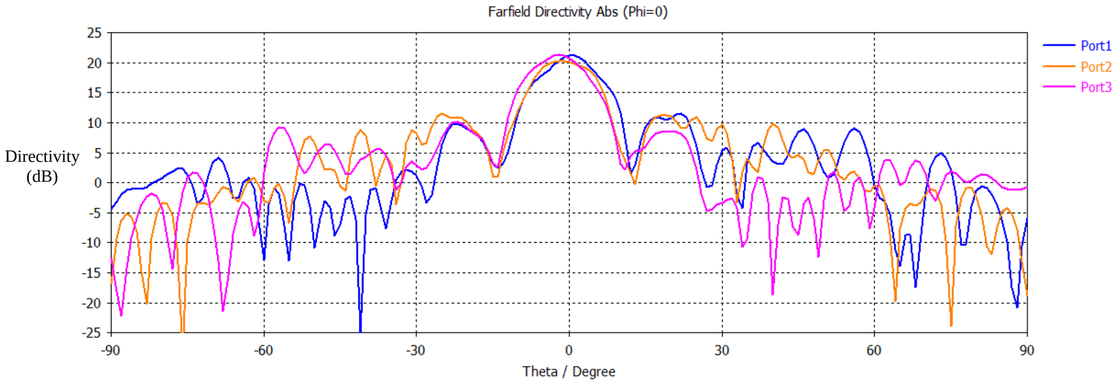

Figure 6-27b: Farfield from the three ports. Each port connects to a patch on the array.

The farfield plot in **Figure 6-27b**, the patch on the far left (pixel 1) had an increase in directivity on its right-hand side and vice versa. The patch in the centre (pixel 2), like before, had side lobes on both sides.

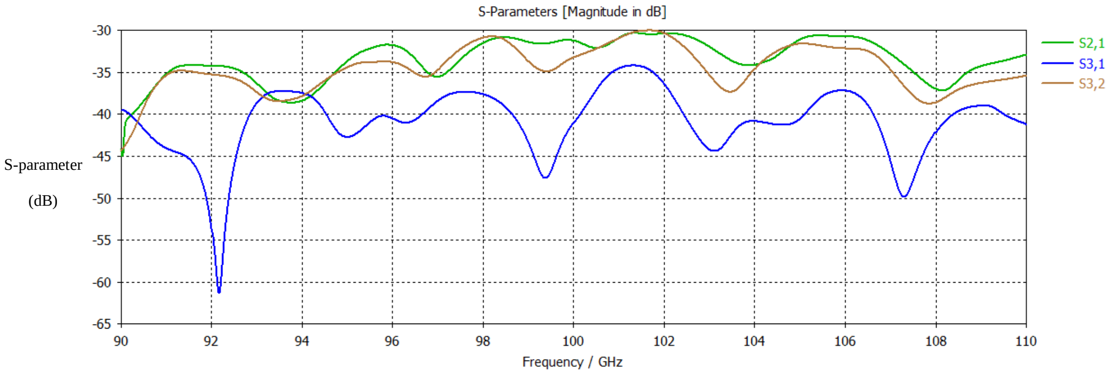

Figure 6-27c: S-parameters of the pixel over a section of the W band frequency range.

The crosstalk between each of the three antennas (shown in **Figure 6-27c**) showed a wide variation over the W band frequency. This was similar to the effect observed in **Figure 6-26c** and will be examined in **Figure 6-28a**.

	S_{11} (dB)	S_{22} (dB)	S_{33} (dB)	S_{21} (dB)	S_{31} (dB)	S_{32} (dB)
Plano-convex lens	-10.4	-11.1	-10.7	-28.5	-39.5	-31.8
Truncated lens	-9.8	-10	-10.2	-31.2	-41	-33.2

Table 6-25: Comparison of S-parameters at 100 GHz between the different tested lens with 3 × 1 patch antenna array.

Table 6-25 shows a comparison of the S-parameters for the two different lenslets. The two lenslets tested were the plano-convex lenses (**Figure 6-26**) and truncated lenses (**Figure 6-27**). The power transferred between the first and second patch, the second and third patch and the first and third patch was smaller with the truncated lenslets than with the plano-convex lenslets. The truncated lens had reduced crosstalk between antennas overall.

	Pixel	Directivity at 100 GHz (dBi)	Angular width
Plano-convex lens	1	17.7	13.5
	2	17.9	5.7
	3	17.9	13.3
Truncated lens	1	21.2	10
	2	20	12.4
	3	20.8	10.9

Table 6-26: Comparison of directivity between the different systems.

Table 6-26 shows that the directivity of the truncated lens array was greater than for the plano-convex array. However, for the truncated lens, the directivity of the second antenna did not increase as much as the first and third antenna.

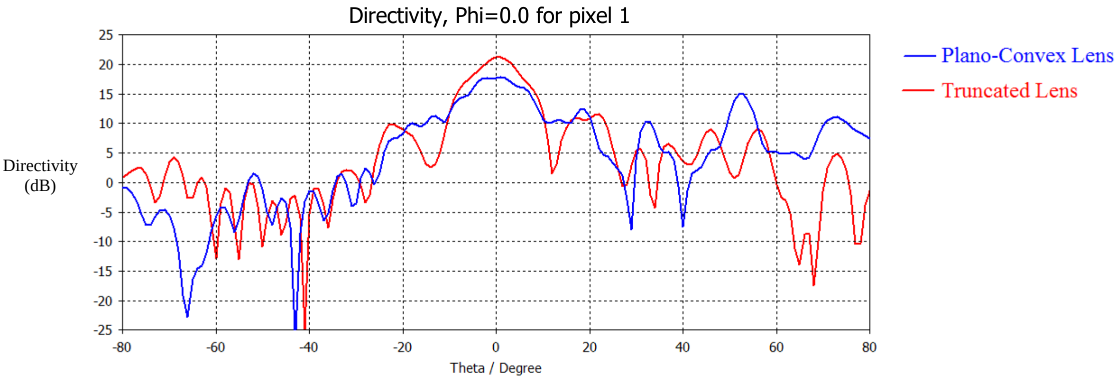

Figure 6-28a: Comparison of the farfield pattern of generated by pixel 1 for the plano-convex and the truncated lens design.

The above figure (**Figure 6-28a**) compares the farfield pattern generated by pixel 1, when either the plano-convex lens or the truncated lens array was placed in front of the device. Compared to the plano-convex lens, the truncated lens had an increased directivity. Side lobes for the truncated lens were smaller than side lobes seen for the plano-convex lens.

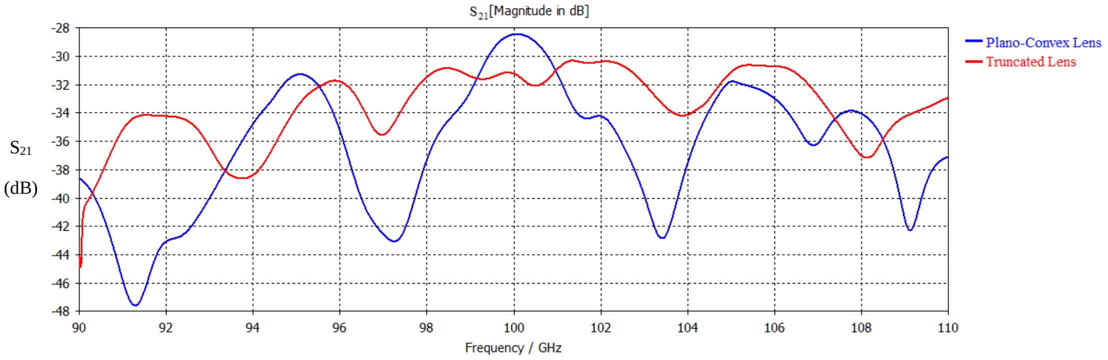

Figure 6-28b: Comparison of the S_{21} parameters for the plano-convex and the truncated lenslets.

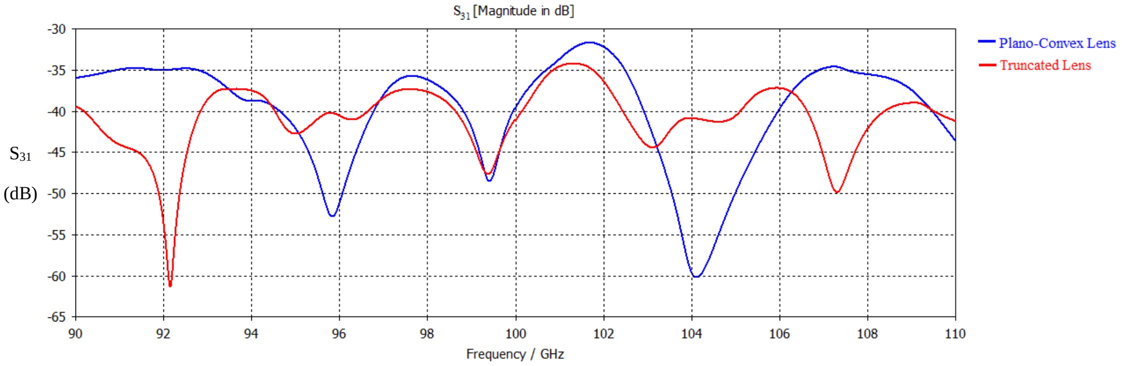

Figure 6-28c: Comparison of the S_{31} parameters for the plano-convex and the truncated lens.

The above figure showed a comparison of the S_{31} parameter for the two lens types. The truncated lens reduces the crosstalk over most of the frequency range the patch antenna radiates most strongly. The truncated lens performs better than the plano-convex lenses with a reduction in crosstalk and side lobes in the farfield pattern.

6.4 Probe array lenslet design

In order to measure a reduction in crosstalk between lenslet pixels with this truncated lens design, a W band signal was needed to feed the lenslets. As outlined in earlier chapters the W band performance of the planar antennas manufactured was poor and with the low level of signals radiated measuring a crosstalk signal would be impossible. So, to get a strong W band signal, it was decided to feed the lenslets via waveguide probes and so ensure experimental verification of a reduction in crosstalk with alternative lens design. These waveguide probe antennas were used to test the lenses as they perform reliably with the VNA, as W band source and detector and allow high dynamic range measurements. Two circular or rectangular waveguide probes could be placed side by side to create an array structure (see **Figure 6-29**). Ideally, smaller lenses should be used in order to compare these crosstalk measurements to the simulations previously shown in this chapter.

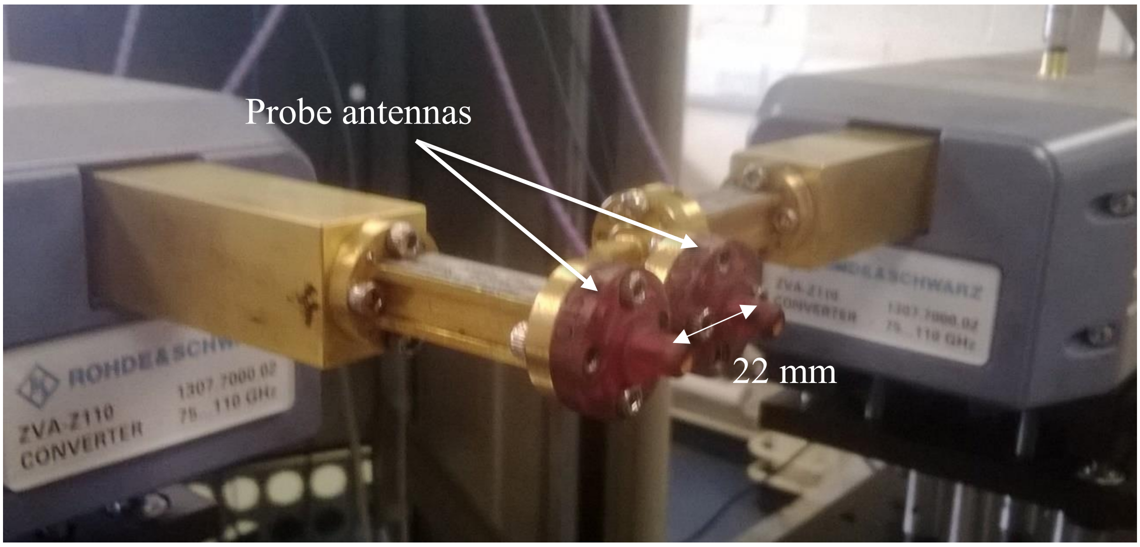

Figure 6-29: Photo of probe array system, with the separation distance shown.

The diameter of the waveguide flanges (22 mm) used with the probes and the waveguide connectors have a limiting factor on how close the centre of the probes could be placed. Each lens was designed and measured by placing it in front of the circular and rectangular waveguide probes used as source antennas. The two different types of plano-convex lenses and the probe antenna were examined in CST prior to manufacture. The development steps taken to reach the experimental step up (**Figure 6-30**) is detailed in this subsection.

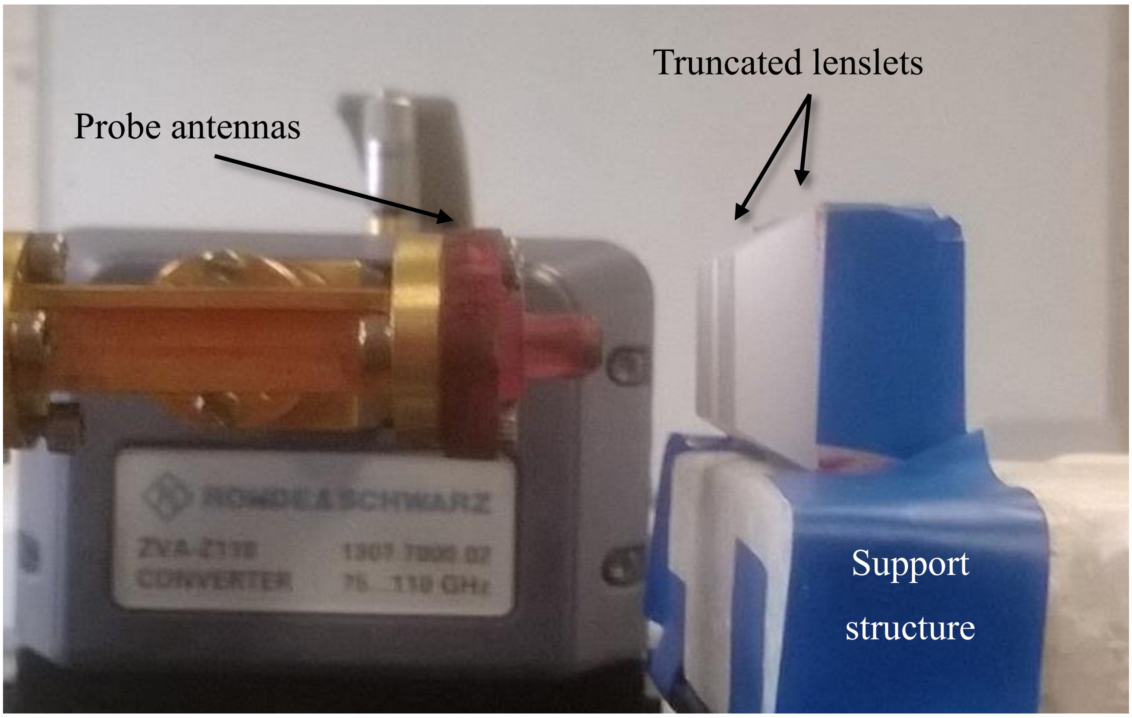

Figure 6-30: Photo of probe array system as viewed from side.

6.4.1 Simulations of waveguide probes

Two probes were used to test the effectiveness of the lenslets: the rectangular and circular waveguide probes. The circular waveguide probe was simulated in CST as shown in **Figure 6-31**, in order to test the probes overall performance.

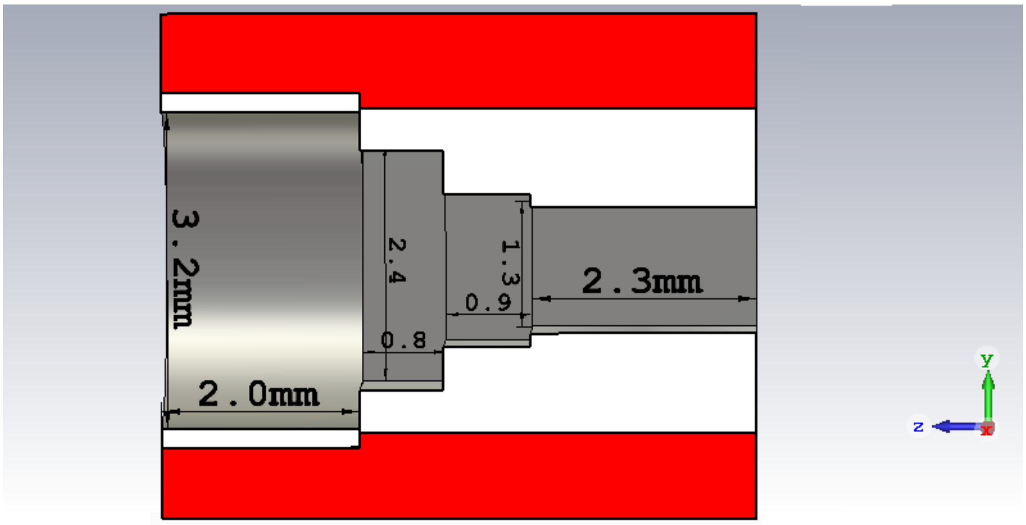

Figure 6-31a: Internal dimensions of the circular waveguide probe.

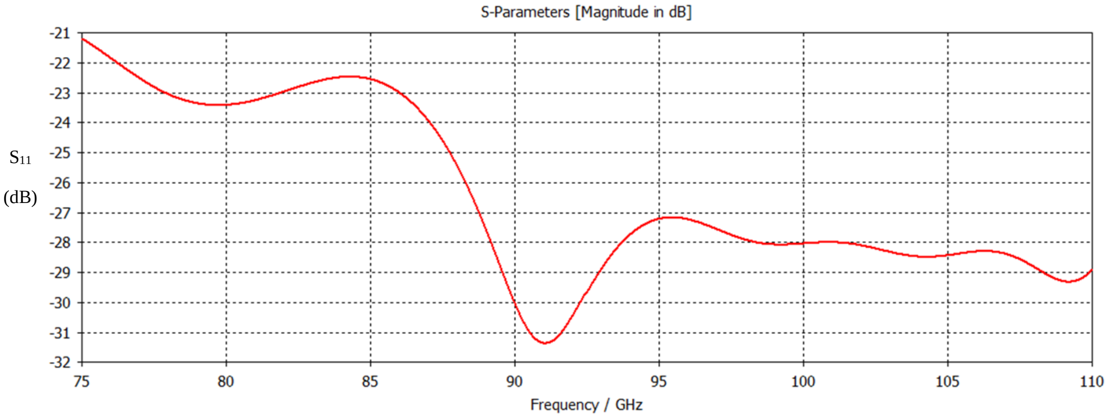

Figure 6-31b: S_{11} parameter of circular waveguide probe.

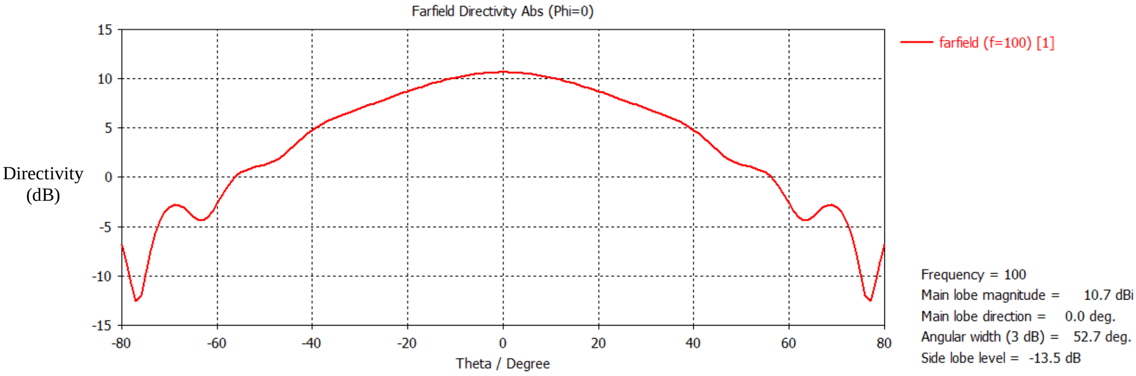

Figure 6-31c: Farfield of antenna at 100 GHz along the $\varphi = 0°$ axis.

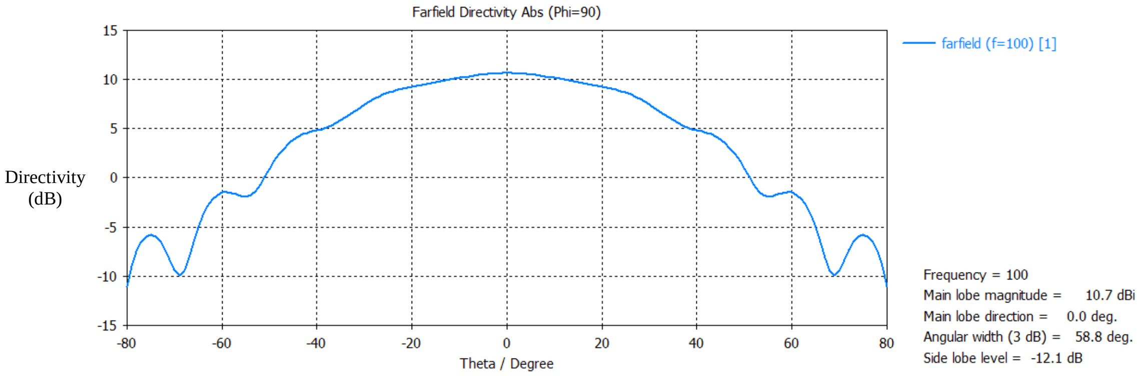

Figure 6-31d: Farfield of antenna at 100 GHz along the φ = 90° axis.

To summarise the results from **Figure 6-31**, over W band frequencies, the S_{11} parameter varies between -21 dB → -31.5 dB, which gives a corresponding reflective coefficient of between 0.1% → 0.8%. The return loss over the entire W band frequencies range was low. The directivity of the antenna was 10.7 dBi at 100 GHz. The beam generated by the antenna was similar along both axes. The antenna produces a relatively directive beam which could be further improved by the dielectric lenses.

A rectangular probe antenna was also used in the following tests. This device was also simulated in CST (see **Figure 6-32**) as it behaved differently to the circular probe.

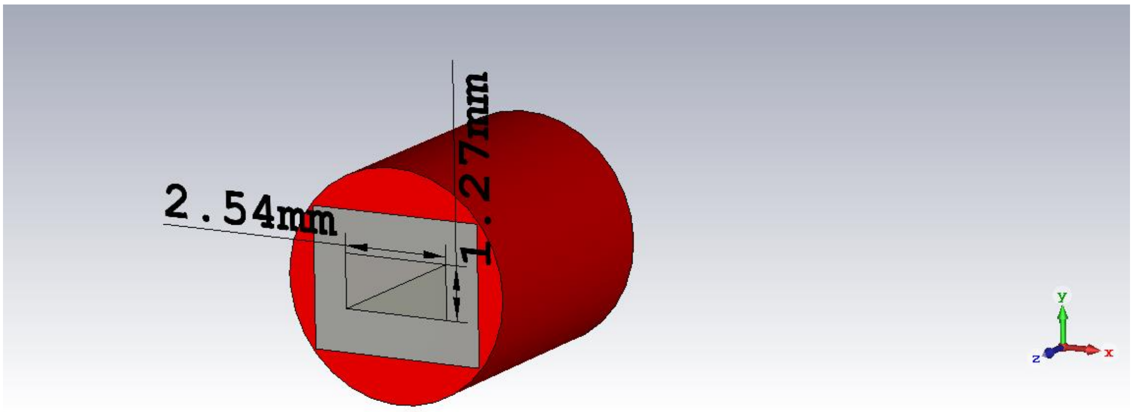

Figure 6-32a: Dimensions of rectangular probe antenna viewed in CST. Only the top portion of the device was examined.

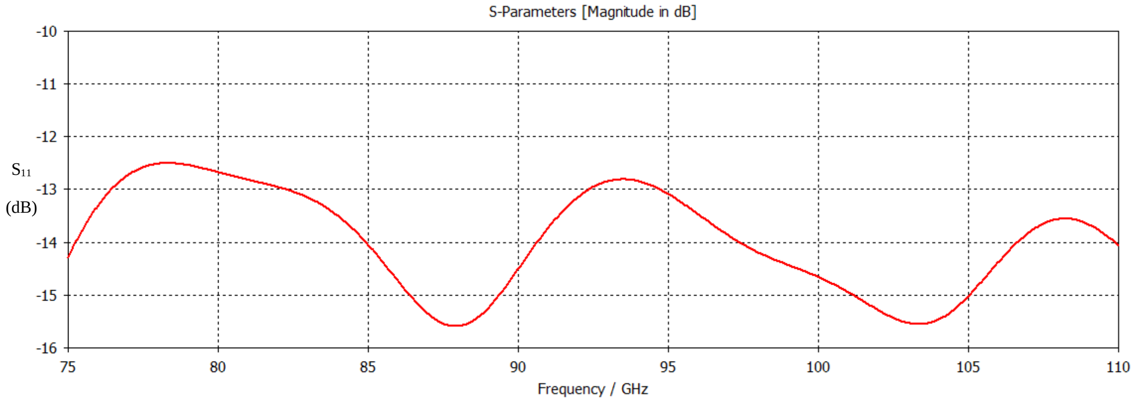

Figure 6-32b: The S_{11} parameter of the device for the entire W band range.

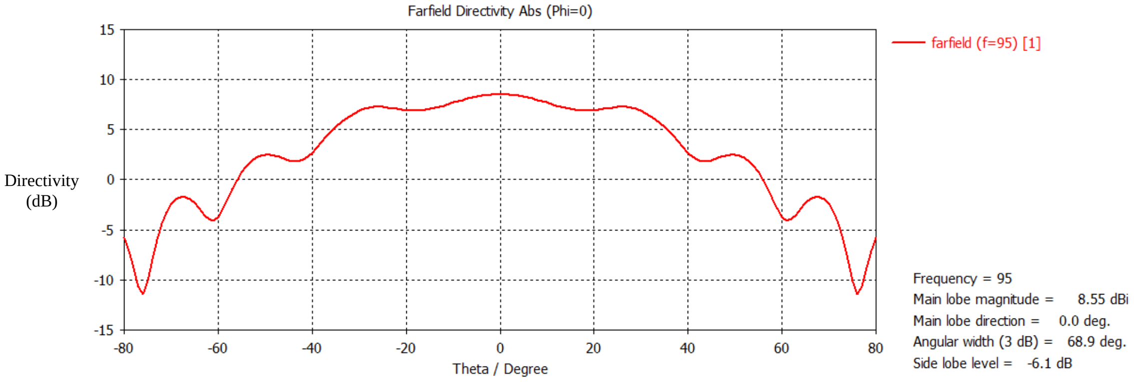

Figure 6-32c: Farfield of antenna at 95 GHz along the φ = 0°.

The S_{11} parameter of the probe antenna (**Figure 6-32b**) was constantly below -10 dB and the directivity of the beam (**Figure 6-32c**) was relatively large for at 8.55 dBi.

The rectangular probe performed best at 95 GHz as opposed to the circular probe in **Figure 6-31** which performed best at 100 GHz.

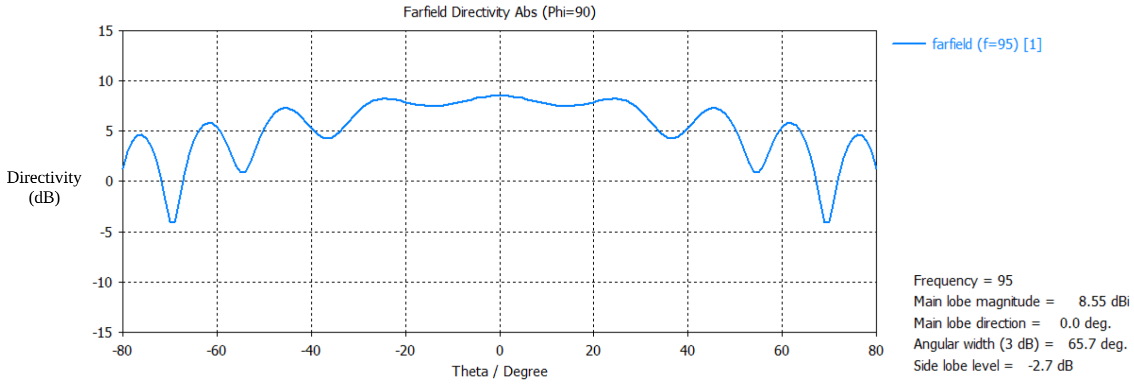

Figure 6-32d: Farfield of antenna at 100 GHz along the φ = 90° axis.

Both the circular probe antenna (**Figure 6-31**) and the rectangular probe antenna (**Figure 6-32**), performed better than the patch antennas tested in **Chapter 3** and **Chapter 4**, as both had a low S_{11} parameter over the W band and higher on-axis directivity.

The circular probe had an on-axis directivity of 10.7 dBi while the rectangular probe had an on-axis directivity of 8.6 dBi. So, while both probes were better than the patch antennas, the circular probe overall performed better than the rectangular probe. As a result, the circular probe antenna was used exclusively for further testing in CST.

6.4.2 Simulations of probe with plano-convex lens

In CST a plano-convex lens was placed in front of this circular waveguide probe in order to test the reflection caused by the introduction of the lenses (see **Figure 6-33**). This was similar to the setup used with the VNA, shown later in **Section 6.5**.

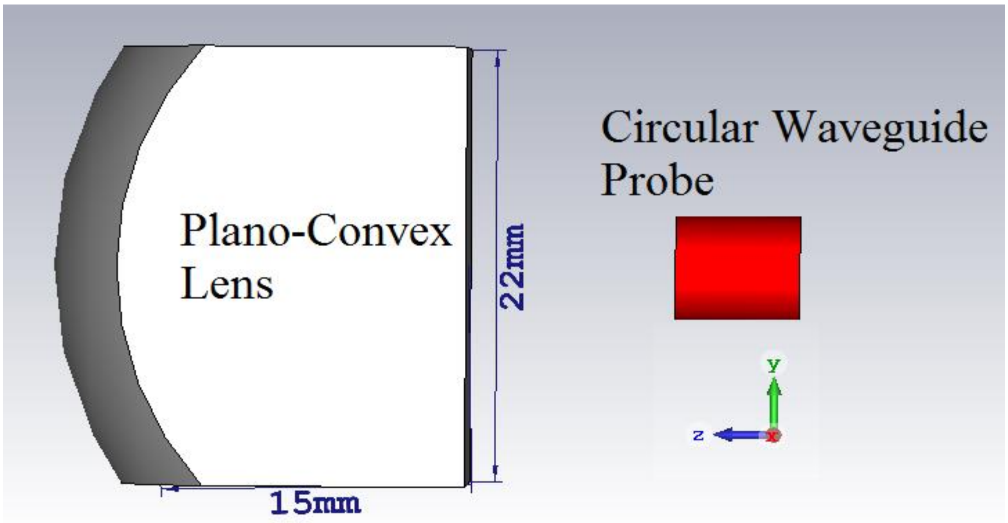

Figure 6-33: Plano-convex lens placed in front of circular probe antenna.

The distance from the probe to the lens was varied from 8 mm to 20 mm. This simulation was an attempt to find the theoretical focal length of the lens (**Figure 6-35a** & **b**). The definition for “focal length” used in this context was the distance between the flat end of the lens and the top of the probe that had the maximum directivity.

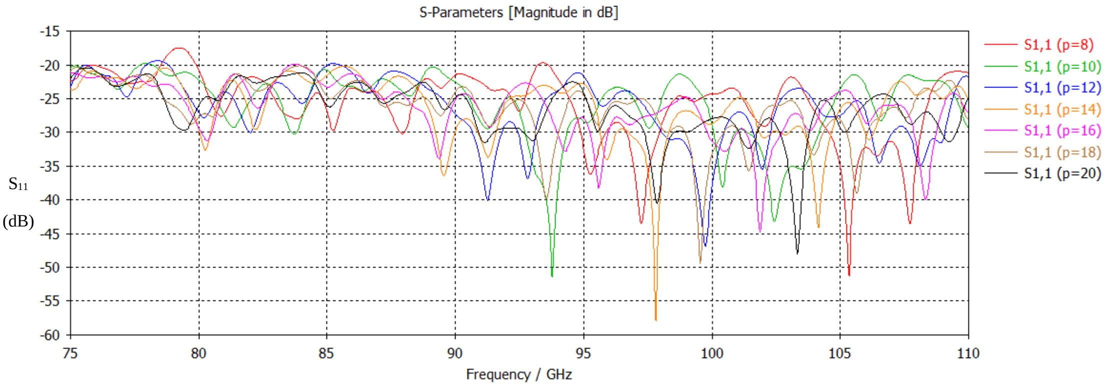

Figure 6-34: S_{11} parameter for plano-convex placed in front of antenna at various distances.

Figure 6-34 shows that the power reflected back into the probe by the lens varies was on average around -30 dB. The power reflected varies between -20 dB and -60 dB, depending on the position of the lens. These large variations over such a small distance difference was possibly due to a standing wave effect caused by reflections of the lens and probe. Overall, a low amount of power was reflected back into the antenna.

The farfield pattern of the probe and lens over a region will be shown in the following figures. The optimum distance between lens and probe will be determined by the distance that gives the maximum directivity.

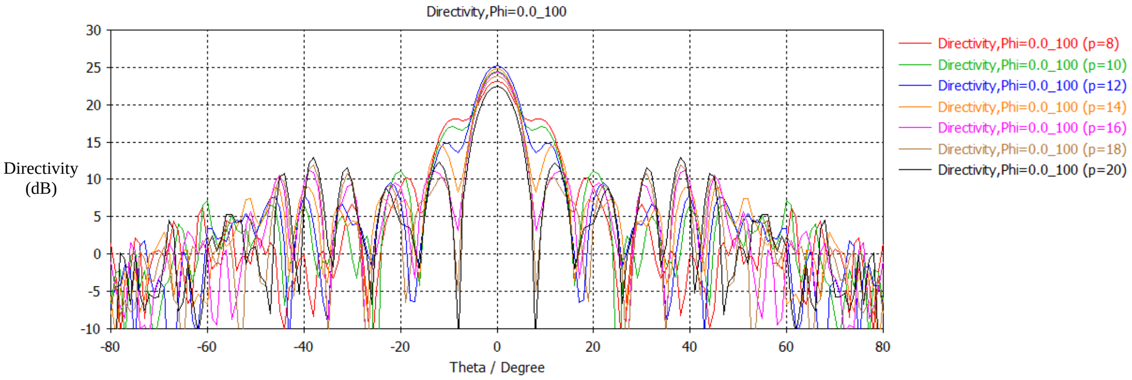

Figure 6-35a: Directivity of antenna at 100 GHz, at various distances cut along the φ = 0° axis.

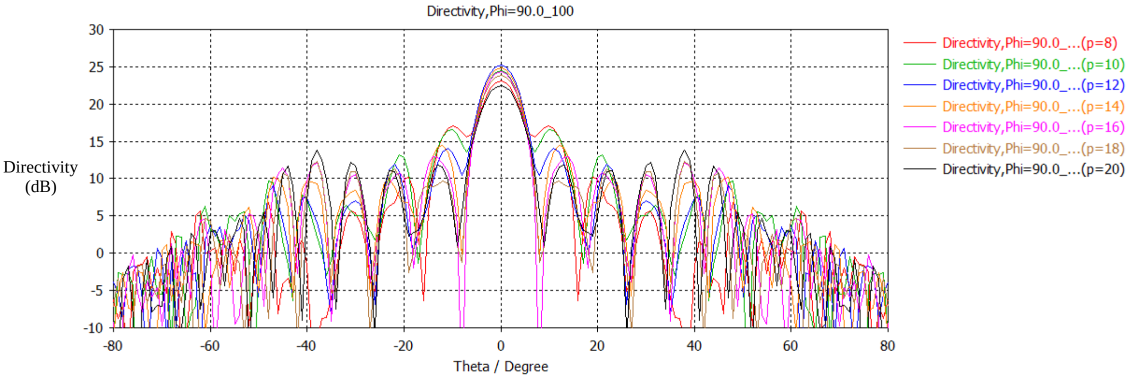

Figure 6-35b: Directivity of antenna at 100 GHz, at various distances cut along the orthogonal φ = 90° axis.

The on-axis directivity in **Figure 6-35a** and **Figure 6-35b** changes by up to 5 dBi over a few millimetres. The beams peak in the centre of both plots, which implied that the beams were propagated in the correct direction (towards the positive *z*-axis). The focal length of the lens (or position of maximum directivity) at 100 GHz was 15 mm for the chosen design.

6.4.3 Simulations of probe with truncated plano-convex lens

The same tests performed in **Section 6.4.2** were repeated for the truncated lens design. Once again, the distance from the probe to the lens was varied from 10 mm to 20 mm and the S_{11} and directivity at each position will be shown in the following diagrams.

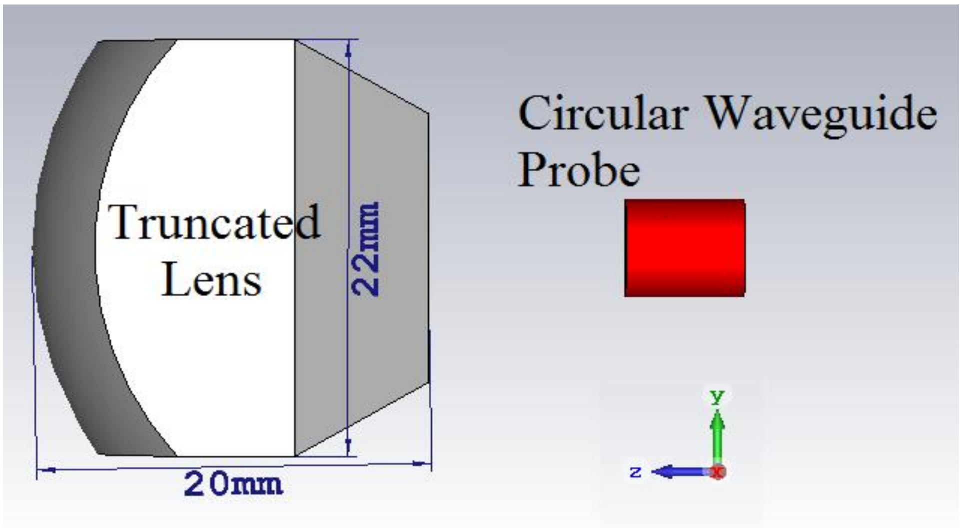

Figure 6-36: Truncated plano-convex lens placed in front of circular probe antenna.

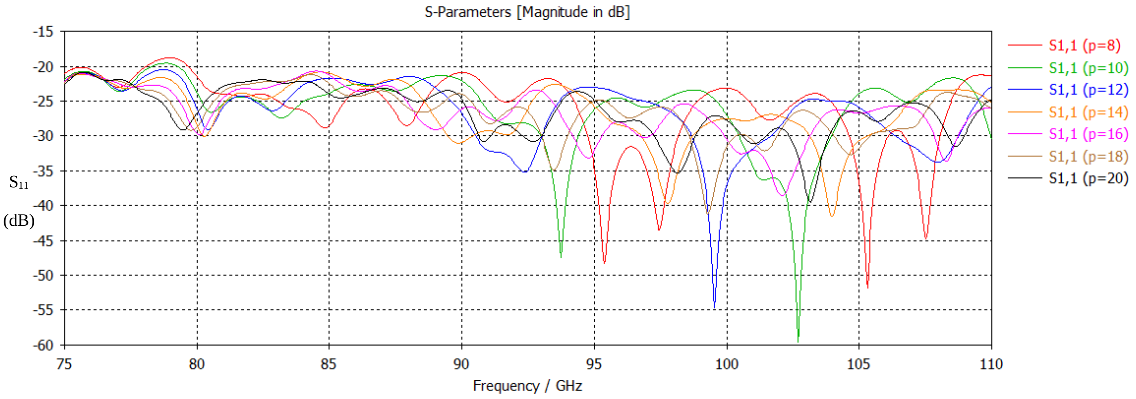

Figure 6-37a: S_{11} parameter for plano-convex placed in front of the patch antenna at various distances.

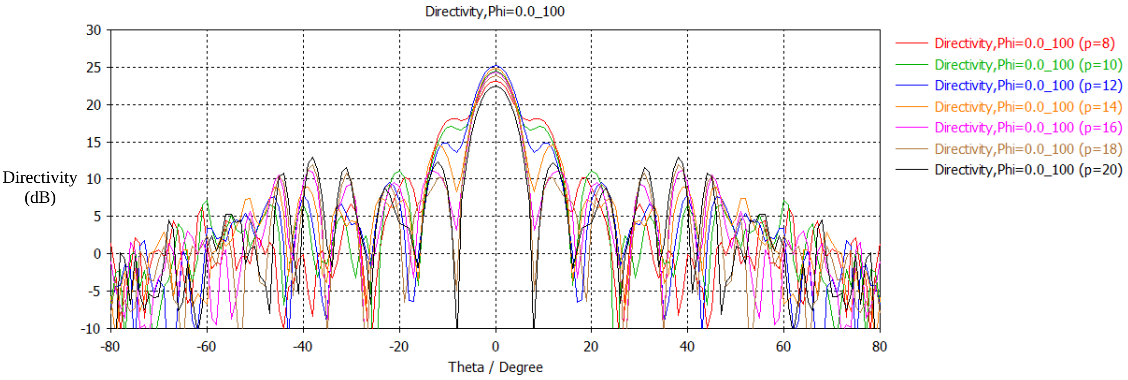

Figure 6-37b: Directivity of antenna at 100 GHz, at various distances cut along the φ = 0° axis.

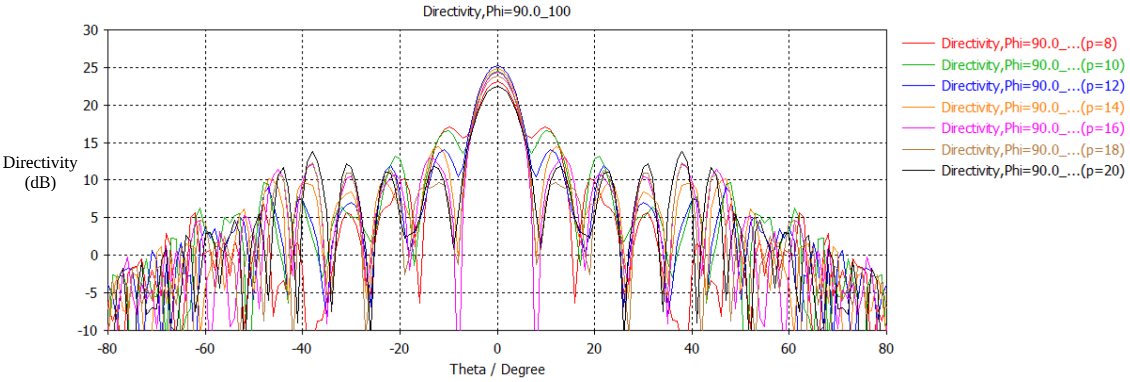

Figure 6-37c: Directivity of antenna at 100 GHz, at various distances cut along the φ = 90° axis.

The overall reflections in **Figure 6-37a** caused by the lens was low. The reflection caused by the truncated lens was equivalent to the reflection observed with the plano-convex lens (**Figure 6-34**).

The farfield beams peak on-axis for both plots **Figure 6-37b** and **Figure 6-37c**, which implied that the beams propagate in the expected direction (towards the positive *z*-axis). The focal length of the truncated lens at 100 GHz was 12 mm. The directivity of the truncated lens appears to be equivalent to the farfield pattern of the plano-convex lens. One difference between these two lenses was the focal length. The truncated lens had, in general, a shorter effective focal length than the plano-convex lens.

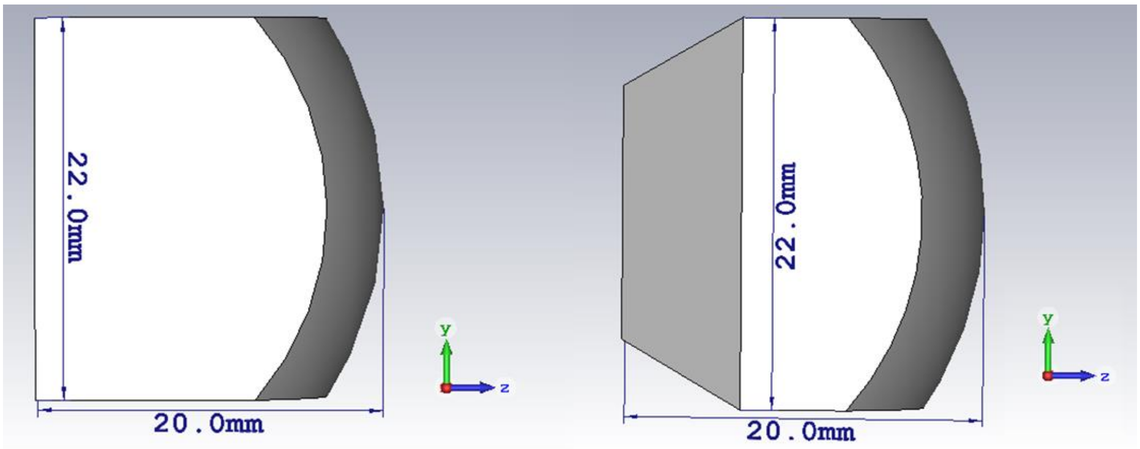

Figure 6-38: Dimensions for plano-convex lens (left) and truncated lens (right).

The lenses have a length and width of 22 mm and a thickness (or flat-to-curve length) of 20 mm. These lenses were larger than the previously tested lenses due to the mechanical restraints of the waveguide probe array, with 22 mm being the minimum size possible.

6.5 Lenses measurement

Two of each lenslet design were manufactured. Both lenses were created from a block of HDPE. These lenses were manufactured in the Experimental Physics department at Maynooth University.

	Radius	Lens thickness	Side length	Back length	Angle of cut
Plano-convex lens	20 mm	20 mm	22 mm	22 mm	-
Truncated lens	20 mm	20 mm	22 mm	14.3 mm	30°

Table 6-27: Measurements of plano-convex and truncated lenslets.

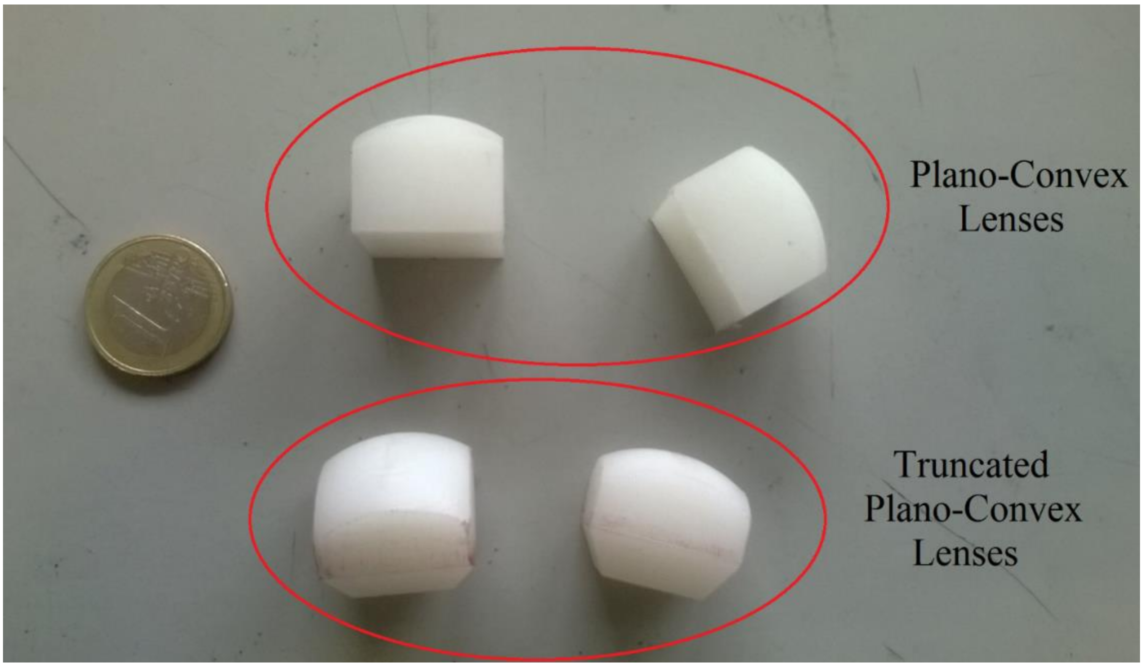

Figure 6-39: Plano-convex lenses and truncated plano-convex lenses, with coin shown for size comparison.

The aim of the following test was to observe the effects of the truncation on the plano-convex lens. To test the lenses, the circular waveguide probes were placed facing each other, with the lens placed in between. The intensity pattern of the probe with either the plano-convex or the truncated lens placed in front was measured. If the truncation had no effect, then the intensity pattern from the two lenslets will be identical. In both cases, the probes remain the same horizontal distance (84 mm ± 1 mm) apart.

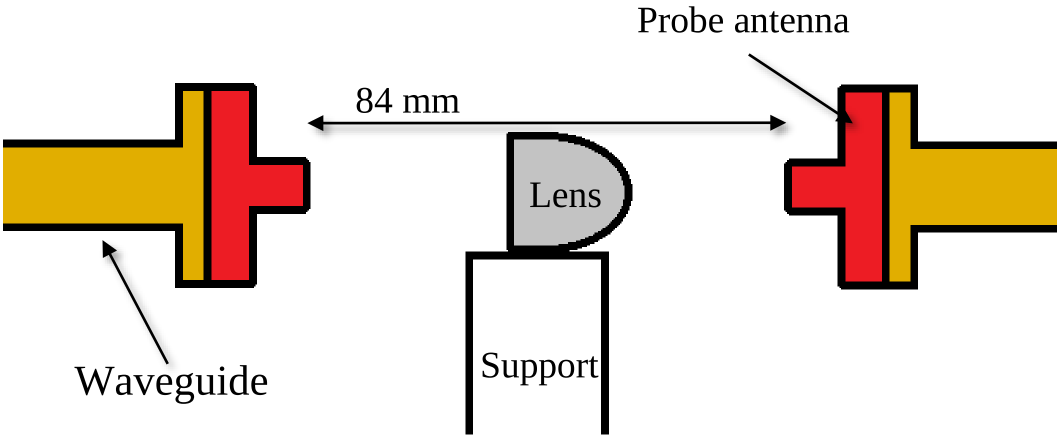

Figure 6-40: Testing lenslets with circular waveguide probes. The lenses were placed on a polystyrene support, which holds the lens in place and isolating the system from the metal supports.

Figure 6-41: Plano-convex lenslet placed in front of a circular waveguide probe in the VNA.

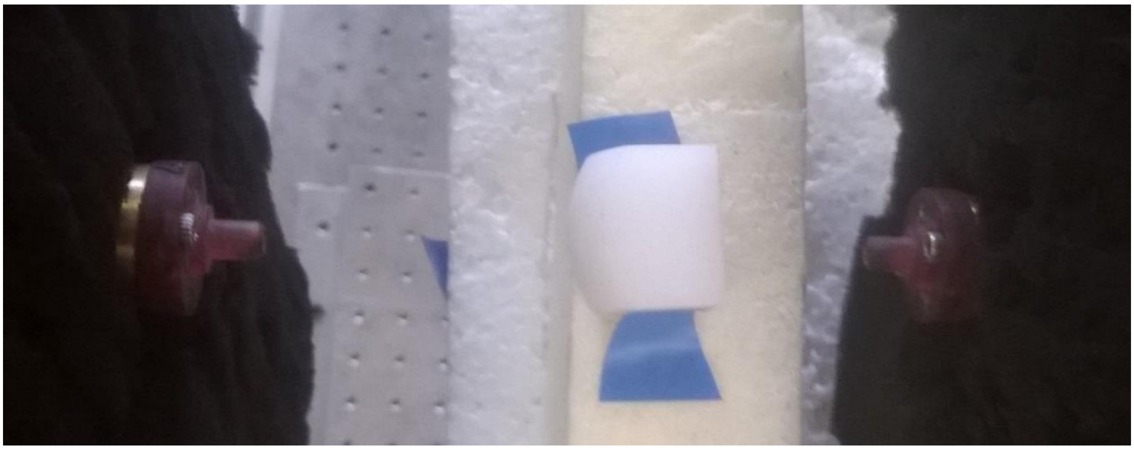

Figure 6-42a: Plano-convex lens placed between to circular waveguide probes. The probe on the left was connected to the scanner, used in previous tests, and could move along the vertical and horizontal axis. The probe and the lens on the right remained stationary.

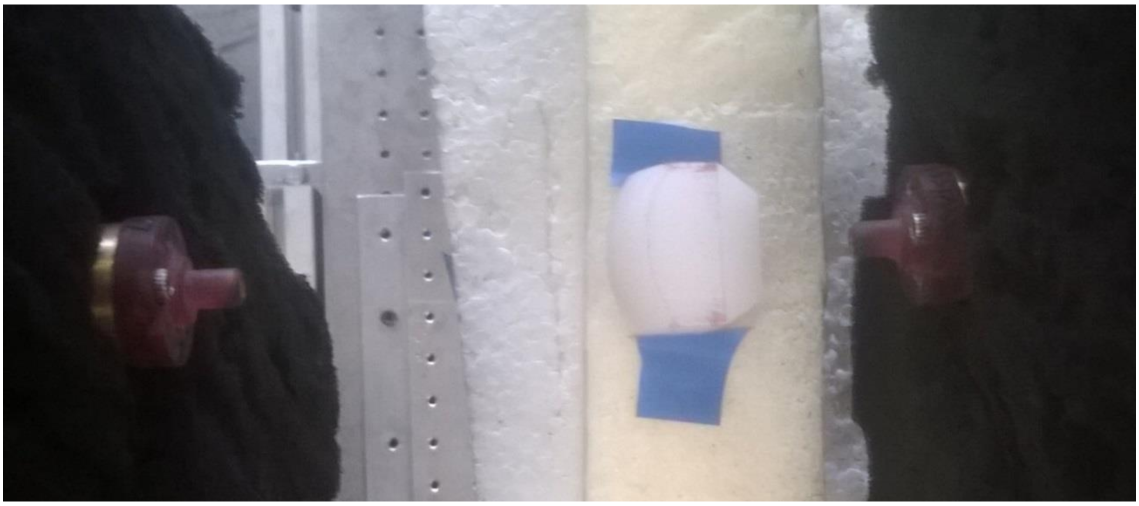

Figure 6-42b: Truncated plano-convex lens between two circular waveguide probes. Small pieces of tape were used to prevent the lens from falling over.

The S-parameters of the probe with and without the lenses were recorded. The scans were performed using the VNA, where each scan extends from -80 mm → 80 mm along both axes.

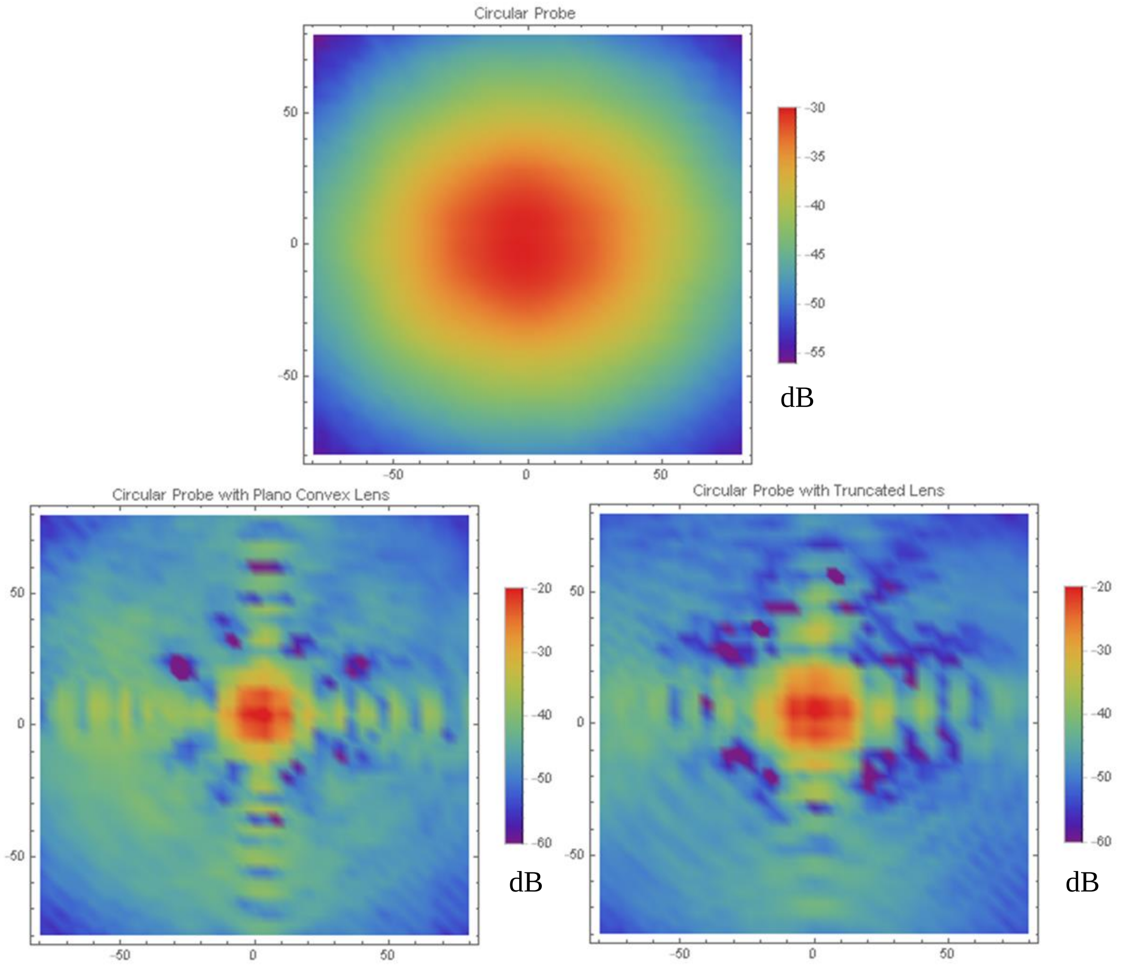

Figure 6-43: Plots at 100 GHz of the circular probe without lens (top plot), the circular probe, with plano-convex lens (bottom left) and the probe with truncated lens in front (bottom right).

The scans of the probes in **Figure 6-43** create a circular pattern, which a maximum S_{21} of -30 dB detected at the centre of the beam. The lenses increase the power transferred between the two probes. The maximum S_{21} parameter detected using the two lenses was -20 dB. The range over which the farfield was at a maximum was smaller with the lens, than without. The lenses have transformed the beam into a smaller, more focused beam.

The measured S_{21} from the VNA scans were normalized in the same way as the results from the simulations. The measured beam of the probes and lenses were compared to their respective simulated farfield. The simulated farfield pattern for the plano-convex lens had the lens at 19 mm (i.e. At the same distance as the measured result). Similarly, the simulated farfield pattern for the truncated lens had the lens at 14 mm. The following figures show the normalized measured pattern of the probe with a lenslet and the corresponding normalized simulated field from CST.

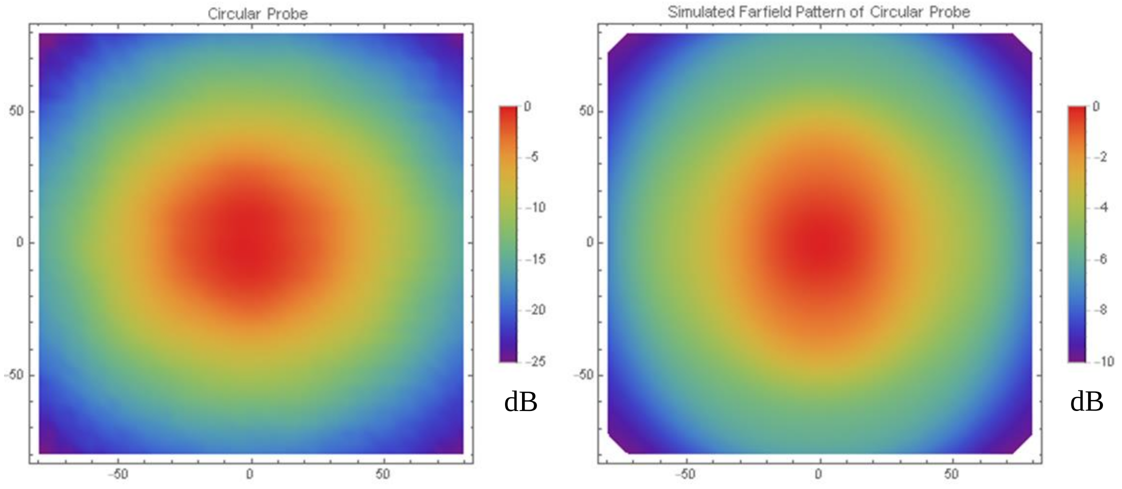

Figure 6-44a: Normalized plots for the circular waveguide probes at 100 GHz, with the measured result on left and simulated farfield on right.

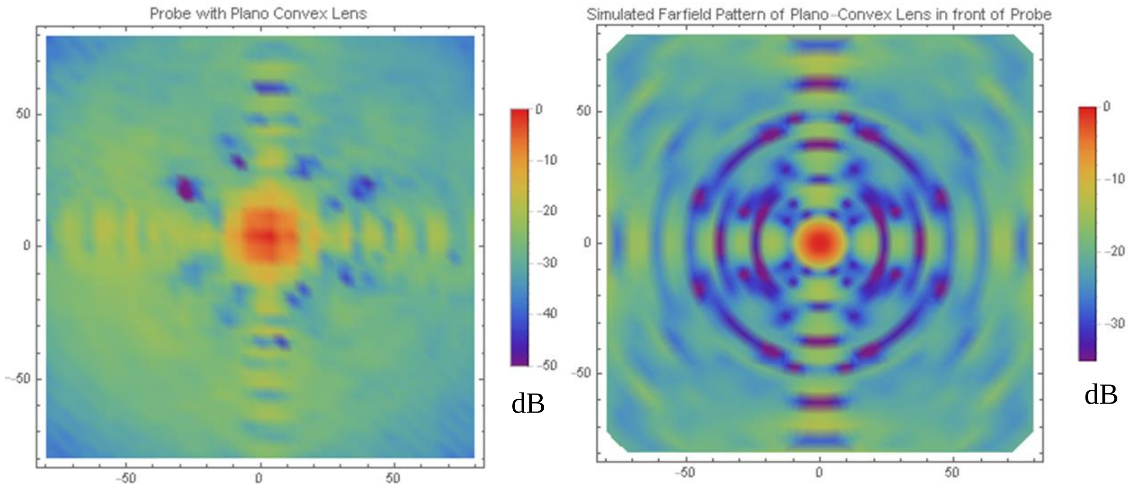

Figure 6-44b: Normalized plots for the circular waveguide probes at 100 GHz with the plano-convex lenslet. Measured result on the left and simulated farfield on the right.

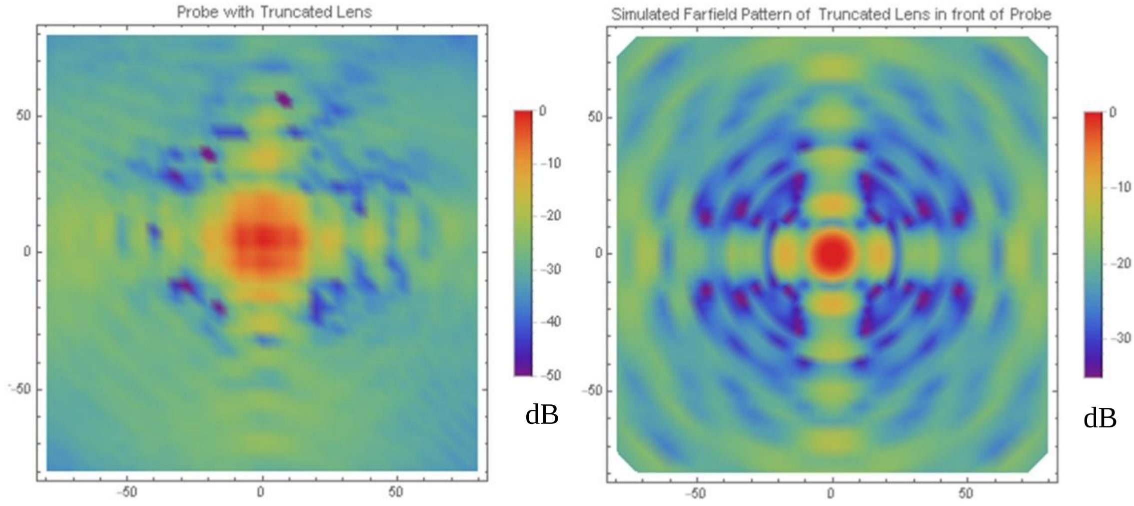

Figure 6-44c: Normalized plots for the circular waveguide probes at 100 GHz with the truncated lenslets. The measured result on the left and simulated farfield on the right.

The lenses increase the power transferred between the two probes as seen in **Figure 6-44**. The truncation of the lens edges had some effect on the pattern, but the effect was relatively small. The power patterns were sufficiently similar that the difference could be caused by difficulty in positioning and alignment of the lenses. Convolution of the measured beam with the probe beam may also be a factor and this was not included in the CST simulations.

6.6 Waveguide probe array crosstalk

6.6.1 Simulation of crosstalk

Two circular waveguide probes were simulated in CST. The centre to centre distance of the probes was 22 mm. The farfield antenna and S_{11} parameter of the circular probes was shown previously in **Figure 6-31**.

Figure 6-45a: The centres of the two circular waveguide probes were placed 22 mm apart in CST. This was the minimum distance that the two probes can be placed due to the flanges connected to these probes.

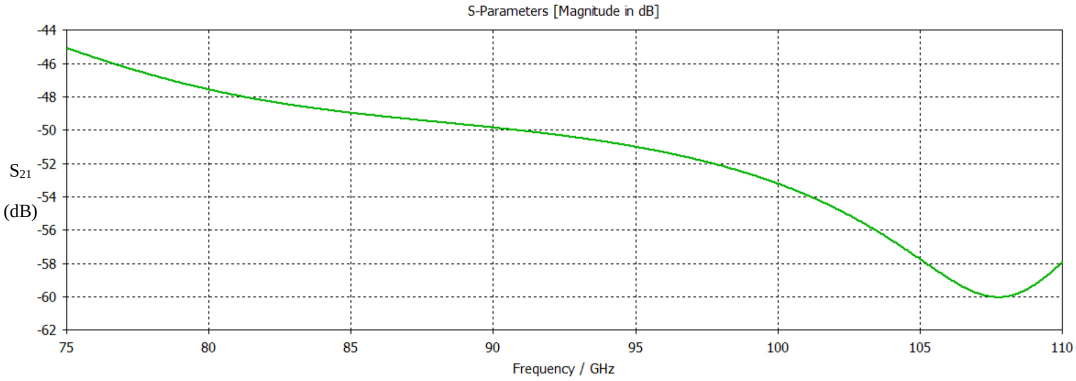

Figure 6-45b: S_{21} parameter (crosstalk) between two probes.

The crosstalk between the two probes as shown in **Figure 6-45b** was small, reaching -45 dB at most at 75 GHz. The crosstalk was small enough that it may be hidden by the background noise.

In CST, a plano-convex array consisting of two lenses was placed in front of these two waveguide probes. The directivity and S-parameter were recorded. The simulation was repeated for a truncated lens array consisting of two of these lens designs.

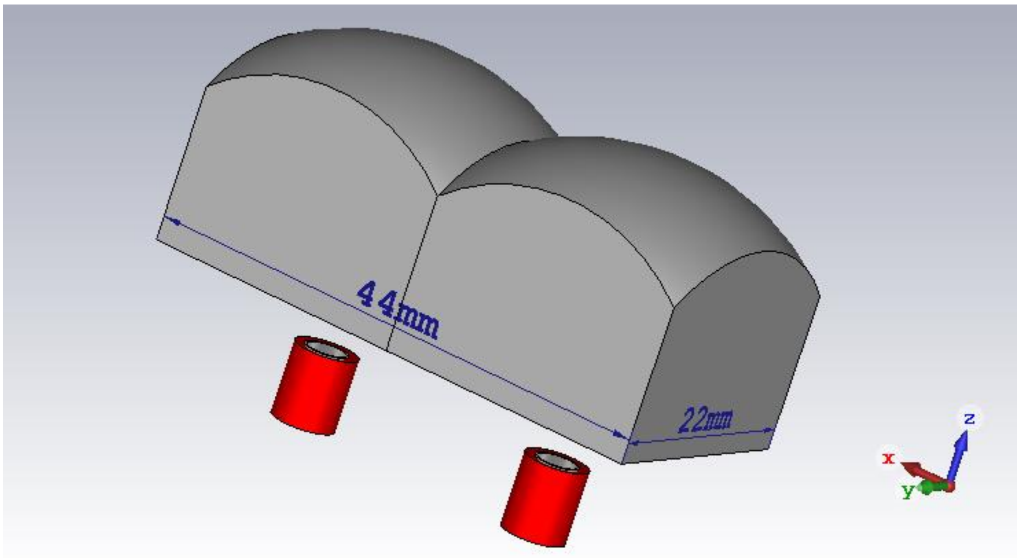

Figure 6-46a: Plano-convex lens array placed in front of two circular probes.

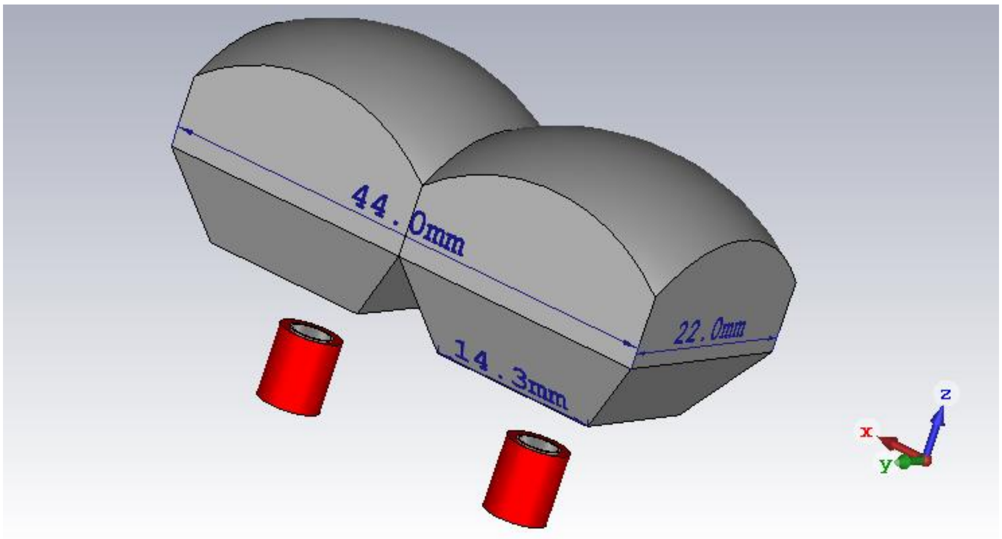

Figure 6-46b: Truncated lens array placed in front of two circular probes.

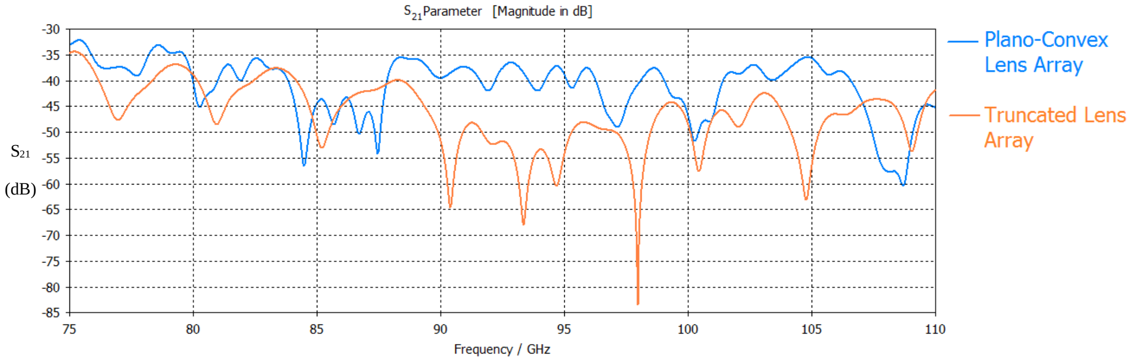

Figure 6-46c: S_{21} parameter between circular probes with lens array placed in front.

Over the frequency range shown in **Figure 6-46c**, the S_{21} parameter caused by the plano-convex lens array (blue) was larger than the S_{21} parameter caused by the truncated lens (orange). Therefore, the crosstalk cause by the plano-convex lens was more than that of the truncated lens.

6.6.2 Measurement of crosstalk

The VNA was used to measure the S_{21} parameter (crosstalk) between two ports. Two circular waveguide probes were placed on two waveguides which were connected to the ports. A H-bend waveguide was placed on one of the port heads, which allow the probes to be placed closer. The probes were aligned such that both were level and point in the same direction. Before any lenses were added, the crosstalk between the two probes was measured. This will be referred to later as the “no lens” case.

The crosstalk between the circular waveguide probes was relatively small. The results were checked against the crosstalk between 2-rectangular probes. Since the two probes have different farfield patterns, there should be different levels of crosstalk.

The crosstalk caused by plano-convex and a truncated plano-convex lens in front of the probes was also tested. The lenses were placed on a polystyrene support and the probes aligned with the centre of the lenses.

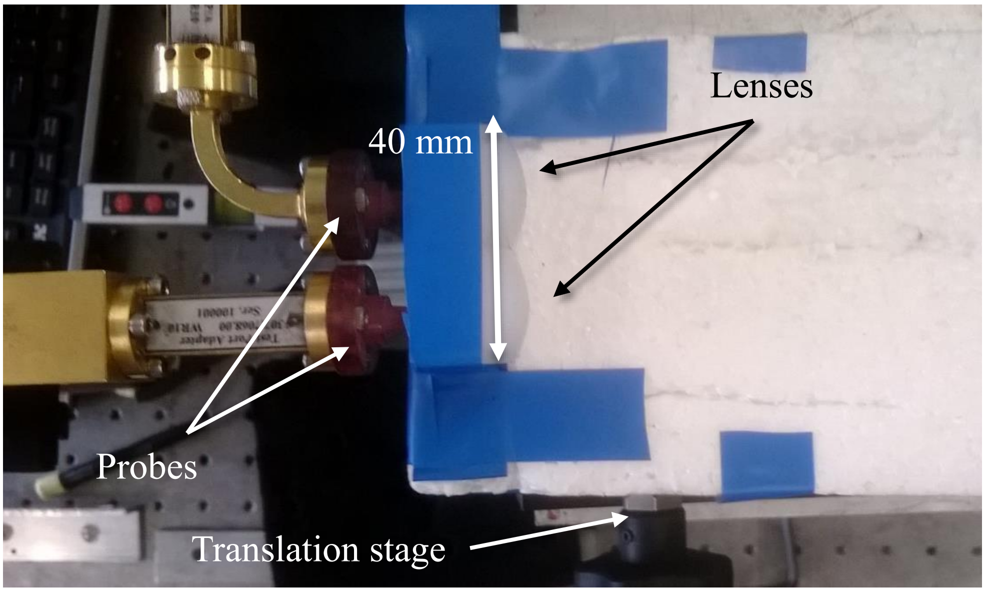

Figure 6-47: Photo of circular probes with truncated lenses (Viewed from top).

The lenses support was placed on top of a translation stage, which was used to move the lenses along the horizontal axis. The translation stage was in turn placed on a hand-crank, which allows manual movement along the vertical axis.

The plano-convex polyethylene lens array was placed in front of the probes. The probes were moved such that the centre of each probe was directly behind the centre of a lens and the S-parameters were recorded. Using the micrometer translation stage, the lenses were moved from this starting position (defined to be 0 mm) to 10 mm in steps of 1 mm, with the S-parameters being recorded at each position.

The circular probes were removed and replaced with rectangular probes. The above process was repeated with these probes. The plano-convex lenses were replaced with a truncated plano-convex lenses array and the previously described lenses tests were repeated.

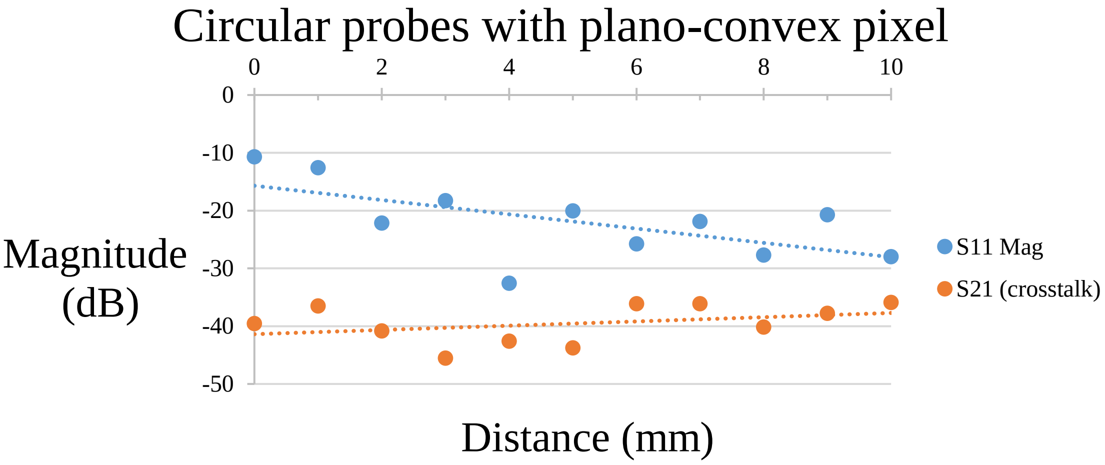

Figure 6-48a: S-parameters at 100 GHz for circular probes with plano-convex lenses.

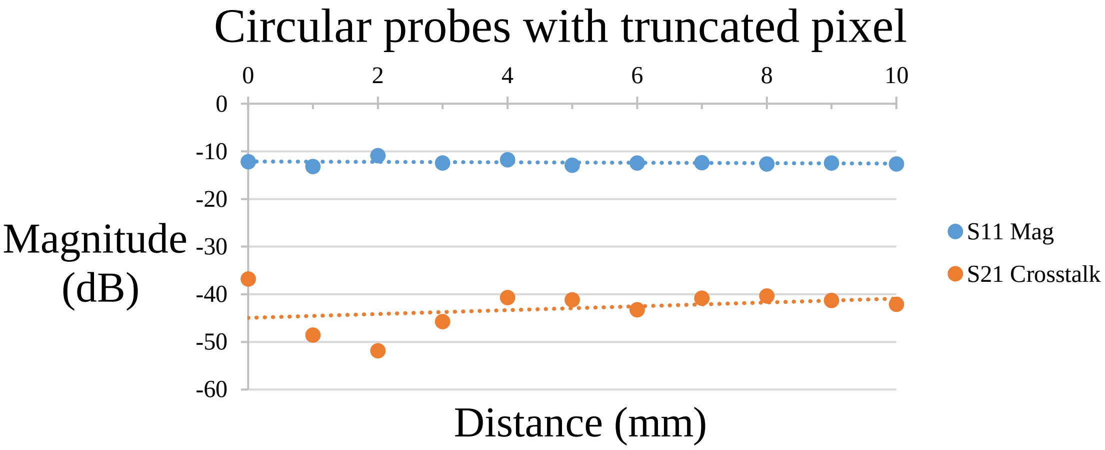

Figure 6-48b: S-parameters at 100 GHz for rectangular probes with plano-convex lenses.

The two previous graphs (**Figure 6-48 a** & **b**) show the S_{11} and S_{21} recorded as the distance between the lens and probe was increased from 0 → 10 mm. The S_{11} for both tests show a gradual trend to decrease as the distance increases. However, there was a periodic structure imposed on this trend. This was possibly due to constructive and destructive interference along the axis between probes. The S_{11} of the first graph (**a**) had a more approximate periodic structure than the S_{11} parameter in the second graph (**b**), but this was due to the circular probe performing slightly better than the rectangular probe.

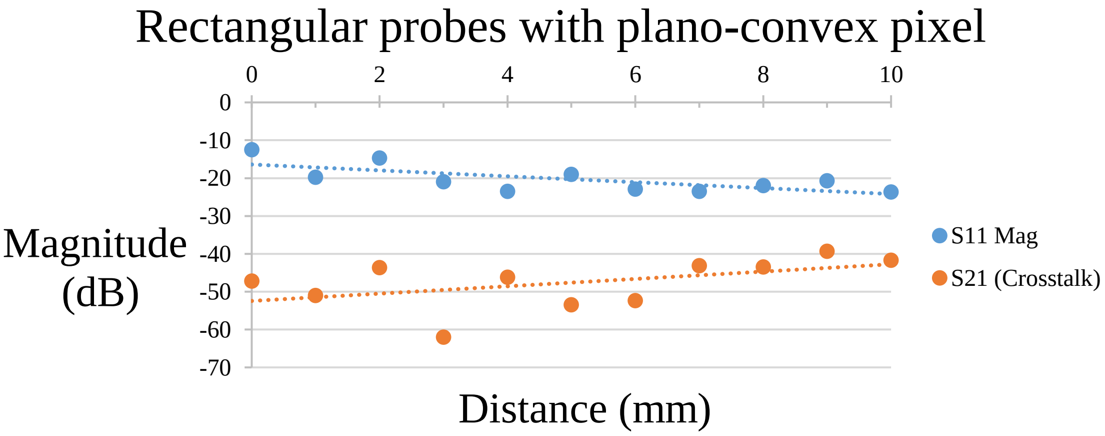

Figure 6-49a: S-parameters at 100 GHz for circular probes with truncated plano-convex lenses.

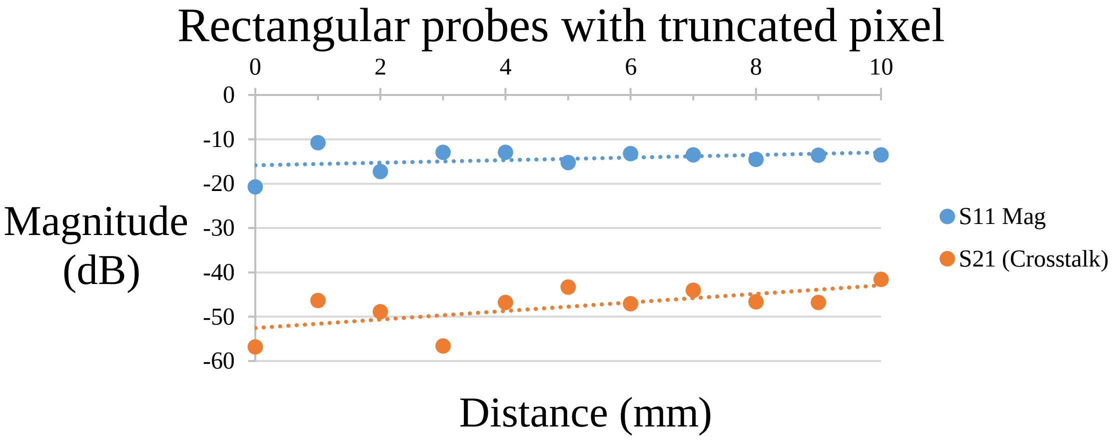

Figure 6-49b: S-parameters at 100 GHz for rectangular probes with truncated lenses.

The two previous graphs (**Figure 6-49a** & **b**) show S-parameters for the truncated lens. The S_{21} for both tests (**a** & **b**), unlike seen previously in (**Figure 6-48**), show a gradual trend to increase as the distance increases.

The tests for the plano-convex lens were carried on 25/08/2017 and the truncated lens test was completed on 01/09/2017 and both used different calibrations. To make sure that the tests were the same, the "no lens" cases were compared to each other. The crosstalk between the circular probes without any lenses should be the same on the 25/08/2017 and on the 01/09/2017. If they differ, this needed to be taken into account.

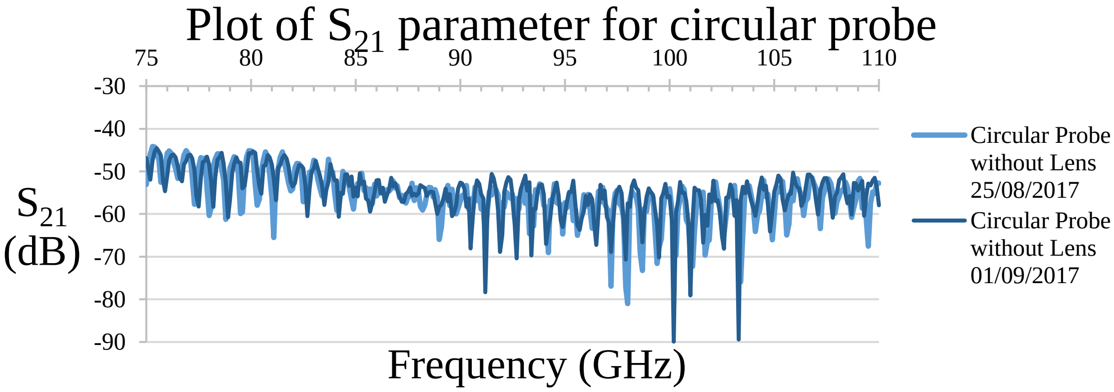

Figure 6-50: Crosstalk between two circular probes on the 25th August and the 1st September. The graph shows that the crosstalk between the circular probes was broadly the same, despite the different calibrations used for each day.

The calibration was correct as the results in **Figure 6-50** from different days do not differ significantly.

Figure 6-51 provides a comparison between plano-convex and truncated lens as measured with the VNA over the W band.

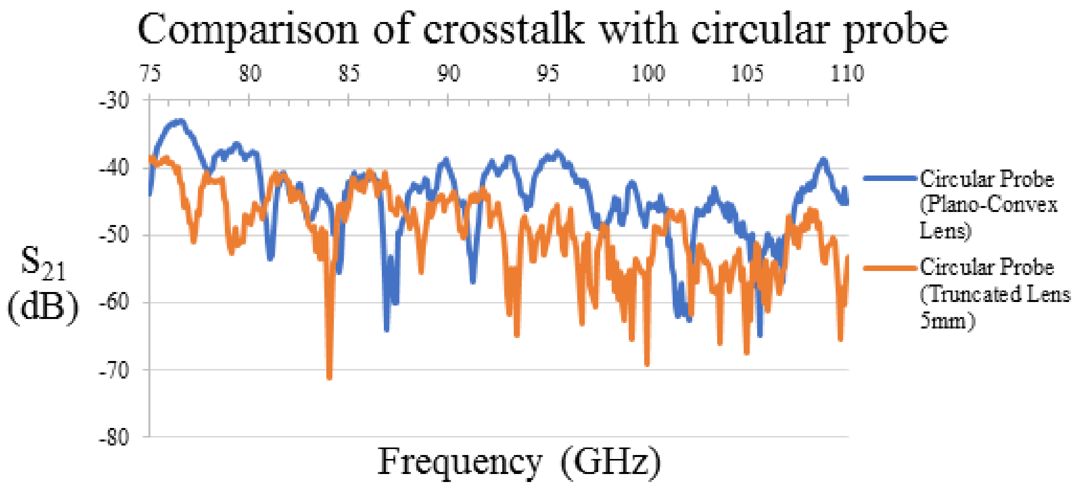

Figure 6-51a: Comparison of crosstalk (S_{21}) between circular probes with plano-convex lens (blue) and truncated lens (orange).

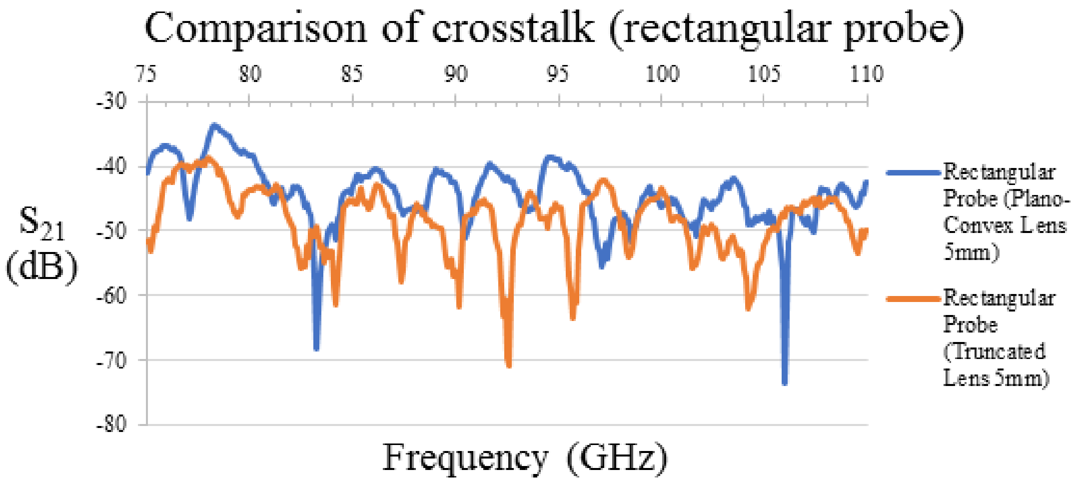

Figure 6-51b: Comparison of crosstalk between rectangular probes with plano-convex lens (blue) and truncated Lens (orange).

Overall, as **Figure 6-51** shows, the truncated plano-convex lens had a smaller level of crosstalk than the plano-convex lens. Over most of the W band frequency the crosstalk due to the truncated lens was less than the crosstalk caused by the plano-convex lens. However, the crosstalk was frequency dependent and there were frequency bands where plano-convex lens had reduced crosstalk. The measured results were compared to the simulated results from CST (**Figure 6-45b** and **Figure 6-46c**) in the following figures.

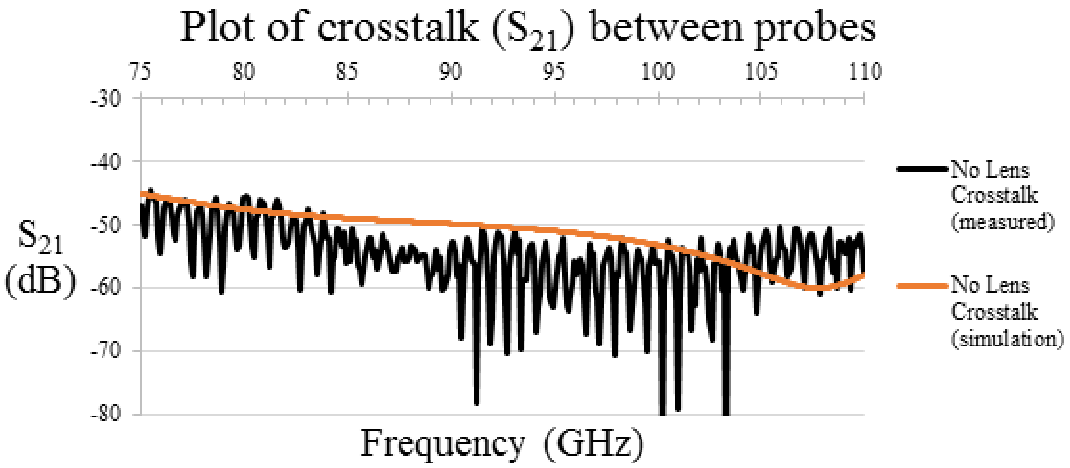

Figure 6-52a: Crosstalk between two circular waveguide probes.

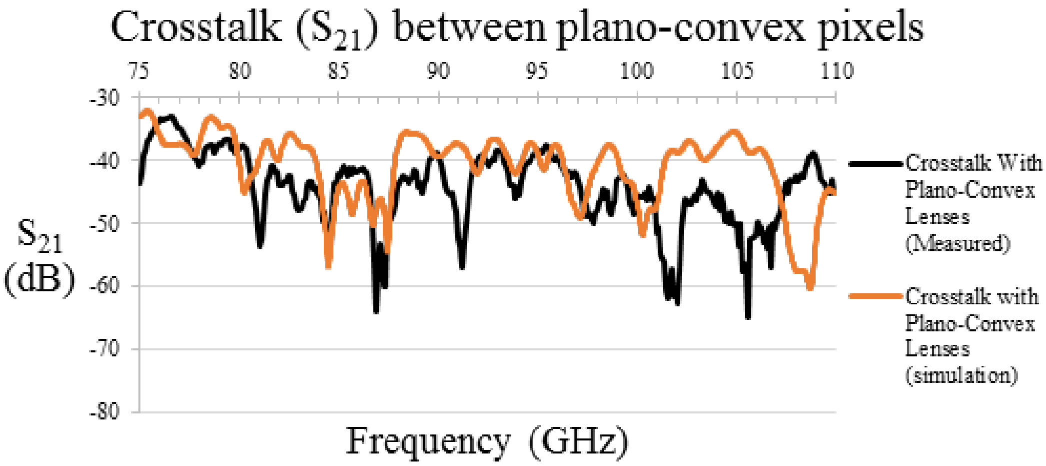

Figure 6-52b: Plot of crosstalk between two circular waveguide probes with plano-convex lenses placed in front.

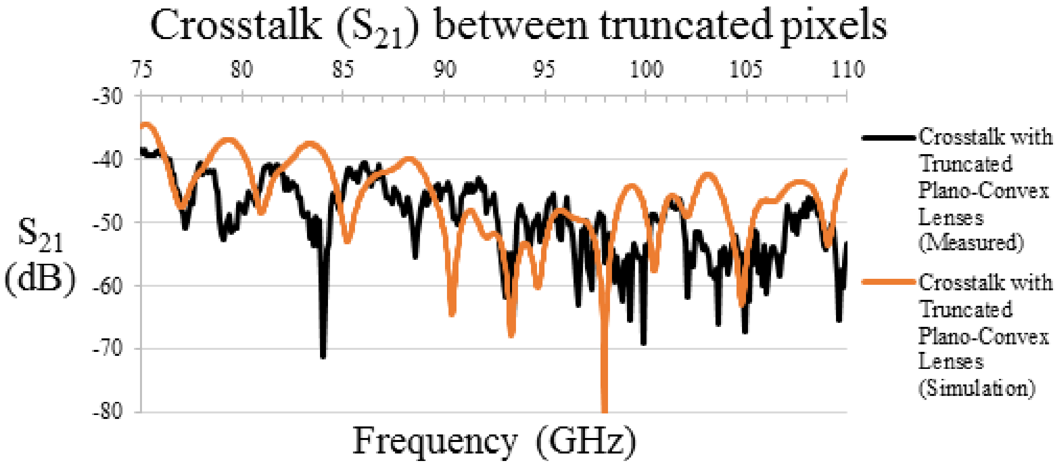

Figure 6-52c: Plot of crosstalk between two circular waveguide probes with truncated plano-convex lenses placed in front.

Each of the previous graphs (**Figure 6-52a**, **b** & **c**) contain a comparison of crosstalk between the measured crosstalk (black) and expected crosstalk (orange). The measured values were plotted alongside the expected crosstalk from the CST simulation. There was a large level of agreement between the measured and simulated crosstalk. The introduction of the dielectric lenses increases the crosstalk between these probes by 10 dB on average. The crosstalk in the CST simulation broadly matches with the level of measured crosstalk at lower frequencies, but deviations occur at higher frequencies. Overall, there was agreement between the measured results and the simulated results from CST.

6.7 Conclusion

The goal of these tests was to design a lens that could be integrated into an array system and increase the directivity of a planar antenna. The five different designs tested were the hemisphere lens, the cylindrical lens, the elliptical cylindrical lens, the plano-convex and the truncated plano-convex lens. The lenses were simulated initially in CST by placing them in front of an idealized rectangular patch antenna. The lenslets were made from HDPE. The lenses were compared to each other based on their maximum directivity. Without any lenses, the patch antenna had a maximum directivity of 7.6 dBi.

The hemisphere lens increases the directivity to 24.4 dBi. This lens would be simple to create, and its directivity was larger than the other lenses designs analysed. However, this lens had poor potential packing capacity in an array configuration due to its spherical shape. The maximum directivity of the cylindrical lens was 20.1 dBi, which was smaller than both the hemisphere and truncated lens. This lens could only be placed along one axis, which places a limitation when integrating the lens into an array structure. An elliptical cylindrical lens had a maximum directivity of 17.4 dBi, which was the lowest of any other lens examined. Both the cylindrical and elliptical cylindrical lenses were not examined further as possible design choices as further optimisation was required. A plano-convex and a truncated plano-convex lens were designed and analysed. The plano-convex reached a maximum directivity of 20 dBi. This was lower than the truncated plano-convex lens, which had a maximum directivity of 21.4 dBi. However, the truncated lens was more difficult to manufacture as more cuts were needed.

Pixels, consisting of neighbouring patch antennas with different dielectric shaped lenses placed in front, were simulated in CST to investigate crosstalk in planar arrays. The lenses tested were the plano-convex and the truncated lens. The crosstalk between two patches placed 10 mm apart was recorded. Without any lenses the crosstalk very small at -72.5 dB. The introduction of the plano-convex and truncated lens increases the crosstalk to -32.1 dB and -50.6 dB respectively. The farfield pattern of the truncated lens also contained smaller side lobes than that generated by the plano-convex lens. The truncated lenses performed better than the plano-convex lenses as the design intends. The crosstalk was recorded for a system with three patches on an array each placed 10 mm apart, with either the plano-convex or the truncated lens pixel. The directivity of the antenna was increased greatly with the introduction of the lenses. The plano-convex lenses increased the directivity to a maximum of 18.9 dBi and 17.7 dBi for the two and three antenna array system respectively. The truncated lenses performed better and increased the directivity to maximum of 20.9 dB and 21.2 dBi for the two and three antenna array system. The truncated lens array did less to reduce crosstalk then initially expected. Its ability to reduce crosstalk was frequency dependent, but the truncated lens reduces the crosstalk at the frequencies at which the patch antenna most strongly resonates. The truncated lenses performed better than the plano-convex lens in reducing side lobes in the farfield pattern. Reducing the area of the back end of the lens facing the antenna reduces the reflected power to neighbouring antennas.

Two plano-convex and truncated plano-convex lenses were manufactured. Probe waveguide antennas, connected to the VNA, were used to propagate a beam through these lenses. The farfield pattern of the probe antenna with each lens was measured in the VNA. Both of the lenses were shown to effectively focus the beam of the probes. Both lenses increase the maximum power detected from -32 dB → -20 dB.

CST was used to model the crosstalk between the circular probes, the plano-convex and the truncated plano-convex lenses, in order to compare to the crosstalk as measured by the VNA. The lenses have a noticeable effect on the crosstalk between the probes. Overall the introduction of the lenses increased the crosstalk by on average 10 dB, a result which agrees with the simulation. The results from the VNA showed that truncated lenslet array had a lower level of crosstalk level than the plano-convex lens and this agrees with the CST simulation. Overall, the truncated lenslet array was the better lenslet design then plano-convex lenslet array as intended in the initial design work.

Chapter 7 Gaussian beam mode analysis

7.1 Overview

At optical and near infrared wavelengths, traditional ray optics is used to accurately represent beam propagation through an optical system. However, at longer wavelengths, traditional ray optics becomes less accurate because diffraction dominates the beam propagation and associated spreading. Physical optics are used to accurately simulate beam characteristics at terahertz frequencies, however, this task is computationally intensive.

As a simpler alternative to physical optics, Gaussian Beam Mode Analysis (GBMA) is a mathematically efficient tool used for analyzing optical systems at long wavelengths [55]. GBMA is based on the propagation of Gaussian beams though the optical system. This technique was used to model truncation effects in a multi-moded optical system described later in **Section 7.4**. An introduction to GBM theory and the associated terminology is presented in **Section 7.2**. This chapter outlines each development stage for the implementation of this code.

The verification of the developed code for simple 1-D and 2-D diffraction aperture fields is presented in this chapter. A multi-moded pyramidal horn was analysed with possible truncation effects included with a truncating aperture window (both circular and rectangular) and effects on the farfield pattern were monitored.

This simple representative system was equivalent to a test setup at Cardiff University where the farfield pattern of a pyramidal horn was to be measured. The tests in Cardiff were performed by the TES development group as part of the initial test of a multimoded horn for the SAFARI mission for SPICA. The author of this thesis was asked to check if the optical arrangement influenced the measurement and to verify that all modes could propagate through the test setup. This is important as if the optical arrangement did not accommodate all modes, then the setup was affecting the farfield pattern and they would not measure the true field pattern.

The horn was used to couple radiation to Transition Edge Sensor detectors (TESs) and so was placed in a cryogenic chamber and illuminated by a terahertz source through a cryostat window. The developed model was written to ensure that the radiation pattern of the horn was unaffected by the finite width of the cryogenic dielectric window used.

The pyramidal horn antenna developed TES development group by the was designed to operate at frequencies between 2.7 and 5 THz or wavelengths of $60-110\ \mu\text{m}$. The horn aperture was 0.65 mm by 1.25 mm and the entrance waveguide dimensions were 0.12 mm by 0.12 mm making it a multi-moded horn with a least 12 waveguide modes propagating at the long wavelength limit. The horn output was analysed at 2.7 THz only to make the modal content as low as possible.

7.2 GBMA Theory

Gaussian beam mode analysis (GBMA) is a scalar analysis technique used for optical analysis of diffraction dominated propagation of long wavelength radiation [56]. Traditional ray tracing can't be used accurately at millimeter wavelengths due to the dominances of beam diffraction between optical elements.

The beam doesn't focus to a point, but rather focuses to beam radius minimum (beam waist), which has a non-zero diameter. The Gaussian beam has a beam width radius, *W*, and an associated phase front radius of curvature, *R*.

7.2.1 Describing the beam propagation

There are several phenomena used to define the beam at some position along the optical path. The beam width, W, is the width of the beam, which is defined as being the distance between the points where the field has fallen to $\frac{1}{e}$ of its on-axis maximum. The phase front radius of curvature, R_c, is the curvature of the wavefront at some distance, z. The Gouy phase ϕ, described the phase slippage between modes. This phase slippage term arises as different modes have different phase velocities [56]. Another useful parameter is the confocal parameter, z_c. The near-field regime operates when $z << z_c$, and when $z >> z_c$ the farfield regime operates.

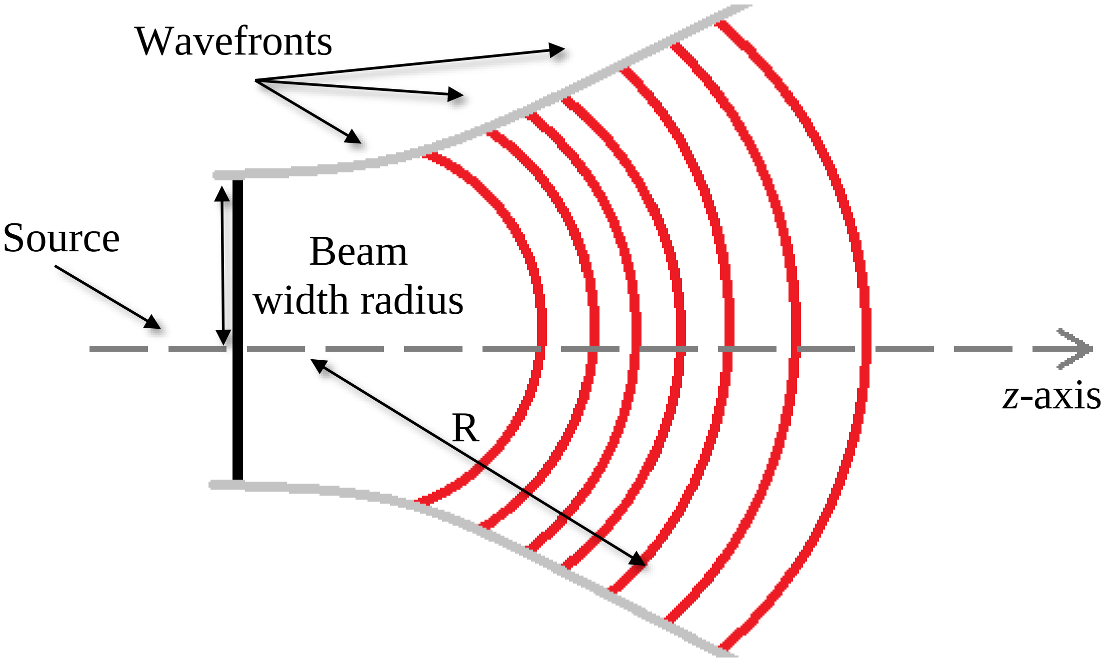

Figure 7-1: Example of a field source in freespace propagating along the *z*-axis.

Once these initial parameters are obtained, they can be calculated at any other distance along the *z*-axis using the following formulas. The beam width radius along the *z*-axis, W, is dependent on the initial beam width radius, W_0, and the wavelength of the beam [55].

$$W(z) = W_0 \times \sqrt{\left(1 + \left(\frac{\lambda \times z}{\pi \times {W_0}^2}\right)^2\right)} \tag{7.1}$$

One thing to note of the above formula, since the parameters λ, z, W_0 can't be complex, the beam width can never be 0. The beam waist is at its minimum, W_0, at z = 0. The beam starts to spread out again after this collimated region.

For this Gaussian beam, each individual wavefront has some curvature, R, and this curvature is the displacement of the wavefront from a plane wave [55].

$$R(\mathrm{z}) = z \times \left(1 + \left(\frac{\pi \times {W_0}^2}{\lambda \times z}\right)^2\right) \tag{7.2}$$

At $z = 0$, the radius of curvature is infinite, i.e. a planar wave-front exists here. The phase slippage term between modes is given as [55]:

$$\phi(z) = \mathrm{ArcTan}\left(\frac{\lambda \times z}{\pi \times {W_0}^2}\right) = \mathrm{ArcTan}\left(\frac{\pi \times W(z)^2}{\lambda \times R(z)}\right) \tag{7.3}$$

The complex scalar electric field $E(x, y, z)$ can be described at any point using the modes ψ_i and weighting coefficients A_i. At some initial starting position along the z-axis, $z_0 = 0$, the beam width radius W_0 is calculated. If the initial electric field profile here is known, E_a (represents the beam generated by the antenna), then the modal decomposition of the beam can be calculated with the appropriate overlap integral. Once these beam parameters at the initial position are found they can be defined at any other position, z.

7.2.2 Gaussian beam decomposition

Gaussian Beam Mode Analysis can also be used to propagate a more complex-shape electric field profile. The electric field at some position along the z-axis can be written as the sum of the product of a weighting factors (mode coefficients) and their corresponding mode [56].

$$E(x, y, z) = \sum_{n=0}^{\infty} A_i \times \psi_i(x, y, z) \tag{7.4}$$

The weighting coefficients A_i, or coefficients are found by integrating the product of the mode and initial known electric field profile E_a (i.e. the electric field of an antenna or a diffraction pattern):

$$A_i = \int {\psi_i}^* \times E_a \, dA \tag{7.5}$$

In this multi-moded case the propagating beam profile is comprised of several modes calculated above, which depend on the initial electric field being decomposed that retain their form as they propagate [55], but evolve relative to one another in terms of phase shift. Each mode propagates independently and can represent more complex beam shapes if required. In analysing a multi-moded horn, each waveguide mode electric field is decomposed into independent Gaussian Beam

Modes and then propagated to the plane of interest to generate the correct evolved electric field profile. A multi-moded horn intensity field is incoherent so the individual modes are added incoherently to get the total farfield intensity pattern,

Depending on the geometry of the electric field to be represented different mode sets are used. These are the Laguerre-Gaussian modes (for circular geometries) and Hermite-Gaussian modes (for rectangular geometries) and these obtain their names as they use the Laguerre polynomials or the Hermite polynomials, respectively. The Hermite modes are primarily used in this thesis (as a pyramidal horn aperture was examined) and the full form of these modes will be shown later in **Equations (7.18)** and **Equation (7.23)** after some other terms have been defined.

7.2.3 Edge taper and truncated plane

For a Gaussian beam, the amplitude reaches a maximum at the centre and gradually decreases off axis. At the beam width, $W(z)$, the beam has fallen to $\frac{1}{e}$ of its maximum. The distribution of power density, P, at some off-axis distance, r, is more formally given by:

$$P(r) = P_0 \operatorname{Exp}\left(-2\left(\frac{r_e}{W(z)}\right)^2\right) \qquad (7.6)$$

In a real optical system, the beam may pass through a lens or a window with a finite size. In this case the edges of the beam may be lost to the optical system [57]. As the beam passes through this plane, the edge part of the beam is truncated or tapered.

The truncated plane model introduces a source of loss to an optical system where the optical elements have finite widths. To simulate a lens or window of finite size, a truncation is applied to the beam at the truncation position, $z_{truncated}$, for some optical element of edge length $x_{truncated}$, outside of which power is effectively lost from the system.

If the truncation of an incident electric field at a symmetric plane where output electric field, E_0, may be written in terms of the incident field E_i as:

$$\begin{aligned} E_0(x) &= E_i(r) \quad x \le a \\ E_0(x) &= 0 \qquad\; x \ge a \end{aligned} \qquad (7.7)$$

where a is the aperture radius and x represents the off axis distance. Both the incident field and the output field may be written in terms of Hermite-Gaussian modes:

$$E_i = \sum_n A_n \psi_n(x) \qquad (7.8)$$

$$E_{out} = \sum_m B_m \psi_m(x), \qquad (7.9)$$

where B_m are the output mode coefficients which will be different to the input set of mode coefficients A_n. Like the input coefficients the output coefficients are given by the overlap integral (assuming the 1-D case):

$$B_m = \int_0^a \psi_m(x) E_o(x) dx \tag{7.10}$$

Within the aperture of width, a, the output field is just the incident field:

$$\begin{aligned} B_m &= \int_0^a \psi_m(x) E_i dx \\ &= \sum_n A_n \int_0^a \psi_m^*(x) \psi_n(x) dx, \end{aligned} \tag{7.11}$$

The output coefficients can be rewritten to show the scattering matrix:

$$B_m = \sum_n S_{mn} A_n \tag{7.12}$$

where S_{mn} is a scattering matrix which re-distributes the power in the input modes into the output modes effected by truncation and relates the output coefficients to the input coefficients and is calculated by the following:

$$S_{mn} = \int_0^a \psi_m^*(x) \psi_n(x) dx \tag{7.13}$$

To include truncation in a 2-D truncation in a Cartesian plane the weighting coefficients are recalculated over a plane at the position of the truncation. Once these new weighting coefficients are calculated, the electric field can be calculated [57]:

$$E(x,y,z) = \sum_{m=0}^{\infty} \sum_{n=0}^{\infty} B_{mn} \times \psi_{mn}(x,y,z) \tag{7.14}$$

In this equation, B_{mn} are the weighting coefficients with the truncation plane. The new weighting coefficients are calculated by:

$$B_{mn} = \int_{-x_{cutoff}}^{x_{cutoff}} \int_{-y_{cutoff}}^{y_{cutoff}} E(x,y,z_t) \times \psi_{mn}(x,y,z_t)\, dy\, dx \tag{7.15}$$

The truncation works by removing all power, beyond the truncation integration limits. The truncation plane is the finite size of the aperture and has an *x*-axis length of $2x_{cutoff}$ and a *y*-axis length of $2y_{cutoff}$. The weighting coefficients can be calculated in terms of scattering matrix, $S_{mnm'n'}$, which represents the relative amount of power transferred between modes at the truncation point:

$$B_{m'n'} = \sum_m \sum_n S_{mnm'n'} A_{mn} \tag{7.16}$$

The scattering matrix is calculated by performing an overlap integral over the product of the modes from the initial beam and the modes of the output beam. The scattering matrix S_{ij} is given by:

$$S_{mnm'n'} = \int_{-x_{cutoff}}^{x_{cutoff}} \int_{-y_{cutoff}}^{y_{cutoff}} \psi_{m'n'}(x,y,z_t) \times \psi_{mn}(x,y,z_t)^* dy\, dx \tag{7.17}$$

Programming code such as *Wolfram Mathematica 10.2* allow the user to define a matrix notation that can deal with this four-index calculation.

7.3 Truncation code implementation

The formulas presented in **Section 7.2** were implemented in the *Wolfram Mathematica 10.2* environment. The Hermite-Gaussian modes were used to model the pyramidal horn beams in freespace. A 1-D model was developed initially and then extended to a full 2-D model. The following section details the different development stages of the code. A classical diffraction of a slit or aperture was used to verify the code.

A 1-D or a 2-D slit aperture was illuminated by a plane wave larger than the aperture dimension meaning that the electric field within the aperture dimensions on the input side was uniformly bright. Each of the plots in the following examples were normalised to unity power.

7.3.1 1-D model of diffraction from a slit

The 1-D case was considered first as it was less computationally intensive and easier to verify. Using this assumption, a 1-D electric field along the *x*-axis was initiated and propagated along the *z*-axis direction. The Hermite polynomial function, $H_m(x)$, was used to define the mode [55]:

$$\psi_m(x,z) = H_m\left(\frac{\sqrt{2}x}{W(z)}\right) \times \left(\frac{1}{2^m\, m!\, \pi\, W(z)^2}\right)^{0.5} \times \mathrm{Exp}\left(-\frac{x^2}{W(z)^2}\right) \times \mathrm{Exp}\left(-I\,k \times \left(z + \frac{x^2}{2\,R(z)}\right) + I\,(m+1) \times \phi(z)\right) \qquad (7.18)$$

Where m was the order of the mode, which have an integer values of 0 and above. The values used to define this beam are described in the following figure.

Aperture width (a)	Wavelength (λ)	Beam width (W_0)	Modes (Ω)
1 mm	0.1 mm	0.5 mm	200

Table 7-1: Parameters used to verify 1-D Hermite Gaussian modes.

The weighting coefficients are calculated when $z = 0$ mm using the form of **Equation (7.5)** and the electric field contains unity power along the slit. At $z = 0$ mm, the radius of curvature was infinite, but this was practically set to 10^9 mm in the code. The electric field of a 1-D square aperture was defined by a "top-hat" or rectangle function,-or more formally:

$$E_0(x,y) = \begin{cases} 1, \text{when } -\frac{1}{2} < x < \frac{1}{2} \\ 0 \text{ elsewhere} \end{cases} \qquad (7.19)$$

The weighting coefficients were calculated by using **Equation (7.5)**. There were two test cases that were performed in order to verify the code. These test cases where the near-field and the farfield case. Firstly, in the nearfield case, when the field was reconstructed at the diffracting plane, the rectangle function should be recreated. Secondly at large distances ($z >> z_c$), the farfield pattern of the rectangular function should be seen. The expected farfield pattern result of the rectangle function is known as the Sinc (θ) function.

$$Intensity\colon I_p = I_0 \left(\frac{Sin\ (\chi)}{\chi}\right)^2 \tag{7.20}$$

$$\text{where } \chi = \frac{a\,\pi}{\lambda}\ Sin\ (\theta) \tag{7.21}$$

Simulations were run in order to test the 1-D case with the simple top hat function as the aperture field. GBM analysis was used to decompose the field and then reconstruct it in the farfield. The total amount of modes in a beam, Ω, determines the accuracy of the simulation, but comes with a larger computational overhead as the mode number increases.

These modes were deconstructed and plotted at *z* = 0 mm to produce the rectangular function (see **Figure 7-2** for results), then propagated to the farfield and re-summed allowing the classic Sinc (θ) function to be reconstructed. The parameters used to verify the code are shown in **Table 7-1**. The Hermite modes in **Equation (7.18)** were used to propagate the beam along the *z*-axis.

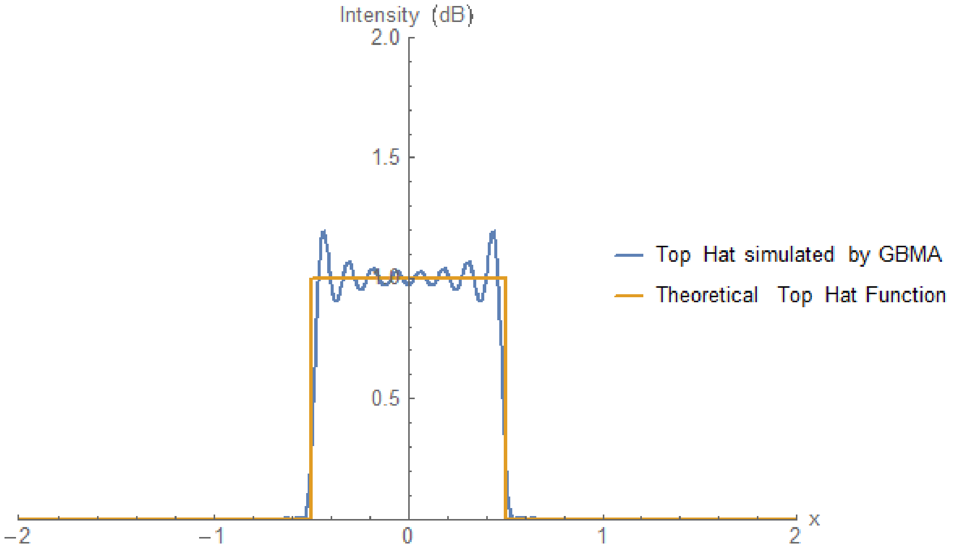

Figure 7-2a: Square aperture as simulated by GBMA (blue) and theoretical top hat (orange).

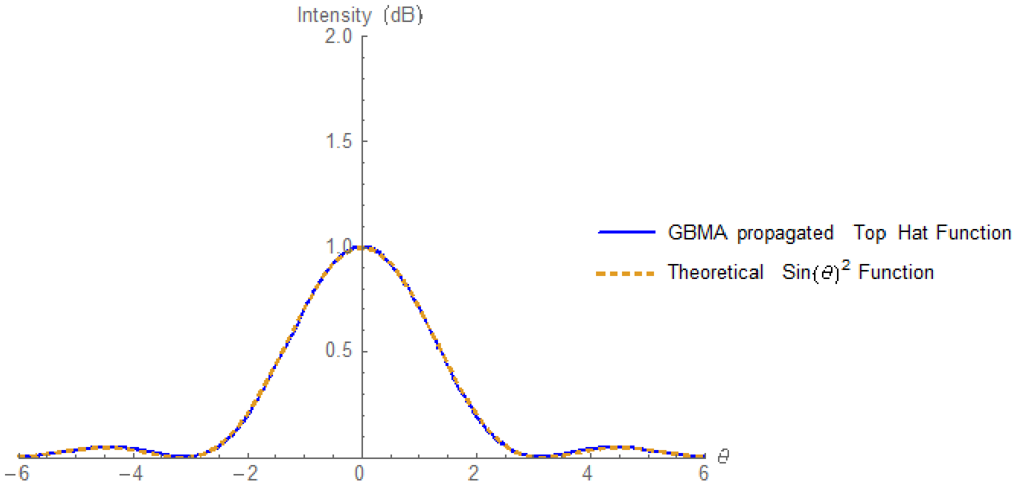

Figure 7-2b: Pattern of top hat function propagated by GBMA (blue) and theoretical Sinc$(\theta)^2$ function (orange).

As shown in **Figure 7-2a,** the simulation generated the approximate shape of the top hat function. The simulation deviates somewhat from the theoretical due to the finite amount of modes generated. In **Figure 7-2b** there was strong agreement between the simulated and the theoretical beam, which indicates that the simulation was behaving as expected. Both plots show strong agreement between the beam recreated using GBMA and the theoretical functions. The simulation was re-run with a different value of W_0 as shown in the following:

Aperture width (a)	Wavelength (λ)	Beam width (W_0)	Modes (Ω)
1 mm	0.1 mm	0.1 mm	200

Table 7-2: Parameters used to test 1-D Hermite Gaussian modes.

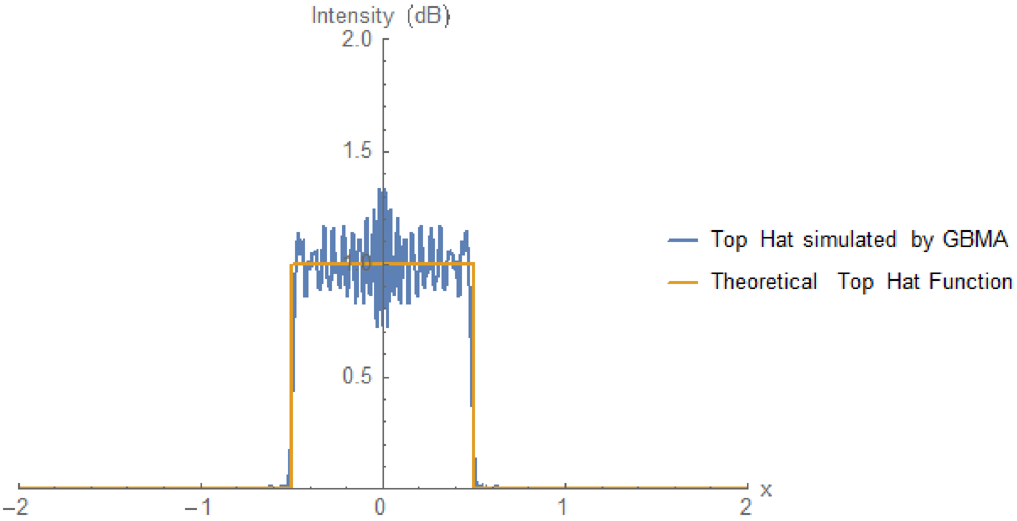

Figure 7-3a: Square aperture as simulated by GBMA (blue) and theoretical top hat (orange).

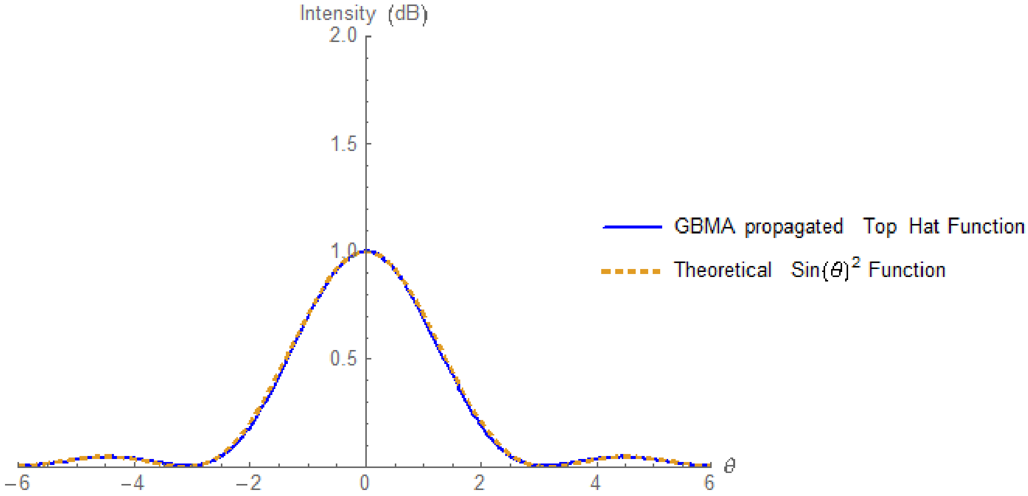

Figure 7-3b: Pattern of top hat function propagated by GBMA (blue) and theoretical Sinc$(\theta)^2$ function (orange).

The smaller W_0 used to generate **Figure 7-3a,** created a less accurate approximate 1-D top hat function than **Figure 7-2a**. However, the propagated pattern in both **Figure 7-2b** and **Figure 7-3b** was as expected. These results show that the rectangle function can be represented by a sum of Gaussian Beam modes. These results verified the model for simple 1-D cases.

7.3.2 2-D model

The 1-D model was extended in order to implement 2-D apertures over an area. This implementation requires changing the Hermite modes to the 2-D Hermite modes as shown in **Equation (7.23)**. As there were two axes, there were significantly more modes required in order to achieve the same level of accuracy. For every Ω modes used in the 1-D simulation there will be Ω^2 modes for the 2-D simulation. This placed a large computational overhead requirement in order to achieve an accurate result.

Aperture width (a)	Wavelength (λ)	Beam width (W_0)	Modes (Ω)
1 mm	0.1 mm	0.065 mm	30

Table 7-3: Parameters used to verify 2-D Hermite Gaussian modes

To test the simulation, a simple 2-D square aperture was defined in the simulation, which was used to represent an idealised square antenna. The electric field of this 2-D square aperture was defined by the 2-D version of the “top-hat” function, which like the 1-D version had a value of 1 in the aperture and 0 everywhere else. The electric field for this 2-D aperture was defined as this rectangular function along both the *x* and *y*-axis, or more formally:

$$E_0(x,y) = \begin{cases} 1, \text{when } -\frac{1}{2} < x < \frac{1}{2} \text{ and } -\frac{1}{2} < y < \frac{1}{2} \\ 0 \text{ elsewhere} \end{cases} \qquad (7.22)$$

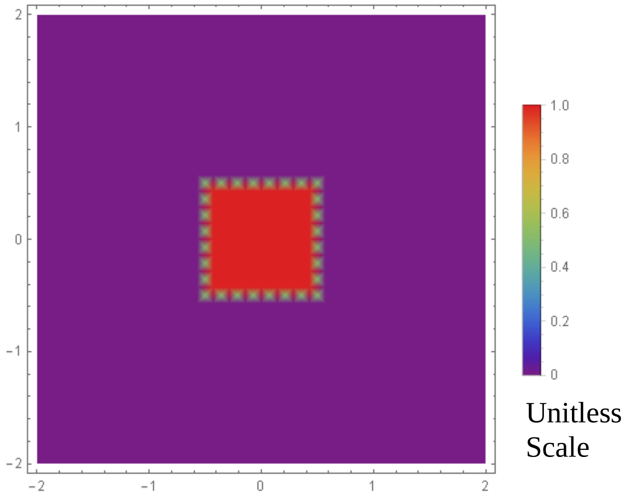

Figure 7-4: The initial electric field E₀(x, y) for a square aperture, as defined by **Equation (7.22)**.

The 2-D Hermite modes were used to propagate this beam. Using the Hermite polynomial to describe the electric field gives the equation for the modes [56]:

$$\begin{aligned}\psi_{mn}(x,y,z) = H_m\left(\frac{\sqrt{2}x}{W(z)}\right) \times H_n\left(\frac{\sqrt{2}y}{W(z)}\right) \\ \times \frac{1}{\sqrt{2^{m+n-1}\, m!\, n!\, W(z)^2}} \times \text{Exp}\left(-\frac{x^2+y^2}{W(z)^2}\right) \\ \times \text{Exp}\left(-ik\left(z + \frac{x^2+y^2}{2 * R(z)}\right) + i(m+n+1)\phi(z)\right)\end{aligned} \qquad (7.23)$$

In **Equation (7.23)**, *m* and *n* are the order of the mode. The order of the mode could have an integer value of 0 and above. Additionally, for simplicity, this formula explicitly assumes that the Gouy phase along the *x* and *y*-axis are identical.

The weighting constant, A_{mn}, for these modes were found by integrating the electric field and modes over the *x* and *y* plane at the truncation plane. Similarly, the 1-D case, the integration was performed at *z* = 0 mm, in order to keep the weighting coefficients real. As there were two dimensions in this simulation, the coefficients A_{mn}, were calculated for Ω^2 modes [56]. The weighting coefficients were found by an integral at some known electric field E_0:

$$A_{mn} = \int\int \psi_{mn}(x,y,\mathrm{z})^* \times E_0(x,y,\mathrm{z})\, dx\, dy \tag{7.24}$$

Initially the number of modes was set to be 50, as this many modes were required for a reasonable beam profile and reasonable computation time. The computer used to run these simulations was a Dell Optiplex 7010 and the code took a few hours to run. The code was verified by recreating the near-field beam and the farfield beam using GBMA.

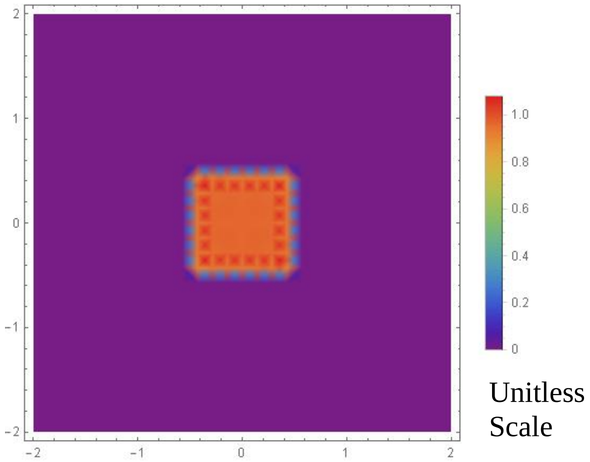

Figure 7-5a: Electric field at *z* = 0 mm recreated by GBMA. the recreated field at the initial aperture.

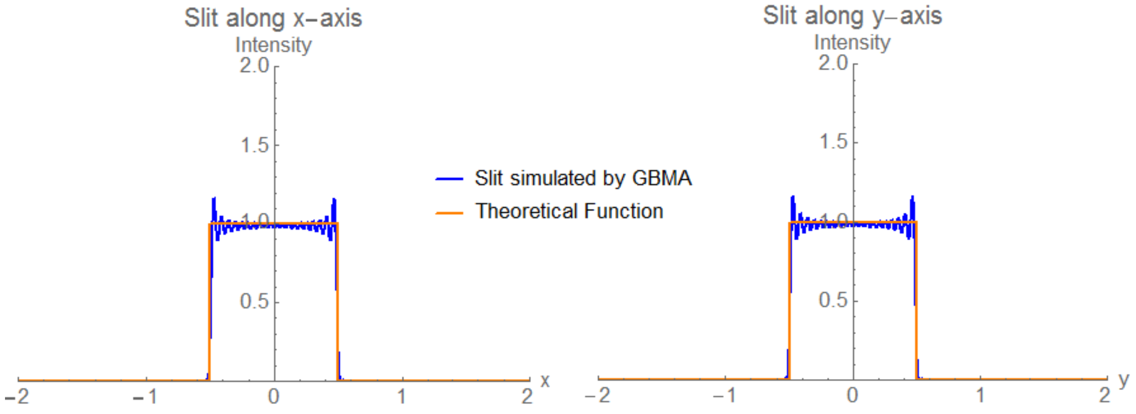

Figure 7-5b: A comparision of theoretical and simulated beams along the *x* and *y*-axis.

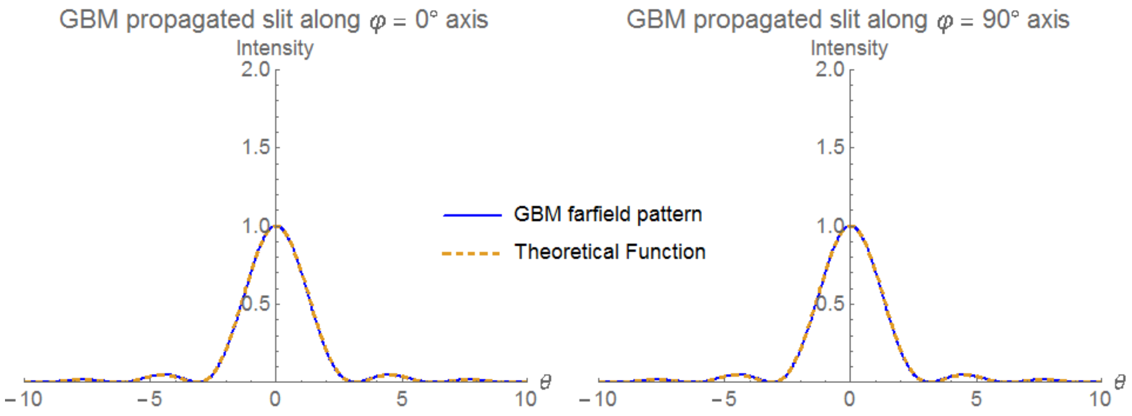

Figure 7-5c: A comparision of theoretical and simulated farfield beams along the *x* and *y*-axis.

Figure 7-5a showed that the recreated beam had a square shape and had a roughly uniform field. This plot is similar in shape to the electric field of the theoretical shown in **Figure 7-4**. There is good agreement between the theoretical and the simulated results in **Figure 7-5b**. Additionally the beam simulated along the *x*-axis is almost identical to the beam simulated along the *y*-axis, which is expcted for this symetrical slit. The simualted farfield in **Figure 7-5c** is also very similar to the theoretical shape. This similarity between the simulated result and the theoretical function confirms the technique for the 2-D case.

7.3.3 Horn antenna with truncation

The model was extended to include a truncation plane in the code of the program. In the general case there was an input plane, a truncation plane and an output plane where the beam is to be reconstructed (see **Figure 7-6** for diagram).

The input electric field at the input plane can be rewritten in terms of Gaussian beam modes. These modes are then propagated to the truncation plane where the appropriate overall integral can be applied to taper the beam. This truncated beam was then propagated to the output plane where the modes were reconstructed with the correct phase slippage between them to account for diffraction and slippage from the diffracting or truncating apertures.

This truncation simulates a blockage around the edges of the beam, which the external part of the beam cannot propagate through. The truncation was modelled to only allow light passing through a square hole, of side length $r_{truncation}$, from the centre. In this model the starting point was defined to be at z = 0 mm, the truncation was located at the point $z_{truncation}$ and the beam was propagated to the output point z_{output}.

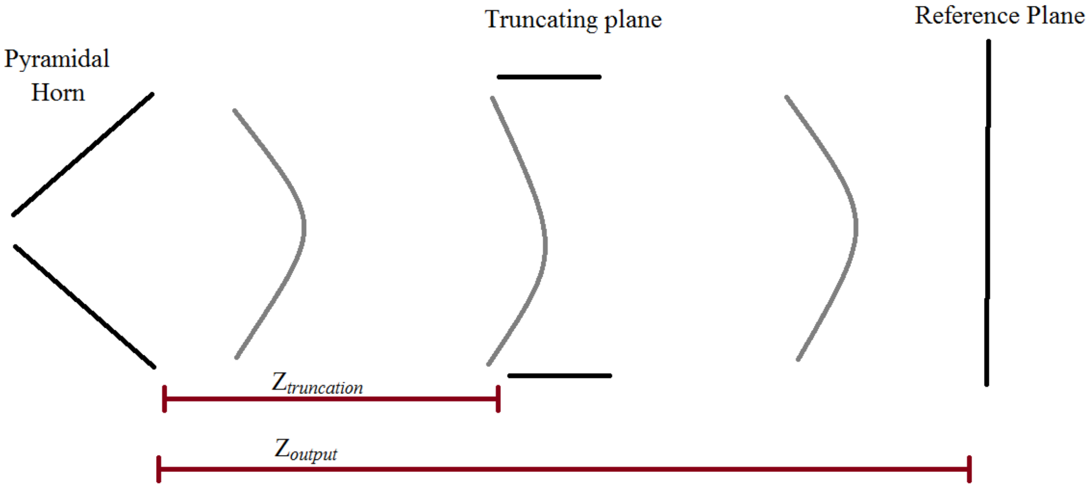

Figure 7-6: Sketch of the experimental setup. The beam propagates from the pyramidal horn, passes through the gap in the truncating plane and propagates to the reference plane.

The region before the truncated plane uses the A_{mn} weighting coefficients to propagate the beam, while the B_{mn} weighting coefficients were used to describe the beam after the truncation point as described above. The scattering matrix, $S_{mnm'n'}$ was used to convert the A_{mn} coefficient into the B_{mn} coefficients and this matrix was calculated by performing an overlap integral at the truncation point around an aperture.

A general algorithm for creating and propagating a beam using this model could be summarized in the following points:

1. Read in initial electric field, E_a, from an external file
2. Some constants, such as the beam width $W_{0,}$ the wavelength, λ, the size of the aperture and the number of modes to be used were defined.
3. Calculate the A_{mn} weighting coefficients at 0 mm
4. Propagate the beam using the Hermite modes and the A_{mn} weighting coefficients from the start (0 mm) to the truncation point, $z_{truncation}$
5. Calculate the scattering matrix, $S_{mnm'n'}$ at the truncation point. Use symmetry to reduce the computation time of the integrals
6. Calculate the B_{mn} weighting coefficients at the truncation point using the scattering matrix
7. Propagate the beam using the Hermite modes and the B_{mn} weighting coefficients to the viewing point at z_{output}.

The scattering matrix was a $\Omega^2 \times \Omega^2$ matrix, where Ω was the number of Gaussian modes. Each element was calculated by performing an overlap integral by **Equation (7.17)**. Calculating this matrix was computationally intensive as Ω^4 integrals were performed. Orthogonal symmetry was used to speed up calculation by only carrying out the integral where coupling exists between the modes. Calculating overlap integrals in *Mathematica* can be slow as the automatic integral functions often spend time calculating high precision values around zero when the integral is actually zero.

Two tests were performed in order to verify that this model was implemented correctly. These tests compared the un-truncated and the truncated beam. This test uses a simple electric field defined by the rectangular function with some edge length, a. The rectangular slit beam was propagated to a point, $z_{truncation}$, and passed through either a small aperture and a larger aperture, as shown in **Figure 7-7**. This test was performed in order to see that the truncation would be evident in the output beam at the correct level.

a	1 mm	$r_{truncation}$	0.1 mm
W_0	a × 0.1 = 0.1 mm	$z_{truncation}$	1 mm
λ	0.1 mm	Ω	30

Table 7-4: Parameters used for small truncation test.

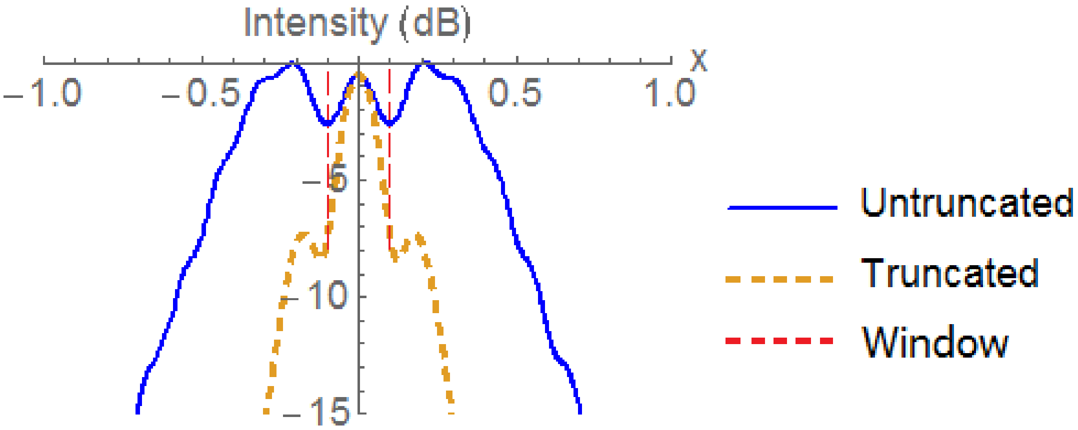

Figure 7-7: Comparison between the beam, when un-truncated (blue) and truncated (orange dashed), plotted at the truncation point.

As **Figure 7-7** shows the un-truncated beam propagated as normal, but for the truncated beam, there was a sharp decline in the intensity at a distance of ~ 0.1 mm off-axis, which was expected. The truncation had a large effect on the beam, which was expected as the truncation was smaller than the beam width. This verifies this part of the truncated plane model.

In the following figures, a beam was propagated though a large aperture truncation. Since the truncation was physically large (a large aperture = low truncation), the beam should not be affected by the truncation.

a	1 mm	$r_{truncation}$	5 mm
λ	0.1 mm	$z_{truncation}$	1 mm
W_0	a × 0.1 = 0.1 mm	Ω	30

Table 7-5: Parameters used for large truncation test. The length of the truncation $r_{truncation}$ was much larger in this test than previously.

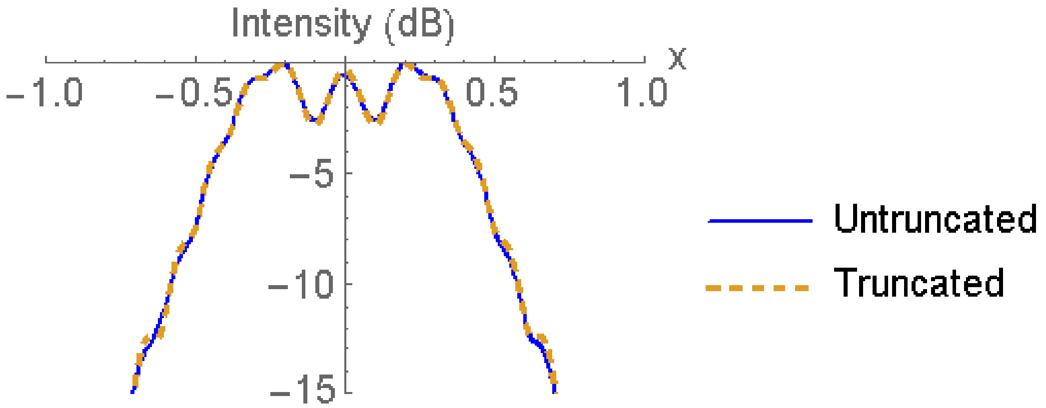

Figure 7-8: Intensity pattern of un-truncated (blue) and truncated (orange dashed) beam along the *x*-axis at the truncation point.

The plot in (**Figure 7-7**) showed that a small optical aperture truncation reduced the width of the beam and (**Figure 7-8**) clearly showed that a large optical aperture truncation had no effect on the beam, which were the expected results. The two beams were found to be identical which verifies this portion of the GBMA code. These two tests verify that the truncated plane code had been correctly implemented.

7.4 Pyramidal horn antenna analysis

This example simulates potential truncation of a multi-moded beam from a rectangular horn antenna passing through a truncating aperture (see **Figure 7-6**). The following section details the simulation used to model experimental measurements performed with a pyramidal horn antenna measured in a cryostat. As the beam propagates from the horn (assuming transmission), it passes through a cryostat window which needs to be large enough to avoid chopping of the beam. The waveguide mode aperture fields from the pyramidal horn (12 in total at the long wavelength limit) were decomposed into freespace modes at the horn aperture and then the individual waveguide modal fields were propagated to the measurement plane via a potential truncating plane of the cryostat window. The total incoherent sum of the modes was checked to analyse any truncation effects at the cryostat window.

7.4.1 Experimental configuration

The multi-moded pyramidal horn antenna was designed to operate at 2.6 and 5.0 THz or 0.10 to 0.06 mm. The antenna had an aperture size of 1.25 mm × 0.65 mm. The horn couples to a TES detector housed in a cavity behind the horn which needs to be cryogenically cooled to operate. A terahertz source illuminates the cryostat and the incident power passed through a 30 mm diameter window in the cryostat wall. The pyramidal horn antenna was placed 25 mm inside the cryostat relative to the cryostat window.

A silicon carbide element source was placed a distance of 470 mm away from the aperture. This device radiated at terahertz frequencies towards the antenna. Due to the finite size of the cryostat window, power from the source moving at an angle of 31° or larger (geometrical angle) would not enter the cryostat window and be lost. If any modal fields from this multi-moded pyramidal horn are outside this entrance, then power will be lost. A simple model of the truncated sum of fields and the equivalent sum of un-truncated fields can be written to check the levels of truncation involved in this measurement.

7.4.2 Simulation of pyramidal horn antenna

The horn antenna aperture electric fields were read in from several text files (12 in total), each of which represents the field at the aperture of the pyramidal horn antenna for each propagating aperture mode supported by the entrance waveguide. Each aperture field was decomposed and propagated individually to the measurement plane (both including or leaving out the truncation). The horn aperture (input plane) was positioned at $z = 0$ mm and each file represented a waveguide mode electric field profile at the aperture of the horn. The truncation plane in this case was the position of the cryostat window at 25 mm and this window had a truncating diameter of 30 mm. The observation plane was the position the beam was propagated to and, in the simulation, was set at z = 495 mm. This distance corresponds to the position of the silicon carbide element source used by the TES development group. In this context, the field detected at the observation plane was equivalent to the farfield pattern.

The aperture was simulated by reading in 24 files, which represents the real and complex values for 12 antenna modes of a pyramidal horn antenna above cut-off. Each of these files was a 51 × 51 grid, which represented the initial electric field at each position along the x and y-axis, which was an equivalent sampling rate of 0.025 mm in the x-axis and 0.013 mm in the y-axis.

One issue with describing the aperture was that the data in the files was discrete in form, but a continuous function was desired. Interpolation was used to convert the discrete array of elements from the file into a continuous function. The *interpolation* function in *Wolfram Mathematic* was used to create a "initial field" function, $E_{a,f}(x,y)$ for each of the 12 antenna modes, where f represents the antenna field for each mode. These "initial fields" were easier to integrate in *Wolfram Mathematic* then a discrete datasheet. The code was modified in order to allow the initial electric field to be set by reading data from some external file. This then allows the electric field to be integrated and thus obtain the weighting coefficients.

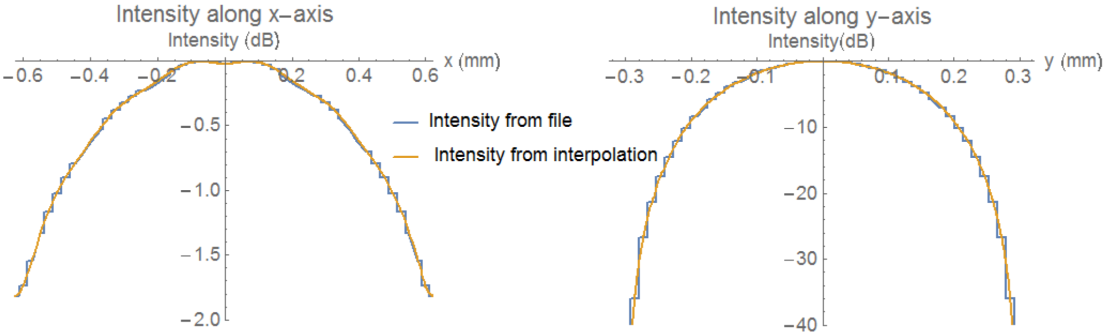

Figure 7-9: Intensity from input file and generated using interpolation along the x-axis (left) and y-axis (right).

The program could read in discrete data and create an approximate function from that data, which allowed *Mathematica* to perform integrals on the real data. After the input plane had been initialised the Hermite-Gaussian modes were used to propagate the beam. The pyramidal horn has dimensions of 1.25 mm × 0.65 mm and as it was longer along the *x*-axis than the y-axis, this introduced the need to have different parameters in the orthogonal directions. $W_x(z)$, $W_y(z)$, $R_x(z)$, $R_x(z)$, $\phi_x(z)$ and $\phi_x(z)$ were the beam width, radius of curvature and the Gouy phase in either the *x* or y-axis respectively. As a result, the Hermite modes need to be rewritten in order to take this asymmetry into account:

$$\begin{aligned}\psi_{mn}(x,y,z) = {} & H_m\left[m,\frac{\sqrt{2}x}{W_x(z)}\right] \times H_m\left[n,\frac{\sqrt{2}y}{W_y(z)}\right] \\ & \times \frac{1}{\sqrt{2^{m+n-1}\, m!\, n!\, \pi\, W_x(z)\, W_y(z)}} \times \mathrm{Exp}\left[-\frac{x^2}{W_x(z)^2} - \frac{y^2}{W_y(z)^2}\right] \\ & \times \mathrm{Exp}\left[-I\left(k\,z + \frac{\pi\, x^2}{\lambda\, R_x(z)} + \frac{\pi\, y^2}{\lambda\, R_y(z)}\right)\right] \\ & \times \mathrm{Exp}\left[\frac{I}{2}\Big((2m+1)\phi_x(z) + (2n+1)\phi_y(z)\Big)\right]\end{aligned} \qquad (7.25)$$

The *A* weighting coefficients were calculated at the input aperture for each waveguide mode and each electric field for each of the 12 input modes, via the overlap integral described in **Equation (7.17)**. Each modal field then written as a free space mode set of Hermite Gaussian modes as shown in **Equation (7.25)**. Each of these modes were propagated separately to be truncated at the correct plane and ultimately propagated to the output plane. After the truncation plane the *B* weighting coefficients were used to reconstruct the beam at the observation plane. The output field plotted was the intensity pattern at 495 mm over a 300 mm × 300 mm observation plane, where the intensity was the square of the electric field.

This is repeated for each modal field from the horn and the intensity pattern of each mode is then summed to obtain the overall intensity pattern of the horn. The real cryostat window used is circular. Different truncating aperture geometries were investigated– both square and circular and the influence of the aperture shape on the farfield pattern.

Increasing the amount of modes, Ω, increases the accuracy of the simulations, but comes with a large computational overhead. As there are Ω^2 modes the scattering matrix is a $\Omega^2 \times \Omega^2$ matrix.

7.4.3 Comparison to expected

The expected farfield pattern was computed using the multi-moded waveguide analysis code SCATTER developed in parallel in the research group. It is the verified farfield pattern of the sum of modes that can propagate from the horn. This expected farfield pattern was compared to the reconstructed GBMA farfield pattern where no truncation is included along both the *x* and y-axis.

The simulated pattern was generated by propagating the beam to *z* = 495 mm having decomposed the aperture field of each mode.

a	1.25 mm	λ	0.101 mm
b	0.65 mm	$W_{0x}(z)$	$a \times 0.11 = 0.1375$ mm
Ω	30	$W_{0y}(z)$	$b \times 0.11 = 0.0715$ mm

Table 7-6: Parameters used in GBMA simulation in the test to compare with the expected results. The truncation plane was not used for this test. More than 30 modes could be used to increase accuracy, but this would increase the simulation time of the program to the order of several days.

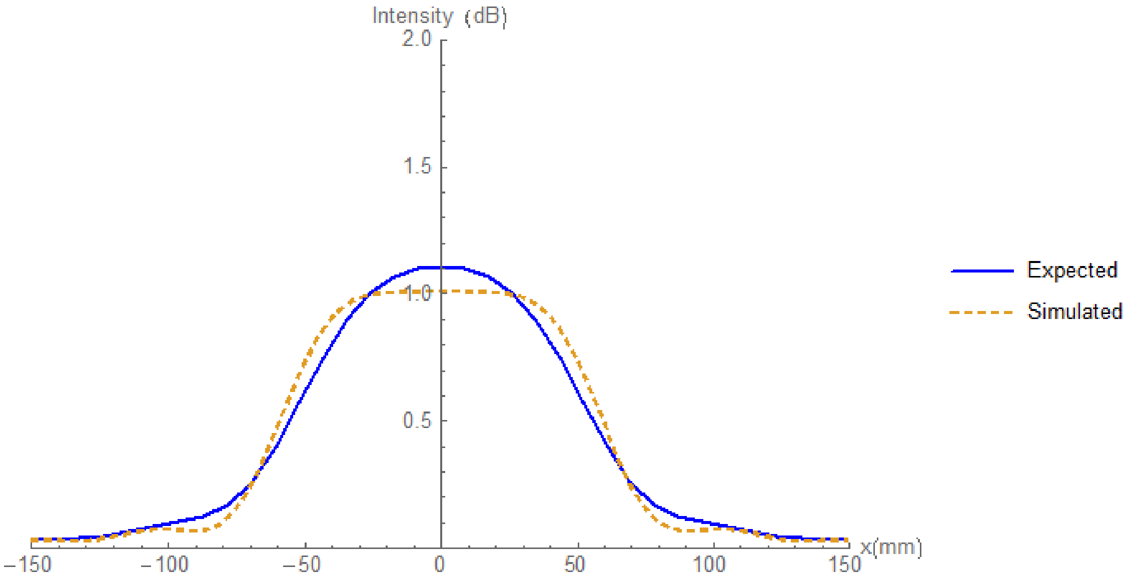

Figure 7-10a: Expected and simulated farfield along the *x*-axis.

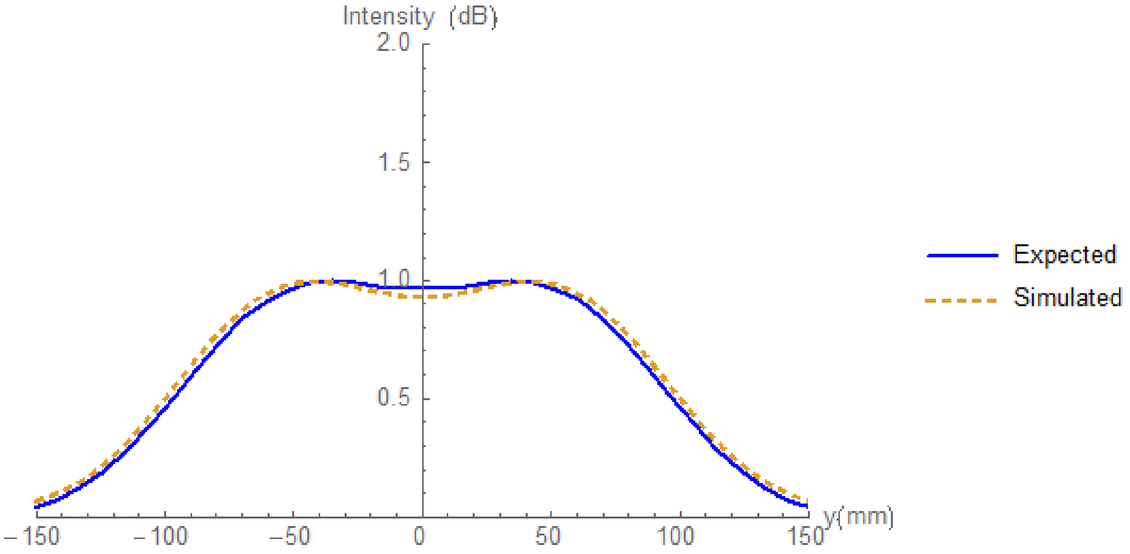

Figure 7-10b: Expected and simulated farfield along the *y*-axis.

Results from **Figure 7-10** were good because the expected results from the farfield and the simulation match to the -16 dB level and there was reasonable agreement with the number of Gaussian beam modes used. There was a good agreement between the expected and simulated beam, however the simulated beam had a larger main lobe then the expected beam.

7.4.4 Rectangular and circular truncation of pyramidal horn fields

The rectangular truncation case was a rectangular plane where $X_{truncation}$ and $Y_{truncation}$ were the limits of the aperture window along the *x* and *y*-axis respectively outside of which the aperture is effectively absorbing all incident power.

As this device was a multi-moded antenna, each aperture mode had a different relative amount of power. The modal power was the proportional amount of power expressed by an aperture mode [56]. The modal power allowed for a comparison of the relative amount of power in each mode and the proportion of the beam that was lost at the truncating plane. This modal power was calculated by squaring the sum of each weighting coefficient.

$$Power\ in\ aperature\ mode\ \propto \sum_{i} |A_{mn}|^2 \qquad (7.26)$$

The pyramidal horn antenna's fields were decomposed into modes and the field at the truncation point was examined.

a	1.25 mm	λ	0.101 mm
b	0.65 mm	Ω	30
$W_{0x}(z)$	a × 0.11 = 0.1375 mm	$X_{truncation}$	30 mm
$W_{0y}(z)$	b × 0.11 = 0.0715 mm	$Y_{truncation}$	30 mm
$z_{truncation}$	25 mm		

Table 7-7: Parameters used to simulate the rectangular truncation for the pyramidal horn.

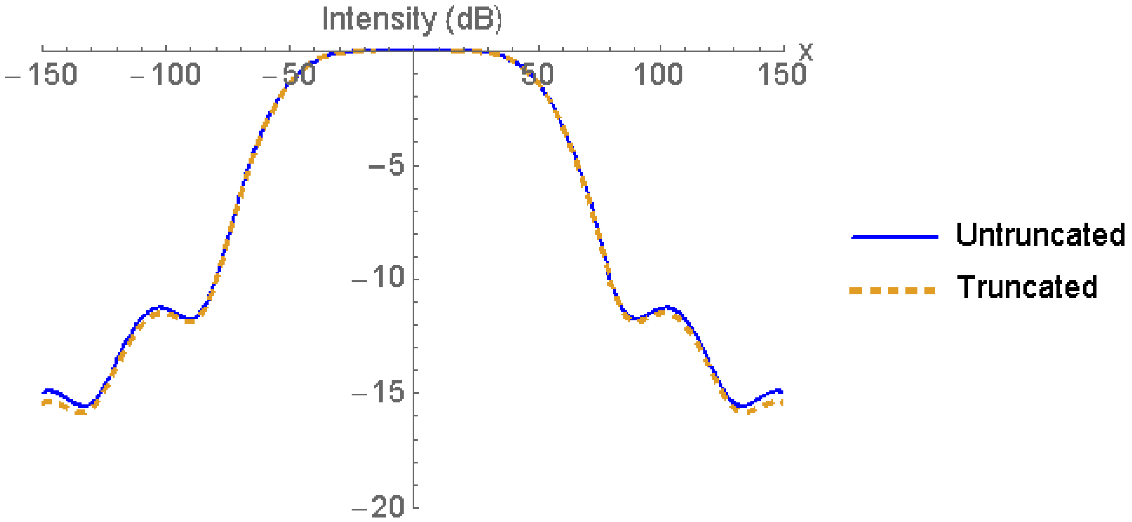

Figure 7-11a: Comparison between truncated and un-truncated at *z* = 495 mm along the x-axis.

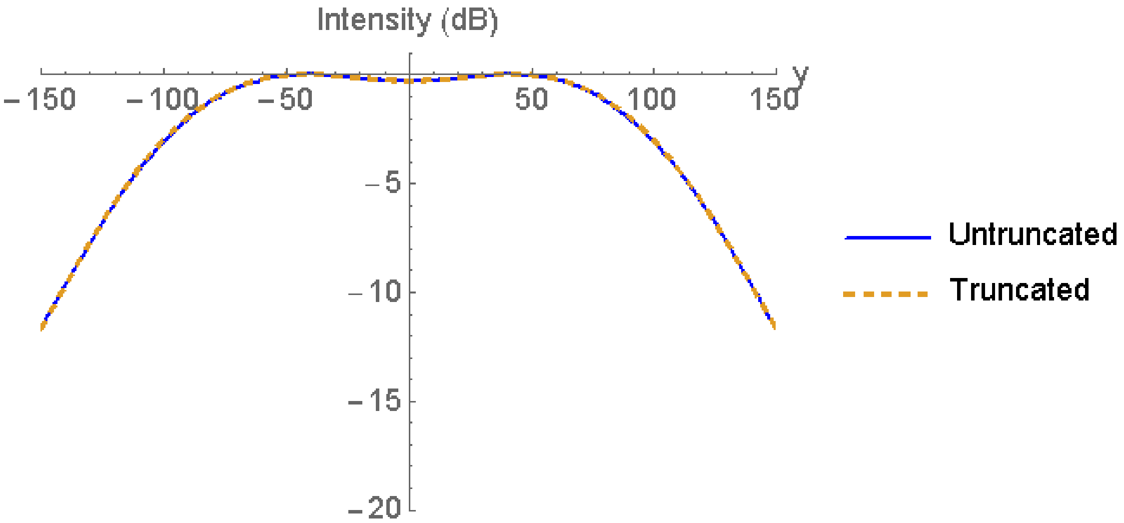

Figure 7-11b: Comparison between truncated and un-truncated at z = 495 mm along the y-axis.

Along both the x-axis (**Figure 7-11b**) and y-axis (**Figure 7-11c**), the truncation had a relatively small effect on the beam pattern shape suggesting truncation effects are insignificant.

Each aperture mode was independent and some modes may be significantly truncated at the truncation point. The modal power for each aperture mode was calculated using the formula in **Equation (7.26)** and compared with and without truncation.

Aperture Mode	Mode power before truncation	Mode power after truncation	% Change
1	0.000338	0.000334	1.3
2	**0.195**	**0.194**	**0.4**
3	4.48E-05	4.38E-05	2.1
4	**0.142**	**0.140**	**0.8**
5	0.0510	0.0506	0.8
6	**0.194**	**0.193**	**0.6**
7	0.0988	0.0978	1.0
8	0.0823	0.0817	0.8
9	0.0483	0.0478	1.0
10	0.101	0.0998	0.8
11	0.0736	0.0728	1.1
12	0.000637	0.000616	3.3

Table 7-8: Modal power in each aperture mode before truncation and after truncation. The aperture modes containing the largest relative power are in bold.

A majority of the power in found in the aperture modes 2, 4 and 6. There was a less than 1% change in the total amount of power in these most prominent modes. The largest relative change in power were in modes 3 and 12. However, these modes contain little power to begin with and the change in power here will have little effect on the overall beam. The following two plots showed the effect the truncation had on two different aperture modes propagated to the observation plane.

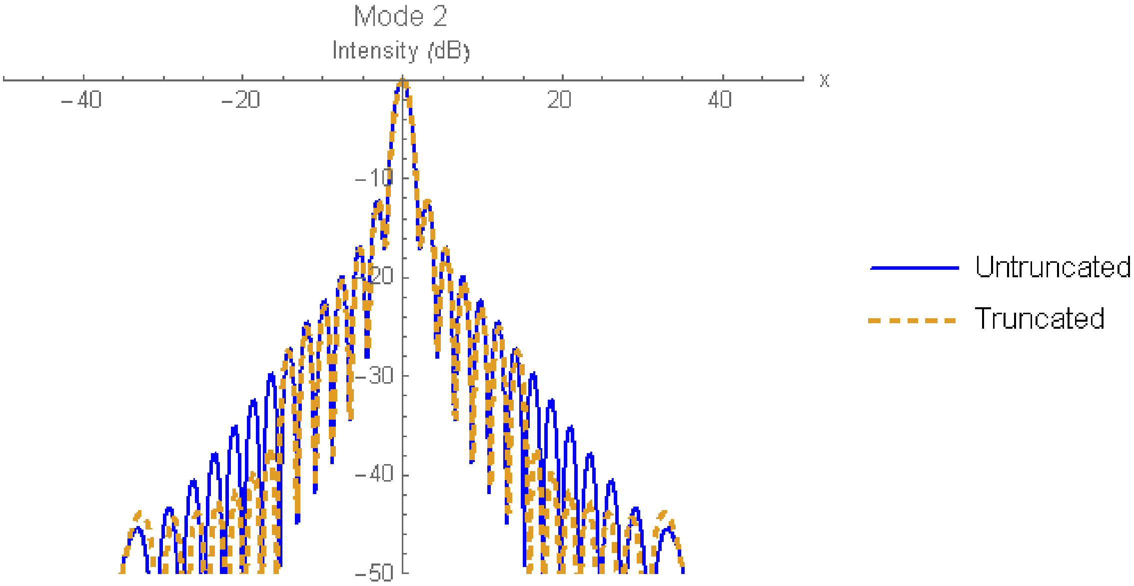

Figure 7-12a: Normalized plot of the beam generated by aperture mode 2 at truncation point (z = 25 mm), by a rectangular truncation.

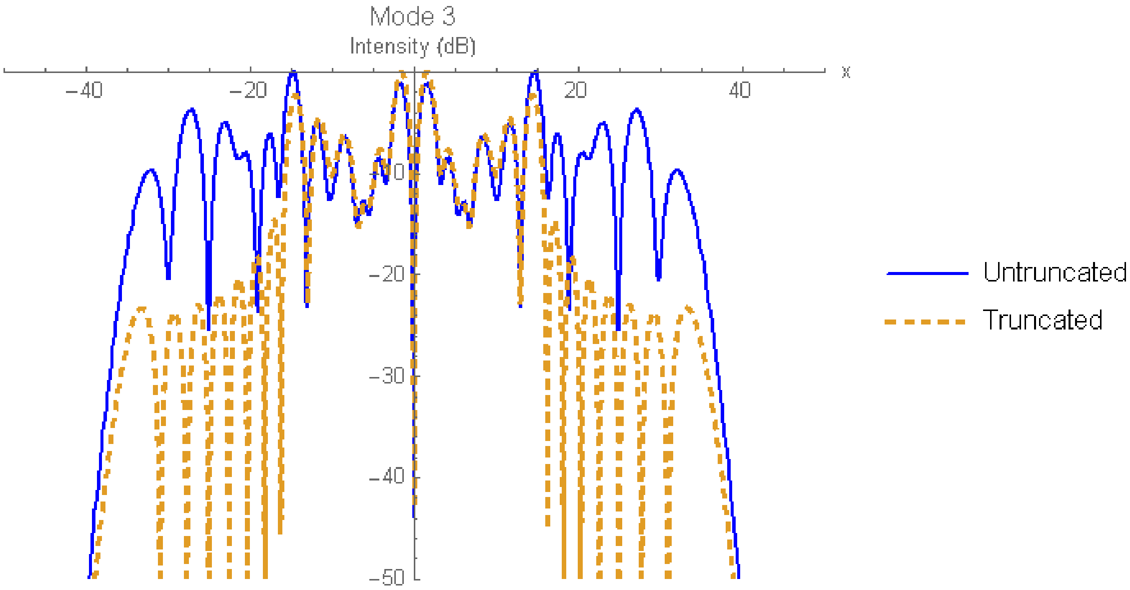

Figure 7-12b: Normalized plot of the beam generated by aperture mode 3 at truncation point, by a rectangular truncation.

There was little difference between the truncated and untruncated in **Figure 7-12a**. Aperture mode 2 was not significantly affected by the truncation. Aperture mode 3 in **Figure 7-12b** was affected by the truncation and this explains the loss of power for mode 3 (although at a low level) as the power beyond the truncation width was cut significantly. The sides of the beam have been noticeably cut at 15 mm. The truncation had a length of 30 mm which was consistent with the cut in the graph. However, since aperture mode 3 had only a relatively small amount of power, the truncation did not affect the beam's overall pattern.

The same simulation was performed again with a circular truncation plane, which more accurately represent the cryogenic window in the TES development group experimental set-up. Most parameters are the same as **Figure 7-11a**, except for $r_{truncation}$, which was the radius of the window. As this aperture area was slightly smaller than the rectangular truncation, it was expected that more power would be blocked by the window.

a	1.25 mm	λ	0.101 mm
b	0.65 mm	Ω	30
$W_{0x}(z)$	$a \times 0.11 = 0.1375$ mm	$r_{truncation}$	15 mm
$W_{0y}(z)$	$b \times 0.11 = 0.0715$ mm	$z_{truncation}$	25 mm

Table 7-9: Parameters used to simulate the rectangular truncation for the pyramidal horn.

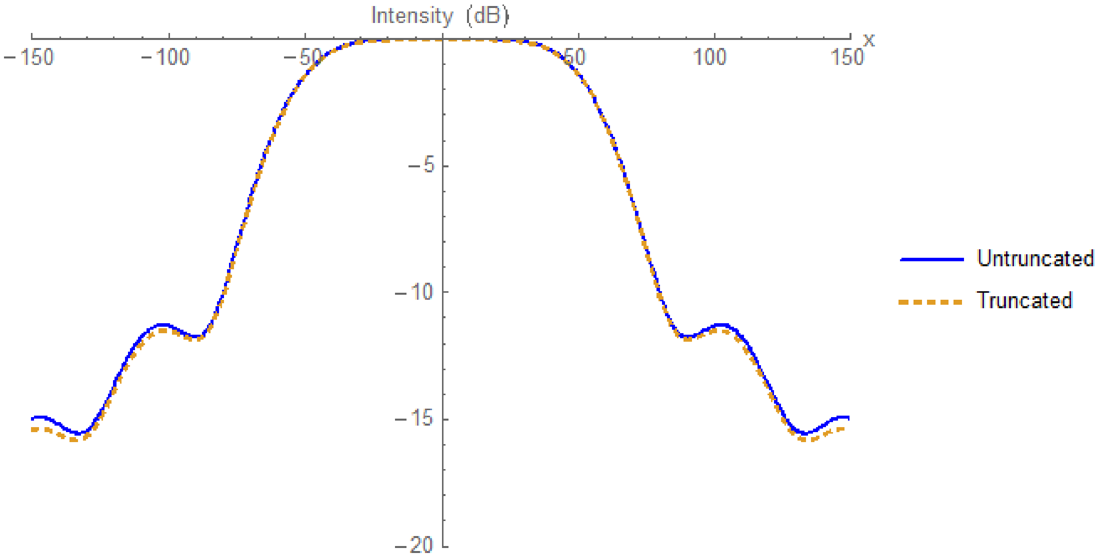

Figure 7-13b: Comparison between truncated and un-truncated at z = 495 mm along the x-axis.

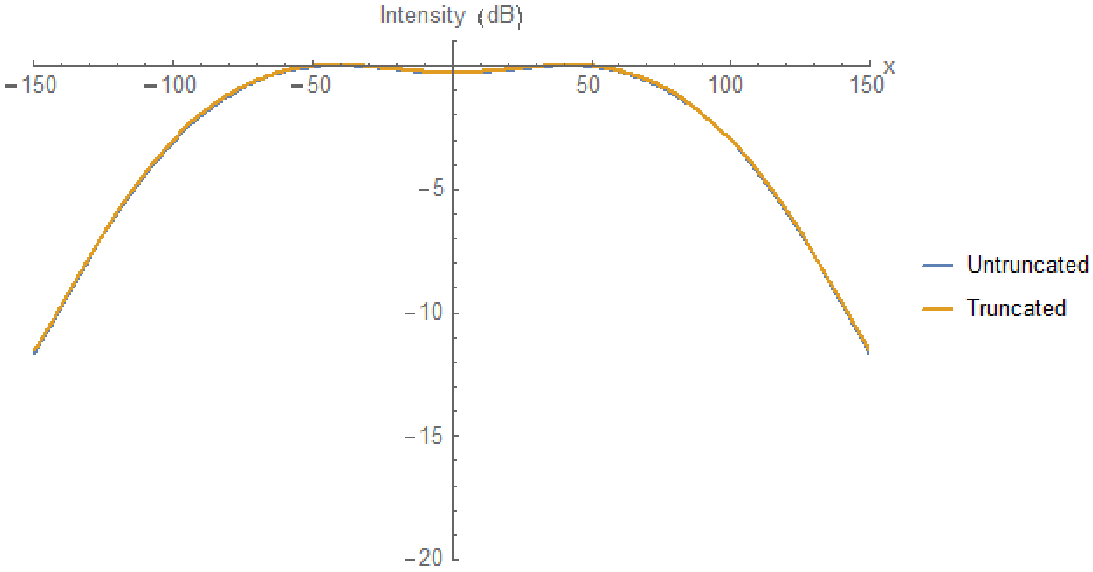

Figure 7-13c: Comparison between truncated and un-truncated beam at z = 495 mm along the y-axis.

The truncation has no apparent effect on the antenna's intensity pattern in either **Figure 7-13b or Figure 7-13c**. It can be concluded that the window was large enough that it had no effect on the device's performance. The modal power for each mode was calculated in order to analyse the effect the beam had on each aperture mode.

Aperture mode	Mode power before truncation	Mode power after truncation	% Change
1	0.000338	0.000334	1.1
2	**0.1950**	**0.194**	**0.5**
3	0.0000448	0.0000436	2.6
4	**0.142**	**0.140**	**0.9**
5	0.0511	0.0506	0.9
6	**0.194**	**0.192**	**0.9**
7	0.0988	0.0981	0.7
8	0.0823	0.0817	0.8
9	0.0483	0.0479	0.7
10	0.101	0.0998	0.8
11	0.0736	0.0726	1.4
12	0.00064	0.00061	4.7

Table 7-10: Table containing the relative amount of power in each mode before truncation (*A*) and after truncation (*B*). The modes which contained the most power are in bold and these modes were almost un-affected by the truncation.

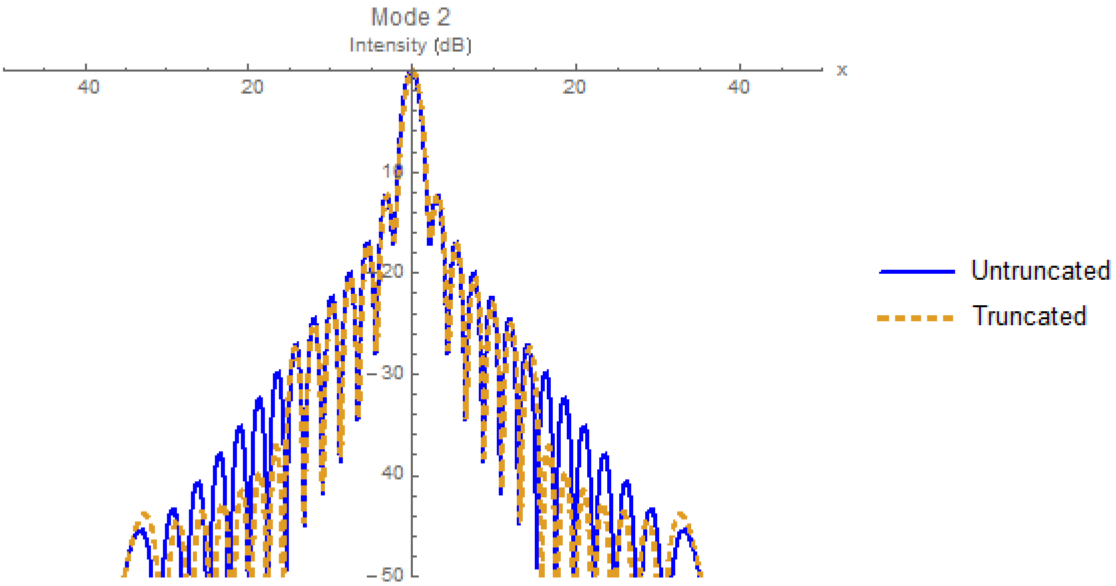

Figure 7-14a: Beam pattern generated by aperture mode 2 plotted at $z = 25$ mm. A reduction of power was seen at ±15 mm for the truncated beam, which was due to the circular truncation.

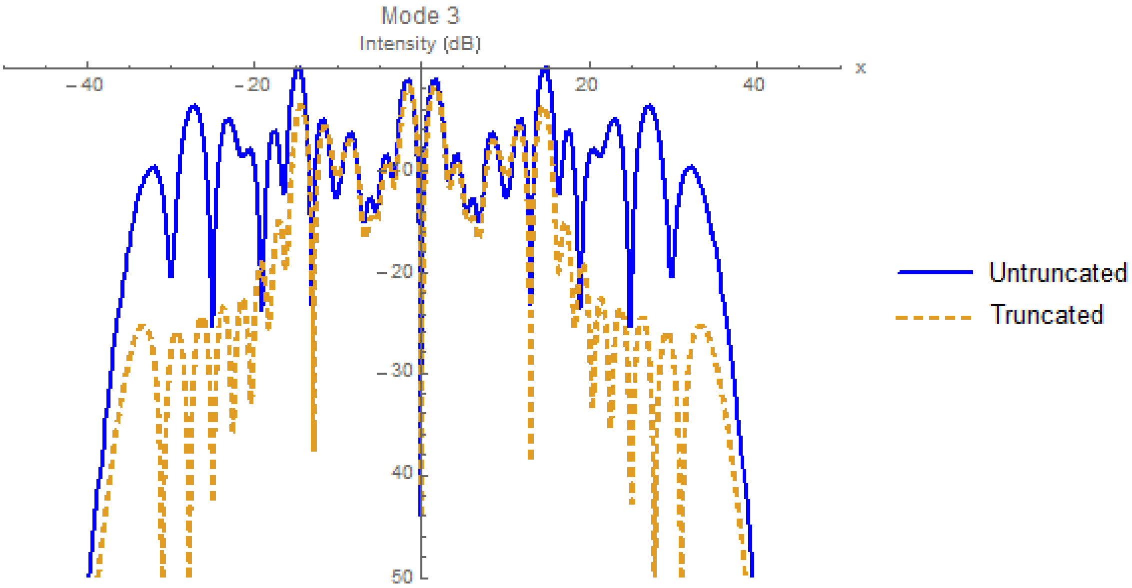

Figure 7-14b: Aperture mode 3 plotted at *z* = 25 mm, for circular truncation.

The power loss in **Figure 7-14a** was relatively small as the majority of the beam passed through the truncation and so the truncation had only a small effect on the beam. In **Figure 7-14b**, the beam sharply decreased in intensity at 15 mm, which was also the width of the truncation plane. This mode was affected by the truncation, but as the mode contains relatively little power, it did not affect the overall beam pattern shown in **Figure 7-13**.

7.5 Conclusion

The goal of this research was to create a program that could simulate any truncation effects of a cryostat window when a multi-moded pyramidal horn antenna illuminated the aperture. The horn modal aperture fields were decomposed using Gaussian beam mode analysis.

The code was verified using a simple 1-D model (**Figure 7-2**) and 2-D model (**Figure 7-5**) of a classical diffracting aperture. The simple model was extended in order to simulate any lost or truncated power from a multi-moded horn beam. There was good agreement between the expected farfield pattern and the pattern generated by the GBMA model (**Figure 7-10**).

Rectangular and circular truncation was applied to the TES development group horn beam. Only low levels of power in modes were affected by the truncation effect of the cryostat window, suggesting the window has no effect on beam characteristics as designed (**Figure 7-13**).

Chapter 8 Conclusion and future work

8.1 Summary

The aim of this research was to examine different planar antennas and feeding mechanisms for W band frequencies (75 – 110 GHz). Simple patch antennas in conjunction with small lenses (lenslets) were designed, simulated and experimentally tested. The issue of crosstalk (reflected power) between pixels was also analysed. Additional work included in the thesis was modelling of a multi-moded horn antenna using Gaussian Beam Mode Analysis (GBMA) to include truncation of the individual waveguide modes with a cryogenic window in carrying out measurements at frequencies between 2.7 and 5 THz. This developed code was used to show the potential influence of truncation on the comparison of measurements and simulations of a pyramidal horn antenna tested in Cardiff University.

Chapter 1 presents the scientific motivation for using the terahertz region of the EM spectrum for astronomy and also terrestrial applications. A brief summary of standard cosmology was provided to outline the context of measuring the polarization of the CMB signal. Several astronomical missions were outlined that target these frequencies and potential commercial applications were highlighted briefly. These areas could be further exploited as technology improves.

Chapter 2 provides an overview of various analysis software and antenna configurations used for this thesis. A core component of this thesis was the analysis of W band planar antennas and common antenna terms and parameters were defined. For this thesis, the desired antenna design should have the largest directivity possible, with a minimised S_{11} over some region of the W band. Several different antenna designs were examined in this thesis: back-fed circular patch, back-fed rectangular patch, planar endfire, planar slot, side-fed rectangular patch and inset patch antennas. The commercial software package CST Microwave Studio was used extensively and a description of some of the software’s algorithms was provided.

Several chapters detail the development process of creating planar antennas. The aim of this work was to design and build an antenna, using the available PCB, which could operate effectively at W band frequencies. Simulations of these devices were run in CST in order to find the design parameters that most effect the devices performance (the position of the feed wire, the size of the patch, the size of the PCB board, the height of the substrate, etc.) and to determine the level of accuracy required to manufacture these devices. The VNA allows for the S-parameters of these antenna to be measured and compared to the simulations. Placing planar antennas in array is also desirable and then crosstalk between neighbouring antennas becomes an issue.

Chapter 3 presented the development stages of the circular and rectangular back-fed patch antenna on the 0.8 mm board. Several back-fed patches were simulated in CST and optimisation tests were run to create a device which would be resonate at a target frequency of 100 GHz. The displacement of the wire from the centre of the antenna and the size of the patch had a large effect on the antenna’s ability to radiate power efficiently. The thickness of the dielectric was found to significantly affect the performance of patch antennas at these high frequencies and with the ATB18 PCB, it was found to be not possible to create a “classical” patch antenna radiating upwards from the patch that could operate at W band frequencies. For conventional lower frequency designs, the dielectric thickness is far smaller than the wavelength but at 100 GHz the thickness is a significant fraction of the board thickness and this leads to poor radiation characteristics in general. A board with a smaller substrate height was required for a classical patch antenna behaviour at these frequencies. Specialist thinner PCB boards are available (0.125 -0.4 mm) but these then become difficult to work with due to their fragility.

Several antennas were manufactured using the 0.8 mm thick ABT18 board and were measured in the VNA using a feed wire coupled from a WR10 waveguide to the patch. The farfield patterns of the antenna did not show a well-defined intensity pattern. The simulated and the measured results do not agree, which could be due to the construction process distorting the shape of the patches. Drilling a specific offset from the patch centre and then soldering the wire to the patch with good electrical contact was very difficult and repeatability of this process was poor. Once a solder was placed on the patch/wire to make a contact, the shape of the patch (in terms of the size of the patch) was intrinsically altered which must affect the quality of the radiation pattern. At lower frequencies a small drilled hole to attach a wire would only be a small area compared to the overall patch area but at W band frequencies, the 1 mm patch is really damaged in the drilling process and this is unavoidable using this back-fed technique. In trying to drill hole accurately and solder the wire in a repeatable manner proved very difficult and must account for a lot of the discrepancy between antenna performance compared to simulations. The planar antennas did radiate at W band frequencies, but the quality of the beam was low and the level of power radiated also make accurate measurements, difficult even with the dynamic range of the VNA. Other techniques were investigated in later chapters to try to improve on this signal coupling technique.

Chapter 4 continued the W band planar antenna development by examining side-fed patch antennas on a 0.4 mm and on the thinner 0.125 mm PCB. While the side fed design does solve the repeatability and damage issues with the back-fed antennas, they also presented new challenges to overcome. One major issue was the unavailability of a calibration kit for the coaxial cable to use with the VNA, which would remove uncertainty caused by the 1 mm coaxial connecting lines. A 1 mm coaxial calibration kit is expensive to purchase (circa €25,000) and was not available. Significant power could be reflected internally within these connections and would also have frequency dependent characteristics, which could not be predicted, that would affect antenna behaviour over the W band frequencies. The critical parameters for the inset antenna design were the size of the patch, the size of the board, the microstrip length and the angle of the inset.

The inset patch antennas were constructed on the 0.4 mm board and tested with the VNA. The simulated farfield was different in shape from the farfield of the measured antennas with the measured beam radiating at some angle to the desired axis of propagation. The manufactured antennas did not perform as well as expected and measurements of their beams disagreed with simulations. Nonetheless being able to measure W band farfield patterns was an achievement but again a number of influences on the beam pattern such as the lack of proper system calibration affected the potential outcomes. An inset patch antenna was also designed on the 0.125 mm PCB. The expected farfield pattern had a maximum directivity of 7.55 dBi, but the farfield pattern contained an unusual "ripple" (peak and trough characteristic) over the main beam. The testing of the microstrip length showed that an antenna with a shorter microstrip did not have this ripple pattern. Altering the microstrip length showed that an antenna fed with a shorter microstrip did not have this ripple pattern. It can be concluded that the non-ideal radiation pattern was due to the microstrip length feeding signal to the device. In the measured farfield pattern the ripple pattern expected from CST were more noticeable. This effect could also be caused by multiple reflections or standing waves in the measurement between antenna and waveguide probe antenna, but this proved to be independent of distance between the source and detector. The influence of reflections within the coaxial cable was another unknown when comparing measurement to simulation. This thinner PCB based antenna performs better than the same device on thicker dielectric boards and radiates in the vertical direction, as expected from lower frequency traditional patch antenna designs.

Chapter 5 provides a summary of the several alternative designs which were manufactured using the 0.8 mm PCB. An endfire antenna, a planar slot design, a superstrate slot, a U slot antenna and a E slot antenna design were constructed and analysed in CST. This was an attempt to use thicker dielectric boards at W band frequencies as the dielectric really influences the radiation characteristics and launches the beam off the vertical direction. Taking this fact into account, several antennas configurations were designed in an attempt to radiate well in this horizontal direction instead. Two endfire antennas were manufactured and their S-parameters were measured using the VNA. The large amount of reflections in the first antenna renders the antenna unsuitable for practical use, which again was limited by feeding the signal wire through the back. Additionally, there was a large difference between the first and second antenna due to the difficulty in reproducing the same alignment and precision for each device. These endfire antennas performed poorly due to manufacturing issues.

The slot antenna design, in contrast, had a much lower S_{11} parameter than the endfire antenna. A flange connector was used to connect the coaxial feed to this slot antenna. The beam pattern contained a strong central beam with two large side lobes. The slot antenna performed better without its support structure, but without the support the antenna was mechanically weak and prone to rotating in the flange, causing problems with aligning the device and repeatability. Three additional devices were simulated in CST: a slot antenna with parasitic patches and windowed metallic superstrate, a U-shaped slot antenna and an E-shaped slot antenna. Each of these devices were designed to operate at lower W band frequencies and were rescaled to operate at 75 GHz in CST. Each of these designs could work at 75 GHz, however each design required a high manufacturing tolerance. For that reason, neither of these devices were manufactured and tested. The planar slot antenna device preformed significantly better than the other antennas. The main issues with this device were its tendency to rotate in the flange and its large side lobes.

Chapter 6 presents the research into dielectric lenses to be used with planar antennas at W band and towards terahertz frequencies. Several lenses of HDPE were designed and simulated in CST and placed with patch antennas operating at 100 GHz. Five different designs of lens were investigated -: the hemisphere lens, the cylindrical lens, the elliptical cylindrical lens, the plano-convex lens and the truncated plano-convex lens. Without any lenses in front, the patch antenna had a maximum directivity of 7.6 dBi. The hemisphere lens increases the directivity to 24.4 dBi. The maximum directivity of cylindrical lens was 20.1 dBi. The plano-convex lens reached a maximum directivity of 20 dBi. The truncated plano-convex lens had a directivity of 21.4 dBi, but this lens was more difficult to manufacture accurately as more cuts were needed to create this lens. The last two designs developed performed well, were relatively easy to integrate into an array type structure and were examined further in CST to investigate crosstalk in planar arrays. The truncated plano-convex pixel had a lower crosstalk in the CST simulation then the plano-convex pixel, which was the reason to introduce the truncated plano-convex design.

Two plano-convex and truncated plano-convex lenses were constructed in house and the farfield pattern of the probe antenna with each lens was measured in the VNA. Both of the lenses were shown to effectively focus the beam of the waveguide probes. The crosstalk between two plano-convex lenses and two truncated plano-convex lenses was measured by the VNA. On average, over the W band frequency range, the truncated lenses performed better than the plano-convex lens in reducing the crosstalk between the antennas.

Chapter 7 detailed the development steps performed of a program that could simulate the truncation effects of a multi-moded pyramidal horn antenna as the beam passed through a cryogenic window. Gaussian beam mode analysis was used extensively in order to validate the influence of this cryogenic window on a farfield plot of a multi-moded pyramidal horn at 2.7 THz. A few simple tests were performed on code using classical diffraction from a simple slit and aperture to verify the model. The technique was then extended in order to simulate any lost or truncated power from a multi-moded pyramidal horn beam propagated through a cryogenic window as part of a THz beam measurement. Twelve individual waveguide aperture fields were decomposed and propagated through apertures (both circular and rectangular) to investigate loss in measurements in the TES development group system. After the truncation was applied, only low levels of power in modes were affected by the truncation effect of the cryostat window, suggesting the window has no effect on the pyramidal horn beam characteristics as designed.

8.2 Future Work

There remains the potential for further development in all parts of this work. This section will provide an overview of how this work could be continued into the future.

There is still the potential for work with the back-fed and side patch antennas. The development of the patch antennas encountered several issues with manufacturing tolerances. As a result, when multiple antennas of the same type were tested, there was some variation between individual antennas. An additional inset side fed antenna, which produced a better beam than the other planar antenna, could be built in order to check the variation in this antenna design. Additionally, an arrangement could be set up in order to determine the crosstalk between two inset antennas.

There are different antenna designs that could be used as an alternative to antennas that were used in this work and these devices could be examined. A few such as U and E slot antennas are simulated but not manufactured in this work. The next step for these antennas would be to manufacture them and see if they perform as well as expected.

There is also the possibility to examine different types of antennas. Only planar antennas are designed in this work, but other types of devices, such as horn antennas, can also be used to make observations of the CMB. The probe antennas coupled well to the lens arrays developed in this work and it is possible that the lens array could also be applied to other devices.

In this work, simulations of more than two antennas are shown, however only up to two antennas are used in the VNA at the same time. The next step in would be to manufacture an array of planar antennas and test them in a laboratory in order to verify that the crosstalk matches that from simulation.

Chapter 9 Appendix

9.1 Glossary of terms

Beam width	The distance between the points where the field has fallen to $\frac{1}{e}$ of its on-axis maximum.
Cosmic Microwave Background (CMB)	Omni directional signal detected at microwave frequencies.
Crosstalk	The unwanted transfer of a signal from one antenna or device to another in the same circuit.
Farfield (Fraunhofer zone)	The region where the beam produced by the antenna retains its angular power distribution with distance. The beam can be considered a plane wave in this zone.
Finite Element Method (FEM)	An analytical technique used to solve EM fields by solving partial differential equations with known boundary conditions.
Gaussian beam mode analysis (GBMA)	Technique used to represent an optical system.
Giant Molecular Clouds (GMC).	A large cloud of dust and molecules in the interstellar medium
Gouy phase	The phase slippage between Gaussian beam modes
Horn antenna	Electrically large antenna consisting of a large aperture which narrows down to a waveguide.
Interstellar medium (ISM)	The collection of dust and gas found in the region between stars.
Kinetic Inductance Detectors (KIDs)	Devices constructed from superconductors and measure changes in impedance due to Cooper pair break up.
Lambda Cold Dark Matter (ΛCDM) model	Model used to explain the formation of the Universe. This model includes several components, such as the Big Bang Theory, Inflation and the accelerated expansion of the Universe.
Patch Antenna	Type of planar antenna consisting of a patch, a ground plate and a dielectric in between.
Phase front radius of curvature	The curvature of the wavefront at some distance from the source
Planar antenna	Antennas built on printed circuit boards.
Stoke parameters	Parameters used to characterize the polarization of a light wave.

S-parameters	Parameters used to describe the transfer of power between ports.
Spectroscopy	Technique used to study the chemical composition of a material by examining the light emitted/absorbed by energy level transitions
Terahertz frequency	The general frequency range between roughly 30 GHz to 3 THz.
Transition Edge Sensor (TES) bolometers	Detectors which operate by absorbing an EM signal and recording the temperature change caused by absorbing that signal.
Vector Network Analyzer	A multi-port system used to measure the internal reflection, gain and loss of a device by directly measuring the S-parameters.

Bibliography

[1] D. Samtleben, S. Staggs and B. Winstien, “The Cosmic Microwave Background for Pedestrians: A Review for Particle and Nuclear Physicists,” *Annual Review of Nuclear and Particle Science,* vol. 57, pp. 245-283, 2007.

[2] NASA, “Electromagnetic Spectrum,” [Online]. Available: https://www.nasa.gov/directorates/heo/scan/spectrum/txt_electromagnetic_spectrum.html. [Accessed June 2018].

[3] M. Smith, The Origin of Stars, London: Imperial College Press, 2004.

[4] NASA, “Diagram of atmospheric window,” [Online]. Available: https://earthobservatory.nasa.gov/Features/RemoteSensing/remote_04.php. [Accessed June 2018].

[5] A. Wootten and A. Thompson, “The Atacama Large Millimeter/Submillimeter Array,” *Proceedings of the IEEE,* vol. 97, no. 8, pp. 1463-1471, 2009.

[6] Z. Ahmed, M. Amiri, S. Benton, J. Bock, R. Bowens-Rubin, I. Buder, E. Bullock, J. Connors, J. Filippini, J. Grayson, M. Halpern, G. Hilton, V. Hristov, H. Hui, K. D. Irwin, J. Kang, K. S. Karkare, E. Karpel, J. M. Kovac, C. L. Kuo, C. B. Netterfield, H. T. Nguyen, R. O'Brient, R. W. Ogburn IV, C. Pryke, C. D. Reintsema, S. Ricter, K. L. Thompson, A. D. Turner, A. G. Vieregg, W. Wu and K. W. Yoon, “BICEP3: a 95GHz refracting telescope for degree-scale CMB”.

[7] J. A. Bonetti, A. D. Turner, J. J. Bock, J. A. Brevik, P. K. Day, J. Filippini, S. R. Golwala, W. Holmes, W. C. Jones, M. Kenyon, J. M. Kovac, C. L. Kuo, H. G. LeDuc, M. Lueker, H. T. Nguyen, R. O'Brient, A. Orlando, M. Runyan, Z. Staniszewski, R. Sudiwala and A. Trangsrud, “Characterization and Fabrication of the TES Arrays for the Spider, Keck and BICEP2 CMB Polarimeters,” *Journal of Low Temperature Physics,* vol. 167, no. 3-4, pp. 146-151, 2012.

[8] ESA, “Planck,” [Online]. Available: http://www.esa.int.

[9] IEEE Aerospace & Electronic Systems Society, “IEEE Standard Letter Designations for radar-Frequency Bands, IEEE standard 521-2002,” 2003.

[10] P. T. P. Ho, P. Altamirano, C.-H. Chang, S.-H. Chang, C.-W. Chang, C.-C. Chen, K.-J. Chen, M.-T. Chen, C.-c. Han, W. M. Ho, Y.-D. Huang, Y.-J. Hwang, F. Ibañez-Romano, H. Jiang, P. M. Koch, D. Y. Kubo, C.-T. Li, J. Lim, K.-Y. Lin, G.-C. Liu, K.-Y. Lo, C.-J. Ma, R. N. Martin, P. Martin-Cocher, S. M. Molnar, K.-W. Ng, H. Nishioka, K. E.

O'Connell, P. Oshiro, F. Patt, P. Raffin, K. Umetsu, T. Wei, J.-H. P. Wu, T.-D. Chiueh, T. Chiueh, T.-H. Chu, C.-W. L. Huang, W. Y. P. Hwang, Y.-W. Liao, C.-H. Lien, F.-C. Wang, H. Wang, R.-M. Wei, C.-H. Yang, M. Kesteven, J. Kingsley, M. M. Sinclair, W. Wilson, M. Birkinshaw, H. Liang, K. Lancaster, C.-G. Park, U.-L. Pen and J. B. Peterson, “The Yuan-Tseh Lee Array for Microwave Background Anisotropy,” *The Astrophysical Journal,* vol. 694, no. 2, pp. 1610 - 1618, 2009.

[11] P. A. R. Ade, R. W. Aikin, D. Barkats, S. J. Benton, C. A. Bischoff, J. J. Bock, J. A. Brevik, I. Buder, E. Bullock, C. D. Dowell, L. Duband, J. P. Filippini, S. Fliescher, S. R. Golwala, M. Halpern, M. Hasselfield, S. R. Hildebrandt, G. C. Hilton, V. V. Hristov, K. D. Irwin, K. S. Karkare, J. P. Kaufman, B. G. Keating, S. A. Kernasovskiy, J. M. Kovac, C. L. Kuo, E. M. Leitch, M. Lueker, P. Mason, C. B. Netterfield, H. T. Nguyen, R. O'Brient, R. W. Ogburn IV, A. Orlando, C. Pryke, C. D. Reintsema, S. Richter, R. Schwarz, Z. K. Staniszewski, R. V. Sudiwala, G. P. Teply, J. E. Tolan, A. D. Turner, A. G. Vieregg, C. L. Wong and K. W. Yoon, “Detection of B-Mode Polarization at Degree Angular Scales by BICEP2,” *PHYSICAL REVIEW LETTERS,* vol. 112, no. 24, 2014.

[12] D. Coe, A. Zitrin, M. Carrasco, X. Shu, W. Zheng, M. Postman, L. Bradley, A. Koekemoer, R. Bouwens, T. Broadhurst, A. Monna, O. Host, S. A. Moustakas, H. Ford, J. Moustakas, A. van der Wel, M. Donahue, S. A. Rodney, N. Benítez, S. Jouvel, S. Seitz, D. D. Kelson and P. Rosati, “CLASH: Three Strongly Lensed Images of a Candidate z = 11 Galaxy,” *The Astrophysical Journal,* vol. 762, 2012.

[13] NASA/WMAP Science Team, “NASA,” [Online]. Available: https://wmap.gsfc.nasa.gov/news/. [Accessed June 2018].

[14] D. J. Fixsen, “The Temperature of the Cosmic Microwave Background,” *The Astrophysical Jornal,* vol. 707, pp. 916-920, 2009.

[15] ESA, Planck Collaboration, “ESA,” March 2013. [Online]. Available: https://www.cosmos.esa.int/web/planck/picture-gallery. [Accessed June 2018].

[16] E. Collett, Field Guide to Polarization, Bellingham: SPIE Press, 2005.

[17] W. Hu and M. White, “A CMB Polarization Primer,” *New Astronomy,* 1997.

[18] QUIET-Collaboration, C. Bischoff, A. Brizius, I. Buder, Y. Chinone, K. Cleary, R. N. Dumoulin, A. Kusaka, R. Monsalve, S. K. Naess, L. B. Newburgh, G. Nixon, R. Reeves, K. M. Smith, K. Vanderlinde, I. K. Wehus, M. Bogdan, S. E. Church, R. Davis, C. Dickinson, H. K. Eriksen, T. Gaier, J. O. Gundersen, M. Hasegawa, C. Holler, K. M. Huffenberger, W. A. Imbriale, K. Ishidoshiro, M. E. Jones, P. Kangaslahti, D. J. Kapner, C. R. Lawrence, E. M. Leitch, E. M. Limon, J. J. McMahon, A. D. Miller, M. Nagai, H. Nguyen, T. J. Pearson, L. Piccirillo, S. J. E. Radford, A. C. S. Readhead, J. L. Richards, J.

L. Samtleben, M. Seiffert, M. C. Shepherd, S. T. Staggs, O. Tajima, K. L. Thompson, R. Williamson, B. Winstein, E. J. Wollack and J. T. L. Zwart, "The Q/U Imaging Experiment Instrument," *The Astrophysical Journal,* vol. 768, no. 1, p. 9, 2013.

[19] Z. K. Staniszewski, M. Amiri, R. W. Aikin, S. J. Benton, C. A. Bischoff, J. J. Bock, J. Bonetti, J. A. Brevik, B. Burger, C. D. Dowell, L. Duband, J. P. Filippini, S. R. Golwala, M. Halpern, M. Hasselfield, G. C. Hilton, V. V. Hristov, K. Irwin, J. Kovac, C. Kuo, M. Lueker, T. Montroy, H. Nguyen, R. Ogburn IV, R. O'Brient, A. Orlando, C. Pryke, C. Reintsema, J. Ruhl, R. Schwarz, C. Sheehy, S. Stokes, K. Thompson, G. Teply, J. Tolan, A. Turner, A. Vieregg, P. Wilson, D. Wiebe and C. Wong, "The Keck Array: A Multi Camera CMB Polarimeter," *Journal of Low Temperature Physics,* pp. 827-833, 2012.

[20] D. T. Chuss, A. Ali, M. Amiri, J. Appel, C. L. Bennett, F. Colazo, K. L. Denis, R. Dünner, T. Essinger-Hileman, J. Eimer, P. Fluxa, D. Gothe, M. Halpern, K. Harrington, G. Hilton, G. Hinshaw, J. Hubmayr, J. Iuliano, T. A. Marriage, N. Miller, S. H. Moseley, G. Mumby, M. Petroff, C. Reintsema, K. Rostem, K. U-Yen, D. Watts, E. Wagner, E. J. Wollack, Z. Xu and L. Zeng, "Cosmology Large Angular Scale Surveyor (CLASS) Focal Plane Development," *Journal of Low Temperature Physics,* vol. 184, pp. 759-764, 2016.

[21] T. Suzuki, P. Khosropanah, R. A. Hijmering, M. Ridder, M. Schoemans, H. Hoevers and J. R. Gao, "Performance of SAFARI Short-Wavelength-Band Transition Edge Sensors (TES) Fabricated by Deep Reactive Ion Etching," *IEEE TRANSACTIONS ON TERAHERTZ SCIENCE AND TECHNOLOGY,,* vol. 4, no. 2, pp. 171-178, 2014.

[22] J. A. Bonetti, A. D. Turner, M. Kenyon, H. G. Le Duc, J. A. Brevik, A. Orlando, A. Trangsrud, R. Sudiwala, H. T. Nguyen, R. K. Day, J. J. Bock, S. R. Golwala, J. M. Kovac, W. C. Jones and C. L. Kuo, "Transition Edge Sensor Focal Plane Arrays for the BICEP2, Keck, and Spider CMB Polarimeters," *IEEE TRANSACTIONS ON APPLIED SUPERCONDUCTIVITY,* vol. 21, no. 3, pp. 219-222, 2011.

[23] J. Baselmans, "Kinetic Inductance Detectors," *Journal of Low Temperature Physics,* vol. 167, pp. 292-304, 2012.

[24] A. Kosowsky, "The Atacama Cosmology Telescope," *New Astronomy Reviews,* no. 47, pp. 939-943, 2003.

[25] R. Keisler, S. Hoover, N. Harrington, J. W. Henning, P. Ade, K. A. Aird, J. E. Austermann, . J. A. Beall, A. N. Bender, B. A. Benson, L. E. Bleem, J. E. Carlstrom, C. L. Chang, H. C. Chiang, H.-M. Cho, R. Citron, T. M. Crawford, A. T. Crites, T. de Haan, M. A. Dobbs, W. Everett, . J. Gallicchio, J. Gao, E. M. George, A. Gilbert, N. W. Halverson, D. Hanson, G. C. Hilton, G. P. Holder, . W. L. Holzapfel, Z. Hou, J. D. Hrubes, N. Huang, J. Hubmayr, K. D. Irwin, L. Knox, A. T. Lee, E. M. Leitch, D. Li, D. Luong-Van, D. P. Marrone, J. J.

McMahon, J. Mehl, S. S. Meyer, L. Mocanu, T. Natoli, J. P. Nibarger, V. Novosad, S. Padin, C. Pryke, C. L. Reichardt, . J. E. Ruhl, B. R. Saliwanchik, J. Sayre, K. K. Schaffer, E. Shirokoff, G. Smecher, A. A. Stark, K. T. Story, C. Tucker, K. Vanderlinde, J. D. Vieira, G. Wang, N. Whitehorn, V. Yefremenko and O. Zahn, “Measurements of Sub-Degree B-Mode Polarization in the Cosmic Microwave,” *The Astrophysical Journal,* vol. 807, 2015.

[26] W. Wu, P. Ade, Z. Ahmed, K. Alexander, M. Amiri, D. Barkats, S. Benton, C. Bischoff, J. Bock, R. Bowens-Rubin, I. Buder, E. Bullock, V. Buza, J. Connors, J. Filippini, S. Fliescher, J. Grayson, M. Halpern, S. Harrison, G. Hilton, V. Hristov, H. Hui, K. Irwin, J. Kang, K. Karkare, E. Karpel, S. Kefeli, S. Kernasovskiy, J. Kovac, C. Kuo, K. Megerian, C. Netterfield, H. Nguyen, R. O'Brient, C. Pryke, C. Reintsema, S. Ricter, C. Sorensen, Z. Staniszewski, B. Steinbach, R. Sudiwala, G. P. Teply, K. Thompson, J. Tolan, C. Tucker, A. Turner, A. Vieregg, A. Weber, D. Wiebe, J. Willmert and K. Yoon, “Initial Performance of BICEP3: A Degree Angular Scale,” *Journal Low Temperature Physics,* vol. 184, pp. 765-771, 2015.

[27] C. De Breuck, “Scientific Requirements of ALMA, and its Capabilities for Key-Projects: Extragalatic,” *Proc. of the Dusty and Molecular Universe: A Prelude to Herschel and ALMA, ESA Special Publications,* vol. 577, 2005.

[28] C. Padilla - AUI/NRAO, “ALMA Observatory,” [Online]. Available: https://www.almaobservatory.org/en/images/. [Accessed June 2018].

[29] G. Pilbratt, J. Riedinger, T. Passvogel, G. Crone, D. Doyle, U. Gageur, A. Heras, C. Jewell, L. Metcalfe, S. Ott and M. Schmidt, “Herschel Space Observatory: An ESA facility for far-infrared and submillimetre astronomy,” *Astronomy and Astrophysics,* vol. 518, 2010.

[30] ESA/Herschel/NASA/JPL-Caltech, T. Pyle & R. Hurt, “ESA-Herschel Space Observatory,” [Online]. Available: http://sci.esa.int/herschel/59586-the-herschel-space-observatory/. [Accessed June 2018].

[31] NASA, “COBE,” [Online]. Available: https://science.nasa.gov/missions/cobe/. [Accessed November 2017].

[32] C. L. Bennett, D. Larson, J. L. Weiland, N. Jarosik, G. Hinshaw, N. Odegard, K. M. Smith, R. S. Hill, B. Gold, E. Komatsu, M. Halpern, M. R. Nolta, L. Page, D. N. Spergel, E. Wollack, J. Dunkley, A. Kogut, M. Limon, S. S. Meyer, G. S. Tucker and E. L. Wright, “Nine-Year Wilkinson Microwave Anisotropy Probe (WMAP),” *The Astrophysical Journal Supplement Series,* vol. 208, 2013.

[33] M. Bersanelli, N. Mandolesi, R. C. Butler, A. Mennella, F. Villa, B. Aja, E. Artal, E. Artina, C. Baccigalupi, M. Balasini, G. Baldan, A. Banday, P. Bastia, P. Battaglia, T. Bernardino, E. Blackhurst, L. Boschini, C. Burigana, G. Cafagna, B. Cappellini, F. Cavaliere, F.

Colombo, G. Crone, F. Cuttaia, O. D'Arcangelo, L. Danese, R. D. Davies, R. J. Davis, L. De Angelis, G. C. DeGasperis, L. DeLaFuente, A. De Rosa, G. DeZotti, M. C. Falvella, F. Ferrari, L. Figini, S. Fogliani, C. Franceschet, E. Franceschi, T. Gaier, S. Garavaglia, F. Gomez, K. Gorski, A. Gregorio, P. Guzzi, J. M. Herreros, S. R. Hildebrandt, R. Hoyland, N. Hughes, M. Janssen, P. Jukkala, D. Kettle, V. H. Kilpia, M. Laaninen, P. M. Lapolla, C. R. Lawrence, D. Lawson, J. P. Leahy, R. Leronardi, P. Leutenegger, S. Levin, P. B. Lilje, S. R. Lowe, P. M. Lubin, D. Maino, M. Malaspina, M. Maris, J. Marti-Canales, E. Martinez-Gonzalez, A. Mediavilla, P. Meinhold, M. Miccolis, G. Morgante, P. Natoli, R. Nesti, L. Pagan, C. Paine, B. Partridge, J. P. Pascual, F. Pasian, D. Pearson, M. Pecora, F. Perrotta, P. Plantania, M. Pospieszalski, T. Poutanen, M. Prina, R. Rebolo, N. Roddis, J. A. Rubino-Martin, M. J. Salmon, M. Sandri, M. Seiffert, R. Silvestri, A. Simonetto, P. Sjoman, G. F. Smoot, C. Sozzi, L. Stringhetti, E. Taddei, J. Tauber, L. Terenzi, M. Tomasi, J. Tuovinen, L. Valenziano, J. Varis, N. Vittorio, L. A. Wade, A. Wilkinson, F. Winder, A. Zacchei and A. Zonca, “Planck pre-launch status: Design and description of the Low Frequency Instrument,” *Astronomy and Astrophysics,* vol. 520, pp. 1-21, 2010.

[34] W. Holmes, J. Bock, B. Crill, T. Koch, W. Jones, A. Lange and C. Paine, “Initial test results on bolometers for the Planck high frequency instrument,” *Applied Optics,* vol. 47, pp. 5996-6008, 2008.

[35] NASA/JPL-Caltech/ESA, “Planck,” [Online]. Available: https://www.nasa.gov/mission_pages/planck/multimedia/pia16874.html. [Accessed June 2018].

[36] M. Bessou, B. Chassagne, J. Caumes, C. Pradère, P. Maire, M. Tonusson and E. Abraham, “Three-dimensional terahertz computed tomography of human bones,” *APPLIED OPTICS,* pp. 6738-6744, 2012.

[37] X. Yang, X. Zhao, K. Yang, Y. Liu, Y. Liu, W. Fu and Y. Luo, “Biomedical Applications of Terahetz Spectroscopy and Imaging,” *Trends in Biotechnology,* vol. 34, no. 10, pp. 810-824, 2016.

[38] N. Karpowicz, H. Zhong, C. Zhang, K. Lin, J. Hwang, J. Xu and X. Zhang, “Compact continuous-wave subterahertz system for inspection applications,” *APPLIED PHYSICS LETTERS,* vol. 86, 2005.

[39] K. W. Kim, K.-S. Kim, H. Kim, J. Park, J.-H. Park, J.-H. Han, S.-H. Seok, J. Park, Y. Choi, Y. I. Kim, J. K. Han and J. -H. Son, “Terahertz dynamic imaging of skin drug absorption,” *Optics Express,* vol. 20, no. 9, 2012.

[40] G. W. Guglietta, B. T. Diroll, E. A. Gaulding, J. L. Fordham, S. Li, C. B. Murray and J. B. Baxter, “Lifetime, Mobility, and Diffusion of Photoexcited Carriers in Ligand-Exchanged

Lead Selenide Nanocrystal Films Measured by Time-Resolved Terahertz Spectroscopy," *American Chemical Society,* vol. 9, no. 2, pp. 1820-1828, 2015.

[41] C. S. Ponseca, Jr. and V. Sundström, "Understanding Charge Carrier Dynamics in Solar Cell Materials using Time Resolved Terahertz Spectroscopy," *IEEE Conference,* 2015.

[42] R. Piesiewicz, C. Jansen, S. Wietzke, D. Mittleman, M. Koch and T. Kürner, "Properties of Building and Plastic Materials in the THz Range," *International Journal of Infrared and Millimeter Waves,* vol. 28, pp. 363-371, 2007.

[43] CST - Computer Simulation Technology, [Online]. Available: https://www.cst.com/.

[44] Computer Simulation Technology., "CST Microwave Studio, Workflow and Solver Overview," 2016.

[45] S. R. Pennock and P. R. Shepherd, Microwave Engineering, New York: McGraw-Hill, 1998.

[46] E. Penard and J. P. Daniel, "Mutual Coupling Between Microstrip Antennas," *Electronics Letters,* vol. 18, no. 14, pp. 605-607, 1982.

[47] S. Drabowitch, A. Papiernik, H. Griffiths, J. Encinas and B. Smith, Modern Antennas, London: Chapman & Hall, 1998.

[48] N. J. Cronin, Microwave and Optical Waveguides, IOP Publishing Ltd, 1995.

[49] S. Silver, Microwave Antenna Theory and Design, New York: McGraw-Hill, Inc., 1949.

[50] "kpc flange launcher 100 311 Datasheet," [Online]. Available: https://www.shf.de/wp-content/uploads/datasheets/datasheet_kpc_flange_launcher_100_311.pdf. [Accessed 11 May 2017].

[51] M. A. Matin and A. I. Sayeed, "A Design Rule for Inset-fed Rectangular Microstrip Patch Antenna," WSEAS TRANSACTIONS on COMMUNICATIONS. Department of Electrical Engineering and Computer Science, North South University, Dhaka, Bangladesh.

[52] Q. C. Q. Z. Z.H. Tu, "High-Gain Slot Antenna with Parasitic Patch," *Progress In Electromagnetics Research Letters,* vol. 15, pp. 27-36, 2010.

[53] K.-F. L. T. Huynh, "Single-layer single-patch wideband," *ELECTRONICS LETTERS,* vol. 31, pp. 1310-1312, 1995.

[54] F. Yang, X.-X. Zhang, X. Ye and Y. Rahmat-Samii, "Wide-Band E-Shaped Patch Antennas for Wireless," *IEEE TRANSACTIONS ON ANTENNAS AND PROPAGATION,,* vol. 49, no. 7, pp. 1094-1100, 2001.

[55] P. Goldsmith, Quasioptical Systems: Gaussian Beam Quasioptical propagation and Applications, IEEE Press., 1998.

[56] J. A. Murphy and A. Egan, “Examples of Fresnel diffraction using Gaussian modes,” *European journal of physics,* pp. 121-127, 1993.

[57] J. A. Murphy, A. Egan and S. Withington, “Truncation in Millimeter and Submillimeter-Wave Optical Systems,” *IEE Transaction on Antennas and Propagation,* vol. 41, no. 10, pp. 1408-1413, 1993.